W Boson Production in Ultrarelativistic Heavy-Ion Collisions at the CERN LHC

Thomas E. Balestri

Submitted in partial fulfillment of the

requirements for the degree

of Doctor of Philosophy

in the Graduate School of Arts and Sciences

STONY BROOK UNIVERSITY

Long Island, New York

2015

Thesis Advisor: Dr. Jiangyong Jia

ABSTRACT

W Boson Production in Ultrarelativistic Heavy-Ion Collisions at the CERN LHC

Thomas E. Balestri

Ultrarelativistic heavy-ion collisions at the CERN Large Hadron Collider (LHC) are capable of producing a medium of deconfined quarks and gluons. This phase of nuclear matter is called a Quark-Gluon Plasma (QGP) and is believed to have been present during the first microseconds following the Big Bang. W bosons are a unique probe in a QGP since they do not carry color charge and thus do not interact with a strongly-coupled medium. Furthermore, the kinematics of W bosons are sensitive to the Bjorken momentum fraction x of partons within nucleons, and therefore W bosons may also be used to constrain parton distribution functions and to detect the presence of nuclear effects. This thesis presents the measurement of W boson production in the dense nuclear environment created in Pb+Pb collisions at a per nucleon pair center-of-mass energy $\sqrt{s_{\mathrm{NN}}} = 2.76$ TeV. The data for this measurement were collected with the ATLAS detector in 2011 and correspond to an integrated luminosity $\int \mathrm{Ldt} = 0.14$ nb^{-1}. The production of W bosons is detected using the $W \rightarrow \mu\nu_\mu$ decay channel, resulting in fiducial yields of 5487 $\pm$96 (stat.) $\pm$86 (syst.) $W^+ \rightarrow \mu^+\nu_\mu$ events and 5262 $\pm$95 (stat.) $\pm$83 (syst.) $W^- \rightarrow \mu^-\bar{\nu}_\mu$ events. These results are combined with yields from the corresponding electron channel $W \rightarrow e\nu_e$, and the combined measurement is used to construct the differential production yields and lepton charge asymmetry as a function of lepton absolute pseudorapidity. The integrated production yields and charge ratio as a function of the mean number of binary nucleon-nucleon collisions $\langle N_{\mathrm{part}} \rangle$ are also presented. The results are compared to predictions based on next-to-leading order QCD calculations. These observables can aid in better understanding nucleon structure within a heavy nucleus as well as provide insight into the mechanism of jet energy loss in a QGP.

Table of Contents

List of Figures

xiii

xvi

List of Tables

Acknowledgments

The acknowledgments go here. The acknowledgments go here. The acknowledgments go here. The acknowledgments go here. The acknowledgments go here. The acknowledgments go here. The acknowledgments go here.

To my father, whose sacrifices allowed for my success.

Chapter 1

Introduction

$W^{\pm}$ bosons were first discovered in $p\bar{p}$ collisions at the CERN SPS collider in 1983 [51] and provided confirmation of the Standard (Glashow-Salam-Weinberg) Electroweak Model. Since then, the cross section for W production has been calculated in pertubative Quantum Chromodynamics (pQCD) up to next-to-next-to-leading order (NNLO) [52, 53]. The firm knowledge of W production has been used extensively at high-energy colliders to test Standard Model (SM) predictions, search for physics beyond the Standard Model (BSM), and provide information about nucleon structure by constraining parton distribution functions (PDFs). However, over the past decades, measurements in high-energy accelerators involving W bosons have strictly been confined to bi-nucleon systems (i.e. pp, $p\bar{p}$).

In 2010, the Large Hadron Collider (LHC) at CERN began colliding Pb ions at the highest center-of-mass energy ever attained in a heavy-ion system, resulting in abundant production of W bosons and enabling the first measurement of W boson production in an $A + A$ system. This is the topic of this thesis, which presents the most current and precise measurements of W boson production in heavy-ion collisions (the corresponding publication may be found in Ref. [40]). W bosons are typically detected through their leptonic e, μ decay channels, which also involve the production of undetectable neutrinos. Thus, an experimental signature in events containing a W boson is the presence of large missing transverse energy (see Figure 1.1).

A question of primary importance is how the physics of free nucleon systems compare to that of bound nucleon systems (so-called nuclear effects). A significant advantage of W production in $A+A$ collisions is the ability to study isospin effects induced by pn and nn interactions. The leading-
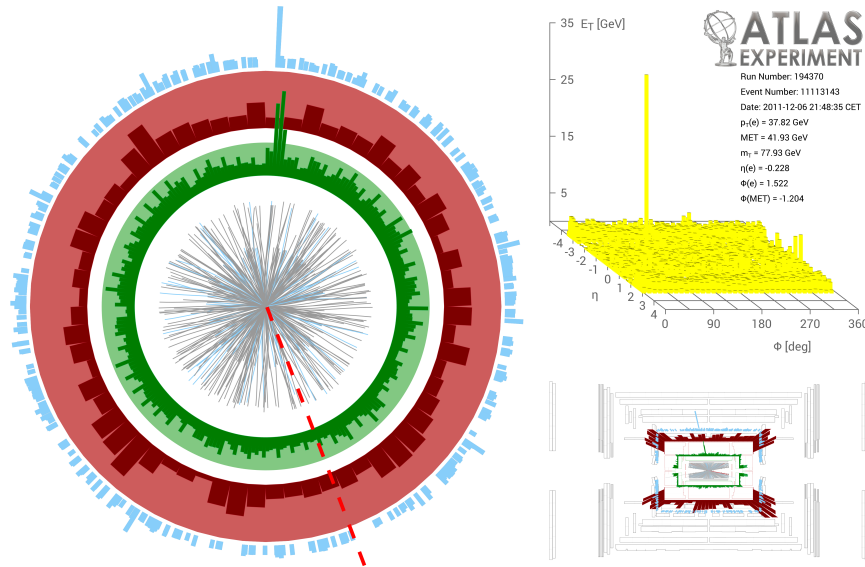
Figure 1.1: Event display of a $W \to e\nu_e$ event during the 2011 heavy-ion run period at the LHC.

order mechanisms for $W^+(W^-)$ production proceed via the annihilation of a $u(d)$ valence quark and $\bar{d}(\bar{u})$ sea quark. Since W bosons and large rapidity are preferentially produced in the direction of the quark with a larger momentum fraction, isospin effects are attributed to the valence quark distribution functions at large Bjorken-x and are expected to alter the W^+/W^- ratio relative to pp and $p\bar{p}$ measurements. Furthermore, parton distribution functions are expected to be modified by the presence of other nucleons within the nucleus and thus, the sensitivity of the W kinematics to the parton momentum fraction may provide a means to observe nuclear effects. This is one of two results presented in this work.

In heavy-ion collisions at ultrarelativistic energies, normal nuclear matter undergoes a phase transition to a deconfined state of quarks and gluons called a Quark-Gluon Plasma (QGP). Since W bosons (and its electroweak decay products) do not carry color charge, they do not interact with this strongly-coupled medium. Thus, the W production rate should be unaffected by the presence of a QGP and should scale with the number of binary nucleon-nucleon interactions. This property can be used to benchmark parton energy loss in a QGP and to provide information on the modified jet fragmentation function. The dependence of W production yields on the number of binary nucleon-nucleon collisions is the second result presented in this work.

This thesis is organized as follows: Chapter 2 discusses the important theoretical and phenomenological developments leading to this measurement. The major findings and results preceding the construction of Quantum Chromodynamics are mentioned. Parton distribution functions are introduced and the correlation of W production with the parton structure of nucleons is discussed. A section on the formation of a QGP is provided and the chapter concludes with a discussion on nuclear effects and the applicability of W bosons in heavy-ion systems.

Chapter 3 describes the operation of the Large Hadron Collider and introduces pertinent experimental terminology. The ATLAS detector and its individual components are then described in detail.

Chapter 4 provides a discussion on the muon identification and reconstruction algorithms used in ATLAS. Descriptions of the methods by which muon measurements in different sub-detectors are combined to form a muon track and various corrections for material effects are applied are included in this chapter.

Chapter 5 details the analytical procedure for locating W bosons in heavy-ion collisions. This chapter includes a list of the datasets used in the current measurement, event selection, construction of missing energy in a heavy-ion collision, detector efficiencies, background determination, and systematic uncertainties.

Chapter 6 presents the results. These include measurements of the differential W production yields as a function of absolute pseudorapidity, the lepton charge asymmetry, and the integrated yields and charge ratio as a function of the mean number of binary collisions.

The final chapter (Chapter 7) provides a summary and outlook for measurements involving W bosons using the current $p + \mathrm{Pb}$ and future Pb+Pb data.

Chapter 2

Background

High-energy physics is concerned with understanding the basic building blocks of matter and the physical laws that govern their interactions. Early in the study of nuclear physics, it was observed that in addition to the gravitational and electromagnetic forces, two additional forces govern the universe: weak interactions responsible for β decay and strong interactions that bind nucleons within the nucleus. At the scale of elementary particles, the dominant forces are the electromagnetic, weak, and strong interactions. These are well described by the Standard Model with gauge group $SU(3) \otimes SU(2) \otimes U(1)$ [54, 55].

Within the Standard Model there are three families of elementary particles: quarks, leptons, and force mediators. These are summarized in Figure 2.1. $SU(2)$ generates W bosons, which are mediators of weak charged-current interactions. The $SU(2) \otimes U(1)$ gauge group generates the Z boson and photon, which are mediators of weak neutral-current and electromagnetic interactions, respectively. The $SU(3)$ [56–58] symmetry group generates the gluon, which is responsible for the strong interaction. Spontaneous symmetry breaking by a scalar field gives rise to the masses of the quarks, leptons, and heavy-gauge bosons via the Higgs mechanism [1].

In 1952, the Brookhaven Cosmotron became the first modern particle accelerator and began producing strange particles in the laboratory [59]. The discovery of internal symmetries of the strong interaction facilitated the classification of hadrons into multiplets. Studies of nuclear reactions showed that, to a good approximation, the strong interactions are independent of the charge of the nucleons. Interchanging a proton and neutron does not change the nature of the strong interaction.
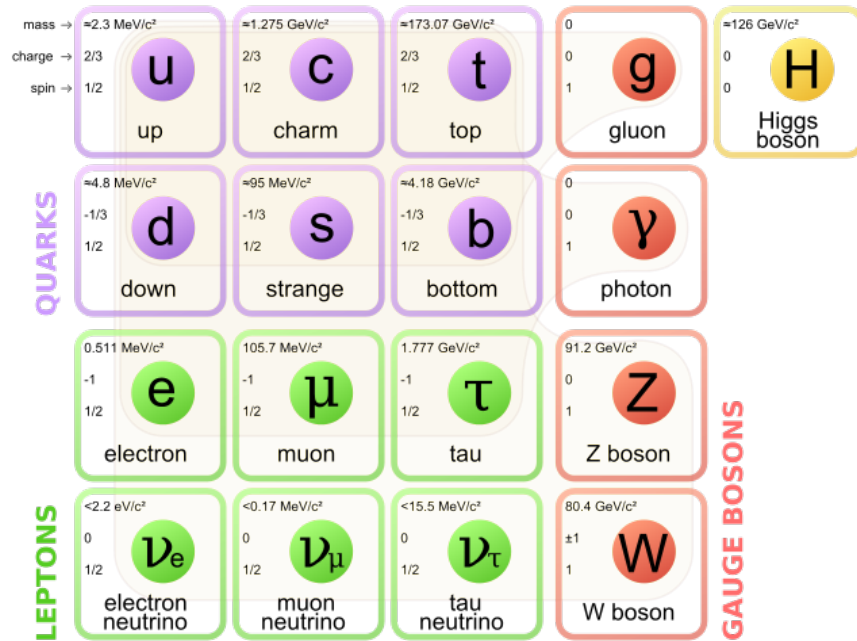
Figure 2.1: Summary of the elementary particles that make up the Standard Model. There are three generations of quarks and leptons. Gauge bosons are mediators of the strong, weak, and electromagnetic forces. The Higgs Mechanism [1] is responsible for the masses of the leptons, quarks, and heavy-gauge bosons.

Therefore, the strong interaction possesses an SU(2) isospin symmetry [1] in which the p and n states form an isospin doublet. The SU(2) generators I_1, I_2, I_3 satisfy the Lie algebra:

$$[I_i, I_j] = i\epsilon_{ijk}I_k \tag{2.1}$$

Acting on the p and n states,

$$I_3 \ket{p} = \frac{1}{2}\ket{p} \qquad I_3 \ket{n} = -\frac{1}{2}\ket{n}$$
$$I_+ \ket{n} = \ket{p} \qquad I_- \ket{p} = \ket{n} \tag{2.2}$$

The isospin can be extended to other hadrons to form additional isospin multiplets (e.g. π^+, π^0, π^- are $I = 1$ isospin triplets).

The observation that heavy baryons like Λ and K particles are copiously produced (at a time scale of $\sim 10^{-23}$ seconds) but decay slowly ($\sim 10^{-10}$ seconds) led to the formulation of a new quantum number: strangeness S. It was postulated [60] that strange particles are produced by the strong force but decay via the weak interaction. Gell-Mann [61] and Nishijima [62] then proposed that the strangeness of a particle is conserved in any strong interaction but is not conserved in a weak interaction. This explained the strangeness-conserving process $\pi^- + p \rightarrow \Lambda^0 + K^0$ and strangeness-changing process $\Lambda^0 \rightarrow \pi^0 + p$ and $K^0 \rightarrow \pi^+ + \pi^-$, where $S(\Lambda^0) = -1$, $S(K^0) = +1$, and S of pions and nucleons are zero.

Strangeness is associated to a $U(1)$ symmetry, like the electric charge Q. Gell-Mann and Nishijima formulated a relation between S, Q, and I_3 (isospin generator) that is conserved under all known interactions:

$$Q = I_3 + \frac{Y}{2} \tag{2.3}$$

with

$$Y = B + S$$

where B is the baryon number. Y is called the hypercharge.

---

[1]This is actually not an exact symmetry since the mass difference within a multiplet is not zero. However, the mass difference is at most a few percent, and thus isospin is an approximate symmetry.

In 1961, Gell-Mann and Ne'eman showed that mesons and baryons with the same spin and parity could be grouped to form representations of the SU(3) group. These representations are known as the *Eightfold-Way*. This scheme was further corroborated by the discovery of the Ω^- [63], which was hypothesized by the model. However, none of the fundamental representations of SU(3) were realized by the observed hadrons. This led to the proposal of the *Quark Model* by Gell-Mann [64] and Zweig [65] who postulated that hadrons are composed of more elementary constituents called quarks.

2.1 Quark Model

There are three types (flavors) of light quarks in the fundamental representation (denoted **3**) of SU(3): the u (up) quark with a charge of 2/3, the d (down) quark with a charge of $-1/3$, and the s (strange) quark also with a charge of $-1/3$. The corresponding antiquarks ($\bar{q}$) belong to the conjugate representation (denoted $\bar{\mathbf{3}}$). Each quark possesses a color quantum number: (anti)red, (anti)green, or (anti)blue. In this formulism, (anti)baryons ($B = 1$) and (anti)mesons ($B = 0$) are qqq ($\bar{q}\bar{q}\bar{q}$) and $q\bar{q}$ "colorless" bound states, respectively. The combinations of light quark mesons are grouped into a SU(3) singlet and octet $\mathbf{3} \otimes \bar{\mathbf{3}} = 8 \oplus 1$, whereas the light quark baryon combinations yield a decuplet, two octets, and a singlet $\mathbf{3} \otimes \mathbf{3} \otimes \mathbf{3} = 10 \oplus 8 \oplus 8 \oplus 1$.

The three color states also generate an SU(3) symmetry. However, the color symmetry is exact whereas the flavor symmetry is approximate due to the different masses of the u, d, and s quarks [2, 66]. The discovery of the c (charm), b (bottom), and t (top) quarks extends the flavor SU(3) group to SU(6). However, the symmetry at higher orders is so poor that the t quark does not form bound states at all.

The Quark Model led to the view that quarks interact via the exchange of colorless gluons, which are an octet of vector fields in the adjoint representation of SU(3). The proton was perceived as consisting of one d and two u quarks that are collectively called "valence" quarks and of quark-antiquark pairs produced from gluon-splitting, forming the quark "sea". However, at this point in time, quarks and gluons were still theoretical entities [56].

2.2 Evidence of Quarks and Gluons

The inner structure of the proton was first studied in deep inelastic [2] scattering (DIS) experiments using leptonic projectiles on a nucleus target. To address this new data, Feynman and Bjorken introduced the parton model [67], which views nucleons as composite objects made up of point-like constituents called partons. The parton model provided a simple framework for calculating scattering cross sections and structure functions of nucleons.

The process $\ell N \to \ell' X$ is shown in Figure 2.2. In this diagram, k and k' are the four-momenta of the incoming and outgoing leptons and P is the four-momentum of a nucleon with mass M. The square of the center-of-mass energy is then:

$$s = (P + k)^2 \tag{2.4}$$
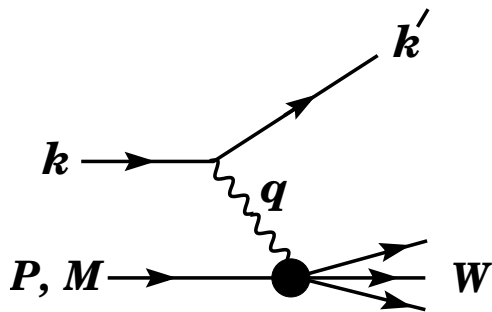
Figure 2.2: Description of deep inelastic scattering $\ell N \to \ell' X$. The quantities k and k' are the four-momenta of the incoming and outgoing leptons, P is the four-momentum of a nucleon with mass M, and $W = (P + q)^2 = M^2 + \frac{1-x}{x} Q^2$ is the mass of the recoiling system X. The exchange particle (γ, W, or Z) transfers four-momentum $q = k - k'$ to the nucleon [2].

The momentum transfered by the virtual photon to the nucleon is $q = k - k'$. The energy loss of the lepton in the rest frame of the nucleon can be expressed as:

$$\nu = E - E' = \frac{q \cdot P}{M} \tag{2.5}$$

---

[2]The process is "deep" since the photon deeply penetrates the proton ($Q^2 >> M^2$). The process is inelastic because the proton breaks up into components with mass $W^2 >> M^2$.

where E and E' are initial and final lepton energies. The energy scale of the collision is conventionally written as $Q^2 \equiv -q^2 > 0$ [3]. Then the fraction of the nucleon's momentum carried by the struck quark can be expressed as:

$$x = \frac{Q^2}{2M\nu} \tag{2.6}$$

This is known as the *Bjorken x*.

The cross section for inclusive inelastic scattering in terms of the structure functions $W_1(\nu, Q^2)$ and $W_2(\nu, Q^2)$ and scattering angle θ is:

$$\left(\frac{d\sigma}{d\Omega dE'} \right)_{\text{lab}} = \frac{\alpha_e^2}{4E^2 \sin^4 \frac{\theta}{2}} \left[W_2(\nu, Q^2) \cos^2 \frac{\theta}{2} + W_1(\nu, Q^2) \sin^2 \frac{\theta}{2} \right] \tag{2.7}$$

Thus, the structure functions can be determined by measuring the energy and angular dependence of the outgoing lepton.

To determine if the leptons are scattering off point-like objects, the behavior of the cross section for point-like scattering can be compared to that for scattering off a charge cloud. The structure functions from elastic scattering off a static charge distribution have electric and magnetic form factors [68] that decrease the elastic cross section with increasing Q^2, making it more likely that the proton breaks up. However, for an electron scattering off partons inside the nucleus, the structure functions have only a weak Q^2 dependence at fixed x. Bjorken reasoned that in the limit that $Q^2 \to \infty$, the structure functions would become:

$$F_1(x) := \lim_{Q^2 \to \infty} MW_1(\nu, Q^2)$$

$$F_2(x) := \lim_{Q^2 \to \infty} \nu W_2(\nu, Q^2)$$

$$\tag{2.8}$$

The dependence of the proton structure functions $F_{1,2}$ only on x is known as Bjorken scaling. The scaling behavior was originally observed in the SLAC experiments and later by other experiments,

---

[3]$-q^2 = 2(EE' - k \cdot k') - m_\ell^2 - m_{\ell'}^2$, where $m_{\ell(\ell')}$ are the initial and final lepton masses. If $EE' \sin^2(\theta/2) >> m_{\ell(\ell')}$, $-q^2 \approx \sin^2(\theta/2)$, where θ is the lepton scattering angle w.r.t. the lepton beam direction.

as shown in Figure 2.3 [69–73]. The data supported the existence of point-like partons within the proton.
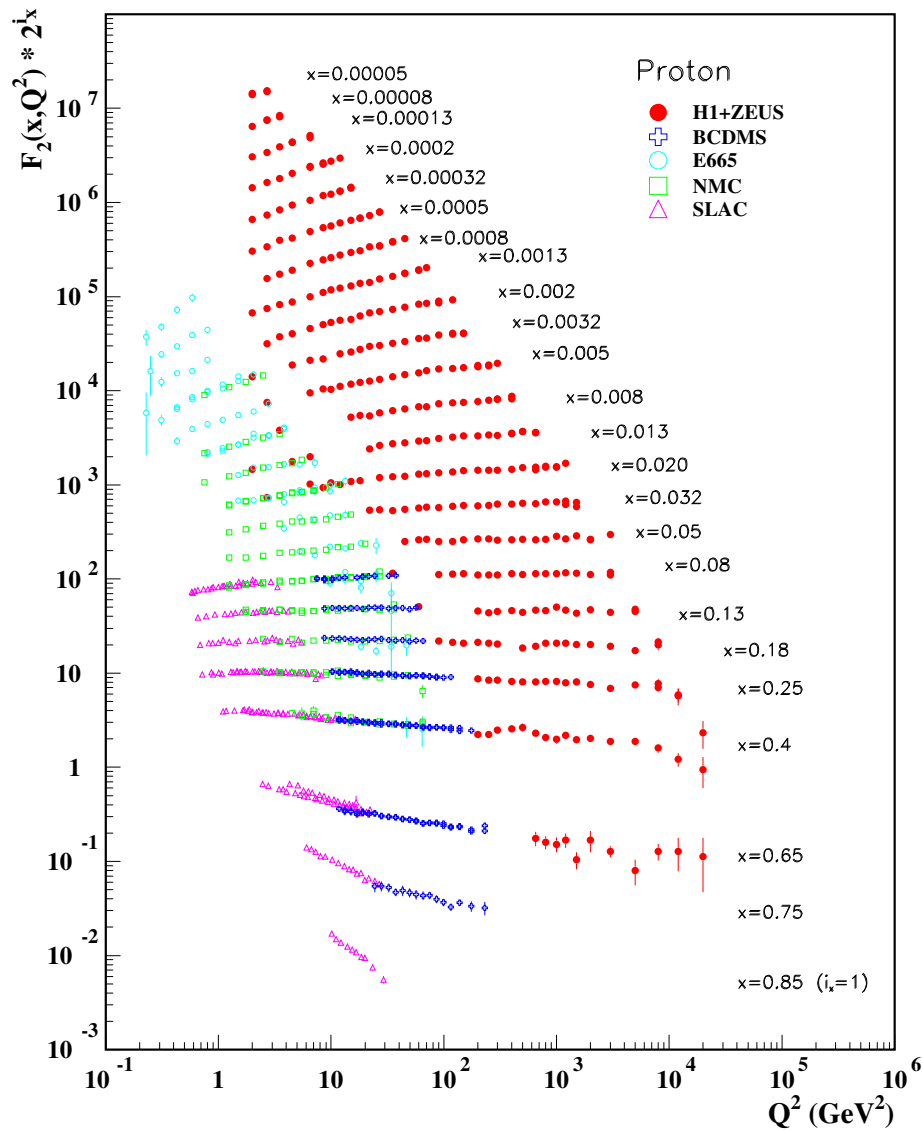
Figure 2.3: The proton structure function F_2 in electromagnetic scattering of electrons and positrons on protons (H1 and ZEUS) and of electrons (SLAC) and muons (BCDMS, E665, NMC) on a fixed target [2]. The data are plotted as a function of Q^2. Scaling violations appear at $x < 10^{-2}$.

In the parton model, the proton structure functions can be expressed in terms of *parton distribution functions*. In the infinite momentum frame of the proton, the parton momentum is collinear with that of the proton. If each parton has charge e_i and a probability $f_i(x)$ to carry momentum fraction x of the total momentum of the parent proton, then the density functions satisfy:

$$\sum_i \int x f_i(x) dx = 1 \tag{2.9}$$

where the summation is over all constituents of the proton. The parton has longitudinal momentum $x p_{L,\text{proton}}$ and mass $x M_{\text{proton}}$. It can be shown [74] that:

$$F_2(x) = x \sum_i e_i^2 f_i(x) \tag{2.10}$$

If the partons are spin-1/2 fermions:

$$F_2(x) = 2x F_1(x) \tag{2.11}$$

This is the Callan-Gross relation and was confirmed by experimental studies [75] (Figure 2.4).
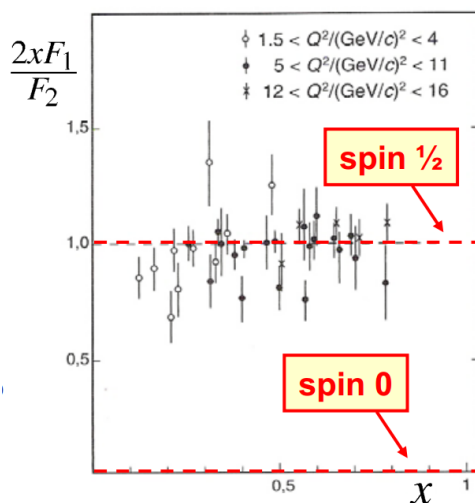
Figure 2.4: Experimental evidence of the Callan-Gross relation, showing that partons are spin-1/2 particles. If partons were spin-0, the magnetic structure function $F_1(x) = 0$.

However, to show that these partons are indeed quarks, the parton distribution functions had to predict the correct flavor mixture in the nucleons. If $q(x)$ $(\bar{q}(x))$ represent the parton distribution

functions of q ($\bar{q}$) quarks, and $d^n(x)(u^n(n)) = u^p(x)(d^p(x)) \equiv u(x)(d(x))$, then from Eqn. 2.10 the proton and neutron structure functions [73, 76, 77] can be expressed as:

$$F_2^{ep} = x \left[\frac{1}{9}(4u_v(x) + d_v(x)) + \frac{4}{3}S \right]$$
$$F_2^{en} = x \left[\frac{1}{9}(u_v(x) + 4d_v(x)) + \frac{4}{3}S \right] \tag{2.12}$$

where v represents valence quarks and S is the contribution of the quark-antiquark pairs from the sea. It was predicted that as $x \to 0$ at fixed Q^2, the number of quarks should increase and contributions from the sea become important. The ratio of the structure functions would then become:

$$\frac{F_2^{e+n}(x)}{F_2^{e+p}(x)} \to 1 \qquad \text{as } x \to 0 \tag{2.13}$$

As $x \to 1$, the valence quarks should dominate and:

$$\frac{F_2^{e+n}(x)}{F_2^{e+p}(x)} \to \frac{u_v(x) + 4d_v(x)}{4u_v(x) + d_v(x)} \qquad \text{as } x \to 1 \tag{2.14}$$

In the proton at large x, the density function $u_v(x) >> d_v(x)$ and Equation 2.14 approaches $1/4$ [4]. This was observed experimentally, as shown in Figure 2.5, and strongly suggested that these partons are quarks. Experimental data from $\nu + N$ scattering at CERN [79, 80] also supported this conclusion.

However, from the DIS data, the u and d valence and sea quarks were found to carry approximately 50% of the total momentum of the proton. Since the virtual photon in $e + p$ scattering only probes charged particles, the additional 50% must be from neutral particles that do not contribute to the cross section. This provided the first evidence of the existence of gluons predicted by field theory and could explain the scaling violations at low-x observed in the experimental data (Figures 2.3 and 2.6). The scaling violation could then be interpreted as the result of radiation of hard gluons from quarks. At the time, the parton model could not predict this behavior, and it was here where the field theory of strong interactions could successfully describe the experimental data.

---

[4]Corrections for nuclear binding and nucleon off-shell effects put this value closer to 3/7 but are model dependent and introduce significant uncertainties [78].
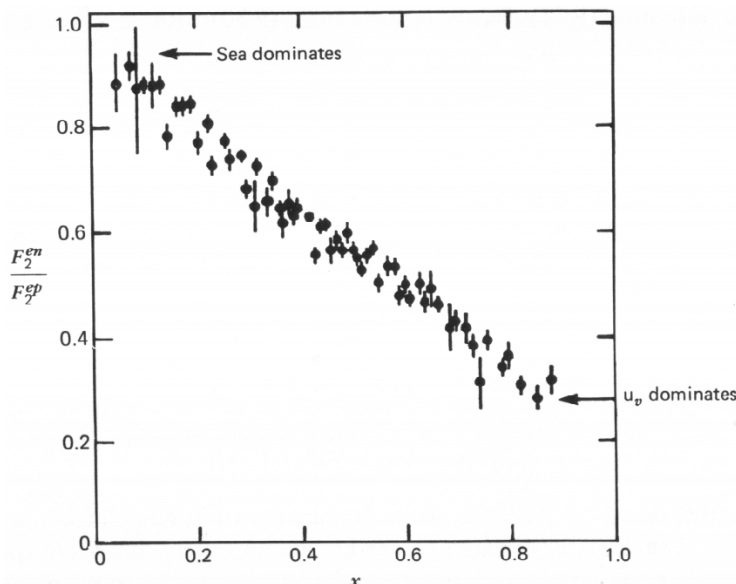
Figure 2.5: Ratio of the proton and neutron structure functions as a function of Bjorken x.

2.3 Quantum Chromodynamics

The strong interactions of quarks and gluons are governed by Quantum Chromodynamics (QCD). This model is described by a non-Abelian Yang-Mills gauge theory with gauge group SU(3) [2, 81–83]. The QCD Lagrangian describes the interaction of three equal-mass Dirac fields (three colors for each quark flavor) with eight massless gluon fields and is given by:

$$\mathcal{L} = \sum_q \bar{\psi}_{q,a}(i\gamma^\mu D_\mu - m_q \delta_{ab})\psi_{q,b} - \frac{1}{4}F^A_{\mu\nu}F^{\mu\nu}_A - \frac{1}{2\alpha_{\mathrm{G}}}\partial^\mu \mathcal{A}^C_\mu \partial_\mu \mathcal{A}^\mu_C - \partial_\mu \bar{\varphi}_C D^\mu \varphi^C \tag{2.15}$$

where repeated indices imply summation. γ^μ are the Dirac γ-matrices, and $\psi_{q,a(b)}$ are the quark-field spinors for quark flavor q and mass m_q. The color indices $a(b)$ run over the number of quark color quantum numbers (i.e. $a, b = 1$ to $N_c = 3$).

The covariant derivative D_μ is associated with local transformations of the quark-field spinors and is given by:

$$D_\mu = \partial_\mu \delta_{ab} - i g_s t^C_{ab} \mathcal{A}^C_\mu \tag{2.16}$$
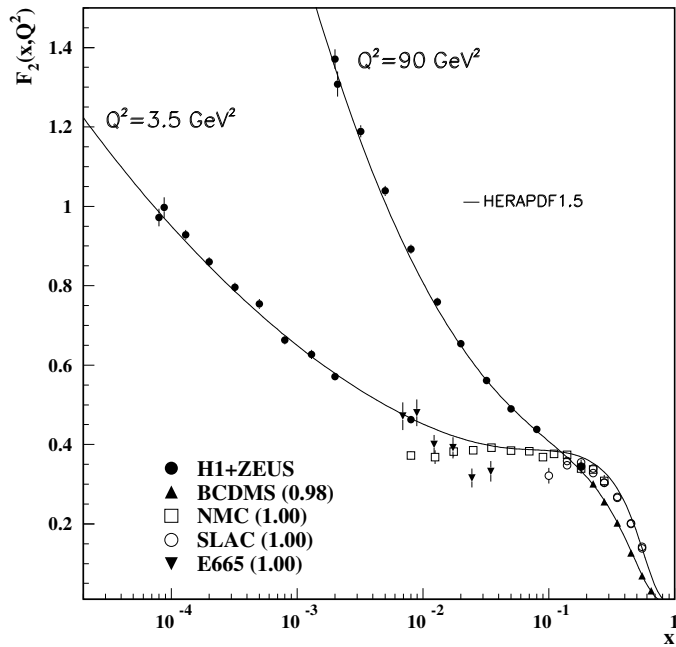
Figure 2.6: Proton structure function at two Q^2 values. Bjorken scaling is observed down to the "pivot point" at $x \sim 0.14$, where scaling violations are observed due to gluon radiation [2].

where $\mathcal{A}_\mu^C$ represents the gluon fields and C [5] runs over the eight colors of gluons (i.e. $C = 1$ to $N_c^2 - 1 = 8$). $t_{ab}^C \equiv \lambda_{ab}^C/2$ represent the eight 3×3 Gell-Mann matrices and are generators of rotations in SU(3) space of the quark color state after interaction with a gluon. $g_s(\equiv 2\sqrt{\alpha_s\pi})$ is the QCD coupling constant.

Under a local color gauge transformation, the physics of the strong interaction does not change. The quark field spinors transform as:

$$\psi(x) \to U(x)\psi(x) \qquad (\bar{\psi}(x) \to \bar{\psi}(x)U(x)^\dagger) \tag{2.17}$$

where

$$U(x) = e^{i\theta^C(x)t^C} \tag{2.18}$$

The fermion sector of the Lagrangian $\bar{\psi}_{q,a}(i\gamma^\mu D_\mu - m_q\delta_{ab})\psi_{q,b}$ must be independently gauge invariant. In its current form, this is not the case due to the extra term in the derivative $\partial_\mu\psi \to U\partial_\mu\psi + (\partial_\mu U)\psi$. Thus, the covariant derivative must transform like the quark fields:

$$D^\mu\psi \to UD^\mu\psi \tag{2.19}$$

which determines the transformation of the gluon field under SU(3):

$$t^C\mathcal{A}_C^\mu \to Ut^C\mathcal{A}_C^\mu U^{-1} + \frac{i}{g_s}(\partial^\mu U)U^{-1} \tag{2.20}$$

The Lagrangian is adjoined with the gluon field tensor $F_{\mu\nu}^A$ with massless gauge field $\mathcal{A}^\mu$:

$$F_{\mu\nu}^A = \partial_\mu\mathcal{A}_\nu^A - \partial_\nu\mathcal{A}_\mu^A - g_s f_{ABC}\mathcal{A}_\mu^B\mathcal{A}_\nu^C \tag{2.21}$$

where f_{ABC} are structure constants for the SU(3) color group and A, B, C run over the eight types of gluons. This last term is necessary to obtain gauge invariance in the gluonic field tensor under local SU(3) transformations. The generators of SU(3) satisfy the Lie algebra:

$$[t^A, t^B] = if_{ABC}t^C. \tag{2.22}$$

The last two terms in Equation 2.15 are, respectively, the gauge-fixing term necessary for covariant quantization of the gluon fields ($\alpha_G = 1$ for the Feynman gauge and $\alpha_G \to 0$ for the

---

[5]Uppercase letters will indicate gluon fields while lowercase letters will indicate quark colors.

Landau gauge) and the Faddeev-Popov ghost term [84] necessary to eliminate unphysical particles and maintain the path integral formulation.

Equation 2.15 can be written as a free Lagrangian $\mathcal{L}_{\text{free}}$ for each participating field and an interaction Lagrangian $\mathcal{L}_{\text{int}}$. The free Lagrangian can be decomposed into:

$$\mathcal{L}_{\text{free}} = \mathcal{L}_{\text{free}}^{\text{gluon}} + \mathcal{L}_{\text{free}}^{\text{quark}} + \mathcal{L}_{\text{free}}^{\text{ghost}} \tag{2.23}$$

where

$$\mathcal{L}_{\text{free}}^{\text{gluon}} = -\frac{1}{4}(\partial^\mu \mathcal{A}_C^\nu - \partial^\nu \mathcal{A}_C^\mu)(\partial^\mu \mathcal{A}_C^\nu - \partial^\nu \mathcal{A}_C^\mu) - \frac{1}{2\alpha_G}\partial^\mu \mathcal{A}_\mu^C \partial_\mu \mathcal{A}_C^\mu \qquad \text{(Proca, spin 1)}$$

$$\mathcal{L}_{\text{free}}^{\text{quark}} = \sum_q \bar{\psi}_{q,a}(i\gamma^\mu \partial_\mu - m_q)\psi_{q,b} \qquad \text{(Dirac, spin 1/2)}$$

$$\mathcal{L}_{\text{free}}^{\text{ghost}} = -\partial_\mu \bar{\varphi}_C \partial^\mu \varphi^C \tag{2.24}$$

The quark-gluon, gluon-gluon, and ghost-gluon field interaction terms determine the vertex factors. These are given by:

$$\mathcal{L}_{\text{int}}^{\text{quark-gluon}} = g_s \mathcal{A}_C^\mu \sum_q \bar{\psi}_{q,a}\gamma^\mu t^C \psi_{q,b}$$

$$\mathcal{L}_{\text{int}}^{\text{gluon-gluon}} = -\frac{g_s}{2}f^{ABC}(\partial^\mu \mathcal{A}_A^\nu - \partial^\nu \mathcal{A}_A^\mu)\mathcal{A}_\mu^B \mathcal{A}_\nu^C - \frac{g_s^2}{4}f^{ABC}f_{ADE}\mathcal{A}_B^\mu \mathcal{A}_C^\nu \mathcal{A}_\mu^D \mathcal{A}_\nu^E$$

$$\mathcal{L}_{\text{int}}^{\text{ghost-gluon}} = g_s f_{ABC}(\partial_\mu \bar{\varphi}^A)\varphi^B \mathcal{A}_\mu^C \tag{2.25}$$

The gluon-gluon coupling is specific to the non-Abelian SU(3) group. In other words, both QED and QCD require massless gauge fields [6], corresponding to photons and gluons, respectively. However, photons themselves do not carry charge, whereas gluons carry color charge and thus can interact with one another. This self-interaction term requires the introduction of the ghost term for a proper quantization of the field. In $\mathcal{L}_{\text{int}}$, the Feynman rules [86] yield a quark-antiquark-gluon vertex, a three-gluon vertex from the three factors of $\mathcal{A}^\mu$, and a four-gluon vertex from the four factors of $\mathcal{A}^\mu$. The corresponding Feynman diagrams are shown in Figure 2.7.

---

[6]Massive gauge fields are introduced through spontaneous symmetry breaking and the Higgs Mechanism, which is responsible for the masses of the weak gauge bosons $W^\pm, Z$ [1, 85]
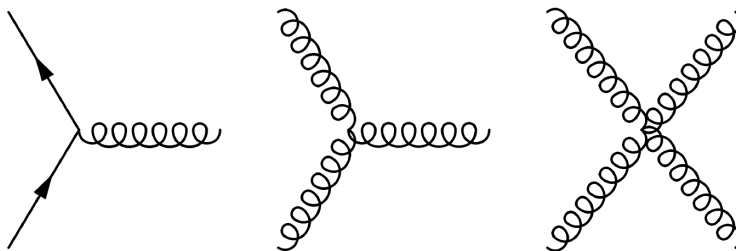
Figure 2.7: Feynman diagrams from the interaction QCD Lagrangian corresponding to $q\bar{q}g$, three-gluon, and four-gluon vertices.

2.3.1 Running Coupling

In perturbation theory, gluon loops in Feynman diagrams result in divergences at large loop momenta. These are called ultraviolet divergences and are absorbed by re-expressing parameters in the Lagrangian with physically observable quantities. This process is called renormalization. Loop corrections to a diagram are applied using a renormalization scale μ_R, which has units of energy and can be chosen [87] at the scale of the momentum transfer of the process [7] i.e. $\mu_R^2 \approx Q^2$. The renormalized coupling is thus a function of the scale and satisfies the renormalization group equation:

$$\mu_R^2 \frac{d\alpha_S}{d\mu_R^2} = \beta(\alpha_S) = -(b_0\alpha_S^2 + b_1\alpha_S^3 + b_2\alpha_S^4 + \dots) \tag{2.26}$$

which gives the rate at which the coupling changes as the renormalization scale increases [82]. In $\beta(\alpha_S)$, the one-loop coefficient $b_0 = (33 - 2n_f)/(12\pi)$, the two-loop coefficient $b_1 = (153 - 19n_f)/(24\pi^2)$, and the three-loop coefficient $b_3 = (2857 - \frac{5033}{9}n_f + \frac{325}{27}n_f^2)/(128\pi^3)$. The negative sign implies that for small n_f, the α_S runs to zero at large Q^2 (i.e. short distances) and the strong interaction decreases. This is called *asymptotic freedom* [88, 89] (Figure 2.8). Thus, in comparison to QED, in which the vacuum polarization functions as a dielectric medium that reduces the effective electric charge at large distances, in QCD, gluons produce an antiscreening effect.

In an energy range where only the light-quark flavors are considered ($n_f = 3$ and $m_q << \mu_R$) and higher-order terms are ignored, the running coupling is:

---

[7]The choice of μ_R should not change the physics in the calculation.
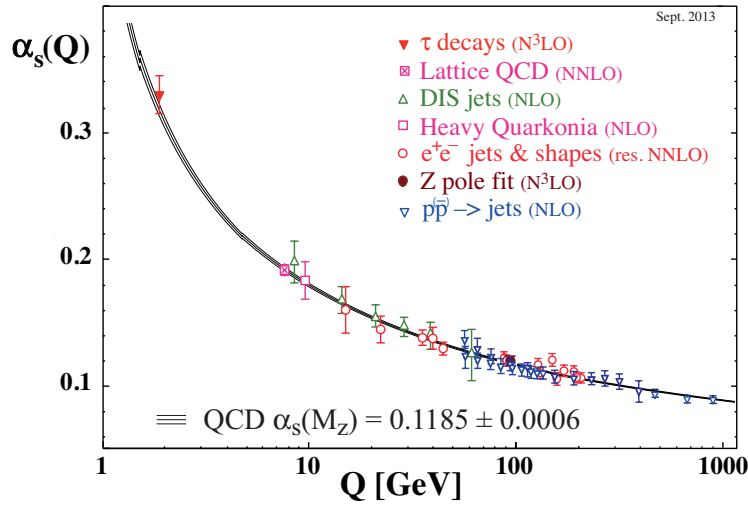
Figure 2.8: Strong coupling α_S as a function of the energy scale Q [3].

$$\alpha_S(\mu_R^2) = \frac{1}{b_0 \ln(\mu_R^2/\Lambda^2)} \tag{2.27}$$

where Λ is the scale at which α_S becomes strong with decreasing Q^2 (i.e. the non-perturbative scale of QCD). Experimental measurements have yielded a value of $\Lambda \approx 200$ MeV. Thus, perturbative QCD calculations are only valid for $Q > \Lambda$, and the strong interaction becomes "strong" at distance scales greater than $\sim 1/\Lambda$, which is roughly the size of the nucleon.

2.4 Factorization and Hard-Scattering

In Section 2.2, experimental evidence from DIS for the existence of quarks and gluons was presented. However, to current date, no experiments have ever directly observed free quarks or gluons [90]. The inability to separate a color-singlet state into its colored components is known as *quark confinement* and is a consequence of the strong coupling at large distances. QCD has been studied in this regime using a scheme introduced by Wilson [91] in which the continuum gauge theory is replaced by a statistical mechanical system on a four-dimensional lattice. This section will discuss how parton distribution functions (PDFs) can be used with perturbative QCD to learn more about nucleon structure.

Factorization theorems [92] enable the derivation of cross sections for hard processes in QCD by separating perturbative from nonperturbative effects. Short-range dynamics are handled perturbatively, whereas soft processes are factorized and are contained within PDFs. Major features of the PDFs are that they are experimentally accessible and universal (i.e. the PDFs are independent of the hard process under consideration). The part of the cross section that remains after factoring the PDFs is the (perturbatively calculable) short distance cross section for the hard scattering of partons.

A hard process between two nucleons is shown schematically in Figure 2.9. The factorization theorem of Drell and Yan [93] postulates that the interaction cross section $\sigma_{AB \to X}$ between hadrons A and B can be obtained by weighting the hard subprocess by the parton distribution functions:

$$\sigma_{AB \to X} = \sum_{a,b} \int \int dx_a dx_b f_{a/A}(x_a, \mu_F^2) f_{b/B}(x_b, \mu_F^2) \left[\hat{\sigma}_{\text{LO}} + \alpha_S(\mu_R^2) \hat{\sigma}_{\text{NLO}} + \ldots \right]_{ab \to X} \quad (2.28)$$
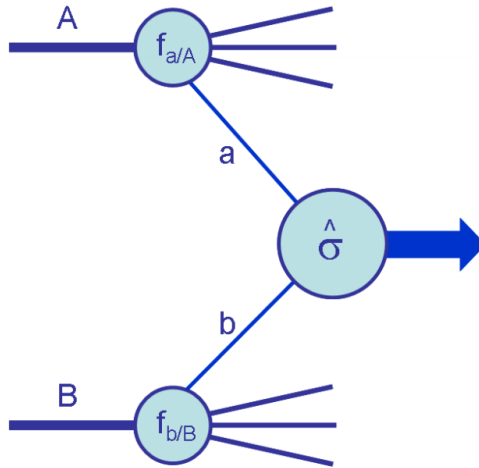
Figure 2.9: Schematic of factorization in nucleon-nucleon cross section calculations. $\hat{\sigma}$ represents the hard-scattering process and $f_{a/A(b/B)}$ are the parton distribution functions in hadron A and B, respectively [4].

The hard-scattering process is represented by $\hat{\sigma}$ and is calculated in perturbative QCD to $\mathcal{O}(\alpha_S^n)$. Higher-order terms correspond to virtual (loop) contributions and radiation components from additional quarks and gluons. $f_{a/A(b/B)}$ is the probability to find parton $a(b)$ in hadron $A(B)$ with

momentum fraction $x_{a(b)}$ (i.e. PDFs). The PDFs depend on the factorization scale μ_F^2, which separates the perturbative and nonperturbative regimes. In principle, perturbation theory should be invariant under changes of the unphysical parameters μ_F and μ_R. However, this is only the case when the perturbation series is extended to a complete set of higher-order corrections. Failing to include these higher-order terms results in a dependence of the cross section on the two scales. To avoid unnatural logarithmic terms, μ_F and μ_R are typically set to $\mu_F = \mu_R = M_X$. Varying the scales results in contributions to the PDF uncertainties.

The PDFs are related to the structure functions in the scattering cross section by choosing a renormalization scheme, of which the most common is the $\overline{MS}$ scheme [94]. In this scheme, the structure function takes the form:

$$F_2(x, Q^2) = x \sum_i e_i^2 q_i(x, Q^2) + \frac{\alpha_S(Q^2)}{2\pi} x \int_x^1 \frac{d\xi}{\xi} \left[\sum_i e_i^2 C_{2,q}(\frac{x}{\xi}) q_i(\xi, Q^2) + e_i^2 C_{2,g}(\frac{x}{\xi}) g(\xi, Q^2) \right]$$

(2.29)

where $C_{2,q}$ and $C_{2,g}$ are the coefficient functions for the contributions from quark and gluon scattering. By requiring that the factorization-scale dependence of F_2 vanish in a perturbative expansion over all orders, a group of differential equations may be derived that relates the PDFs at one scale to those at another scale. These are called the DGLAP equations [95–98].

PDFs used in cross section calculations are solutions to the DGLAP equations [8]:

$$\frac{\partial q_i(x, Q^2)}{\partial \log Q^2} = \frac{\alpha_S}{2\pi} \int_x^1 \frac{d\xi}{\xi} \left[P_{q_i q_j}(\xi, \alpha_S) q_j(\frac{x}{\xi}, Q^2) + P_{q_i,g}(\xi, \alpha_S) g(\frac{x}{\xi}, Q^2) \right]$$

$$\frac{\partial g(x, Q^2)}{\partial \log Q^2} = \frac{\alpha_S}{2\pi} \int_x^1 \frac{d\xi}{\xi} \left[P_{g q_j}(\xi, \alpha_S) q_j(\frac{x}{\xi}, Q^2) + P_{gg}(\xi, \alpha_S) g(\frac{x}{\xi}, Q^2) \right]$$

(2.30)

where $P_{ab}(x, \alpha_S)$ are the splitting functions (kernels), which give the probability of a parent parton a to emit a gluon with momentum fraction $1 - z$, thereby producing a daughter parton b with momentum fraction z. The splitting functions can be perturbatively expanded in powers of the running coupling:

$$P_{ab}(x, \alpha_S) = P_{ab}^0(x) + \frac{\alpha_S}{2\pi} P_{ab}^1(x) + \cdots$$

(2.31)

---

[8]The DGLAP equations sum leading powers of $[\alpha_S \log Q^2]^n$ generated by multiple gluon emission in a region of phase space where the p_T is strongly ordered. This contribution dominates at $\log(Q) >> \log(1/x)$.

2.4.1 Extraction of Parton Distribution Functions

The DGLAP equations can be used to obtain the evolution of the parton density with Q^2. However, cross section calculations also require knowledge of the x dependence, which must be determined from global fits to data from DIS, Drell-Yan, and jet measurements at current energy ranges. The dependence of the parton momentum fraction on the energy scale $Q = M_X$ and center-of-mass energy is given by:

$$x_a = \frac{M_X}{\sqrt{s}} e^{+y_X}, \qquad x_b = \frac{M_X}{\sqrt{s}} e^{-y_X} \tag{2.32}$$

where y_X is the longitudinal boost (rapidity) of the produced resonance X:

$$y_X = \frac{1}{2} \ln \frac{E + p_z}{E - p_z}$$
$$y_X = \frac{1}{2} \ln \frac{x_a}{x_b} \tag{2.33}$$

HERA data [99, 100] provide information of the PDFs at low-x, whereas fixed target DIS [70, 72, 101–103] and DY [104, 105] experiments probe the high-x region. Jet measurements [106, 107] in colliders also provide a wealth of information over a broad range of x and Q^2, especially for gluon distributions. W/Z production at high-energy colliders probe the regions $10^{-3} < x < 10^{-1}$ at $|y| < 2.5$ and $10^{-4} < x_a < 10^{-3}$ and $0.1 < x_b < 1$ at $2 < |y| < 5$. Figure 2.10 presents the parton kinematic phase-space accessible at the LHC. Also shown are the regions accessed by the TeVatron, HERA, and fixed-target experiments.

To determine the PDFs, a general ansatz is used to parametrize the parton distributions at a pertubative "starting scale" Q_0^2. The DGLAP equations are then used with the parametrized functions to obtain PDFs at any Q^2 [9]. The DGLAP evolution extrapolates the PDFs to different Q^2 where measurements from data are available. The theory predictions are fit to the experimental data, thus constraining the input parameters and yielding PDFs in (x, Q^2) space. The fit minimizes a global χ^2 function that describes the compatibility between the data and theory [112].

Figure 2.11 presents (momentum weighted) PDFs $xf_i(x)$ for the proton from the CTEQ collaboration [113]. The antiquark PDFs are denoted by $x\bar{f}_i(x)$. The PDFs obey the sum rules [114, 115],

---

[9]DGLAP evolution no longer becomes applicable at very low x. In this region, a BFKL [108–111] description may be used.
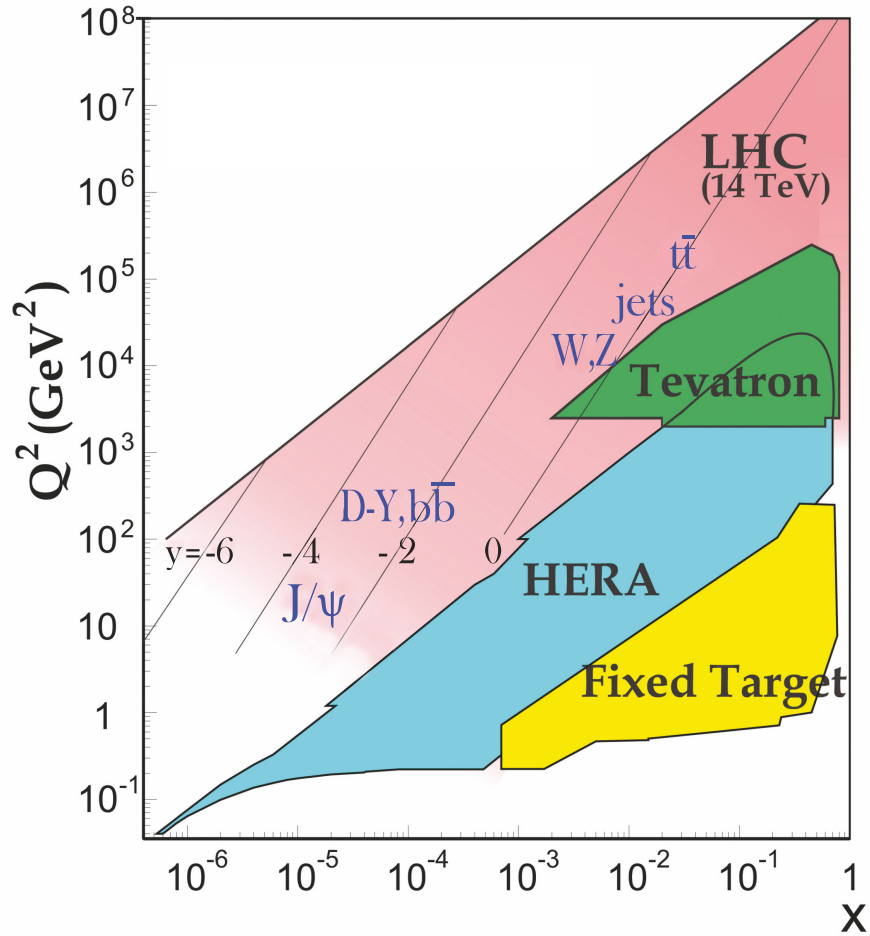
Figure 2.10: Parton kinematic range in (x, Q^2) space probed by fixed-target and collider experiments. The incoming partons have $x_{1,2} = (M/14 \text{ TeV})e^{\pm y}$ with $Q = M$ [2].

which for the proton (neutron) are:

$$\int_0^1 \left[u(x) - \bar{u}(x)\right] dx = 2(1) \qquad \int_0^1 \left[d(x) - \bar{d}(x)\right] dx = 1(2) \qquad \text{(valence)} \qquad (2.34)$$

and

$$\int_0^1 \left[q(x) - \bar{q}(x)\right] dx = 0 \qquad \text{(sea)} \qquad (2.35)$$

which satisfies the valence structure of the proton (neutron): *uud* (*udd*). The valence quark distributions are defined as $u_v(x) = u(x) - \bar{u}(x)$ and $d_v(x) = d(x) - \bar{d}(x)$, the gluon distribution as $xg(x)$, and the light-sea distribution as $xS(x) = x[2(\bar{u}(x) + \bar{d}(x) + \bar{s}(x))]$. From momentum conservation:

$$\int_0^1 \sum_i^{n_f} x \left[q_i(x) + \bar{q}_i(x)\right] + xg(x) dx = 1 \qquad (2.36)$$

where the summation is over the parton flavors.

The PDF uncertainties in Figure 2.11 are determined using the Hessian Method [112], which explores the χ^2 in the neighborhood of its minimum. This involves diagonalizing an n-dimensional Hessian matrix [10], where n is the number of free parameters in the global fit, resulting in an orthonormal basis set from which the PDF errors can be determined. The PDFs are varied along the positive and negative directions of each eigenvector, resulting in a displacement from the best-fit point S_0 of $T = \sqrt{\Delta\chi^2}$ (e.g. 90% C.L., 68% C.L.). The uncertainty analysis yields $2n$ PDF sets: eigenvector basis sets in the positive and negative direction along each eigenvector $S_1^+, S_1^-, ..., S_n^+, S_n^-$. Let X be an observable. Then the value of X using the central PDF set is X_0 and, for the ith eigenvector, the variations in the positive and negative direction are given by X_i^+, and X_i^-, respectively. The PDF error for the observable can be calculated using the "Master Equation":

$$\Delta X_{\text{max}}^+ = \sqrt{\sum_{i=1}^n [\max(X_i^+ - X_0, X_i^- - X_0, 0)]^2}$$

$$\Delta X_{\text{max}}^- = \sqrt{\sum_{i=1}^n [\max(X_0 - X_i^+, X_0 - X_i^-, 0)]^2} \qquad (2.37)$$

---

[10]The Hessian is the matrix of second derivatives of the χ^2.
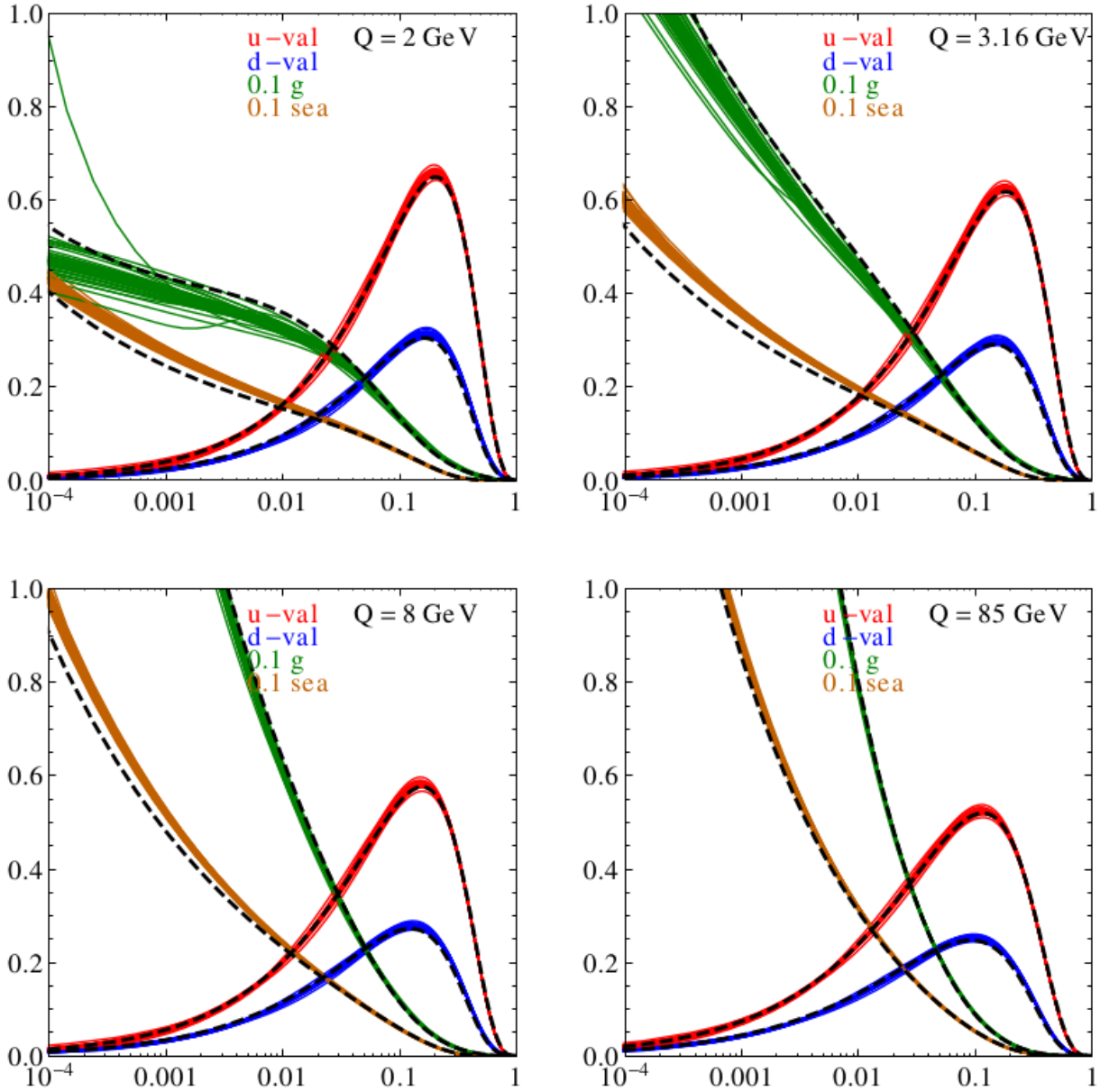
Figure 2.11: CT10 parton distribution functions at different energy scales Q. In each figure, $xu_{\text{valence}} = x(u - \bar{u})$, $xd_{\text{valence}} = x(d - \bar{d})$, $xg/10$, and $xq_{\text{sea}}/10$ are shown. The dashed curves are from the central fit.

where $\Delta X^+_{\max}$ adds in quadrature the PDF error contributions that result in an increase in the observable X and $\Delta X^-_{\max}$ adds in quadrature those that result in a decrease in X. The maximum difference is used since, in some instances, both X^+_i and X^-_i result in variations of the observable in the same direction. In this case, $\Delta X^+_{\max}$ is calculated with the most positive variation and $\Delta X^-_{\max}$ with the most negative.

The neutron PDF is related to the proton PDF by isospin symmetry:

$$u(x) := u_v(x) + u_s(x) = u^p(x) = d^n(x)$$

$$d(x) := d_v(x) + d_s(x) = d^p(x) = u^n(x) \tag{2.38}$$

where v is the valence and s is the sea contributions. All other parton distributions are the same for the proton and neutron:

$$S := u_s(x) = \bar{u}_s(x) = d_s(x) = \bar{d}_s(x) = s_s(x) = \bar{s}_s(x) \tag{2.39}$$

where heavy quarks have been omitted. The structure functions can then be expressed in the form of Eqn. 2.10:

$$\frac{1}{x} F_2^p(x) = \frac{1}{9}(4u_v(x) + d_v(x)) + \frac{4}{3}S$$

$$\frac{1}{x} F_2^n(x) = \frac{1}{9}(4d_v(x) + u_v(x)) + \frac{4}{3}S \tag{2.40}$$

2.5 Parton Distribution Functions and W Rapidity

To leading order, W boson production proceeds via the Drell-Yan mechanism $q\bar{q}' \to W$, as depicted in Figure 2.12. In the narrow width approximation in which the decay width Γ_W of the gauge boson is neglected, the cross section for W production is [86]:

$$\hat{\sigma}^{q\bar{q}' \to W} = \frac{\pi}{3}\sqrt{2}G_F M_W^2 |V_{qq'}|^2 \delta(sx_1 x_2 - M_W^2) \tag{2.41}$$

where G_F [11] is the Fermi coupling constant and represents the strength of the weak interactions at energies much less than M_W, $sx_1 x_2 = M_W^2$ is the squared parton center-of-mass energy, and

---

[11]The Fermi coupling constant can also be expressed as $G_F = \sqrt{2}\frac{g^2}{8M_W^2}$, where $g = \frac{e}{\sin\theta_w}$ is the weak interaction coupling constant. θ_w is the weak mixing angle, which is related to the mass of the massive gauge bosons $\cos\theta_w = \frac{M_W}{M_Z}$.

$M_W = 80.385$ GeV [2] is the mass of the W boson. $V_{qq'}$ is the appropriate quark-mixing matrix element from the Cabibbo-Kobayashi-Maskawa (CKM) matrix [116, 117]:

$$V_{CKM} = \begin{pmatrix} V_{ud} & V_{us} & V_{ub} \\ V_{cd} & V_{cs} & V_{cb} \\ V_{td} & V_{ts} & V_{tb} \end{pmatrix}$$

The CKM matrix is unitary. Thus, $V_{ij}V_{ik}^* = \delta_{jk}$, $V_{ij}V_{kj}^* = \delta_{ik}$, and $V_{ik}V_{jk}^* = 0$, resulting in six vanishing combinations that are represented as *unitarity triangles* in a complex plane [2].
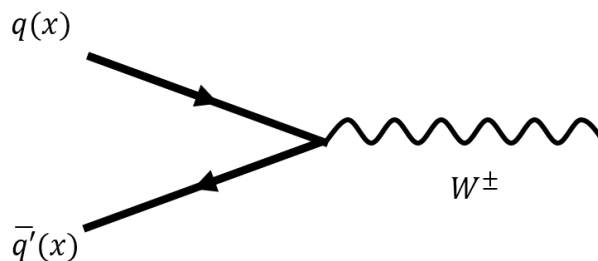
Figure 2.12: Leading-order Feynman diagram for W boson production.

In the leading-order diagram, W bosons are most likely to couple with the light-flavor quarks (i.e. $q(x) = u(x)$ or $d(x)$ and $\bar{q}'(x) = \bar{d}(x)$ or $\bar{u}(x)$). This can be seen from Figure 2.13, which presents the parton decomposition of Drell-Yan processes as a percentage of the LO cross section in pp and $p\bar{p}$ collisions at the LHC and TeVatron, respectively. The u and d flavor contributions are reversed in nn collisions in a Pb+Pb system (see Equation 2.40), whereas in np collisions the u and d contributions to the cross section become equal. Since matrix elements in the CKM matrix decrease when mixing across families (i.e. Cabibbo suppression), some contributions are much smaller than others. NLO and NNLO corrections (e.g. $q\bar{q}' \to Wg$) increase the LO cross section by approximately 25% and 5% [3], respectively.

The rapidity of the W boson and parton are related by Equations 2.32 and 2.33, which imply that W bosons at large rapidity are produced in the direction of the parton with larger momentum fraction in the hard scattering process. Since at high x, on average, $u_v(x) > \bar{d}_s(x)$ [12] and $d_v(x) >$

---

[12]Here, $q_v(x)$ is the valence quark distribution whereas $q_s(x)$ is the sea quark distribution. This notation is adopted for clarity since the proton and neutron valence quark distributions are reversed.
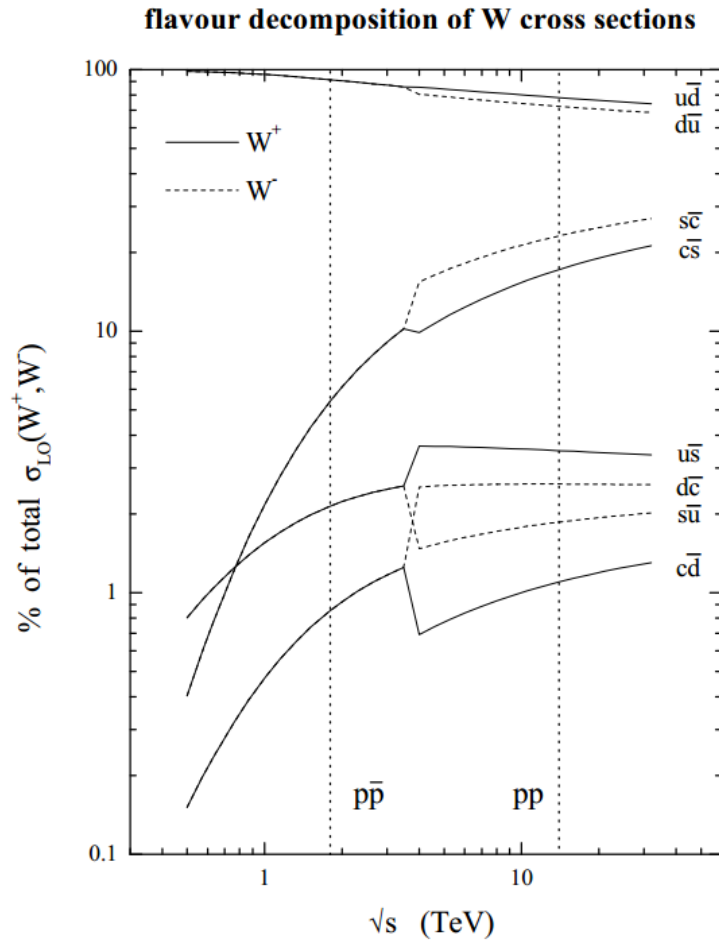
Figure 2.13: Parton decomposition of the W^+ (solid line) and W^- (dotted line) total cross sections as a function of $\sqrt{s}$. Individual contributions are shown as a percentage of the total cross section [5]. In a nn collision, the u and d flavor contributions are reversed, whereas in a np collision they are the same.

$\bar{u}_s(x)$ (Figure 2.11), the W is preferentially produced in the direction of the valence quark. In Pb+Pb collisions, for $W^+(W^-)$, this is in the direction of the valence $u(d)$ quark. Moreover, in $pp(nn)$ collisions, a larger number of $W^+(W^-)$ bosons are produced at forward rapidity since on average $u_v^p(x) > d_v^p(x)(d_v^n(x) > u_v^n(x))$. This results in an asymmetric rapidity distribution between W^+ and W^- bosons and is primarily driven by the difference in the $u_v(x)$ and $d_v(x)$ distribution functions. In the case of np or pn collisions, the asymmetry depends on the direction of the incoming valence quarks: more $W^+(W^-)$ bosons are produced at forward rapidity in the $p(n)$-going direction. The asymmetry in each collision system can be implied from Figure 2.14, which presents the W rapidity distributions in simulation for pp, np, and nn collisions. The explicit dependence of the $W^\pm$ differential cross section on the parton distribution functions (at leading order) is [118]:

$$\frac{d\sigma}{dy}(AB \to W^+ X) = \frac{2\pi G_F}{3\sqrt{2}} x_1 x_2 \{|V_{ud}|^2 \left[u(x_1)\bar{d}(x_2) + \bar{d}(x_1)u(x_2)\right] + |V_{us}|^2 \left[u(x_1)\bar{s}(x_2) + \bar{s}(x_1)u(x_2)\right]$$

$$+ |V_{cs}|^2 \left[c(x_1)\bar{s}(x_2) + \bar{s}(x_1)c(x_2)\right] + |V_{cd}|^2 \left[c(x_1)\bar{d}(x_2) + \bar{d}(x_1)c(x_2)\right]$$

$$+ |V_{ub}|^2 \left[u(x_1)\bar{b}(x_2) + \bar{b}(x_1)u(x_2)\right] + |V_{cb}|^2 \left[c(x_1)\bar{b}(x_2) + \bar{b}(x_1)c(x_2)\right]\} \quad (2.42)$$

$$\frac{d\sigma}{dy}(AB \to W^- X) = \frac{2\pi G_F}{3\sqrt{2}} x_1 x_2 \{|V_{ud}|^2 \left[\bar{u}(x_1)d(x_2) + d(x_1)\bar{u}(x_2)\right] + |V_{us}|^2 \left[\bar{u}(x_1)s(x_2) + s(x_1)\bar{u}(x_2)\right]$$

$$+ |V_{cs}|^2 \left[\bar{c}(x_1)s(x_2) + s(x_1)\bar{c}(x_2)\right] + |V_{cd}|^2 \left[\bar{c}(x_1)d(x_2) + d(x_1)\bar{c}(x_2)\right]$$

$$+ |V_{ub}|^2 \left[\bar{u}(x_1)b(x_2) + b(x_1)\bar{u}(x_2)\right] + |V_{cb}|^2 \left[\bar{c}(x_1)b(x_2) + b(x_1)\bar{c}(x_2)\right]\} \quad (2.43)$$

where $AB = pp$, np, or nn and $q(x_{1,2})$ and $\bar{q}(x_{1,2})$ are the appropriate quark/antiquark distributions in the proton or neutron for each parton in the hard scattering process.

Considering only the light flavor u and d quarks, the cross section for W production becomes:

$$\frac{d\sigma_{W^+}}{dy} = \frac{2\pi G_F}{3\sqrt{2}} x_1 x_2 |V_{ud}|^2 \left[u(x_1)\bar{d}(x_2) + \bar{d}(x_1)u(x_2)\right]$$

$$\frac{d\sigma_{W^-}}{dy} = \frac{2\pi G_F}{3\sqrt{2}} x_1 x_2 |V_{ud}|^2 \left[\bar{u}(x_1)d(x_2) + d(x_1)\bar{u}(x_2)\right] \quad (2.44)$$

The charge asymmetry in the W rapidity distributions is defined as:

$$A_W(y) = \frac{d\sigma_{W^+}/dy - d\sigma_{W^-}/dy}{d\sigma_{W^+}/dy + d\sigma_{W^-}/dy} \quad (2.45)$$
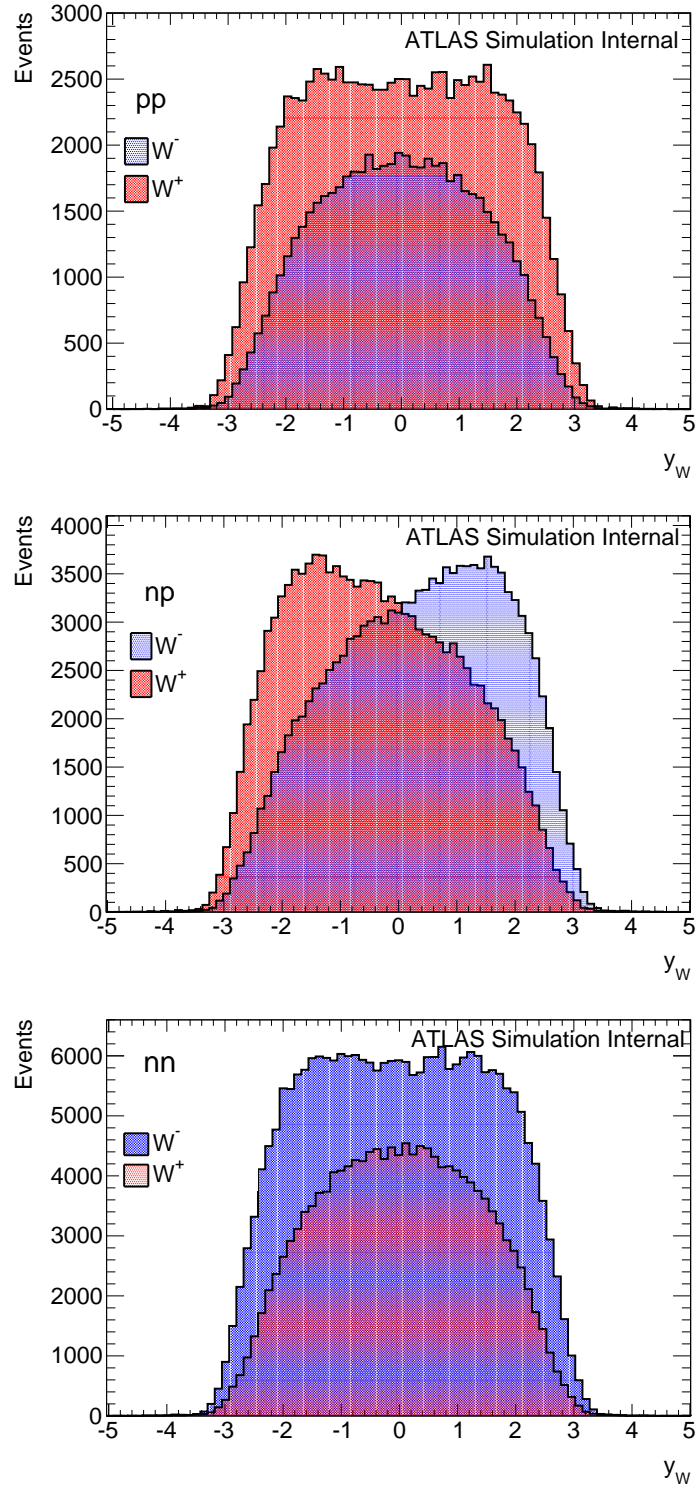
Figure 2.14: Simulated W rapidity distributions for W^+ (red) and W^- (blue) bosons in pp (Top), np (Middle), and nn (Bottom) collisions at $\sqrt{s} = 2.76$ TeV. The distributions for W^+ and W^- are normalized by their respective cross sections predicted by POWHEG in each collision system.

To see how the rapidity asymmetry can be used to constrain $u(x)/d(x)$ [119], consider Equation 2.46 for pp collisions:

$$\frac{d\sigma_{W^+}}{dy} = \frac{2\pi G_F}{3\sqrt{2}} x_1 x_2 |V_{ud}|^2 \left[u_p(x_1)\bar{d}_p(x_2) + \bar{d}_p(x_1)u_p(x_2) \right]$$

$$\frac{d\sigma_{W^-}}{dy} = \frac{2\pi G_F}{3\sqrt{2}} x_1 x_2 |V_{ud}|^2 \left[\bar{u}_p(x_1)d_p(x_2) + d_p(x_1)\bar{u}_p(x_2) \right] \tag{2.46}$$

Assuming that $\bar{u}_p(x) = \bar{d}_p(x)$, the asymmetry can be written as:

$$A(y) = \frac{(u_p(x_1) - d_p(x_1))\bar{u}_p(x_2) + \bar{u}_p(x_1)(u_p(x_2) - d_p(x_2))}{(u_p(x_1) + d_p(x_1))\bar{u}_p(x_2) + \bar{u}_p(x_1)(u_p(x_2) + d_p(x_2))} \tag{2.47}$$

In the limit that $x_1 \sim 1$ and $x_2 << 1$, $\bar{u}_p(x_1)$ is negligible and the asymmetry becomes:

$$A(y) \approx \frac{u_p(x_1) - d_p(x_1)}{u_p(x_1) + d_p(x_1)} \tag{2.48}$$

Since the W rapidity distributions in pp collisions are symmetric (see Figure 2.14), the rapidity charge asymmetry does not change when $x_1 \leftrightarrow x_2$ ($y \leftrightarrow -y$). Therefore, the ratio of the parton distribution functions are directly sensitive to the asymmetry by:

$$\frac{d_p(x)}{u_p(x)} \approx \frac{1 - A(y)}{1 + A(y)} \qquad (pp) \tag{2.49}$$

Using the isospin symmetry in Equation 2.38, the same procedure can be applied to nn and pn collisions (see Appendix D). For nn, the result is:

$$\frac{d_p(x)}{u_p(x)} \approx \frac{1 + A(y)}{1 - A(y)} \qquad (nn) \tag{2.50}$$

In the case of np collisions, the rapidity distributions are asymmetric and $\frac{d\sigma_{W^+}(y)}{dy} = \frac{d\sigma_{W^-}(-y)}{dy}$, from which it follows that $A_W(+y) = -A_W(-y)$. The sensitivity of the asymmetry on the parton distributions becomes:

$$\frac{d_p(x_1)}{u_p(x_1)} \approx \frac{1 + A(y)}{1 - A(y)} \qquad (np; \; x_1 \sim 1, x_2 << 1)$$

$$\frac{d_p(x_2)}{u_p(x_2)} \approx \frac{1 - A(y)}{1 + A(y)} \qquad (np; \; x_1 << 1, x_2 \sim 1) \tag{2.51}$$

The result for pn may be obtained by the tranformation $A(y) \rightarrow -A(y)$ in the relations above. Equations 2.49-D.14 show that direct access to parton distribution functions is provided by the rapidity charge asymmetry in $W^\pm$ production.

2.6   Leptonic W Decays

The W boson cannot be directly detected since it is a very short-lived particle. Furthermore, the four-momentum of the W cannot be easily determined experimentally because the z component of the neutrino is unknown – momentum conservation is only expected in the transverse plane because an unknown amount of energy of the incoming hadrons escapes down the beam pipe. Leptonic observables are more readily attainable and thus, leptonic decays are usually used in physics analyses to identify the presence of a W boson.

From the Lagrangian for the standard model of electroweak interactions [120–122], the charged-current term is:

$$- \frac{g_W}{2\sqrt{2}} \sum_i \bar{\psi}_i \gamma^\mu (1 - \gamma^5)(T^+ W_\mu^+ + T^- W_\mu^-)\psi_i \tag{2.52}$$

where ψ_i are spinor fields, γ^μ are the Dirac matrices, $\gamma^5 = i\gamma^0\gamma^1\gamma^2\gamma^3$, θ_W is the Weinberg angle, and $g_W = e/\sin\theta_w$. T^+ and T^- are the isospin raising and lowering operators and $W_\mu^\pm \equiv (W_\mu^1 \mp iW_\mu^2)/\sqrt{2}$ are the charged-boson fields.

Using the Feynman rules, one obtains from Equation 2.52 the charged-current weak interaction vertex factor:

$$- i\frac{g_W}{\sqrt{2}}\gamma_\mu \left(\frac{1 - \gamma^5}{2}\right) \tag{2.53}$$

It can be seen from Equation 2.53 that the coupling of W bosons to a lepton and neutrino takes the form of a vector minus axial-vector: $\bar{\psi}_\nu\gamma_\mu(1 - \gamma^5)\psi_\ell$. This is referred to as "V-A coupling".

The V-A structure is related to the helicity operator, which is the projection of the spin $\mathbf{S}$ onto the direction of the momentum $\hat{p}_i$:

$$h \equiv \hat{p} \cdot \mathbf{S} = \frac{1}{2}\hat{p}_i \begin{pmatrix} \sigma^i & 0 \\ 0 & \sigma^i \end{pmatrix}$$

Every particle has a chirality state of ± 1 with chirality operator γ^5. In the ultrarelativistic limit, chiral states correspond to helicity states. Thus, ultrarelativistic particles with positive helicity eigenvalues are *right-handed* (ψ_R), whereas those with negative helicity eigenvalues are *left-handed* (ψ_L) [82]. The term $\frac{1}{2}(1-\gamma^5)$ is the projector of left-handed chiral particle states, and therefore this

term in Equation 2.52 selects left-handed helicity components of particle spinors and right-handed components of antiparticle spinors. The V-A structure in W decays results in an anisotropic lepton angular distribution of the form [13]:

$$\frac{d\sigma}{d\cos\theta^*} \propto (1 - \lambda q \cos\theta^*)^2 \tag{2.54}$$

where q is the charge of the lepton, θ^* is the lepton polar angle of emission in the rest frame of the W with respect to the incoming quark [14], and λ signifies the helicity of the W boson. The V-A structure dictates that the spin of the W is aligned with the antiquark [124]. Thus, in most cases in Pb+Pb collisions, the W is left-handed. However, at central rapidity, the probability that the sea quark carries a larger momentum fraction increases and thus the helicity state of the W becomes an admixture of left-handed and right-handed states [125].

Equation 2.54 has a simple qualitative interpretation that applies to all nucleon combinations in Pb+Pb collisions. Consider the process $u\bar{d} \to W^+ \to \mu^+\nu$. Since W bosons at large rapidity are preferentially produced in the direction of the valence quarks, the W^+ boson is boosted in the direction of the u quark. The lepton decay product ℓ^+ (antiparticle) must be in a right-handed helicity state due to V-A coupling. Therefore, to conserve angular momentum, the lepton is produced in the direction of the incoming $\bar{d}$ antiquark and follows an angular dependence $\propto (1 - \cos\theta^*)$ with maximum decay amplitude at $\theta^* = \pi$ i.e. ℓ^+ is produced in the opposite direction of W^+. Conversely, for the process $d\bar{u} \to W^- \to \mu^-\bar{\nu}$, the W^- boson is boosted in the direction of the d quark. The particle ℓ^- is left-handed and thus is also produced in the direction of the d quark. The angular dependence is $\propto (1 + \cos\theta^*)$ with maximum amplitude at $\theta^* = 0$ i.e. ℓ^- is boosted in the direction of the W^- boson. The angular dependence of the lepton and neutrino in the rest frame of the W is presented schematically in Figure 2.15.

The rapidity of the charged lepton is a convolution of the V-A coupling and W rapidity. In

---

[13]Higher-order contributions to the cross section can alter the angular distribution [123]

[14]Alternatively, the amplitude may be expressed as $\propto (1 + \cos\theta^*)^2$ if θ^* is defined with respect to the direction of the down quark or antiquark [86]

Spin
Momentum

$x_a > x_b$

u_a $\bar{d}_b$ W rest frame d_a $\bar{u}_b$

μ^+ θ^* ν_μ $\bar{\nu}_\mu$ θ^* μ^-

W^+ boost W^- boost

$$\frac{d\sigma}{dcos\theta} \propto (1 - cos\theta^*)^2 \qquad \frac{d\sigma}{dcos\theta} \propto (1 + cos\theta^*)^2$$
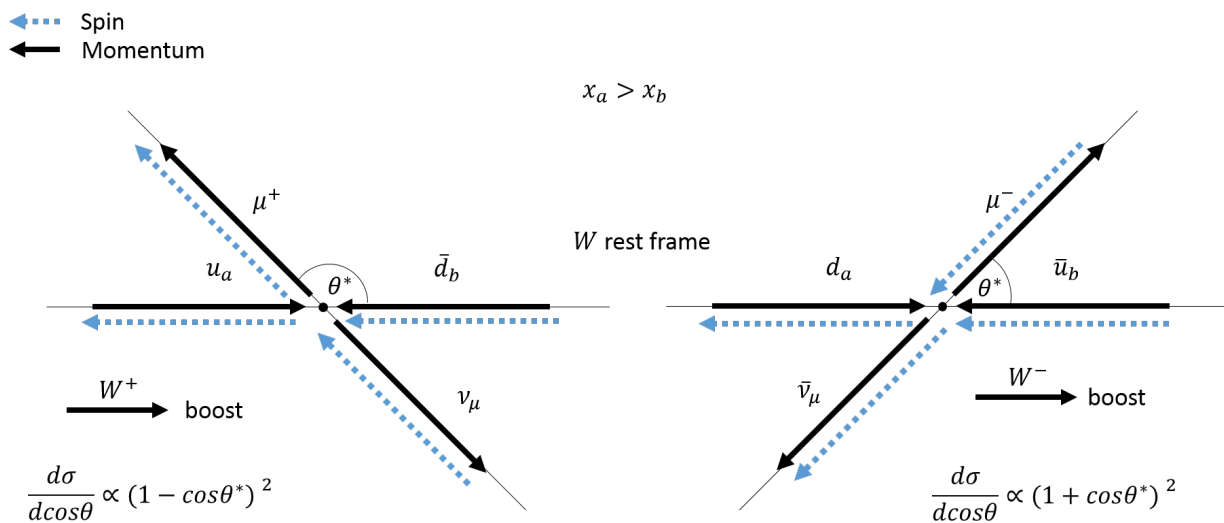
Figure 2.15:   Schematic representation of the lepton angular dependence in $q\bar{q}' \rightarrow W \rightarrow \mu\nu$ processes. The momentum and spin vectors are not drawn to scale. The angular dependence in the $q\bar{q}' \rightarrow \mu\nu$ system is expressed within the rest frame of the W. The decay distributions follow the form $(1 \pm \cos\theta^*)^2$. Both W^+ (Left) and W^- (Right) processes are shown.

terms of the boson rapidity y_W and rapidity of the lepton in the W rest frame y_ℓ^* [126]:

$$
\begin{aligned}
y_\ell &= y_W \pm y_\ell^* \\
&= \frac{1}{2}\ln\frac{x_1}{x_2} \pm \frac{1}{2}\ln\frac{1 + \cos\theta^*}{1 - \cos\theta^*}
\end{aligned}
\tag{2.55}
$$

where the upper sign is for $y_W > 0$ and the lower for $y_W < 0$. Thus, the accessible phase space in x is restricted by the rapidity acceptance of the measurement. For negatively (positively) charged leptons, $\cos\theta^*$ is most likely positive (negative), and therefore the lepton rapidity is shifted to more forward (backward) rapidity relative to the parent W (i.e. $|y_{\ell^-}| > |y_{W^-}|$ and $|y_{\ell^+}| < |y_{W^+}|$). This behavior can be seen in Figure 2.16, which presents the W and lepton rapidities for each collision system.

The relative contribution of the V-A coupling and W rapidity to the lepton rapidity distribution depends on the kinematic phase space of the lepton. The kinematics of the W and decay lepton are well described by using the narrow-width approximation [15]. At LO in pQCD, the W is produced

---

[15]This assumes that the total decay width is much smaller than the mass M_W.
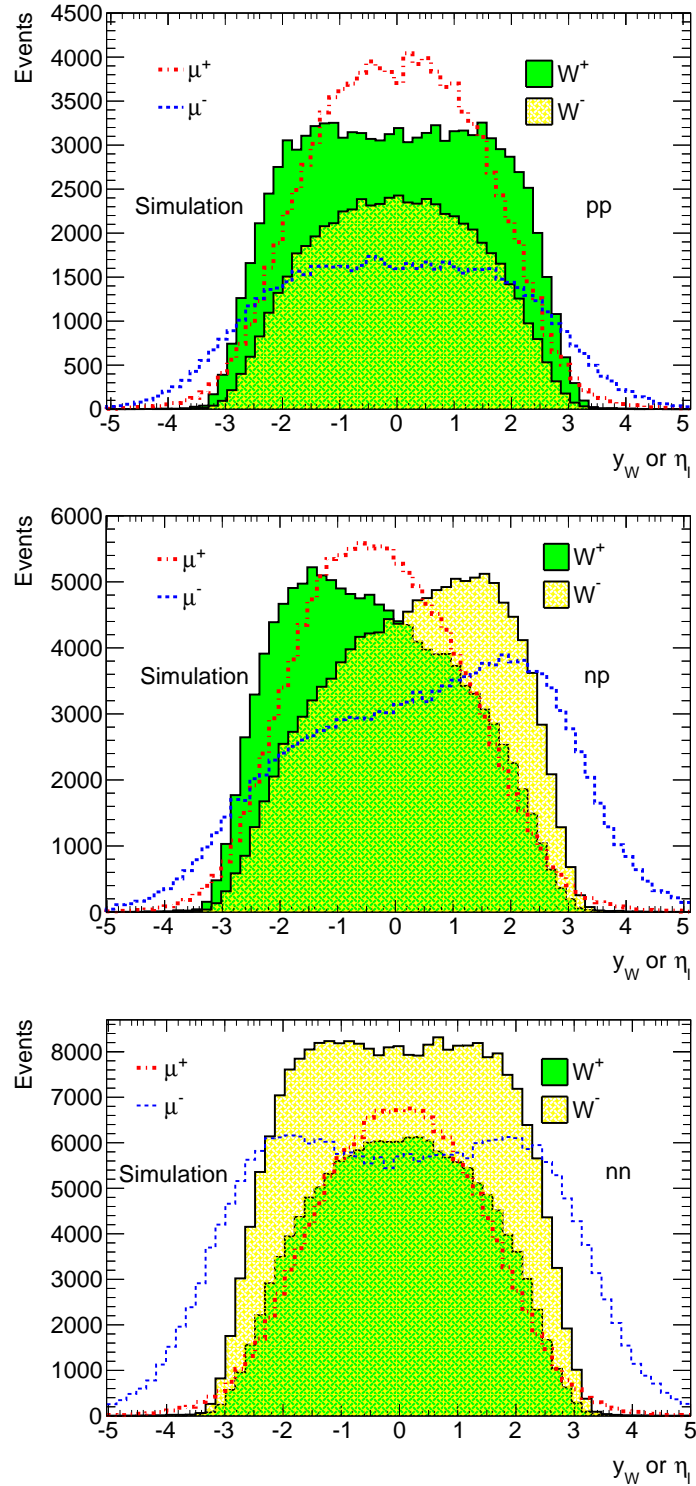
Figure 2.16: W boson rapidity and lepton pseudorapidity in simulated pp (Top), np (Middle), and nn collisions. Predictions are made at NLO using the CT10 PDF sets. The distributions for W^+ and W^- are normalized by their respective cross sections predicted by POWHEG in each collision system.

with vanishing p_T and thus [86]:

$$\cos\theta^* = \left(1 - \frac{4p_{T,\ell}^2}{M_W^2}\right)^{\frac{1}{2}} \tag{2.56}$$

and

$$\frac{1}{\sigma}\frac{d\sigma}{dp_{T,\ell}^2} = \frac{3}{M_W^2}\left(1 - \frac{4p_{T,\ell}^2}{M_W^2}\right)^{\frac{1}{2}}\left(1 - \frac{2p_{T,\ell}^2}{M_W^2}\right) \tag{2.57}$$

This distribution peaks at $p_{T,\ell} = M_W/2$, which is referred to as the *Jacobian peak*.

Information from the neutrino can also be considered by defining the transverse mass:

$$M_T^2 = 2|\vec{p}_{T,\ell}||\vec{p}_{T,\nu}|(1 - \cos\Delta\phi_{\ell\nu}) \tag{2.58}$$

In the absence of any quark transverse momentum, $|\vec{p}_{T,\ell}| = |\vec{p}_{T,\nu}|$ and $\cos\Delta\phi_{\ell\nu} = \pi$. Thus, $M_T = 2p_{T,\ell}$ and also has a Jacobian peak at $M_T = M_W$.

At fixed $p_{T,\ell} \leq \frac{1}{2}M_W$, the rapidities of the W and lepton are related by:

$$|y_W - y_\ell| = \ln\left[\frac{M_W}{2p_{T,\ell}} + \sqrt{\left(\frac{M_W}{2p_{T,\ell}}\right)^2 - 1}\right] \tag{2.59}$$

Thus, at $p_{T,\ell} = \frac{1}{2}M_W$, the rapidities of the lepton and boson are equal and the contribution from the V-A coupling is diminished. Using $y_W = \ln\frac{x_1}{x_2}$, Equation 2.59 can be written as:

$$\frac{1}{2}\left|\ln\frac{x_1}{x_2}\right| = \left|y_\ell \pm \ln\left[\frac{M_W}{2p_{T,\ell}} + \sqrt{\left(\frac{M_W}{2p_{T,\ell}}\right)^2 - 1}\right]\right| \tag{2.60}$$

which implies that for a given lepton rapidity, different values of the ratio x_1/x_2 are probed depending on the lepton p_T.

2.7 QCD Phase Transition

Since this thesis is concerned with W boson production in heavy-ion collisions, the following section will discuss the QCD phase transition that takes place within this type of system. Rolf Hagedorn in the late 1960s first posited the concept of a transition from ordinary nuclear matter to a deconfined state of quarks and gluons [127, 128]. He developed a statistical bootstrap method to use in the

analysis of particle production in high-energy collisions and observed that the number density of resonance states $\rho(m)$ increases exponentially with the mass of observed hadrons:

$$\rho(m) \propto m^{-5/2} e^{m/T_H} \tag{2.61}$$

This behavior implied a singularity in the equation of state of hadronic matter and was understood to be representative of a limiting temperature at which hadrons "melt." The melting point of hadrons was called the Hagedorn temperature with empirical values within the range $150 < T_H <$ 200 MeV. However, the statistical bootstrap model could not provide a physical interpretation for the structure of matter at temperatures greater than T_H.

The resolution came in 1975 when Perry and Collins [129] used the concept of asymptotic freedom in QCD to argue that since the interaction strength of quarks at short distances is weak, matter at high densities consists of freely interacting quarks. Later in that year, Cabibbo and Parisi [130] interpreted the singularity in the equation of state as a phase transition from hadronic gas to plasma of quarks and gluons. They argued that at sufficiently high temperature or density, finite-size hadrons overlap and quarks and gluons are free to move over large space-time distances. The Hagedorn temperature was considered the point at which the phase transition proceeds and was thus coined the transition temperature T_c.

2.7.1   Phenomenology of the Phase Transition

To better understand the quark-hadron phase transition, several models have been proposed. The MIT-Bag model [131] is one example. In this simplified model, a region of space which contains hadron fields is called a "bag." The bag has a radius $R \sim \Lambda_{QCD}^{-1} \approx 1\text{fm}$ and a constant energy density. Quarks within the bag are massless, and hadron confinement is interpreted as the balance of the outward pressure due to the kinetic energy of the quarks and the inward bag pressure from the difference between the energy densities inside and outside the bag. The inward bag pressure B is called the bag constant and ranges between 145 MeV to 235 MeV [132, 133]. When nuclear matter is heated or the baryon density increases, the outward pressure from the quantum kinetic energies of the quarks can overcome the inward bag pressure, thus creating a deconfined state of matter.

In the case of increasing the temperature at zero net baryon density, the total pressure and energy density of a quark-gluon plasma is given by:

$$P = g\frac{\pi^2}{90}T^4$$
$$\epsilon = g\frac{\pi^2}{30}T^4 \tag{2.62}$$

where $g = g_g \times \frac{7}{8}(g_q + g_{\bar{q}})$ represents the degeneracy numbers of the gluons, quarks, and antiquarks. For gluons, $g_g = 8 \times 2$ whereas for (anti)quarks $g_q = g_{\bar{q}} = 3$ colors $\times$ 2 spins $\times$ 2 flavors. The critical temperature at which the quark-gluon pressure is equal to the bag pressure is given by (see Ref. [134]):

$$T_c = \left(\frac{90}{37\pi^2}\right)^{1/4} B^{1/4} \tag{2.63}$$

Above this temperature, the quark-gluon pressure exceeds the bag pressure, and the system is comprised of a deconfined state of quarks and gluons.

In the case where the temperature is held constant and the baryon density increases, the quark-gluon pressure increases as a result of the Pauli exclusion principle. Quarks are fermions and thus cannot occupy the same state. Therefore, when the baryon density increases, the quarks occupy different states by increasing their momentum. This increases the outward quark pressure and energy density. In the case of a quark gas, these are given by:

$$P_q = \frac{g}{24\pi^2}\mu_q^4$$
$$\epsilon_q = \frac{g}{8\pi^2}\mu_q^4 \tag{2.64}$$

The hadron-quark transition occurs when the pressure from the degenerate quark matter equals the bag pressure, which occurs at:

$$\mu_q = \left(\frac{24\pi^2}{g}B\right)^{1/4} \tag{2.65}$$

Though conceptually useful, the bag model has a number of limitations, of which most notable

is chiral symmetry [16] violation at the bag boundary. In 1961, chiral symmetry and spontaneous breaking in a vacuum was first hypothesized by Nambu and Jona-Lasinio (NJL), who formulated a relativistic field theory for point-like interacting nucleons of vanishing mass. In the context of QCD, the nucleons are replaced with nearly massless u and d quarks. Considering only the lightest quarks, the fermionic part of the QCD Lagrangian reads:

$$\mathcal{L} = \bar{u}i\not{D}u + \bar{d}i\not{D}d - m_u\bar{u}u - m_d\bar{d}d \tag{2.66}$$

where $\not{D}$ is the Dirac operator. In the limit of massless quarks, chiral symmetry is upheld. However at low momentum scales (i.e. strong coupling α_S), the QCD vacuum contains a condensate of quark-antiquark pairs i.e. the vacuum expectation value $\langle \bar{q}_L q_R + \bar{q}_R q_L \rangle \neq 0$. The u and d quarks thus acquire an effective mass as they move through the vacuum and the chiral symmetry is spontaneously broken. This "constituent" mass is $\approx 300 - 400$ MeV and explains the mass scale of nucleons. For the u and d quarks, almost 99% of the mass is dynamical and thus created through the nonperturbative structure of the QCD vacuum. According to Goldstone's theorem, spontaneous symmetry breaking is accompanied by the production of massless bosons. The Goldstone bosons of QCD are pions, which are the lightest hadrons. The nonzero mass of the pions is related to the finite bare mass of the u and d quarks.

Since the NJL model incorporates spontaneous chiral symmetry breaking and mass generation, it was widely used to model the QCD phase diagram in the 1980s and 1990s. It could also be used to study chiral symmetry restoration at the critical temperature and quark chemical potential where $\langle \bar{q}_L q_R + \bar{q}_R q_L \rangle$ vanishes and the quarks becomes massless. A prediction of the evolution of the chiral condensate with temperature and quark-chemical potential for u and d quark masses is shown in Figure 2.17. In this figure, a smooth restoration of chiral symmetry is observed along the $T-$axis, whereas along the μ_q-axis, a first-order phase transition is apparent where the condensate ratio increases discontinuously. The transition becomes weaker with increasing T until the critical point is reached. The phase transition is second-order at temperatures above the critical point.

---

[16]Chiral symmetry implies rotating the left-handed and right-handed components independently does not affect the theory.
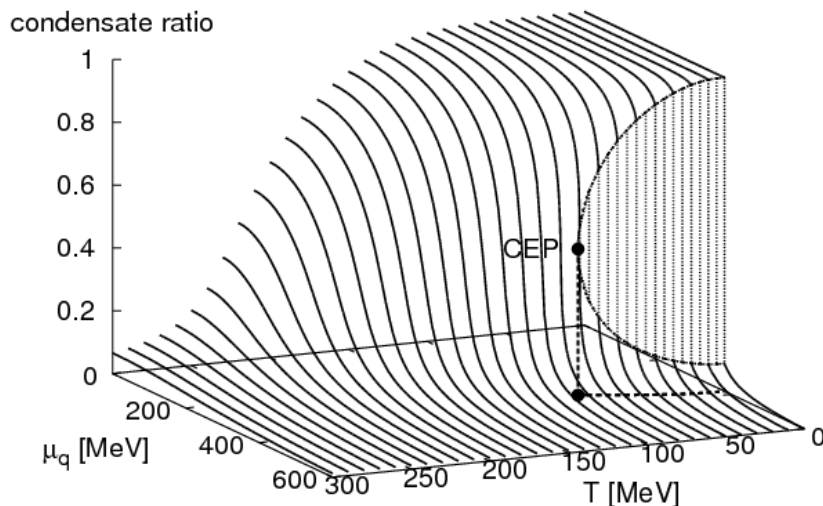
Figure 2.17: Evolution of the chiral-condensate ratio $\langle \bar{q}q \rangle_{T,\mu_q} / \langle \bar{q}q \rangle$ as a function of temperature and quark chemical potential. The region where the ratio jumps discontinuously corresponds to a first-order phase transition. The critical end-point (CEP) is also shown [6].

2.7.2 Lattice QCD

Since the phase transition takes place in the strong coupling regime of QCD, nonperturbative methods must be applied to describe the transformation from hadronic to quark matter. The bag model and NJL model described above provide a conceptual understanding of the deconfining transition. However, determining the QCD equation of state (EoS) involves solving the QCD equations in the strong coupling region, for which lattice gauge theory has proven useful [7, 135, 136]. The lattice QCD calculations relate the thermodynamic partition function to the path integral formulation of quantum mechanics. Rather than using renormalization methods (applicable in pQCD), lattice QCD avoids ultraviolet divergences by placing quark fields on lattice space-time points linked by gauge fields in between sites. The lattice points are separated by a minimum distance, thus defining the upper momentum threshold that renders the quantum field theory finite. The lattice spacing is determined by the distance at which the lattice calculations agree

with the behavior of the coupling constant α_S as a function of the scale Q^2. Lattice calculations provide a theoretical means to understand the dynamics of a QCD plasma with quark and gluon degrees of freedom.

The QCD partition function [7] on a hypercubic lattice of size $N_\sigma^3 N_\tau$ is obtained from the relation between Feynman's path integral formulism in imaginary time $\tau = it$ and the statistical mechanics of a system with temperature $T = 1/\tau$:

$$\mathcal{Z}(\beta, N_\sigma, N_\tau) = \int \prod dU_{x,\mu} e^{-S(U)} \tag{2.67}$$

where β represents the gauge coupling, $U_{x,\mu} \in SU(3)$ are the gauge field variables (labeled x and μ) defined on the links between lattice points, and $S(U)$ is the Euclidean action and includes gauge and fermionic parts:

$$S(U) = \beta S_G(U) - S_F(U) \tag{2.68}$$

The trace of the energy-momentum tensor (also referred to as the *trace anomaly*) $\Theta^{\mu\mu}$ [137] is the most convenient quantity to calculate on the lattice and is used to calculate the EoS. It is defined as the total derivative of $\ln Z$ with respect to the lattice spacing a:

$$\Theta^{\mu\mu} = -\frac{T}{V} \frac{d \ln Z}{d \ln a} \tag{2.69}$$

The trace anomaly is related to the pressure and energy density of the system by:

$$\frac{\Theta^{\mu\mu}(T)}{T^4} = \frac{\epsilon - 3p}{T^4} = T \frac{\partial}{\partial T}(p/T^4) \tag{2.70}$$

The pressure of the system can be obtained by integrating $\Theta^{\mu\mu}/T^5$ over the temperature:

$$\frac{p(T)}{T^4} = \frac{p(T_0)}{T_0^4} + \int_{T_0}^{T} dT \frac{1}{T^5} \Theta^{\mu\mu}(T) \tag{2.71}$$

where T_0 is an arbitrary value that is usually chosen at low temperatures where the pressure and other thermodynamic quantities are exponentially suppressed by Boltzmann factors associated to pions.

Equations 2.70 and 2.71 may be used to calculate the energy ϵ and entropy $s = \epsilon + p$ densities as a function of T. The appropriate second-order derivatives of the QCD partition function with respect

to T can be used to obtain the specific heat and speed of sound of the system. Thermodynamic quantities at low temperatures are well-described by the hadron resonance gas (HRG) model [138, 139], which is used in the continuum extrapolation of $\Theta^{\mu\mu}$. With these basic thermodynamic observables, a parametrization of the QCD EoS may be obtained.

Continuum extrapolated estimates of the pressure, energy density, and entropy density are shown in Figure 2.18 for recent lattice QCD calculations. In this figure, a sharp turn-on is observed in a narrow temperature range, signifying the liberation of quark and gluon degrees of freedom. The turn-on is described as a crossover from hadronic matter to quark-gluon plasma rather than a true phase transition. The crossover is caused by a singularity in the QCD partition function that is expected in the chiral limit (i.e. $m_q \rightarrow 0$).
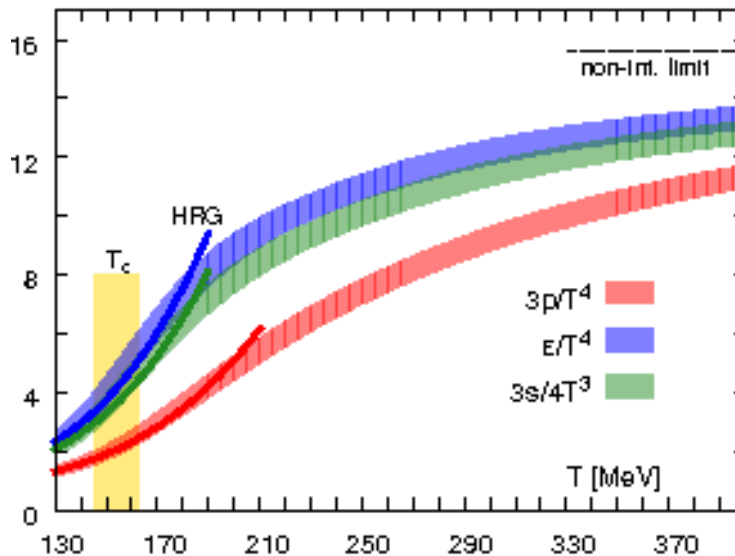
Figure 2.18: Continuum extrapolation of the normalized pressure, energy density, and entropy density as a function of temperature [7]. The horizontal line at $95\pi^2/60$ corresponds to the ideal gas limit for the energy density and the vertical band indicates the crossover region $T_c = (154\pm 9)$ MeV.

The phase structure of QCD can also be studied by analyzing observables that at certain limits become order parameters for chiral symmetry restoration ($m_q \rightarrow 0$) or deconfinement ($m_q \rightarrow \infty$). The chiral condensate is used as an order parameter for spontaneous symmetry breaking in the limit of vanishing quark masses. It can be written as:

$$\langle\bar{\psi}\psi\rangle_q = \frac{T}{V}\frac{\partial\ln Z}{\partial m_q}, \qquad q = l, s \tag{2.72}$$

$\langle\bar{\psi}\psi\rangle_q$ is nonzero at $T < T_c$ and vanishes above T_c. The chiral condensate is renormalized to eliminate singularities and the result is unity at low temperatures and zero at T_c for $m_l = 0$, as shown in Figure 2.19.
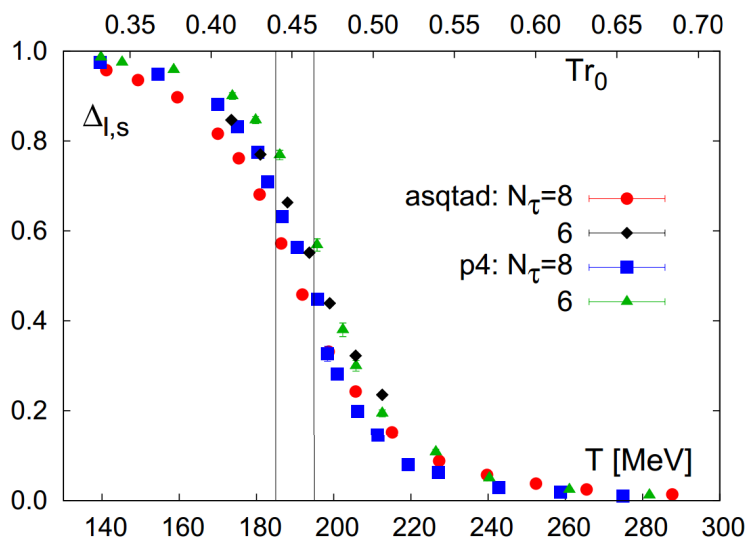
Figure 2.19: The normalized chiral condensate: $\Delta_{l,s} = \frac{\langle\bar{\psi}\psi\rangle_{l,T}-\frac{m_l}{m_s}\langle\bar{\psi}\psi\rangle_{s,T}}{\langle\bar{\psi}\psi\rangle_{l,0}-\frac{m_l}{m_s}\langle\bar{\psi}\psi\rangle_{s,0}}$. The band corresponds to the temperature range $185 \leq T \leq 195$ MeV [8]

The deconfinement transition can be observed using the quark number susceptibilities χ_q, defined in terms of the light and strange quark chemical potentials:

$$\frac{\chi_q}{T^2} = \frac{1}{VT^3}\frac{\partial^2\ln Z}{\partial(\mu_q/T)^2}, \qquad q = l, s \tag{2.73}$$

The quark number susceptibilities are sensitive to the thermal fluctuations of the quark degrees of freedom and change rapidly in the transition region. This can be seen in Figure 2.20, which presents the light-quark number susceptibility.

The expectation value of the trace of the Polyakov loop, which is related to the free energy of a static quark source in a hot gluonic medium, can also be used as an order parameter of the deconfinement transition [140–143]:
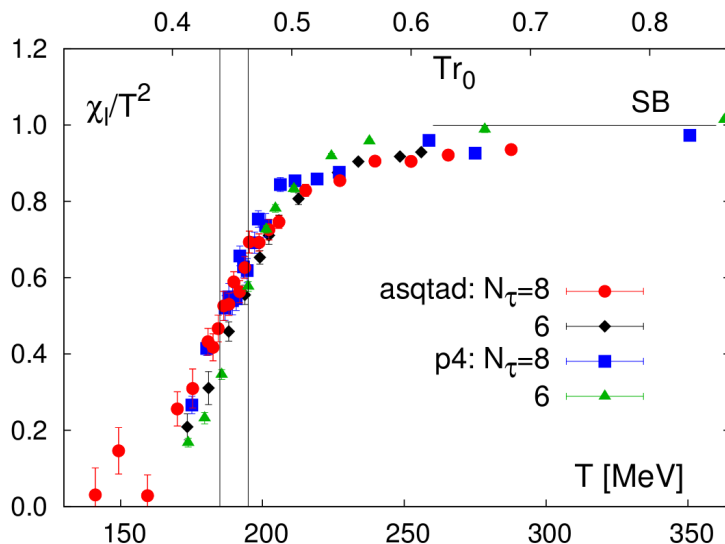
Figure 2.20: The light quark number susceptibility calculated on the lattice. The band corresponds to the temperature range $185 \leq T \leq 195$ MeV [8]

$$\langle L \rangle = \frac{1}{V} \left\langle \sum_{\vec{x}} \text{Tr} L(\vec{x}) \right\rangle \tag{2.74}$$

where $L(\vec{x})$ denotes a closed line integral over gluon fields, representing a static quark source:

$$L(\vec{x}) = \exp\left[-\int_0^{1/T} dx_0 A_0(x_0, \vec{x}) \right] \tag{2.75}$$

Figure 2.21 shows the Polyakov loop as a function of the temperature. The variation in the transition region indicates a more effective screening of static quarks and reduction in the free energy.

The rapid variation of the chiral condensate in the same temperature range as for the bulk thermodynamic observables, chiral susceptibility, and Polyakov loop indicates that the chiral symmetry restoration occurs in the same temperature region as deconfinement.

2.8 Nucleus-Nucleus Collisions

Results from lattice QCD at low baryochemical potential and finite temperatures in combination with empirical data can be used to construct a QCD phase diagram, as shown Figure 2.22. High-energy nucleus-nucleus collisions provide a means to create matter at extremely high temperature
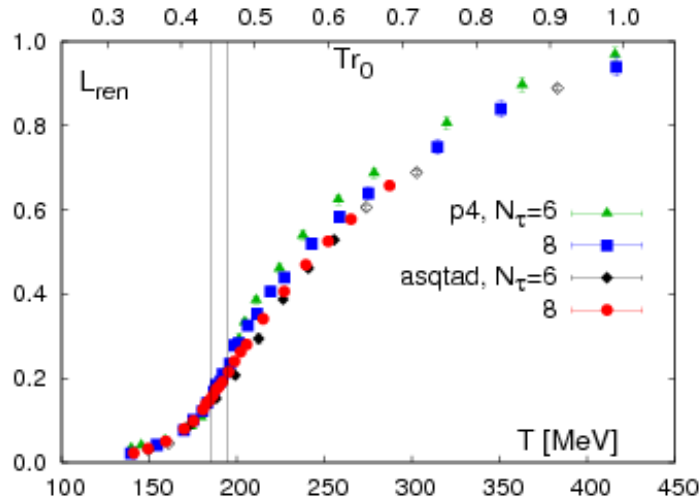
Figure 2.21: Polyakov loop from lattice QCD calculations [8].

and/or baryochemical potential and thus enable exploration of the QCD phase diagram in the laboratory. The high temperatures and densities are attainable partly due to the occurence of multiple collisions. During a collision, a single nucleon may collide with many nucleons in the other nucleus and in so doing deposit a large amount of energy into the colliding system. The amount of energy deposited by the projectile nucleon depends on the thickness of the target nucleus, and thus the larger the radius of the target nucleus, the larger amount of energy lost by the projectile nucleon. This implies that the energy density in a Au + Au collision will not be the same as that in a Pb+Pb collision at the same center-of-mass energy.

2.8.1 Ultrarelativistic Heavy-Ion Collisions and QGP Formation

In an ultrarelativistic heavy-ion collision, the nuclei are substantially Lorentz contracted in the longitudinal direction and may be represented as two thin disks. Upon colliding, a large amount of energy is deposited in a small region of space. The collision region has a large energy density but small baryochemical potential. In the 1980s, Bjorken [144] posited that these conditions could be conducive to QGP formation. In the Bjorken scenario, the plasma formation time is $\tau_f \sim 1/\Lambda_{QCD} \sim 1$ fm/c. The plasma equilibrates at time τ_{ther} and evolves according to the laws of relativistic hydrodynamics. The expansion of the "fireball" results in a decrease in temperature
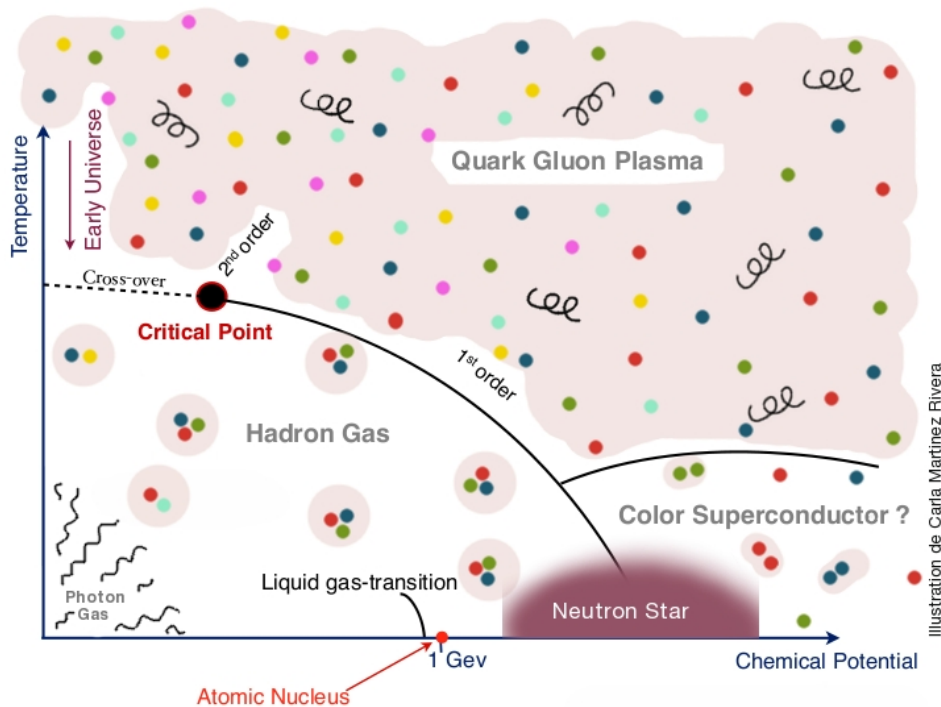
Figure 2.22: QCD phase diagram as a function of T and baryochemical potential. Regions accessible by the LHC are at low baryochemical potential and large T [9].

and conversion to a gas of hadron resonances (freeze-out). Final-state interactions are modelled by a Boltzmann transport equation. The collision evolution is shown schematically in Figure 2.23.

The Bjorken formulism may be used to estimate the initial energy density:

$$\epsilon = \frac{1}{\tau_f \pi R_A^2} \frac{dE_T}{dy} \approx \frac{3}{2} \frac{\langle m_T \rangle}{\tau_f \pi R_A^2} \frac{dN_{ch}}{dy} \tag{2.76}$$

where y is the rapidity, E_T is the transverse energy, πR_A^2 is the transverse area of the overlap region between the two nuclei with $R_A \approx 1.2 A^{1/3}$[fm], and m_T is the transverse mass of secondary particles. To create QGP in the laboratory, the energy density must be in excess of ~ 0.5 GeV/fm^3 [145]. At the LHC in central Pb+Pb collisions, $\epsilon \approx 15$ GeV/fm^3 [146], well above the minimum threshold for QGP formation and approximately three times higher than the energy density reported at RHIC [147]. The increase in energy density corresponds to at least a 30% increase in temperature to $T \approx 300$ MeV using the conservative estimate that the formation time τ_f remains constant at
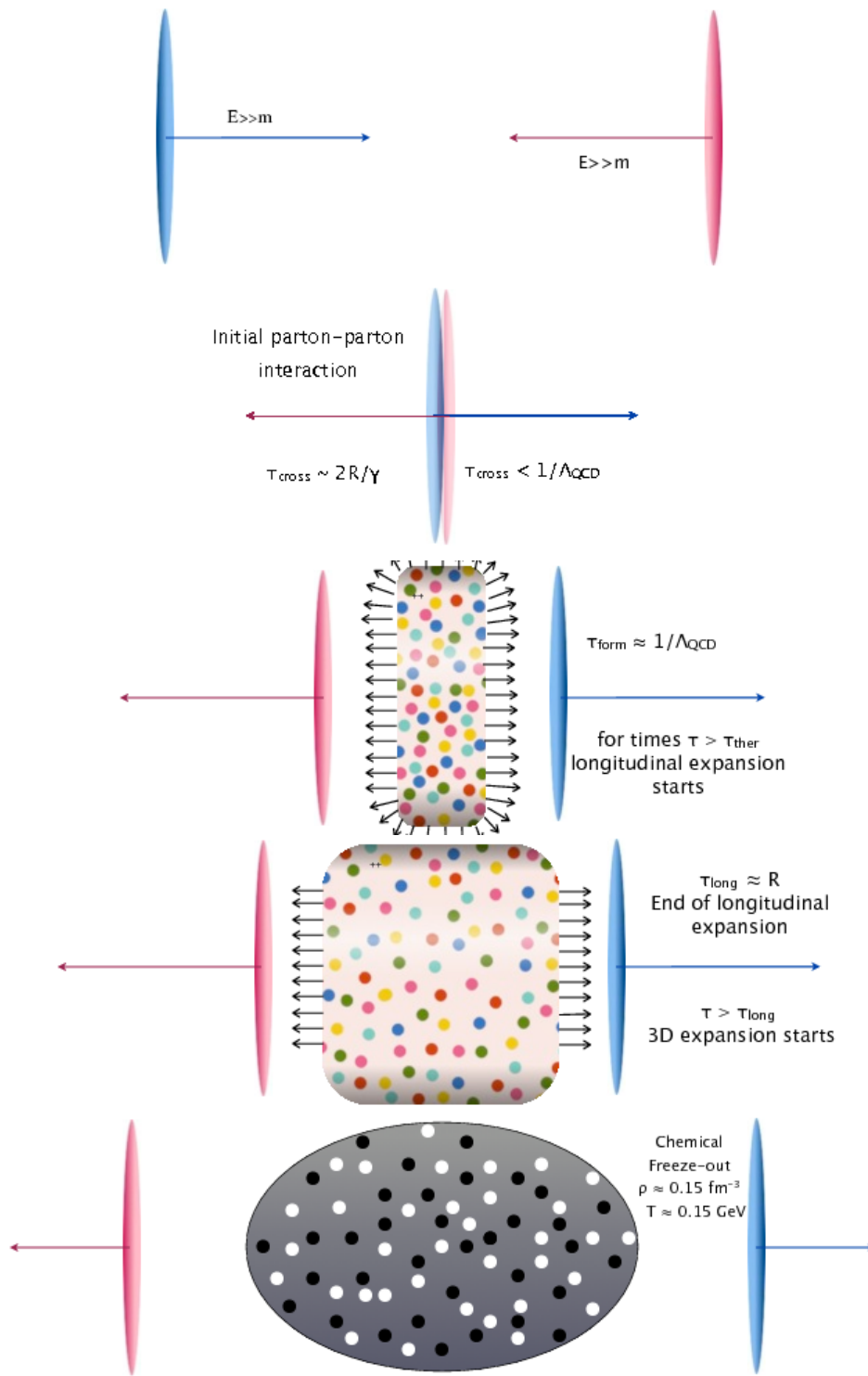
Figure 2.23: Bjorken scenario for the formation of QGP in an ultrarelativistic heavy-ion collision [9].

RHIC and the LHC.

The dynamics of a QGP starting at time τ_f are described by the energy density field ϵ, pressure field p, temperature field T, and four-velocity field $u^\mu = dx^\mu/d\tau$ at different space-time points during the evolution. The energy density, pressure, and temperature are related by the equation of state $\epsilon = \epsilon(p, T)$. The energy-momentum tensor $T^{\mu\nu}$ in the absence of viscosity and heat conduction (i.e. an ideal fluid) is given by:

$$T^{\mu\nu} = (\epsilon + p)u^\mu u^\nu - g^{\mu\nu}p \tag{2.77}$$

The initial configuration of the system is approximately Lorentz invariant, thus making it more feasible to study the hydrodynamics of the QGP. The equation of motion for the QGP is governed by energy-momentum and charged-current conservation:

$$\partial_\mu(J^\mu) = 0, \qquad \partial_\mu T^{\mu\nu} = 0 \tag{2.78}$$

where $J^\mu = nu^\mu$ is the conserved charge current with number density n [17]. The equations above can be closed with the EoS and solved with a hydrodynamical solution in the functional form of ϵ, p, T, u^μ, and n [148–151].

Dissipative fluid dynamics require the inclusion of higher-order terms in the gradients. The most widely used theoretical framework for viscous relativistic fluid dynamics is the Israel-Stewart theory [152]. At the LHC, the main transport coefficients controlling the collective dynamics are the bulk ζ and shear η viscosities and relaxation times for the bulk and shear viscous pressures. These are usually reported with the entropy density s as specific viscosities: η/s and ζ/s. These quantities are difficult to extract from QCD and thus alternative approaches are used that exploit the AdS/CFT correspondence relating strongly-coupled conformal field theories (CFT) to classical gravity in Anti-de-Sitter (AdS) space-time geometries [153]. This method has established a strong-coupling limit for $\eta/s \approx 1/(4\pi)$ [154, 155], which is significantly below the pQCD estimate [156].

Experimentally, the transport properties of a QGP are studied in collisions with an initial-state spatial anisotropy in the overlap region of the colliding nuclei [157–159]. The spatial anistropy gives rise to a final-state momentum anisotropy of emitted particles. This momentum anisotropy is

---

[17]In the strong interaction, the conserved charge currents are isospin, strangeness, and baryon number

sensitive to the viscous properties of the system and provides information of the expansion history. By determining the azimuthal anisotropy coefficients of the measured angular distributions for charged particles (i.e. the charged-particle v_n), hydrodynamic models can be used to extract empirical η/s and ζ/s values.

2.8.2 Glauber Model

In nucleus-nucleus collisions, final-state observables may be affected by the size of the interaction region. The size and shape of the interaction region are correlated with the distribution of nucleons within the incoming nuclei. The geometric configuration of colliding nuclei may be modeled using the Glauber Model [11, 160]. The model is formulated in the optical limit, in which the overall phase shift of the incoming wave is taken as the summation over all possible bi-nucleon phase shifts [161, 162]. At high energies, it is assumed that the nucleons carry sufficient momentum such that they pass through the nucleus undeflected and independently of the other nucleons. The baryon-baryon cross section is assumed constant during the collision [18]. These assumptions allow for construction of analytic expressions for the nucleus-nucleus cross section in terms of the more basic nucleon-nucleon cross section. Below, the main geometric quantities obtained from the Glauber model will be discussed using the notation from Ref. [134].

Let the probability for a baryon-baryon collision within a transverse area element $d\mathbf{b}$ at impact paramter $\mathbf{b}$ be defined as $t(\mathbf{b})d\mathbf{b}$, where $t(\mathbf{b})$ is the baryon-baryon thickness function. Since the collision occurs at some impact parameter, integrating over all impact parameters gives $\int t(\mathbf{b})d\mathbf{b} = 1$. In the collision process, diffractive and elastic collisions result in little or no energy loss of the baryon and therefore only the non-diffractive inelastic component of the nucleon-nucleon cross section is considered. The probability of one baryon at impact parameter $\mathbf{b}$ to interact with another is then $t(\mathbf{b})\sigma_{inel}$.

The collision of a beam nucleus B with target nucleus A is shown schematically in Figure 2.24. The probability to locate a baryon in volume element $d\mathbf{b}_{B(A)}dz_{B(A)}$ in nucleus $B(A)$ at position $\mathbf{b}_{B(A)}, z_{B(A)}$ is given by $\rho_{B(A)}(\mathbf{b}_{B(A)}, z_{B(A)})d\mathbf{b}_{B(A)}dz_{B(A)}$, where ρ is the number density function divided by the number of baryons in the nucleus. The probabilities are normalized to unity. The

---

[18]In principle a baryon can be excited during the collision, thus changing the cross section. However, assuming the cross section to be constant provides an understanding of many of the geometrical concepts in the collision process.

total probability for a baryon-baryon interaction in an $A + B$ collision at impact paramter **b** can then be represented as the product:

$$T(\mathbf{b})\sigma_{inel} = \int \rho_A(\mathbf{b}_A, z_A)d\mathbf{b}_A dz_A \rho_B(\mathbf{b}_B, z_B)d\mathbf{b}_B dz_B t(\mathbf{b} - \mathbf{b}_A - \mathbf{b}_B)\sigma_{inel} \tag{2.79}$$

where the first (second) term represents the probability for finding a baryon from nucleus $A(B)$ in volume element $d\mathbf{b}_{B(A)}dz_{B(A)}$ in nucleus $B(A)$ at position $(\mathbf{b}_{B(A)}, z_{B(A)})$ and the last term is the probability for a baryon-baryon inelastic collision. Equation 2.79 defines the *nuclear thickness function $T(\mathbf{b})$* for the collision $A + B$:

$$T(\mathbf{b}) = \rho_A(\mathbf{b}_A, z_A)d\mathbf{b}_A dz_A \rho_B(\mathbf{b}_B, z_B)d\mathbf{b}_B dz_B t(\mathbf{b} - \mathbf{b}_A - \mathbf{b}_B) \tag{2.80}$$

The thickness function can also be expressed in terms of the individual thickness functions for nuclei A and B:

$$T(\mathbf{b}) = \int d\mathbf{b}_A d\mathbf{b}_B T_A(\mathbf{b}_A)T_B(\mathbf{b}_B)t(\mathbf{b} - \mathbf{b}_A - \mathbf{b}_B) \tag{2.81}$$
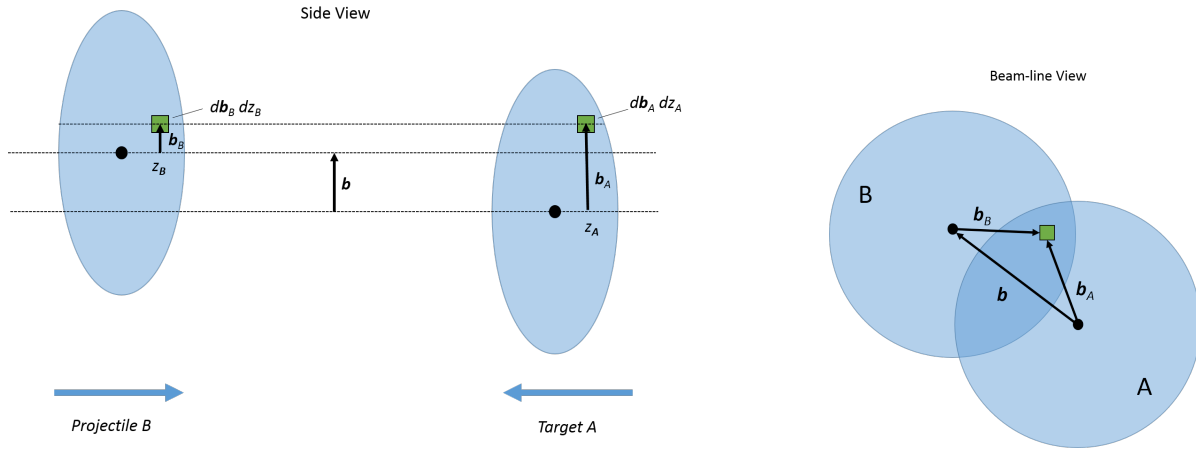
Figure 2.24:   The collision of projectile nucleus B with target nucleus A at impact parameter **b** viewed from the side (left) and along the beam axis (right).

Given the thickness functions, the probability for n inelastic baryon-baryon collisions at impact parameter **b** out of AB possible collisions is a binomial distribution:

$$P(n, \mathbf{b}) = \begin{pmatrix} AB \\ n \end{pmatrix} [T(b)\sigma_{inel}]^n [1 - T(b)\sigma_{inel}]^{AB-n} \qquad (2.82)$$

Integrating Equation 2.82 over the impact parameters gives the total inelastic cross section for an $A + B$ collision:

$$\sigma_{inel}^{AB} = \int d\mathbf{b}(1 - [1 - T(b)\sigma_{inel}]^{AB}) \qquad (2.83)$$

The probability for n inelastic baryon-baryon collisions in Equation 2.82 can be used to obtain the mean number of binary nucleon-nucleon collisions at impact paramter b:

$$N_{coll}(\mathbf{b}) = \sum_{n=1}^{AB} nP(n, b) = ABT(b)\sigma_{inel} \qquad (2.84)$$

The number of nucleons in nucleus A and B that interact inelastically at least once are called "participants" or "wounded nucleons." The number of participants at impact parameter b is given by [163, 164]:

$$N_{part}(\mathbf{b}) = A \int T_A(\mathbf{b}_A)(1 - [1 - T_B(\mathbf{b}_B)\sigma_{inel}]^B)d^2b_A$$
$$+ B \int T_B(\mathbf{b}_B)(1 - [1 - T_A(\mathbf{b}_A)\sigma_{inel}]^A)d^2b_A \qquad (2.85)$$

where the terms represent the number of wounded nucleons from nucleus A passing through nucleus B and vice versa and the integration runs over a plane orthogonal to the collision axis.

2.8.2.1 Inputs to Glauber Calculations

To calculate the geometric quantities described above using the Glauber formulism, the model requires the nuclear charge densities and energy dependence of the inelastic nucleon-nucleon cross section determined from experimental data. The nuclear charge density can be taken from low-energy electron scattering experiments and is parametrized by a Fermi distribution:

$$\rho(r) = \rho_0 \frac{1 + w(r/R)^2}{1 + \exp\left(\frac{r-R}{a}\right)} \qquad (2.86)$$

where ρ_0 and is the nuclear density at the center of the nucleus, R is the nuclear radius, a is the "nuclear skin thickness," and w accounts for deviations from a spherical geometry. Relevant for

this work is the lead nucleus,$^{208}_{82}$Pb, which has a radius $R = 6.62 \pm 0.06$ fm and skin thickness $a = 0.546 \pm 0.01$ fm [165]. Figure 2.25 presents an idealized nuclear charge density for Pb.
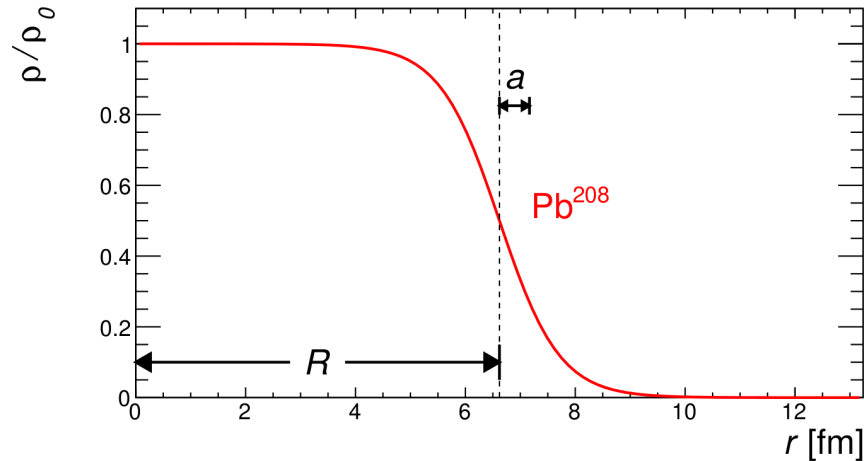
Figure 2.25: Woods-Saxon potential for $^{208}_{82}$Pb [10]

The inelastic nucleon-nucleon cross section σ^{NN}_{inel} can be obtained either from direct measurements [166, 167] at a given $\sqrt{s}$ or indirectly from the total cross section σ_{tot} and elastic cross section $\sigma_{elastic}$ extracted from fits to the world data (see Figure 2.26). At $\sqrt{s_{\text{NN}}} = 2.76$ TeV, $\sigma^{NN}_{inel} = 64 \pm 5$mb. The uncertainty in this value constitutes a major systematic uncertainty in the calculation of Glauber quantities.

2.8.2.2   Glauber Monte Carlo

In the optical limit approximation, terms that describe event-by-event local density fluctuations are neglected [11, 164], implying that the projectile "sees" the target as a smooth density. These effects can be included using a Monte Carlo method [168] in which the nucleons are stochastically distributed event-by-event and geometric quantities are obtained by averaging over multiple events. The optical and Monte Carlo Glauber calculations give similar results for N_{part} and b but deviate for quantities sensitive to event-by-event fluctuations (e.g. event eccentricity).

The Glauber Monte Carlo (GMC) approach allows for relating experimental (e.g. charged particle multiplicity) to geometric quantities. The GMC distributes the nucleons in nucleus A and nucleus B in a three-dimensional coordinate system according to $\rho(r)_A$ and $\rho(r)_B$. An impact
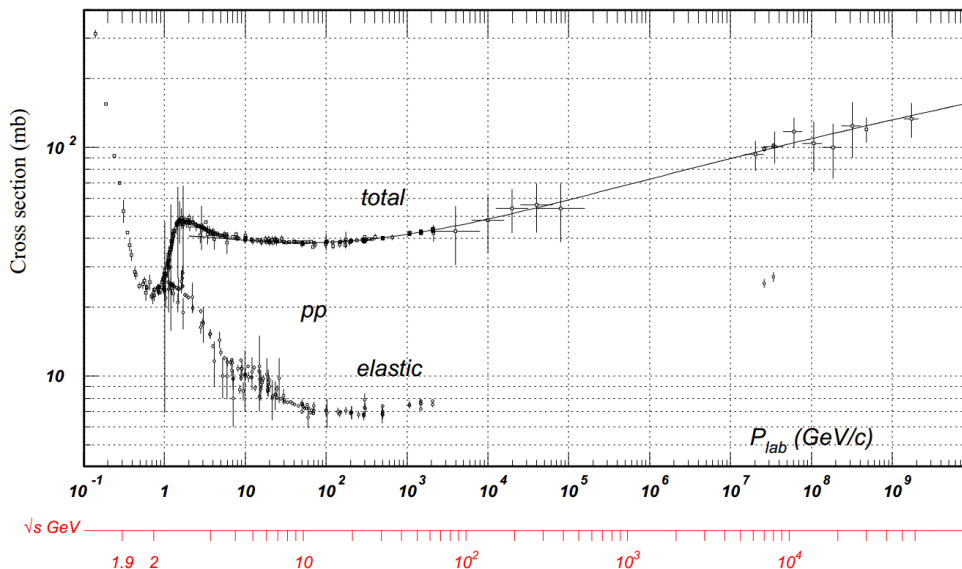
Figure 2.26:   Total and elastic cross section for *pp* collisions as a function of laboratory beam momentum and total center-of-mass energy [2].

parameter b is sampled from the distribution $\mathrm{d}\sigma/\mathrm{d}b = 2\pi b$. The nucleons in each nucleus travel on straight-line trajectories (eikonal approximation), and the nucleons either undergoe a collision (i.e. are wounded) or are tagged as "spectators." The collision process is treated as a sequence of independent binary nucleon-nucleon collisions. A binary collision occurs if the distance between the nucleons d in the transverse $(x - y)$ plane satisfies the condition:

$$d \leq \sqrt{\sigma_{inel}^{NN}/\pi} \tag{2.87}$$

where the right-hand term is called the "hard-disk radius." If a nucleon interacts inelastically at least once, it becomes a participant. The total number of participants and binary nucleon-nucleon inelastic interactions in a collision are designated by N_{part} and N_{coll}, respectively. The mean number of participating nucleons $\langle N_{\mathrm{part}} \rangle$ and binary nucleon-nucleon collisions $\langle N_{\mathrm{coll}} \rangle$ are determined by simulating many nucleus-nucleus collisions and averaging over events. An example of a GMC event for a Au+Au collision with $b = 6$ fm is shown in Figure 2.27.
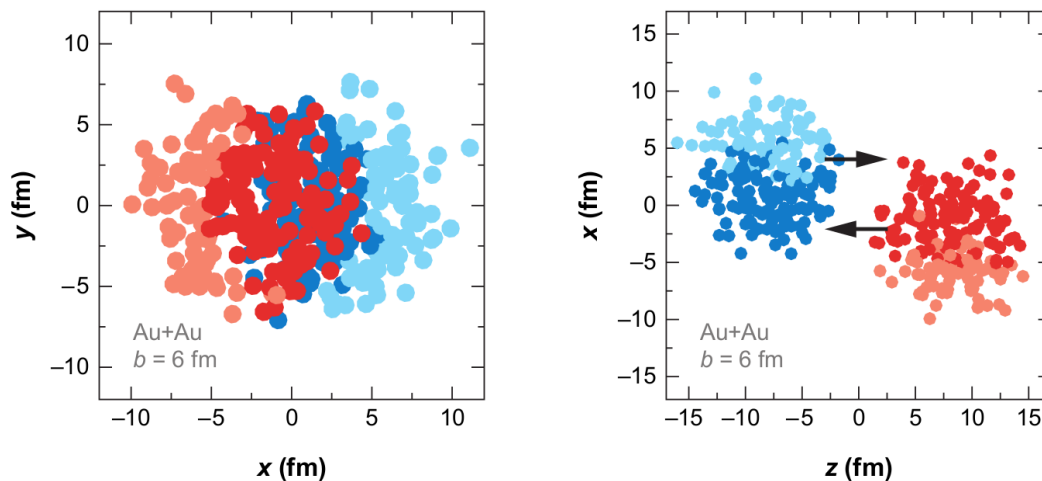
Figure 2.27: Example of Glauber MC event with $b = 6$ fm along the transverse plane (left) and along the beam direction (right). Participants are shown as darker disks [11].

2.8.2.3   Mapping the Glauber Model to Experimental Data

$\langle N_{\text{part}} \rangle$ and $\langle N_{\text{coll}} \rangle$ cannot be measured directly, and therefore distributions from experimental data must be mapped to corresponding Glauber quantities. Measureable quantities with distributions similar to N_{part} and N_{coll} distributions (e.g. total charged particle multiplicity or total transverse energy) are typically chosen for the mapping procedure. The mapping is performed by defining *centrality classes* in both the measured and Glauber distributions.

The construction of centrality classes assumes that the impact parameter b (and thus N_{part} and N_{coll}) is monotonically related to the particle multiplicity. Events with large b are expected to have low multiplicity and are referred to as *peripheral* collisions, whereas events with small b are expected to have high multiplicity and are referred to as *central* collisions. Suppose some final-state observable ξ is used to determine the centrality classes and the integral of the distribution of ξ is known. Then by binning the distribution, the fraction of total events within each bin can be used to define the centrality classes.

When defining the centrality classes, the integration is typically performed from large to small values of ξ, and the centrality is typically reported as a percentage. In this manner, the $a - b\%$ centrality class is defined by bin boundaries n_a to n_b in the distribution of ξ such that:

$$100 \left(\frac{\int_{\infty}^{n_a} \frac{\mathrm{d}N_{\mathrm{evt}}}{\mathrm{d}\xi} \mathrm{d}\xi}{\int_{\infty}^{0} \frac{\mathrm{d}N_{\mathrm{evt}}}{\mathrm{d}\xi} \mathrm{d}\xi} \right) = a[\%] \text{ and } 100 \left(\frac{\int_{\infty}^{n_b} \frac{\mathrm{d}N_{\mathrm{evt}}}{\mathrm{d}\xi} \mathrm{d}\xi}{\int_{\infty}^{0} \frac{\mathrm{d}N_{\mathrm{evt}}}{\mathrm{d}\xi} \mathrm{d}\xi} \right) = b[\%] \tag{2.88}$$

This methodology is illustrated in Figure 2.28.

Once the centrality classes in the data have been determined, Glauber quantities must then be related to each centrality class. This is performed using the "two-component" model [169, 170]. In this model, nuclear collisions are segmented into two components: a "soft" component, which is assumed to be proportional to N_{part}, and a "hard" component, which is proportional to N_{coll}. The Glauber quantity ξ_G can then be described by the linear combination:

$$\xi_G = (1 - x)\frac{N_{\mathrm{part}}}{2} + xN_{\mathrm{coll}} \tag{2.89}$$

where $0 < x < 1$ and is determined from fitting the distribution $\mathrm{d}N_{\mathrm{evt}}/\mathrm{d}\xi_G$ from a Glauber MC sample to the measured $\mathrm{d}N_{\mathrm{evt}}/\mathrm{d}\xi$. The distribution of ξ_G can be divided into centrality classes using the same procedure as applied in the data. The $\langle N_{\mathrm{coll}} \rangle$ and $\langle N_{\mathrm{part}} \rangle$ for each centrality class in the data can then be determined by averaging over the N_{coll} and N_{part} in the same centrality class from the Glauber MC sample.

2.9   Nuclear Modification to Parton Distribution Functions

Free nucleon parton distribution functions were introduced in the preceding sections (see Sec. 2.4). However, in the 1980s it was discovered that the momentum distributions for quarks and gluons in bound nucleon systems were different than those in free or loosely bound nucleons [171]. This implied that the nuclear structure functions are not simply the superposition of the structure functions from each individual nucleon. Later measurements of the ratio between the structure function of various nuclei $F_2^A(x, Q^2)$ and of deuterium $F_2^D(x, Q^2)$ revealed deviations from unity [172]. This garnered interest among nuclear physicists to accomodate nuclear effects into pre-existing PDFs, resulting in sets of nuclear PDFs (nPDFs) [12, 173–175].

The nPDFs are assumed to evolve according to the same DGLAP equations as in the free nucleon PDFs but with a modified initial parametrization. Given the trivial modification due to the presence of both protons and neutrons in a nucleus, which have different valence quark
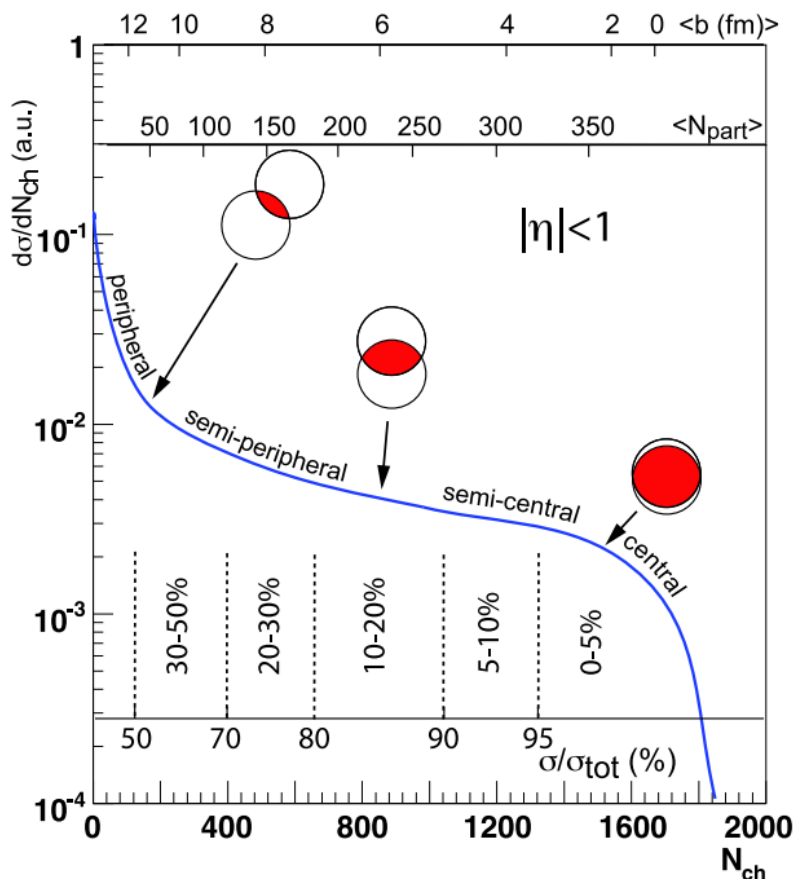
Figure 2.28: Schematic of the mapping of experimental observables (here the number of charged particles N_{ch}) with Glauber quantities $(b, \langle N_{\text{part}} \rangle)$ [11].

distributions, the nPDF for a bound nucleon within a nucleus with mass number A, proton number Z, and neutron number $A - Z$ may be expressed as [13, 176]:

$$f_i^A(x, Q^2) = \frac{Z}{A} f_i^{p/A}(x, Q^2) + \frac{A - Z}{A} f_i^{n/A}(x, Q^2) \tag{2.90}$$

where i designates the parton flavor, and the bound neutron PDF $f_i^{n/A}$ is obtained from the bound proton PDF $f_i^{p/A}$ using isospin symmetry (see Eqn. 2.38). Eqn. 2.90 implies that observables sensitive to valence quark distributions (e.g. $W \rightarrow \ell \nu_\ell$ charge asymmetry) are expected to be modified in bound nucleon systems. This sensitivity stems from the difference in the valence quark distributions in the proton and neutron at large x values and is typically referred to as *isospin*

effects.

Additional nuclear modifications can be quantified by the ratio between the bound and free proton PDFs:

$$R_i^A(x, Q^2) = \frac{f_i^{p/A}(x, Q^2)}{f_i^p(x, Q^2)} \tag{2.91}$$

The nuclear PDFs can be obtained from a global analysis [173] that imparts a nuclear A-dependent parametrization for $f_i^{p/A}(x, Q^2)$ at some energy scale Q_0 or from a parametrization of $R_i^A(x, Q^2)$ at an initial scale using a well-established free proton PDF set as a baseline [12]. The latter is more widely used and takes into account the following nuclear effects in different regions of x (Figure 2.29):

- Shadowing at $x \lesssim 0.01$; $R_i^A < 1$; In most models, the origin is related to the hadronic behavior of the virtual photon [177]. A destructive interference effect reduces the flux and interactions in the interior and back face of the target nucleus. The target nucleon sees less of an incoming flux and is shadowed by elastic interactions on the front face of the nucleus [178], thus reducing the effective nucleon cross section.

- Antishadowing at $x \sim 0.1$; $R_i^A > 1$; This effect is usually explained on the basis that anti-shadowing is required to restore the momentum sum rule in nuclei, thereby compensating for the shadowing and EMC-effects [179].

- EMC-effect [19] at $0.3 \lesssim x \lesssim 0.7$; $R_i^A < 1$; A parton model interpretation ascribes this effect to valence quarks within the nucleus carrying a smaller momentum fraction than those within a free nucleon.

- Fermi-motion at $x \to 1$ and beyond; $R_i^A > 1$; This effect stems from nonstationary nucleons within the nucleus.

These nuclear effects are empirically observed and at present have no unique theoretical description. An overview of several models to describe these effects may be found in Refs. [172, 180, 181].

The nuclear modifications obtained from the EPS09 nuclear PDF set for valence quark, sea quark, and gluon density functions in Pb at two different energy scales are presented in Figure 2.30.

---

[19]EMC stands for European Muon Collaboration
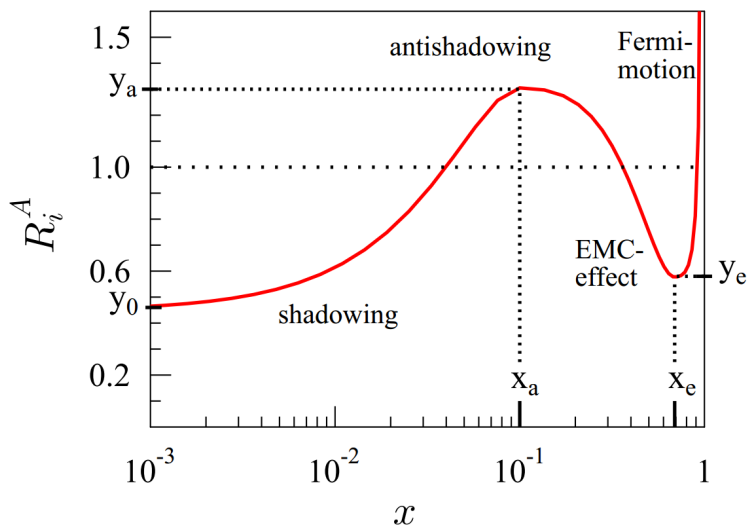
Figure 2.29: Schematic of $R_i^A(x, Q^2)$ as a function of x and the different nuclear effects in each x region [12]. In this figure, y_0 is the height at which shadowing levels out as $x \to 0$, x_a and y_a are the position and height, respectively, at which antishadowing is maximum, and x_e and y_e are the position and height at which the EMC-effect is a minimum.

The errors are calculated using the Hessian method (Eqns. 2.37) and are weighted by the proton and neutron number in the Pb nucleus.

2.9.1   Spatial dependence of nPDFs

Since the nuclear thickness depends on the transverse position in the nucleus, the nuclear modification depends on the point at which it is probed. This so-called "spatial dependence" corresponds to a centrality dependence in the nPDFs, and thus impact-parameter dependent nPDF sets have also been proposed [13]. The spatial dependence is introduced into the nPDFs by defining a spatially dependent nuclear modification $r_i^A(x, Q^2, s)$ for parton flavor i that is assumed to be a function of the nuclear thickness $T_A(\mathbf{s})$:

$$R_i^A(x, Q^2) \equiv \frac{1}{A} \int d^2\mathbf{s}\, T_A(\mathbf{s}) r_i^A(x, Q^2, \mathbf{s}) \tag{2.92}$$

where T_A is the thickness function and is normalized to A. The case where $R_i^A = r_i^A = 1$ corresponds to no nuclear effects. Using Eqn. 2.92, the number distribution of an observable k in an $A + B$
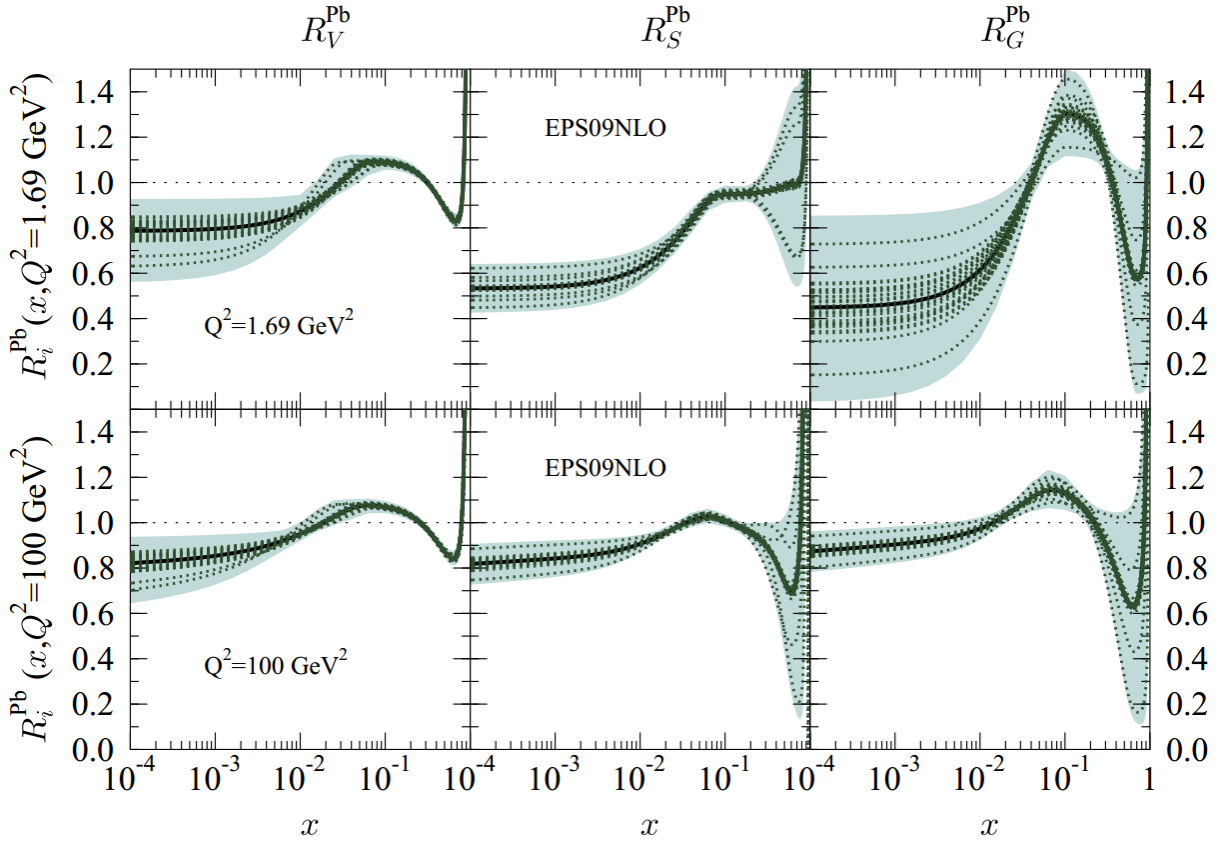
Figure 2.30: Nuclear modifications at initial scales $Q_0 = 1.69$ GeV^2 and 100 GeV^2 in Pb. The black lines indicate the best-fit results and the dotted-green lines are the error eigensets. The shaded bands are calculated from 31 nPDF sets using the Hessian method [12].

collision at impact parameter **b** is given by:

$$dN^{AB \to k+X}(\mathbf{b}) = T_{AB}(\mathbf{b})d\sigma^{AB \to k+X}$$

$$= \sum_{i,j,X'} \sum_{N_A,N_B} \int d^2\mathbf{s_1} T_A(\mathbf{s_1}) r_i^A(x_1, Q^2, \mathbf{s_1}) f_i^{N_A}(x_1, Q^2) \otimes$$

$$\int d^2\mathbf{s_2} T_B(\mathbf{s_2}) r_j^B(x_2, Q^2, \mathbf{s_2}) f_j^{N_B}(x_2, Q^2) \otimes d\hat{\sigma}^{ij \to k+X'} \delta(\mathbf{s_2} - \mathbf{s_1} - \mathbf{b}) \quad (2.93)$$

where $N_{A(B)}$ are the number of nucleons in nucleus $A(B)$. The x and spatial dependence for the EPS09s NLO nuclear modification for the valence and sea u quark and for the gluon is shown in Figure 2.31.

2.9.2 W Bosons as a Tool for Detecting Nuclear Modification

Earlier in this chapter, it was shown that W bosons provide an excellent tool for constraining free nucleon PDFs. It should therefore come as no surprise that they should, in principle, provide a powerful means to study nuclear modifications. W bosons at $\sqrt{s_{\mathrm{NN}}}$=2.76 TeV probe the region $10^{-3} < x < 10^{-1}$ at $|y| < 2.5$, and thus measurements of W production at the LHC can potentially detect effects related to shadowing/antishadowing.

Rapidity distributions of the W in Pb+Pb collisions have already been determined from theory [14]. Figure 2.32 shows the absolute rapidity distribution for $W^{\pm}$ bosons with and without EPS09 nuclear effects at $\sqrt{s_{\mathrm{NN}}}$= 2.7 and 5.5 TeV [20]. These distributions are normalized to the integrated cross section over all rapidity at the corresponding collision energy. The differences between the distributions with and without EPS09 corrections are small but noticeable and demonstrates that the W is indeed sensitive to nuclear effects.

2.10 W Bosons as Benchmarks for Jet Energy Loss

In addition to providing a method for studying parton distribution functions and nuclear modification thereof, W bosons can also be used to benchmark strongly-interacting processes in a QGP. W

---

[20]These are the two collision energies available at the LHC for the Pb+Pb runs periods. This thesis presents the result from 2.76 TeV. Collisions at 5.5 TeV are anticipated in November 2015.
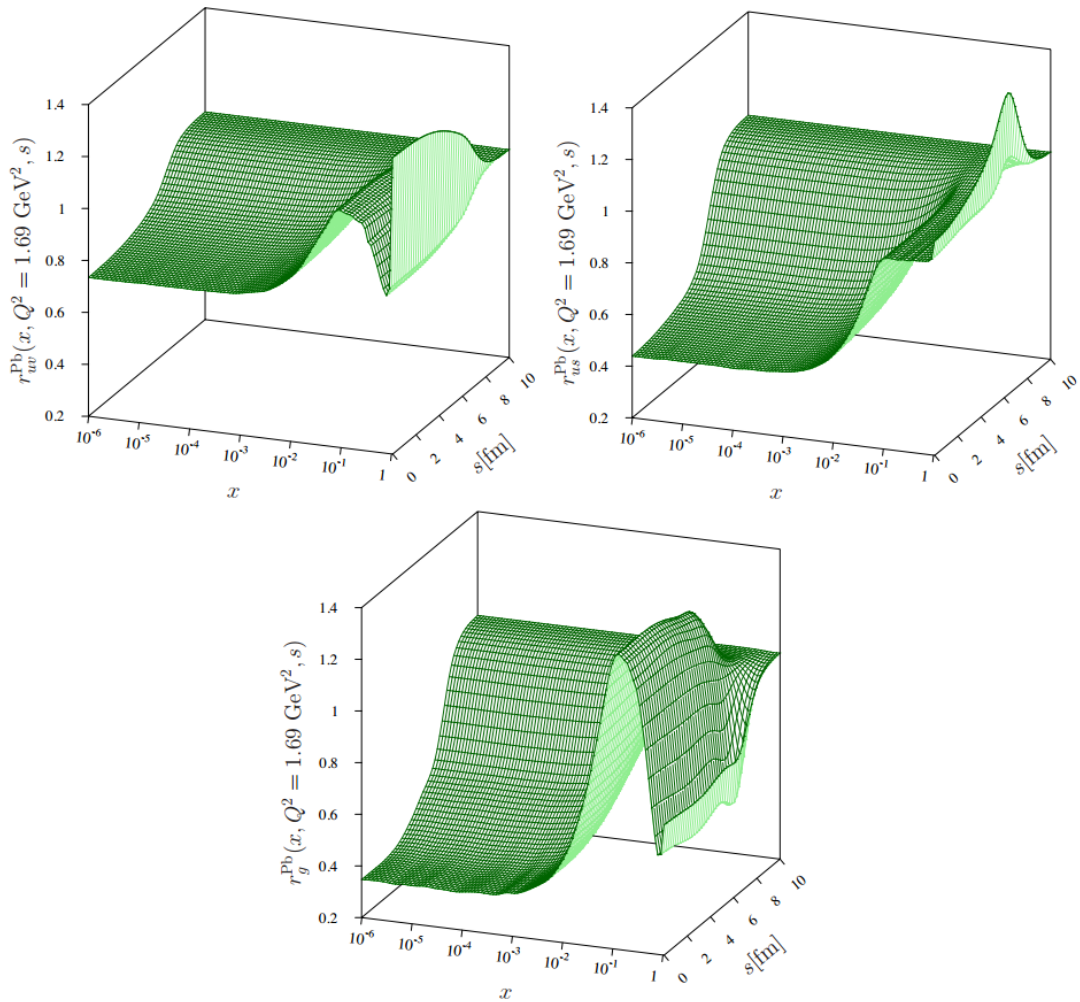
Figure 2.31: The x and spatial dependence of the EPS09s NLO nuclear modification for u valence (upper left), sea (upper right), and gluon (lower) PDFs at $Q^2 = 1.69$ GeV^2 for Pb [13].
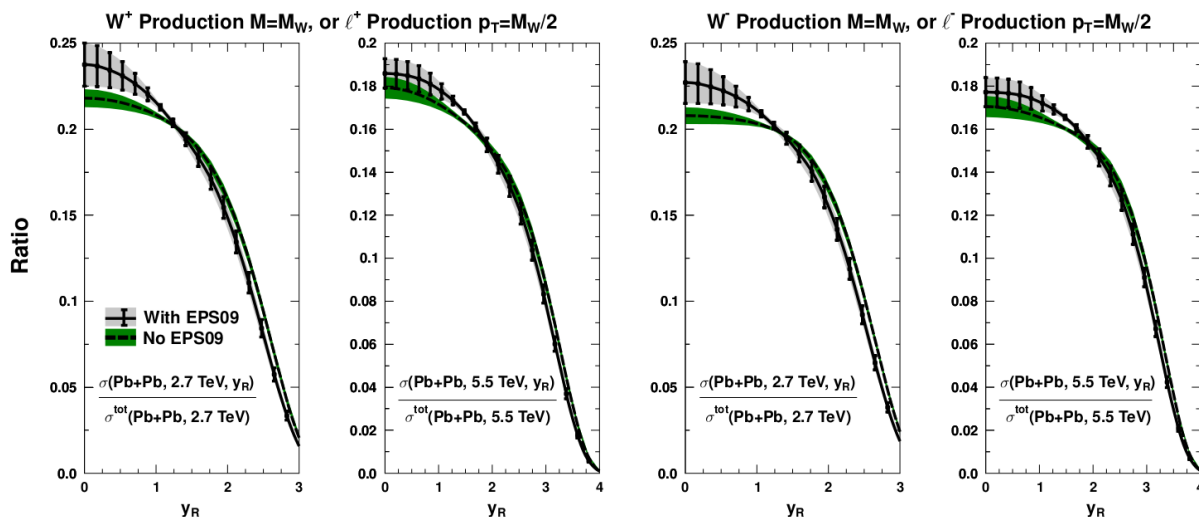
Figure 2.32: Predicted $W^{\pm}$ rapidity distributions in Pb+Pb collisions at $\sqrt{s_{NN}}=$ 2.7 and 5.5 TeV [14]. The cross sections are normalized to the integrated cross section over all rapidity. The green band is the prediction without nuclear effects, whereas the gray-shaded distribution applied EPS09 nuclear corrections. σ^{tot} indicates the cross section integrated over the rapidity.

bosons and their leptonic decay products are not expected to interact with a strongly-coupled QGP, and thus W production rates should scale with the number of binary nucleon-nucleon collisions. One of the goals of this thesis is to show that binary scaling holds in the case of W production, thus implying that Glauber calculations accurately model the geometry of nucleus-nucleus collisions.

A hallmark signature for QGP formation is the interaction of jets with the medium. This phenomenon is referred to as *jet quenching* and has received widespread attention in the heavy-ion community. The concept is that back-to-back jets produced in a heavy-ion event may experience different path lengths as they traverse the medium. A highly energetic jet close to the edge of the fireball may emerge from the medium while its partner travels a longer distance and thus loses a large fraction of its energy from multiple interactions and gluon radiation. Jet-quenching has been directly observed at the LHC [36, 182, 183] and indirectly at RHIC [184, 185]. An in-depth description of jet-quenching is outside the scope of this thesis. However, a nice discussion of the physics models for parton energy loss in a QGP may be found in Ref. [10] and the references therein.

The exact mechanism of jet-quenching remains to be elucidated. One of the limiting factors

is the inability to determine the initial energy of the jet since, in principle, the leading jet may experience some degree of quenching. Wang et al. [15] proposed a resolution to study jet-quenching in events where an electroweak probe (i.e. W, Z, γ) is produced in the opposite direction of the jet. The initial energy of the produced jet could then be approximated as the energy of the electroweak boson after correcting for initial-state radiation i.e. $E_T^{jet,initial} \approx E_T^{boson}$. Measurements of the momentum imbalance in boson+jet events have already been conducted at the LHC [186–188].

To relate parton energy loss to single particle measurements, a fragmentation function $D_i^h(z, Q)$ [2] is used. $D_i^h(z, Q)$ is defined as the probability that a hadron of type h carries longitudinal momentum fraction z of the momentum $\mathbf{p}_i$ of parent parton type i. Pertubative QCD calculations have shown that the p_T spectrum of charged hadrons with moderate p_T in the direction opposite the electroweak boson is a good approximation of the jet fragmentation function:

$$\frac{dN_{ch}^{jet}}{dyd^2p_T} = \sum_{i,h} r_i(E_T^{boson}) \frac{D_i^h(p_T/E_T)}{p_T E_T} \frac{C(\Delta y, \Delta \phi)}{\Delta y \Delta \phi} \tag{2.94}$$

where $C(\Delta y, \Delta \phi)$ is the acceptance factor for finding jet fragments in a given kinematic range. The summation is over the jet-type and hadron species and $r_i(E_T^{boson})$ is the fractional production cross section of jet type i associated to the electroweak boson. The averaged inclusive fragmentation function in a boson-tagged event can then be extracted from the relation:

$$D_{AA}^{boson}(z) = \int \frac{d^2 r T_A^2(r)}{T_{AA}(0)} \sum_{i,h} r_i(E_T^{boson}) D_i^h(z, \Delta L) \tag{2.95}$$

where ΔL is the distance traveled by the scattering parton before escaping from the medium, $T_{AA}(0)$ is the nuclear overlap function in $A + A$ collisions at zero impact parameter, and $T_A(r)$ is the nuclear thickness function for nucleus A at impact parameter r.

Equations 2.94 and 2.95 imply that measurements of the p_T spectra of charged particles produced in the opposite direction of the W boson in $W + $ jet events (e.g. $q\bar{q}' \to Wg$ or $gq \to Wq$) can be used to reliably extract inclusive jet fragmentation functions. The fragmentation functions can then be compared to (unmodified) fragmentation functions measured in pp, pA, or peripheral $A + A$ collisions to determine modification due to jet quenching. An example of this procedure from simulation is presented in Figure 2.33 for photon-tagged jets. This type of measurement can help constrain jet energy loss in a QGP and discriminate against different parton energy loss formulisms.

However, unlike for photons and Z bosons, the p_T for W bosons must be reconstructed from the missing energy of the event (a proxy for the neutrino), which will introduce additional experimental uncertainties.
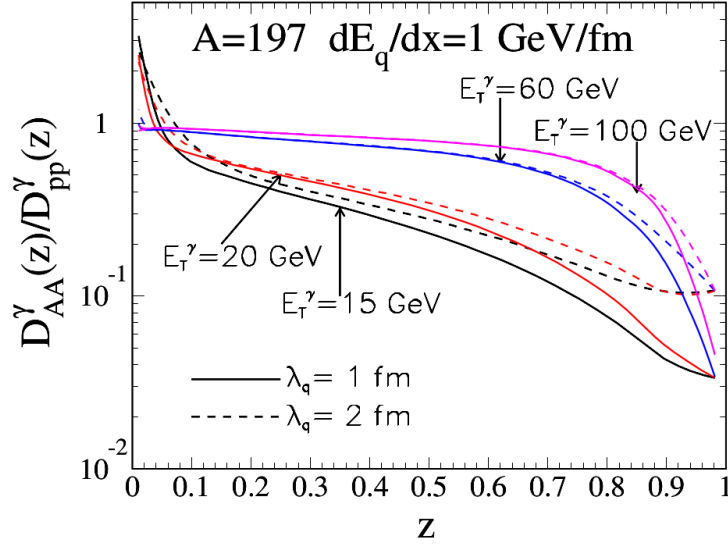
Figure 2.33: Ratio of inclusive fragmentation function of a photon-tagged jet with and without energy loss in central $Au + Au$ collisions as a function of longitudinal momentum fraction z from simulation [15]. Energy loss is observed for larger jet energies (large z). dE_q/dx designates the energy loss of the parton in the medium and λ_q indicates the mean-free path.

Chapter 3

The Large Hadron Collider and the ATLAS Detector

This chapter begins with an overview of the operation of high-energy colliders. This is followed by a description of the Large Hadron Collider at CERN. The chapter concludes with a detailed discussion about the ATLAS detector and the components used to collect the data presented in this work.

3.1 High-Energy Colliders

Particle accelerators are a fundamental tool for understanding the physics of sub-atomic processes. According to the de Broglie equation $\lambda = h/|\vec{p}|$, larger beam energies correspond to shorter wavelengths and thus provide access to a smaller length scale. The utility of particle accelerators was first observed in 1911, when Rutherford discovered the nucleus by scattering α-particles off aluminum foil. In the 1930s, scientists were able to further study the inner structure of matter at the MeV scale. Today, technologic advances and collaboration have allowed scientists to probe deeper into the structure of the nucleus than ever before, constructing machines capable of accelerating particles up to several TeV. This has opened up exciting opportunities for new physics discoveries.

3.1.1   Beam Dynamics

A beam of particles may be collided in two ways: collision with another beam or collision with a fixed target. In the latter, the center-of-mass energy $E_{CM} = \sqrt{2mc^2 E_{inc}}$, where m is the mass of the beam-target system and E_{inc} is the energy of the incident beam. In the case of a collision with two counter-rotating beams, $E_{CM} = 2E_{inc}$. Therefore, higher energies are much more attainable using a colliding beam configuration.

The most basic way to accelerate a particle is by using an electrostatic field between two electrodes. The energy gain by the particle is given by $q\Delta V$, where q is the charge on the particle and ΔV is the voltage potential. However, at high energy scales, insulation problems limit the maximum amount of energy a particle can gain. These limitations can be overcome by using radio-frequency (RF) acceleration, in which an RF oscillator supplies voltages to a series of drift tubes separated by gaps. While a particle is within a tube, it is shielded from the electric field. Reversing the polarity of the field causes the particle to accelerate at each gap.

This technique is used in circular accelerators, of which the first was the cyclotron. In a cyclotron, a constant magnetic field $\vec{B}$ is applied across two hollow D-shaped electrodes connected to an RF electric voltage generator, as shown in Figure 3.1.
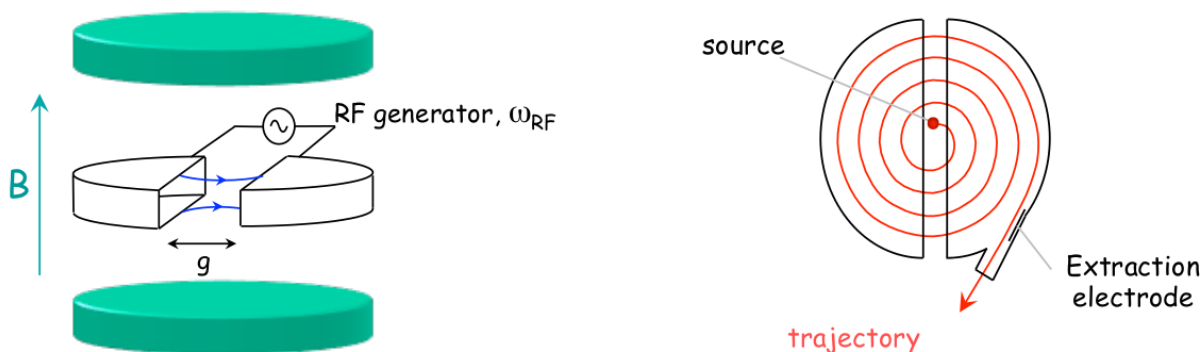
Figure 3.1: Schematic of the particle trajectory in a cyclotron [16].

Particles generated by a source at the center may be accelerated between the electrode gap if the frequency of the RF oscillation ω_{RF} is synchronous with the angular frequency of the particle ω_s:

$$\omega_{RF} = \omega_s = \frac{qB}{m} \tag{3.1}$$

This condition holds as long as the velocity of the particle $v << c$. However, as the particle approaches the speed of light, its frequency is no longer independent of its velocity, and thus to remain in phase the cyclotron frequency must depend on the relativistic Lorentz factor $\gamma(t)$ of the particle:

$$\omega_{RF}(t) = \omega_s(t) = \frac{qB}{m\gamma(t)} \tag{3.2}$$

Equation 3.2 shows that synchronization of the particle and RF oscillator can be achieved by decreasing the radio frequency during the acceleration cycle according to $\gamma(t)$. This type of system is called a synchrocyclotron and generates pulsed beam bunches. The synchrocyclotron can accelerate protons up to ~500 MeV but the energy attainable is limited by the size of the magnet [16].

In 1945, E.M. McMillan [189] and V. Veksler [190] discovered a phase focusing principle that evolved the cyclotron into an accelerator that could guide the particle orbit while tuning the RF system and magnetic field to synchronize with the revolution frequency of the particle. This type of machine is called a *synchrotron*. In a synchrotron, the nominal particle trajectory is held at a constant radius. Synchronism occurs when a particle's angular revolution frequency is in phase with the RF system and remains so after a complete turn. To achieve this, the angular radio frequency ω_{RF} must be a multiple of the angular revolution frequency ω_r:

$$\omega_{RF} = h\omega_r \tag{3.3}$$

where h is the harmonic number. Equation 3.3 means that the number of synchronous particle locations is equal to the harmonic number and are equally spaced around the accelerator ring.

High-energy accelerator facilities consist of an ion source that produces the beam in *bunches*, which are groups of particles oscillating around a (hypothetical) synchronous particle. The bunches are accelerated at RF cavities located around the ring. The synchronous particle by definition is in phase with the RF system and thus experiences no voltage kick at the cavities. However, other particles in the bunch may arrive with slightly higher or lower energy than the energy of the synchronous particle, experiencing a decelerating or accelerating force that returns their energy to

that of the synchronous particle (see Figure 3.2). The shape of the bunch can be circular or elliptic, depending on the size of the restoring force and the voltage of the cavity. The bunch is contained in what is called an *RF bucket* or *separatrix* (Figure 3.3). The separatrix is a region of phase-space which corresponds to stable motion of the bunch.
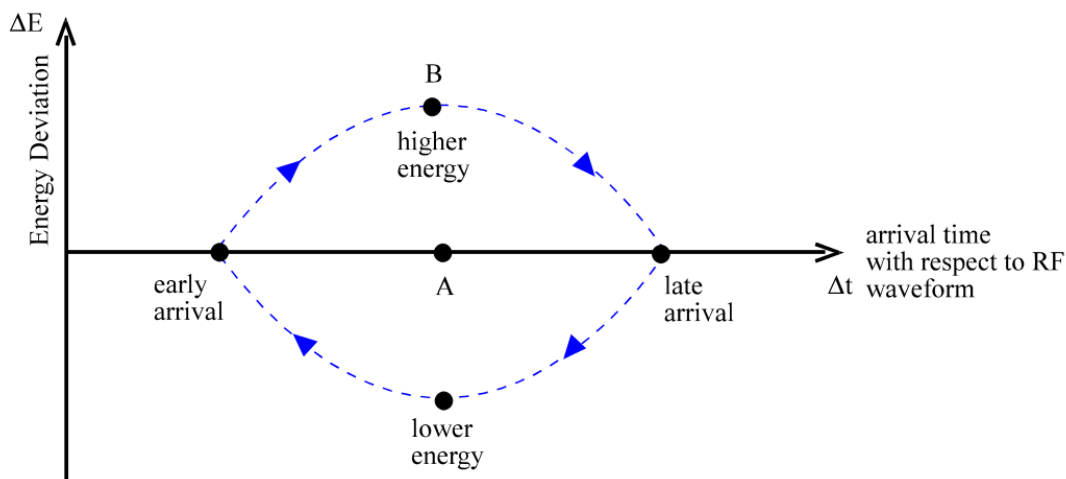
Figure 3.2: Schematic of a bunch. Particles in the bunch will revolve around the synchronous particle in the bunch [17].

The horizontal displacement of particles around the synchronous particle is called betatron oscillation and forms the basis for transverse motion in a bunch. The beam dynamics are influenced by accelerator magnets that are classified by field type. Dipole magnets provide beam orbit control, and quadrupole magnets control the beam size. Sextupole and higher-order multipole magnets control for chromatic and geometric aberrations.

The bending angle θ in a dipole field with bending radius ρ may be derived from the Lorentz force:

$$\theta = \frac{e}{p_0} \int_{s_1}^{s_2} Bdl = \frac{1}{B\rho} \int_{s_1}^{s_2} Bdl \qquad (3.4)$$

where p_0 is the momentum of the beam. The term $B\rho = p_0/e$ represents the magnetic field strength required to bend a particle at a given radius and energy and is called the momentum rigidity of the beam. The total bending angle for a circular accelerator is 2π, and thus the integrated dipole
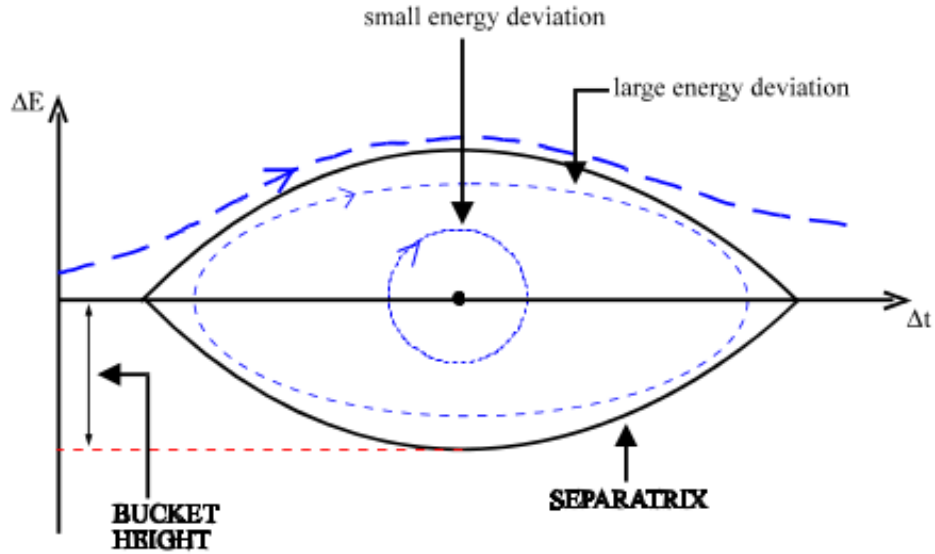
Figure 3.3: Schematic of a bucket or separatrix. Buckets may or may not be filled with bunches [17].

field along the design orbit is:

$$\oint Bdl = 2\pi p_0/e = 2\pi B\rho \tag{3.5}$$

The magnetic field of an ideal quadrupole is given by:

$$\mathrm{B} = \partial_x B_y(y\hat{x} + x\hat{y}) \tag{3.6}$$

Charged particles passing through the center of a quadrupole experience no magnetic field or force. However, at a displacement (x, y) from the center, a gradient field is generated and the Lorentz force for a particle of charge e and velocity v along the azimuthal direction $\hat{\phi}$ is:

$$\vec{F} = ev\partial_x B_y \hat{\phi} \times (y\hat{x} + x\hat{y}) = -ev\partial_x B_y y\hat{y} + ev\partial_x B_y x\hat{x} \tag{3.7}$$

with equations of motion:

$$\frac{1}{v^2}\frac{\mathrm{d}^2 x}{\mathrm{d}t^2} = \frac{e\partial_x B_y}{\gamma m v}x, \qquad \frac{1}{v^2}\frac{\mathrm{d}^2 y}{\mathrm{d}t^2} = -\frac{e\partial_x B_y}{\gamma m v}y \tag{3.8}$$

Therefore, it can be seen from Equation 3.8 that the quadrupole acts as a focusing lens in the horizontal plane and defocusing lense in the vertical plane (or vice versa if the quadropoles are rotated). The focusing and defocusing quadrupoles are commonly setup in focusing-orbit-defocusing-orbit (FODO) patterns separated by non-focusing drift spaces [191]. These patterns are referred to as lattice points on the ring. This arrangement focuses diverging particles back to the central trajectory, as illustrated in Figure 3.4.
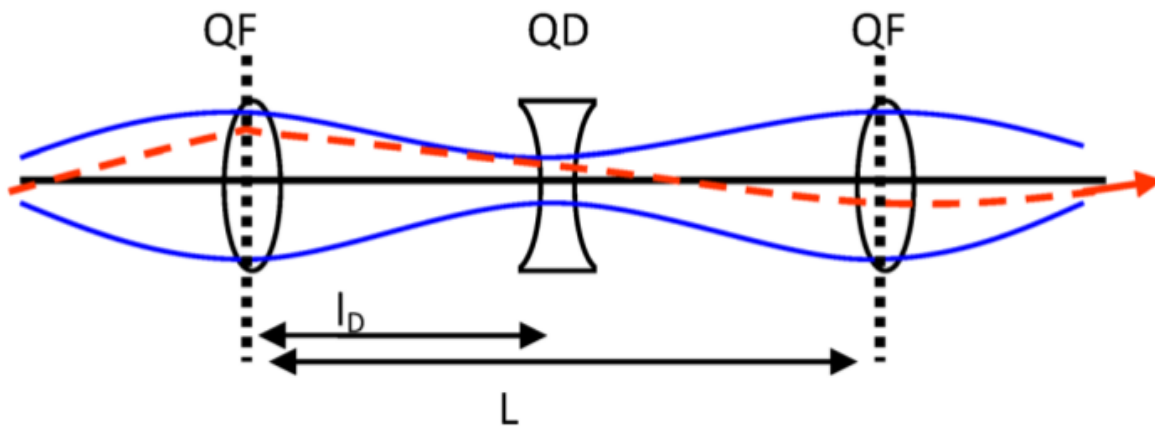
Figure 3.4: Schematic of a FODO cell with quadrupole focusing (QF) and defocusing (QD) magnets [17].

The magnetic fields are normalized to the momentum of the particles. For a dipole field, the bending angle from Equation 3.4 becomes:

$$\theta = \frac{1}{B\rho} \int B ds = \frac{1}{\rho} L_{eff} \tag{3.9}$$

where L_{eff} is called the effective magnetic length and $1/\rho$ is the normalized bending strength of the dipole. Similarly, for the quadrupole, Equation 3.6 is normalized to the momentum rigidity of the beam and is given by:

$$k = \frac{1}{B\rho} \partial_x B_y \tag{3.10}$$

The equation of motion for particle trajectories under the influence of dipole and quadrupole fields may be written as [192]:

$$x'' + Kx = 0 \tag{3.11}$$

where x'' is taken with respect to orbit coordinate s, x is the horizontal coordinate of the particle with respect to the beam orbit (see Figure 3.5), and K is a combination of the focusing strength k from Equation 3.10 and $1/\rho$ from Equation 3.9:

$$K = -k + 1/\rho^2 \tag{3.12}$$

Horizontal (de)focusing occurs when $k < 0$ ($k > 0$). Equation 3.12 in the vertical plane is slightly different. Since generally no vertical bending strength is present in most accelerators, the $1/\rho^2$ term vanishes. Moreover, the sign of the gradient changes ($k \to -k$) due to the geometry of the quadropole field lines. Thus, $K = k$ in the case of vertical displacement [18].
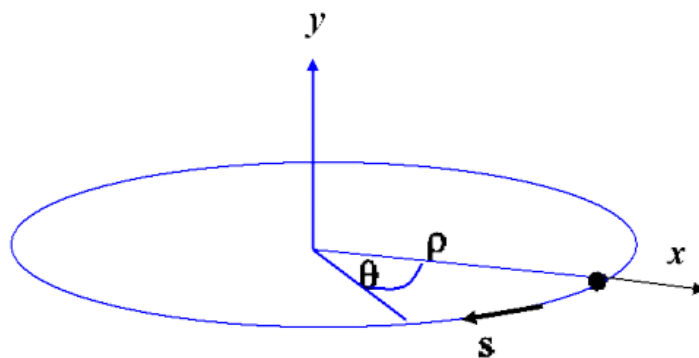
Figure 3.5: Coordinate system for the orbit of an ideal particle in cirular motion [18].

Equation 3.12 can be solved using a linear approximation and the general solution for the position and angle of the trajectory for a focusing lens with initial conditions x_0 and x_0' are:

$$x(s) = x_0 \cos(\sqrt{K}s) + \frac{x_0'}{\sqrt{K}} \sin(\sqrt{K}s) \tag{3.13}$$

$$x'(s) = -x_0\sqrt{K} \sin(Ks) + x_0' \cos(\sqrt{K}s) \tag{3.14}$$

or equivalently,

$$\begin{pmatrix} x \\ x' \end{pmatrix}_s = M \begin{pmatrix} x \\ x' \end{pmatrix}_0$$

where M is called the transfer matrix and depends on the properties of the magnet. Using this relation, the amplitude x_0 and angle x'_0 before the lattice element may be used to determine their values after.

Equations 3.13 and 3.14 can be extended to describe many turns around the ring using the periodicity of the focusing elements. The lattice elements (FODO) result in periodically repeating focusing properties. Therefore, the restoring force K in Equation 3.11 becomes a function of the orbit coordinate s:

$$x''(s) + K(s)x(s) = 0 \tag{3.15}$$

Since $K(s) = K(s+L)$, Equation 3.15 becomes the Hill equation [193] and may be solved using Floquet's theorem, resulting in a solution of the form:

$$x(s) = \sqrt{\epsilon}\sqrt{\beta}\cos(\psi(s) + \phi) \tag{3.16}$$

$$x'(s) = \frac{-\sqrt{\epsilon}}{\sqrt{\beta(s)}}\sin(\psi(s) + \phi) + \alpha(s)\cos(\psi(s) + \phi) \tag{3.17}$$

The β-function depends on the position and angle of the transverse oscillation of the beam and ϵ is the beam emittance, which represents the beam volume in the six dimensional phase space $(x, x', y, y', \phi, \delta)$ that contains 98% of the beam particles; x, y are the transverse positions, x', y' are the transverse angles, ϕ is the relative phase of the beam, and δ is the relative beam energy. $\psi(s)$ describes the phase advance of the oscillation and is found by inserting Equation 3.16 into the Hill equation:

$$\psi(s) = \int_0^s \frac{ds}{\beta(s)} \tag{3.18}$$

A large β implies that the beam has a large transverse dimension and the phase advance is small. Integrating 3.18 around the closed ring results in the number of betatron oscillations per revolution, or tune Q:

$$Q = \frac{1}{2\pi} \oint \frac{\mathrm{d}s}{\beta(s)} \tag{3.19}$$

Equations 3.16 and 3.17 describe a mono-energetic synchronous particle. Since the actual beam contains particles with a distribution of momenta and energies, a dispersion term is included of the functional form $D(s) = x_i(s)/(\Delta p/p)$ where $\Delta p/p$ is relative to the synchronous particle and is typically $\sim 10^{-3}$ [194]. $D(s)$ vanishes at the collision point, however.

The tune dependence on the beam energy is described by what is called the chromaticity $\xi = \Delta Q/(\Delta p/p)$, where ΔQ is the tune shift. ΔQ is induced by the finite energy spread of the beam and can be minimized by keeping the chromaticity close to zero.

The size of the beam is given by the envelope of the overlapping trajectories and is represented by $\hat{x} = \sqrt{\epsilon\beta(s)}$, as shown in Figure 3.6. The transverse particle density typically follows a Gaussian distribution and the beam size is represented by one standard deviation $\sigma = \sqrt{\epsilon\beta}$. The beams must be extremely focused at the point of a collision, and thus the β-function is minimized here. This minimum is called β^*. Figure 3.7 illustrates the beam squeeze at the collision interaction point.
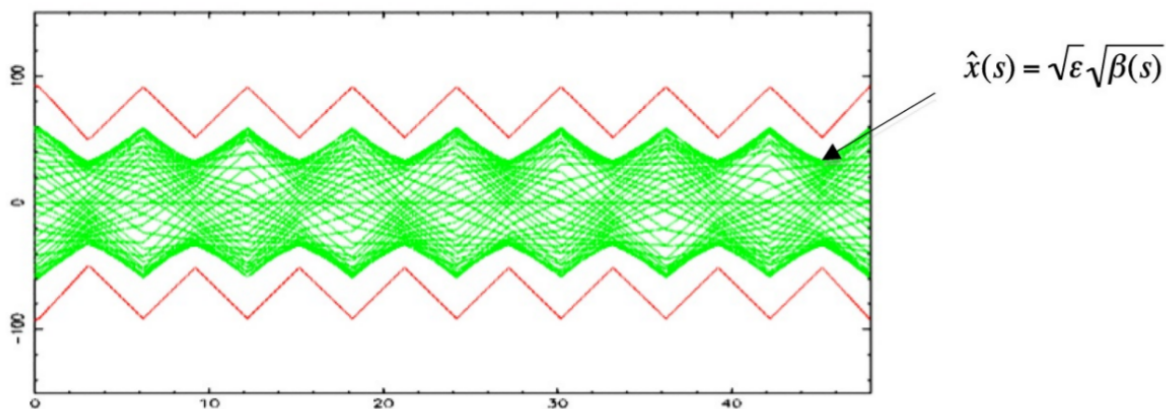
Figure 3.6: Overlapping trajectories of particles, defining the beam cross-section [18].

3.1.2 Luminosity

The production rate of an event increases with the center-of-mass energy. Therefore, the energy available for particle production is of utmost importance in high-energy nuclear and particle physics
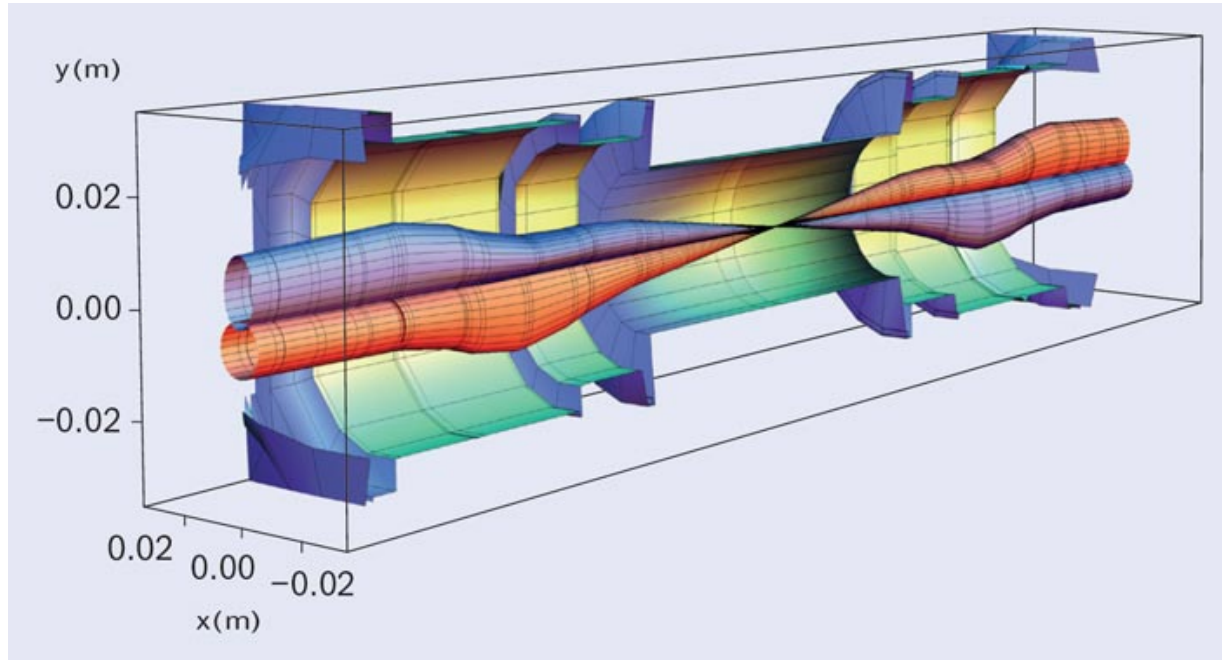
Figure 3.7: Illustration of a beam squeeze at the collision interaction point. The β-function is minimized here.

experiments. This is particularly important for the study of rare processes with a small cross-section (for example, Higgs boson production). The ability of a particle accelerator to produce the required number of interactions to study such processes can be evaluated using the luminosity $\mathcal{L}$. The *instantaneous luminosity* is defined as the particle flux per unit time and is stated in units of $\mathrm{cm}^{-2}\mathrm{s}^{-1}$. For a process with cross-section σ and event rate dN/dt, $\mathcal{L}$ can be expressed as:

$$\frac{\mathrm{d}N}{\mathrm{d}t}\frac{1}{\sigma} = \mathcal{L} \tag{3.20}$$

For a collider operating at a revolution frequency f with N_b bunches crossing at the interaction point, $\mathcal{L}$ can also be written as:

$$\mathcal{L} = \frac{\mu N_b f}{\sigma} \tag{3.21}$$

where μ is the average number of interactions per bunch crossing. The luminosity can be determined by measuring the fraction of bunch crossings in which a specified detector registers an event. Equation 3.21 can then be rewritten as:

$$\mathcal{L} = \frac{\mu N_b f}{\sigma} = \frac{\mu^{vis} N_b f}{\epsilon \sigma} = \frac{\mu^{vis} N_b f}{\sigma_{vis}} \qquad (3.22)$$

where ϵ is the efficiency of the detector to register an event and $\mu^{vis} \equiv \epsilon\mu$ is the average number of interactions per bunch crossing actually registered by the detector. The visible cross-section $\sigma^{vis} \equiv \epsilon\sigma$ relates the measurable quantity μ^{vis} to $\mathcal{L}$. For small μ^{vis}, the average number of visible interactions per bunch crossing is $\approx N/N_{BC}$, where N is the number of events detected and N_{BC} is the number of bunch crossings in the same time interval. For larger μ^{vis}, multiple interactions can occur per bunch crossing (pileup) and μ^{vis} is no longer linear with the number of detected events. In this case, the number of interactions per bunch crossing follows a Poisson distribution, and this is used to determine σ_{vis} (see, for example, Ref. [195]).

In a colliding beam experiment, the luminosity is a convolution of the 3-D beam density distribution functions ρ, as illustrated in Figure 3.8. The overlap integral depends on the longitudinal
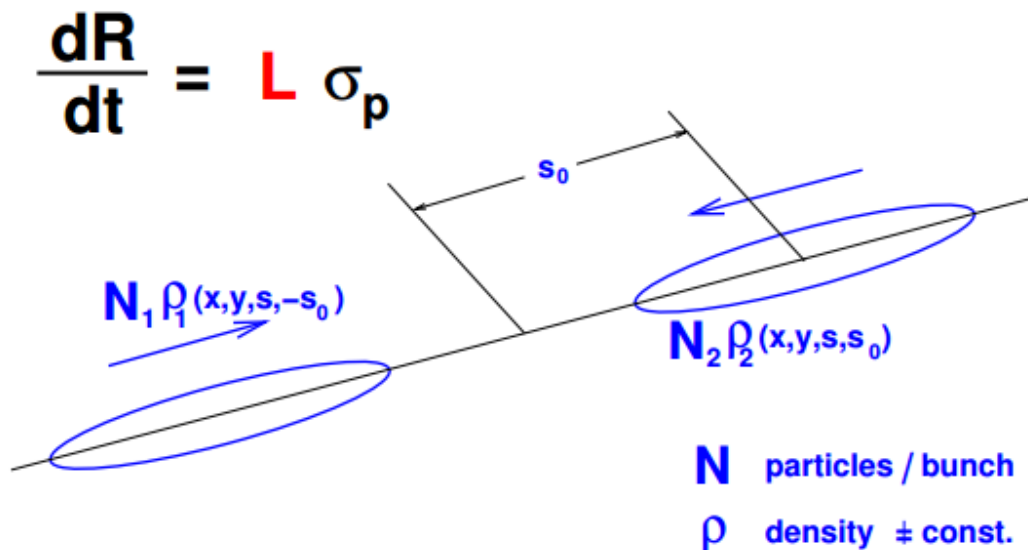
Figure 3.8: Schematic of a colliding beam interaction [19].

position of the bunch and the distance of each bunch to the interaction point s_0. The overlap integral is proportional to the luminosity and can be written as:

$$\mathcal{L} \propto \int \int \int \int_{-\infty}^{+\infty} \rho_1(x, y, s, -s_0)\rho_2(x, y, s, s_0)dxdydsds_0 \tag{3.23}$$

where $\rho_1(x, y, s, -s_0)$ and $\rho_2(x, y, s, -s_0)$ are the time-dependent beam density distribution functions. For beams moving towards one another, the kinematic pre-factor K is [196]:

$$K = \sqrt{(\vec{v}_1 - \vec{v}_2)^2 - (\vec{v}_1 \times \vec{v}_2)/c^2} \tag{3.24}$$

For head-on collisions, it is assumed that $\vec{v}_1 = -\vec{v}_2$ and that all densities are uncorrelated in all planes. The luminosity then becomes:

$$\mathcal{L} = 2N_1N_2fN_b \int \int \int \int_{-\infty}^{+\infty} \rho_1(x)\rho_1(y)\rho_{1s}(s - s_0)\rho_2(x)\rho_2(y)\rho_{2s}(s + s_0)dxdydsds_0 \tag{3.25}$$

where N_1 and N_2 are the number of particles per bunch, f is the revolution frequency, and N_b is the number of colliding bunches. Assuming Gaussian beam profiles in all directions:

$$\rho_{iz}(z) = \frac{1}{\sigma_z\sqrt{2\pi}}\exp\left(-\frac{z^2}{2\sigma_z^2}\right), \quad i = 1, 2; z = x, y \tag{3.26}$$

$$\rho_s(s \pm s_0) = \frac{1}{\sigma_s\sqrt{2\pi}}\exp\left(-\frac{(s \pm s_0)^2}{2\sigma_s^2}\right) \tag{3.27}$$

For equal beams ($\sigma_{1x} = \sigma_{2x}, \sigma_{1y} = \sigma_{2y}, \sigma_{1s} = \sigma_{2s}$), as the bunches approach the speed of light $K \to 2$. The integral in Equation 3.25 becomes:

$$\mathcal{L} = \frac{2N_1N_2fN_b}{(\sqrt{2\pi})^6\sigma_s^2\sigma_x^2\sigma_y^2} \int \int \int \int e^{-\frac{x^2}{\sigma_x^2}}e^{-\frac{y^2}{\sigma_y^2}}e^{-\frac{s^2}{\sigma_s^2}}e^{-\frac{s_0^2}{\sigma_{s_0}^2}}dxdydsds_0 \tag{3.28}$$

Integrating Equation 3.28 results in the luminosity for a head-on collision with Gaussian beam profiles:

$$\mathcal{L} = \frac{N_1N_2fN_b}{4\pi\sigma_x\sigma_y} \tag{3.29}$$

This relationship implies that the luminosity depends on the size of the beam and the number of particles per bunch.

Equation 3.29 assumes an ideal head-on collision with Gaussian beam profiles. In practice, however, there are additional effects that need to be taken into consideration. For instance, the crossing-angle of the beams can affect the luminosity. The transverse beam sizes may depend

on its longitudinal position (hourglass effect) and thus the densities may become correlated in different dimensions. Dispersion at the interaction point may increase the beam size and decrease the luminosity. The β function may not be minimized at the interaction point, modifying the beam size. Each of these effects are important but will not be discussed in detail here. A good discussion may be found in Ref. [19] and references therein.

An accurate calculation of σ_{vis} requires a proper luminosity calibration. The horizontal σ_x and vertical σ_y beam profiles in Equation 3.29 can be determined by recording the interaction rate as a function of the transverse beam separation. This method is called a Van Der Meer scan [197]. In this method, the overlap integrals from Equation 3.25 can be calculated from the luminosity at a beam separation distance δ and from the luminosity at zero beam separation. In the case of a horizontal beam displacement, the overlap integral becomes:

$$\int \rho_1(x)\rho_2(x)dx = \frac{L_x(0)}{\int L_x(\delta)d\delta} \tag{3.30}$$

from which the width of the beam profile σ_x may be extracted:

$$\sigma_x = \frac{1}{\sqrt{2\pi}}\frac{\int L_x(\delta)d\delta}{L_x(0)} \tag{3.31}$$

In practice, the $\sigma_{x(y)}$ are determined from fitting the luminosity distribution as a function of the beam separation. An example of this is shown in Figure 3.9. As discussed previously, the exact form of the beam profiles may deviate from a Gaussian, and thus the distribution may be fit with various functional forms (e.g. double Gaussian) to achieve accurate parameter estimation. Once the beam profiles are determined, $\mathcal{L}$ can be calculated from Equation 3.29, and thus σ_{vis} can also be calculated from Equation 3.22 with the measured μ^{vis}.

The *integrated luminosity* is typically the quantity reported in high-energy experiments. It has units of inverse cross-section (e.g. μb^{-1} or nb^{-1}) and is defined as:

$$\mathcal{L}_{int} = \int_0^T \mathcal{L}(t)dt \tag{3.32}$$

and is directly related to the number of observed events N_{ev} by:

$$\mathcal{L}_{int}\sigma = N_{\text{ev}} \tag{3.33}$$
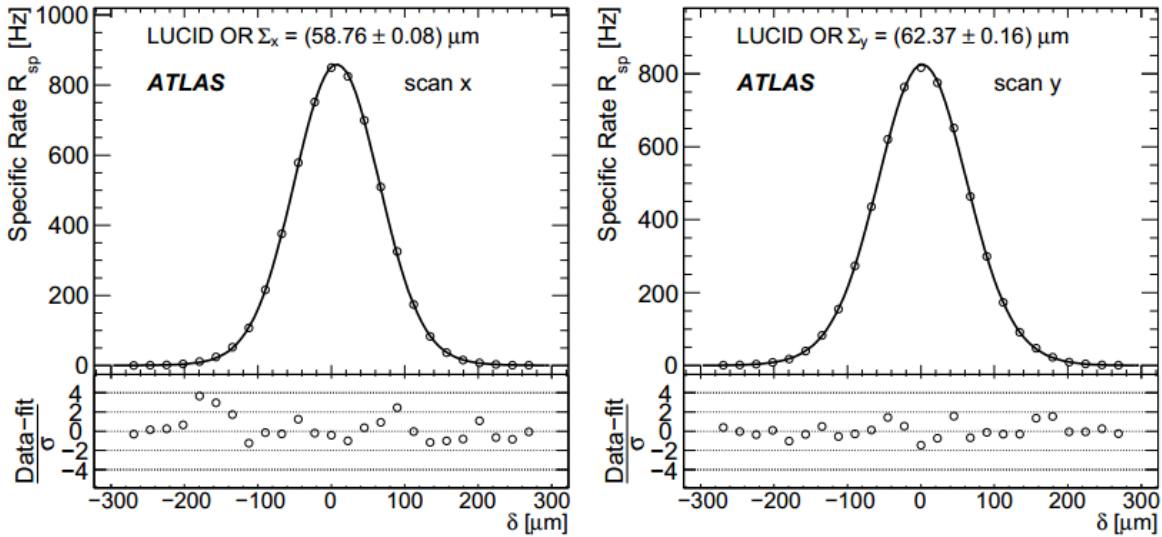
Figure 3.9: Fits to the Van Der Meer luminosity scan in the x and y direction. Distributions are fitted to a double Gaussian [20].

The luminosity exponentially decays with time:

$$\mathcal{L}(t) \rightarrow \mathcal{L}_0 \exp\left(-\frac{t}{\tau}\right) \tag{3.34}$$

where τ is the lifetime and may depend on the decay of the beam intensity, transverse emittance, and bunch length. The performance of a collider depends on maximizing the average luminosity $\langle \mathcal{L} \rangle$.

3.2 The Large Hadron Collider

The Large Hadron Collider (LHC) [21] is a two-ring superconducting synchrotron designed to reveal physics within and beyond the Standard Model. Currently, this machine is the largest and most powerful accelerator ever built, measuring 26.7 km in circumference and capable of accelerating protons and heavy ions to center-of-mass energies of 14 TeV and 5.5 TeV per nucleon pair, respectively. The LHC rings consist of eight arc regions and eight straight sections with beams circulating in opposite directions (Figure 3.10). The beams in each ring are guided in the horizontal plane using 1,232 dipole magnets and are focused in the vertical plane using 392
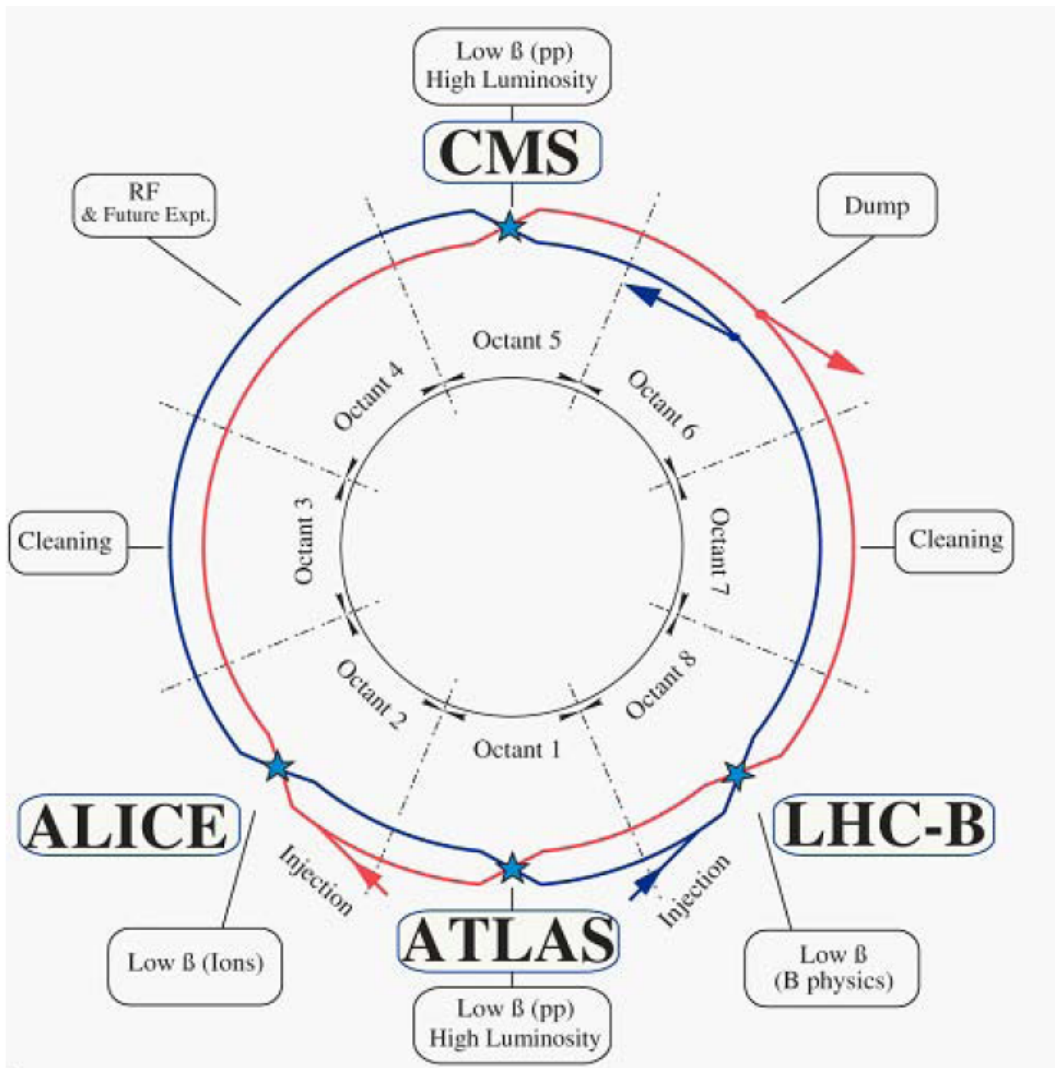
Figure 3.10: Schematic of the LHC rings and interaction regions [21].

quadrupole magnets. The superconducting magnets use NbTi Rutherford cabling technology and are maintained at a temperature below 2 K using superfluid helium cryostats to maximize the field strength. A cross-section of the dipole magnetic system is shown in Figure 3.11.

ALIGNMENT TARGET

MAIN QUADRIPOLE BUS-BARS

HEAT EXCHANGER PIPE

SUPERINSULATION

SUPERCONDUCTING COILS

BEAM PIPE

VACUUM VESSEL

BEAM SCREEN

AUXILIARY BUS-BARS

SHRINKING CYLINDER / HE I-VESSEL

THERMAL SHIELD (55 to 75K)

NON-MAGNETIC COLLARS

IRON YOKE (COLD MASS, 1.9K)

DIPOLE BUS-BARS

SUPPORT POST
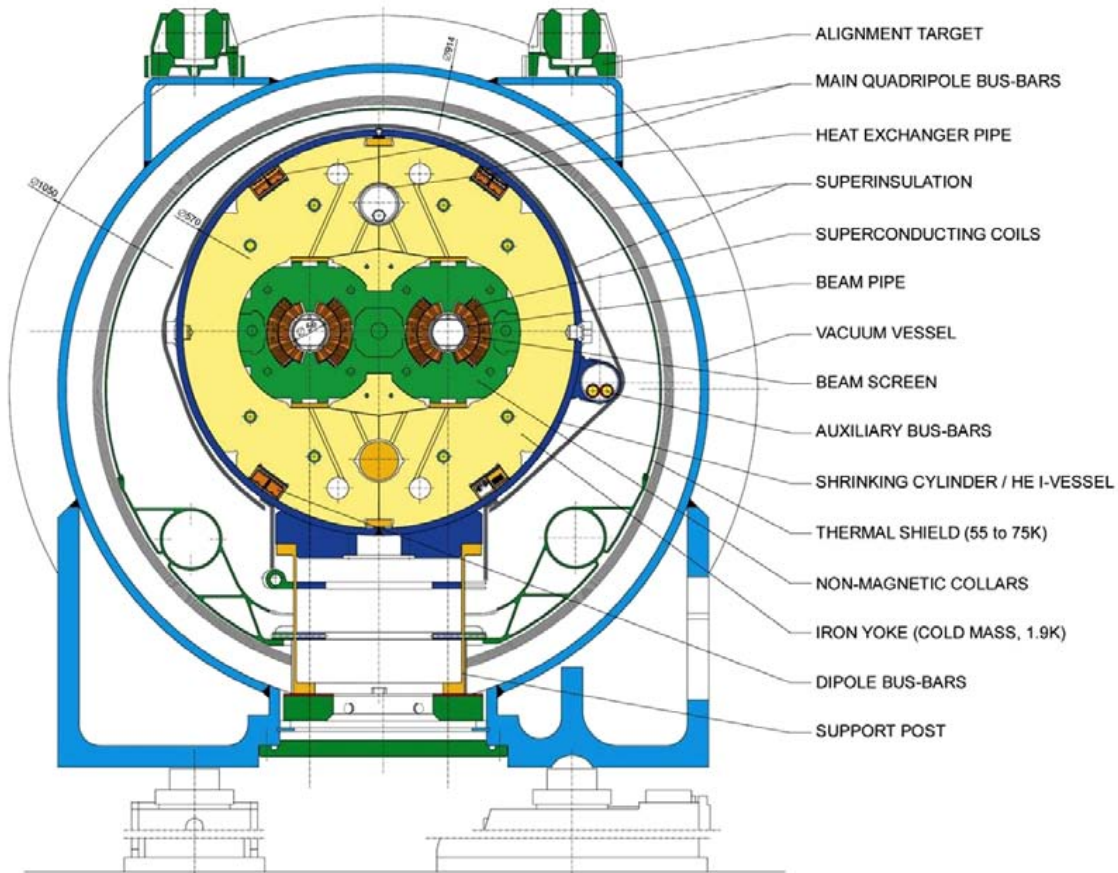
Figure 3.11: Cross-section of the dipole magnetic system in the LHC ring [21].

The beams collide at four interaction regions (IRs) between the straight segments of the ring where seven experimental detectors are located. The ATLAS (A Toroidal LHC ApparatuS) [22] and CMS (Compact Muon Solenoid) [198] detectors are general-purpose detectors located at IR1 and IR5, respectively. They are intended to allow for high precision measurements of QCD, electroweak interactions, and flavor physics at high luminosity in both pp and Pb+Pb collisions. ALICE (A Large Ion Collider Experiment) [199] is located at IR2 and is designed to explore strongly interacting matter produced in Pb+Pb collisions. LHCb (Large Hadron Collider Beauty) [200] is located at IR8 and is dedicated to measurements of CP violation and rare B hadronic decays. There are also

smaller detectors at the LHC that share IRs with the larger experiments. LHCf (Large Hadron Collider Forward) [201] is located at IR1 and is specialized for cosmic ray astrophysics. MoEDAL (Monopole and Exotics Detector at the LHC) [202] shares IR8 and is primarily designed to search for the magnetic monopole and other highly ionizing stable massive particles. TOTEM (TOTal Elastic and diffractive cross section Measurement) [203] shares IR5 and its primary purpose is to measure total cross sections, elastic scattering, and diffractive processes.

3.2.1 LHC Injection Chain

Heavy ions are supplied to the LHC by an injection chain [204] consisting of a Linac, Low-Energy Ion Ring (LEIR), Proton Synchrotron Booster (PSB), Proton Synchrotron (PS), and Super Proton Synchrotron (SPS), as shown in Figure 3.12. In the Linac 3, Pb^{27+} ions are stripped into Pb^{+54} ions using a thin carbon foil and are accelerated to 4.2 MeV/nucleon. The ions are further accelerated in the LEIR to 72 MeV/nucleon. At the PS, the ions reach an energy of 6 GeV/nucleon and are fully stripped into the Pb^{+82} state using an aluminum foil before entering the SPS. In the SPS, the ions are accelerated to 177 GeV/nucleon before entering the LHC. Beams are injected into Ring-1 at IR2 and into Ring-2 at IR8. The beam abort systems are located at IR6, where the beams are kicked into an iron septum magnet that steers them into graphite absorbers in a separate tunnel.

A Radio Frequency (RF) system consisting of 8 cavities per ring is used to accelerate the beams. In order for the beam particles to experience an accelerating voltage at each cavity, (as mentioned in Sec. 3.1.1) the RF frequency must be an integer multiple (the harmonic number) of the beam revolution frequency. The LHC operates using a 400 MHz cavity system, corresponding to a harmonic number of 35640. The 400 MHz RF system corresponds to a bucket size of 2.5 ns. However, due to boundary conditions imposed by the beam requirements, the design configuration for the bunch spacing is limited to 25 ns (40 MHz). For a beam traveling at $\approx c$, this corresponds to 3564 buckets. Empty buckets are used to allow the magnetic system time to inject beams into the next part of the injection sequence, ultimately resulting in 39 injections of 72 bunches (called bunch trains) from the PS. This is shown schematically in Fig 3.13. During the runs, bunches are designated by a bunch-crossing identifier (BCID).
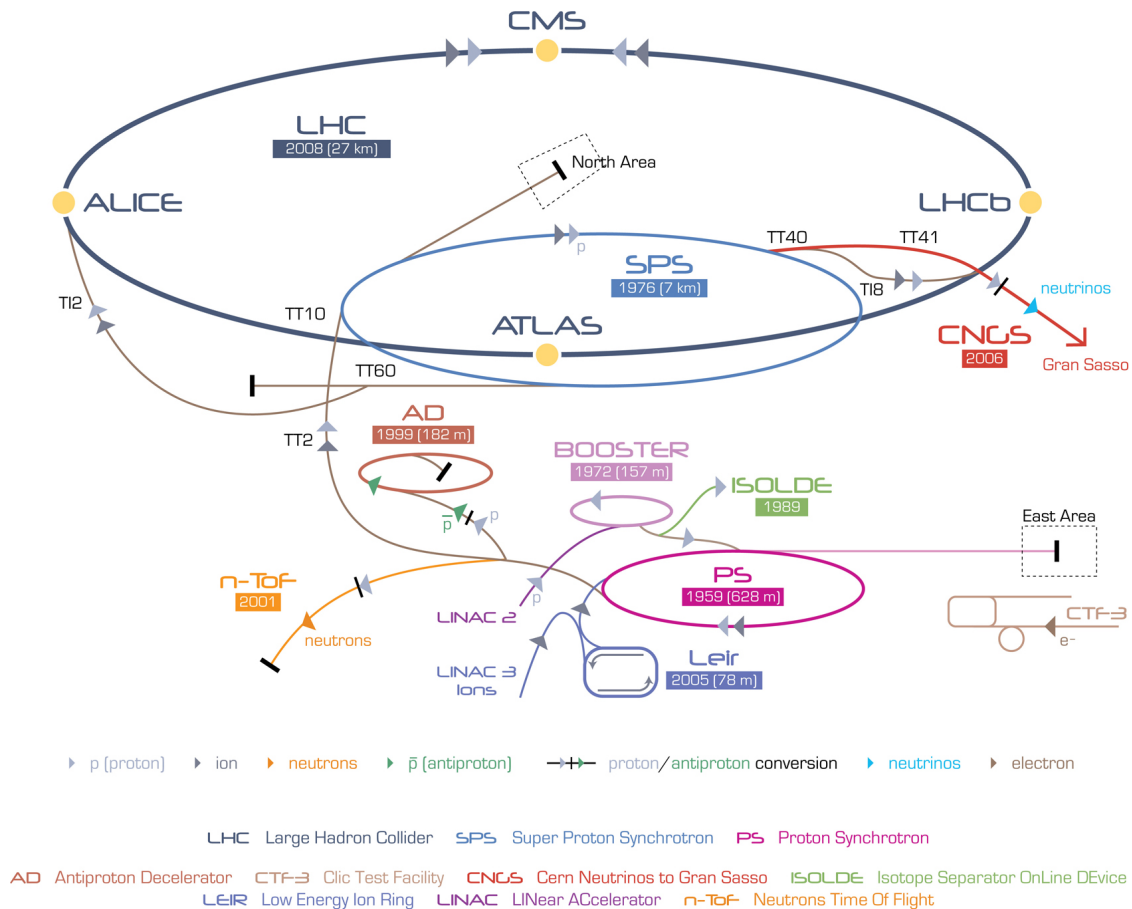
Figure 3.12: Schematic of the LHC injection chain. Heavy ions are stripped of their electrons in the Linac3 and between the PS and SPS lines.

3.3   The ATLAS Detector

The ATLAS detector was used to collect the data in this work. The detector requirements [205] were defined to enable the observation of new physics signatures at the TeV scale such as the Standard Model Higgs boson, new heavy-gauge bosons, supersymmetric particles, and graviton emission. To achieve these goals, the detector is capable of withstanding high radiation doses while efficiently reconstructing charged particles, electrons, photons, jets, and muons. The detector is also able to measure missing energy and to identify seconday vertices for τ-lepton tagging.

ATLAS is forward–backward symmetric with respect to the interaction point and is comprised of three main regions: an inner detector (ID), calorimeter, and muon spectrometer (MS). The ID

Bunch Disposition in the LHC, SPS and PS

LHC (1-Ring) = 88.924 μs

3-batch   4-batch

τ_3

SPS = 7/27 LHC

τ_4

Filling Scheme

3564 = {[(72b + 8e) x 3 + 30e] x 2+[(72b + 8e) x 4 + 31e]} x 3
+{[(72b + 8e) x 3 + 30e] x 3+ 81e}

τ_2

PS = 1/11 SPS

72 bunches
25ns spacing

τ_1

τ_5

Beam Gaps

$\tau_1 = 12$ missing bunches (72 bunches on h=84)

$\tau_2 = 8$ missing bunches (SPS Injection Kicker rise time = 220 ns.)

$\tau_3 = 38$ missing bunches (LHC Injection Kicker rise time = 0.94 μs.)

$\tau_4 = 39$ missing bunches ("   )

$\tau_5 = 119$ missing bunches (LHC Dump Kicker rise time = 3 μs.)

Figure 3.13: Schematic of the bunch filling scheme in the PS, SPS, and LHC ring. One LHC ring is filled in ∼3 minutes. The filling scheme is described using filled (b) and empty (e) buckets [21].

is surrounded by a thin superconducting solenoid and the calorimeters are encompassed by three superconducting toroids arranged in an eight–fold azimuthal symmetry. A layout of the detector is shown in Figure 3.14.

3.3.1   Kinematic Variables

ATLAS uses a right-handed coordinate system with the nominal interaction point defined as the origin. The beam axis is defined as the z-axis, and the $x - y$ plane is transverse to the beam. The x-axis is in the direction of the LHC ring center and the y-axis points directly upward. The azimuthal angle ϕ is measured around the beam axis in the $x - y$ plane, and the polar angle θ is measured in the $y - z$ plane from the beam axis.

The kinematics of a particle are typically described by its transverse $(x - y)$ and longitudinal (z) components. This segmentation is useful in collider physics since an unknown amount of energy of the incoming hadrons escapes down the beam–pipe, and thus the net momentum of a particle
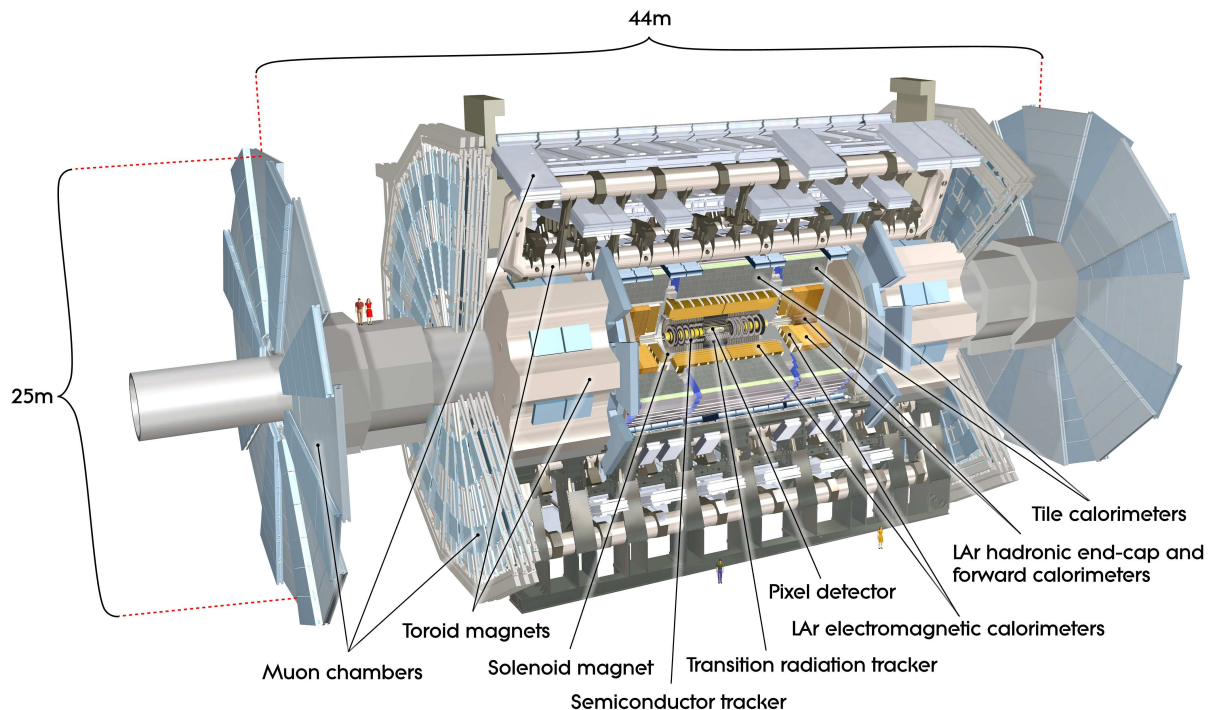
Figure 3.14: Transverse view of the ATLAS detector [22].

can only be constrained in the transverse plane. Variables used to describe the kinematics of a particle in the transverse plane include the transverse momentum p_{T}, transverse energy E_{T}, and missing transverse momentum $p_{\mathrm{T}}^{\mathrm{miss}}$ or energy $E_{\mathrm{T}}^{\mathrm{miss}}$. The missing transverse variables are used to identify particles that cannot be detected (e.g. neutrinos) and are calculated from the sum of the transerve momentum vectors from all visible final states:

$$\vec{E}_T^{\mathrm{miss}} = -\sum_i \vec{p}_T(i), \tag{3.35}$$

The mass of heavy particles whose decay products include invisible final state particles can be constrained using the transverse mass m_{T}. If the daughter particles have mass $m_1 \approx m_2 \approx 0$, m_{T} can be written as [206]:

$$m_{\mathrm{T}} = \sqrt{2p_{\mathrm{T}}^i p_{\mathrm{T}}^j (1 - \cos \Delta\phi_{i,j})}, \tag{3.36}$$

where $\Delta\phi_{i,j}$ is the difference between the direction of the visible and invisible particles in the

azimuthal plane. The m_T values possess an end-point at the true mass of the mother particle (i.e. $m_T \leq m$).

The amount of energy a particle has in the longitudinal direction is quantified using the rapidity:

$$y = \frac{1}{2}\ln\left(\frac{p_0 + p_z}{p_0 - p_z}\right) \tag{3.37}$$

where p_0 is the energy of the particle and p_z is the longitudinal momentum. However, in practice, it is more feasible to measure the angle of the particle relative to the beam axis θ and characterize the detected particle using the pseudorapidity defined by:

$$\eta = -\ln\tan\left(\frac{\theta}{2}\right) = \frac{1}{2}\ln\left(\frac{\sqrt{(m^2 + p_T^2)\cosh^2 y - m^2} + \sqrt{m^2 + p_T^2}\sinh y}{\sqrt{(m^2 + p_T^2)\cosh^2 y - m^2} - \sqrt{m^2 + p_T^2}\sinh y}\right), \tag{3.38}$$

When the momentum of a particle is much larger than its mass, the momentum is approximately equal to the energy and thus $\eta \approx y$ [134].

3.4 Inner Detector

The ATLAS inner detector (ID) is the component closest to the beam axis and is contained within a cylindrical envelope of length $z \pm 3512$ mm and radius 1150 mm. A layout of the ID is shown in Figure 3.15. The ID is immersed in a 2 T axial magnetic field generated by the central solenoid (Figure 3.16), which extends a length of 5.3 m and a diameter of 2.5 m. The ID provides hermetic pattern recognition and excellent momentum resolution for charged tracks above 0.5 GeV within a pseudorapidy range $|\eta| < 2.5$. The detector component is designed to provide a p_T resolution of $\frac{\sigma_{p_T}}{p_T} = 0.05\%\ p_T \oplus 1\%$. There are three complementary sub-detectors: the silicon pixel layer, semiconductor tracker (SCT), and transition radiation tracker (TRT). An illustration of charged tracks traversing the ID layers at small and large η is shown in Figure 3.17. At inner radii, the pixel layer and SCT provide high-resolution pattern recognition capabilities using discrete space-points. At larger radii, the TRT is comprised of many layers of gaseous straw tube elements interleaved with transition radiation material. The properties of each of these subregions will be discussed below.
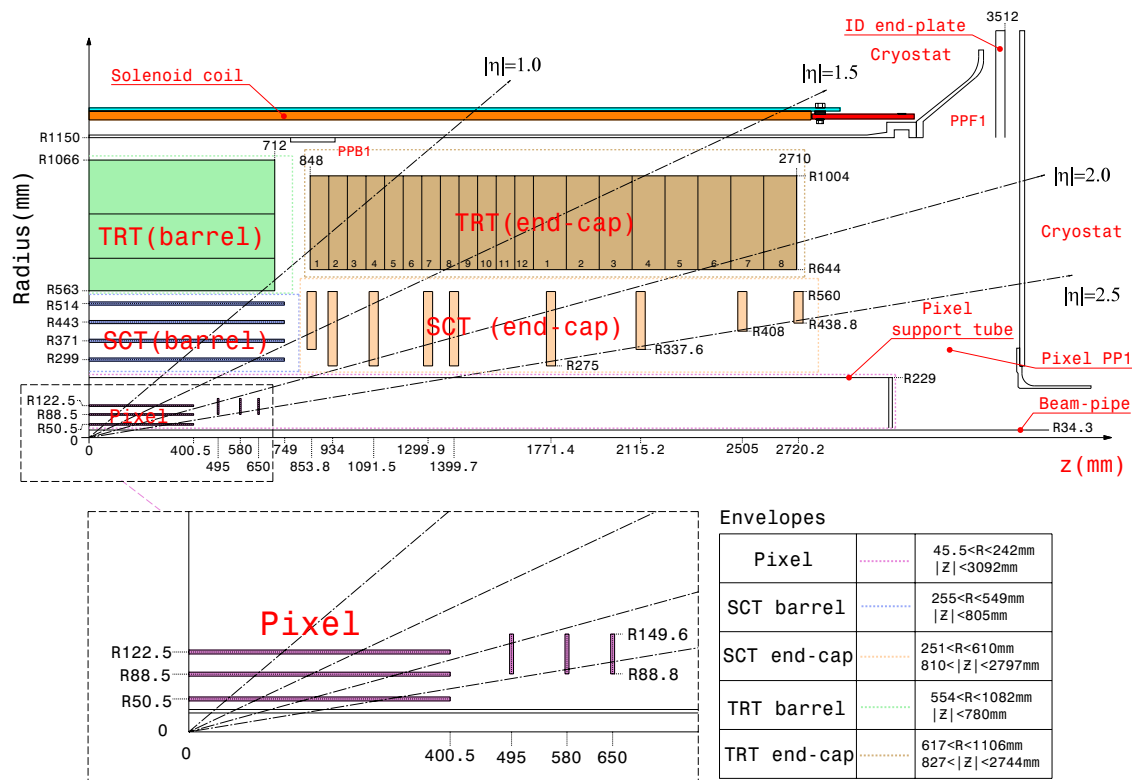
Figure 3.15: Dimensions and major elements of the ATLAS inner detector [22].

3.4.1 Silicon Pixel Layer

The pixel layer [207] is the innermost ID layer. It consists of 1744 sensors and modules, which are arranged in three concentric barrel layers and in three disk layers at each endcap (Figure 3.15). The barrel layers are $z \pm 400.5$ mm in length and are situated at radial distances $R = 50.5, 88.5$, and 122.5 mm. The end-cap disks are located at $z \pm 495, \pm 580$, and ± 650 mm and extend a radial distance $88.8 < R < 149.6$ mm. The layers typically provide three measurement points for particles originating from the interaction point.

The pixels operate as semiconductor detectors with double-sided sensors: n$^+$-implants placed in n-bulk material in the outer region and the p-n junction and multi-guard rings on the back side. This setup allows the 250 μm thick sensors to operate when the voltage has been depleted. The sensors are kept at -5°C to -10°C in order to decrease the leakage current induced by large radiation doses. Each sensor contains 47232 pixels with most pixel sizes 50×400 μm^2, resulting in a total of
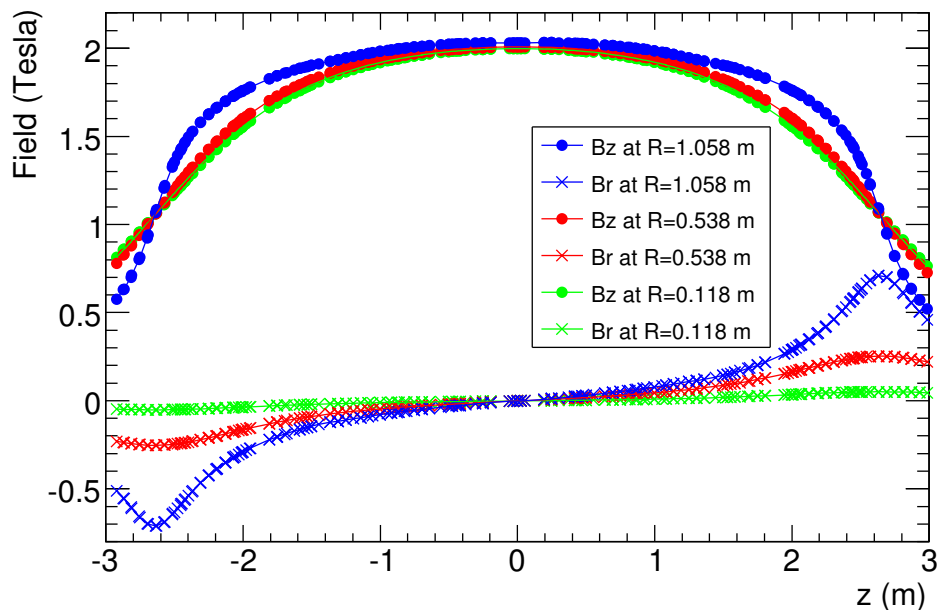
Figure 3.16: R- and z-dependence of the radial (Br) and axial (Bz) magnetic field components in the inner detector cavity at fixed ϕ [22].

~80.4 million readout channels in the pixel detector. If a signal exceeds a tunable threshold, the hits in a pixel are read out. The intrinsic accuracies are 10 μm $(R - \phi)$ and 115 μm (z) in the barrel and are 10 μm $(R - \phi)$ and 115 μm (R) in the end-cap disks.

3.4.2 Silicon Microstrip Detector (SCT)

The silicon microstrip (SCT) layer [208] surrounds the pixel layer. It consists of 4088 modules of silicon-strip detectors arranged in four coaxial cylindrical layers in the barrel region and in nine disk layers in each end-cap. The barrel layers are located at $R = 299, 371, 443$, and 514 mm and extend $z \pm 749$ mm. The end-cap disks are located at $839 < |z| < 2735$ mm and have a radial extension of $275 < R < 560$ mm.

As with the pixel layer, the SCT is a semiconductor detector. However, the sensors are single-sided and use p-in-n technology with AC-coupled readout strips. The sensors are 280 μm thick and each contain 768 active microstrips. Tracks typically cross eight strip layers (four space-points), and
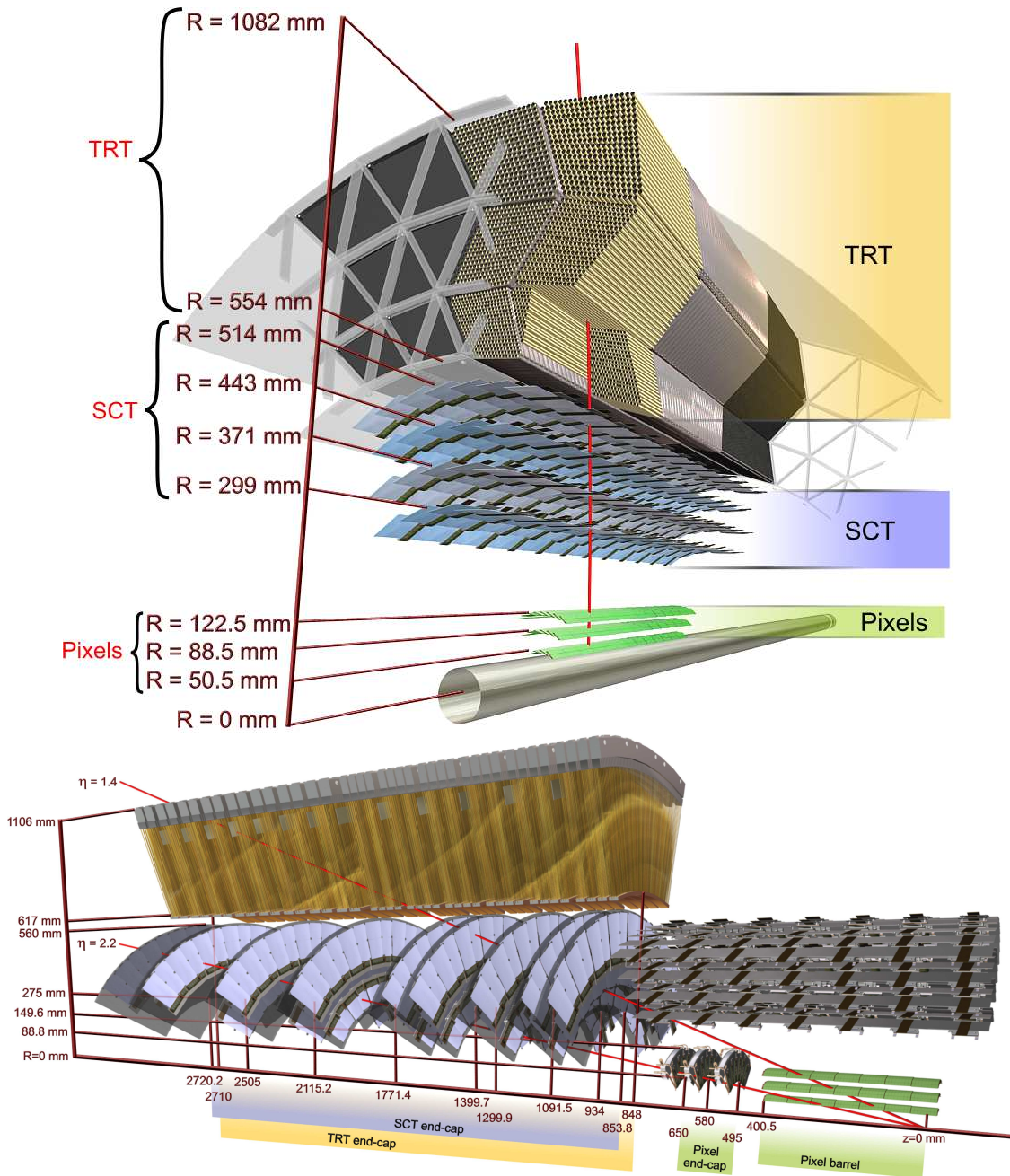
Figure 3.17: (Top) A charged track with $\eta = 0.3$ traversing the ID layers. (Bottom) Two charged tracks with $\eta = 1.4$ and 2.2 traversing the ID layers. The TRT extends only to $|\eta| = 2$ [22].

a hit is registered if the pulse height exceeds a preset threshold.. In the barrel, modules contain two daisy-chained rectangular sensors per side. The four sensors are rotated by ± 20 mrad to measure $R - \phi$ and z coordinates. In the end-cap regions, the modules are radially oriented and each contain two sets of trapezoidal sensors glued back-to-back and rotated by ± 20 mrad to give space-point information. The intrisic accuracies are 17 μm $(R - \phi)$ and 580 μm (z) in the barrel and are 17 μm $(R - \phi)$ and 580 μm (R) in the end-cap disks.

3.4.3 Transition Radiation Tracker (TRT)

The transition radiation tracker (TRT) covers radial distances $554 < R < 1004$ mm and $|z| < 2710$ mm. The detector has 298304 polyimide drift tubes (straws), each 4 mm in diameter, filled with a gas mixture of 70% Xe, 27% CO_2, and 3% O_2 that allows good X-ray absorption, increased electron drift velocity, and photon-quenching. In the barrel, straws are cylindrically arranged around the beam axis and are 144 cm long. In the end-caps, the straws are arranged radially and are 37 cm long.

Straws act as cathodes and are kept at high voltage of negative polarity. In the center of the straws are gold-plated tungsten wires that act as anodes. The TRT contains 73 layers of straws interleaved with polypropylene fibers in the barrel and 160 straw planes interleaved with foils in the end-cap region. The fibers and foils provide transition radiation that is used for electron identification. This is possible because the energy of transition photons is proportional to the Lorentz factor of the charged particle [209]. Thus, electrons will radiate transition photons with energies much higher than those emitted by particles with smaller Lorentz factors (e.g. pions). The particle separation is achieved with a high-threshold discriminator in the front-end electronics. All charged tracks with $p_\mathrm{T} > 0.5$ GeV and $|\eta| < 2.0$ will traverse > 30 straws except in the barrel-to-end-cap transition region $0.8 < |\eta| < 1.0$, where the tracks traverse as low as 22 straws. The TRT only provides $R - \phi$ information and has an intrinsic accuracy of 130 μm per straw.

3.5 Calorimeters

The ATLAS calorimeter system is shown in Figure 3.18. It covers a range of $|\eta| < 4.6$ and utilizes various techniques that are suited for different physics processes and radiation levels. The

calorimeters provide good containment of electromagnetic and hadronic showers, limiting punch-through into the muon system.
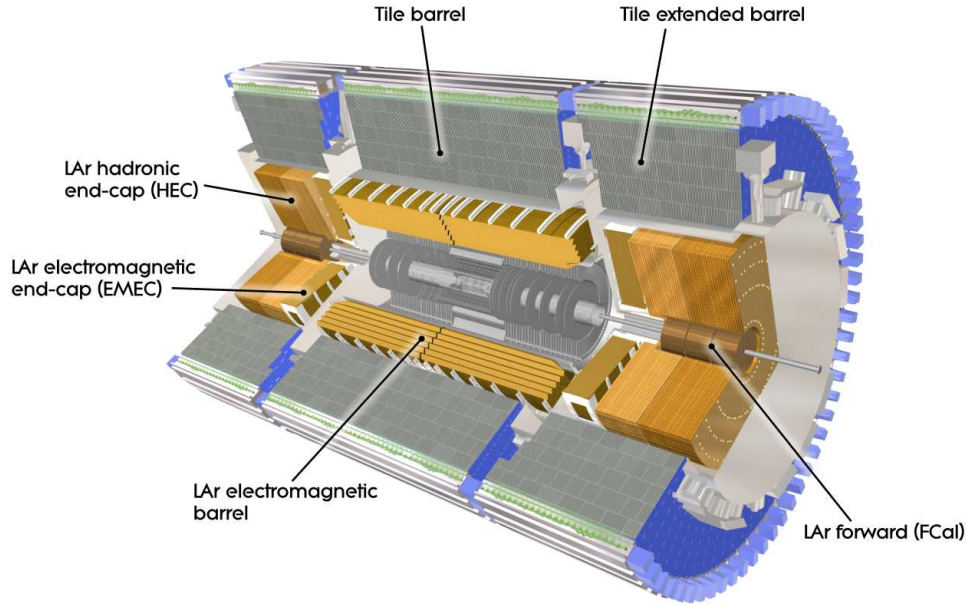
Figure 3.18: Cut-away view of the ATLAS calorimeter system [22].

3.5.1 Electromagnetic Calorimeters

The electromagnetic (EM) calorimeter has a total thickness of > 22 radiation lengths X_0 in the barrel and > 24 X_0 in the end-cap regions. The EM is divided into a barrel ($|\eta| < 1.475$) and two end-cap ($1.375 < |\eta| < 3.2$) components housed in separate cryostats. The electromagnetic calorimeters are lead-liquid argon detectors with accordion-shaped kapton electrodes and lead absorber plates. This geometry allows for complete azimuthal ϕ coverage and several active layers in depth: three in the precision-measurement region $0 < |\eta| < 2.5$, two in the forward region at $2.5 < |\eta| < 3.2$, and two in the barrel/end-cap overlap region. Presamplers – an instrumented argon layer – at $0 < |\eta| < 1.8$ are used to correct for energy lost by electrons and photons upstream of the calorimeter.

3.5.2 Hadronic Calorimeters

The hadronic calorimeters consist of the tile calorimeter, liquid-argon (LAr) hadronic end-cap calorimeter (HEC), and liquid-argon forward calorimeter (discussed below). The tile calorimeter is a sampling calorimeter that uses steel as the absorber and scintillator as the active medium. It is located at $|\eta| < 1.7$ and is behind the LAr EM calorimeter. The detector thickness is approximately 7.4 interaction lengths λ.

The HEC consists of copper plates interleaved with LAr as the active medium. It covers $1.5 < |\eta| < 3.2$. The HEC is located behind the electromagnetic end-cap calorimeter and shares two LAr end-cap cryostats with the electromagnetic end-cap and forward calorimeters.

3.5.3 Forward Calorimeters

The Forward Calorimeters (FCal) can be used to calculate the total transverse energy of an event and are used to determine the centrality of a heavy-ion collision. They are located in end-cap cryostats at $\sim z \pm 4.7$ m from the interaction point and provide coverage over the region $3.1 < |\eta| < 4.9$. Each FCal consists of three modules with a total depth of ~ 10 interaction lengths: an electromagnetic module (FCal1) and two hadronic modules (FCal2 and FCal3). This is illustrated in Figure 3.19. FCal1 uses copper as the absorber to optimize resolution and heat removal. FCal2 and FCal3 use tungsten to minimize the spread of hadronic showers. In addition, a copper alloy shielding plug is located behind FCal3 to reduce background in the muon end-caps.
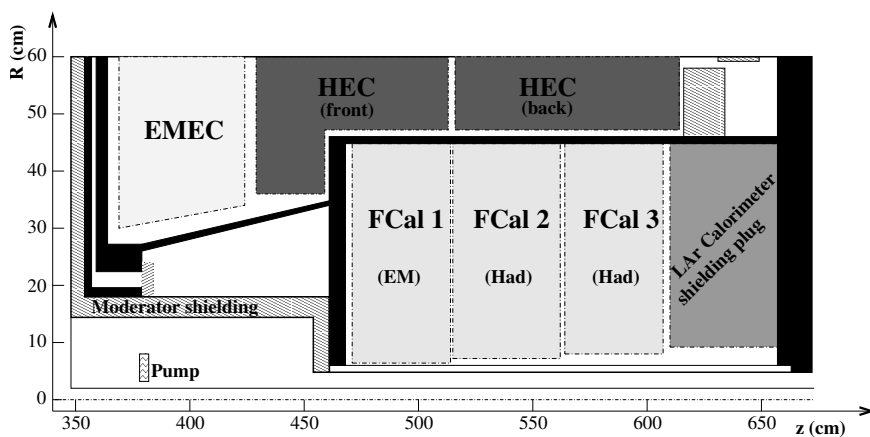
Figure 3.19: Schematic of the three FCal modules in the end-cap cryostat [22].

The FCal uses liquid-argon as the ionization medium. Electrodes are formed by inserting absorber rods (anode) into copper tubes (cathode), which are parallel to the beam axis. The LAr is located in gaps within the tubes. The sizes of these gaps are smaller than those in traditional LAr calorimeters to accomodate the high particle fluxes at large η. The anode and cathode are separated by a radiation-hard plastic fiber that maintains the narrow LAr gap.

FCal1 is closest to the interaction point and is made up of copper plates perpendicular to the beam axis with holes where the electrodes are inserted. Each electrode consists of a co-axial copper rod and tube. This structure is shown in Figure 3.20. In this figure, the Molière radius is also shown, representing the size of the electromagnetic shower initiated by an incident electron or photon. FCal2 and FCal3 are geometrically similar to FCal1 except they use tungsten as the absorber material in the rods. The modules consist of two 2.35 cm thick copper end-plates that span the electrode structures. The space between the end-plates and copper tubes is filled with tungsten slugs.
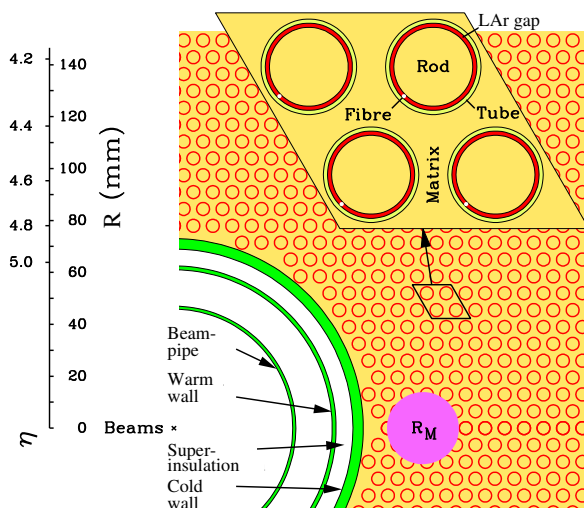
Figure 3.20: Electrode structure of FCal1. The matrix is made up of copper plates with copper tubes and rods with a LAr gap [22].

3.5.4   Zero Degree Calorimeters

The Zero Degree Calorimeters (ZDC) [210] detect neutral particles (mainly spectator neutrons) at $|\eta| > 8.3$ and are used in heavy-ion collisions for triggering on minimum bias events. The ZDCs are

located at ± 140 m from the interaction point. They consist of four modules: one electromagnetic (EM) module about $29X_0$ deep and three hadronic modules about 1.14λ thick. The EM and hadronic modules are made of 11 tungsten plates perpendicular to the beam axis. A total of 96 quartz rods penetrate the plates and run parallel to the beam direction. Incident particles impinge on the tungsten plates and produce a shower of particles. The rods pick up the Cerenkov light generated by the shower and transmit it to multi-anode phototubes at the top of the module. The intensity of the light corresponds to the energy of the incident particle.

3.6 Muon Spectrometer

The outermost part of the ATLAS detector is the muon spectrometer (MS). Positioning the MS behind the calorimeter system is advantageous since dE/dx for muons in the calorimeter is small and in the minimum ionizing region, below where radiative effects become important [2]. In contrast, photons and electrons have a short radiation length and interact with the calorimeter by producing a cascade of pair production and Bremsstrahlung (electromagnetic showering). Moreover, hadrons interact with the calorimeter through strong interactions and fragment into various electromagnetic and secondary hadronic components (hadronic showering) [211]. This ultimately screens the MS from unwanted particles produced in the collision and allows for precise measurements of muon parameters.

The MS is designed to detect muons in the range $|\eta| < 2.7$ and to measure muon momenta with resolutions $< 2.5\%$ at $3 < p_{\mathrm{T}} < 200$ GeV and $< 10\%$ up to 1 TeV. This unprecedented performance is attributed to large superconducting air-core toroid magnets, low multiple scattering in the toroid material, high precision measurements of the muon trajectory, and alignment of the muon chambers with respect to the overall detector. A diagram of the MS is shown in Figure 3.21 and a summary of its main parameters is listed in Table 3.1.

There are three toroids that generate the magnetic field for the MS: two in the end-cap region $(1.05 < |\eta| < 2.7)$ and one in the barrel region $(|\eta| < 1.05)$. Precision-tracking chambers in the barrel region are located between and on the toroid coils. The end-cap chambers are in front of and behind the end-cap toroids. The chamber system consists of eight octants that are symmetrically arranged in azimuth ϕ. Each octant is subdivided into two sectors (large and small), resulting in ϕ

overlap regions. The overlap regions minimize gaps in the detector coverage. The chambers in the barrel region are arranged in three cylindrical layers around the beam axis at ~ 5 m, 7.5 m, and 10 m. The end-cap chambers form large wheels perpendicular to the z-axis and are located at $|z| \approx 7.4$ m, 10.8 m, 14 m, and 21.5 m from the interaction point. At the center of the detector ($|\eta| \approx 0$) gaps exist to allow for services to the solenoid magnet, calorimeters, and ID. The size of the gaps differ in each sector, but the largest gaps measure 1-2 m. Additional gaps due to the detector support structures (feet) also exist. These poorly covered areas affect the muon reconstruction and momentum resolution.
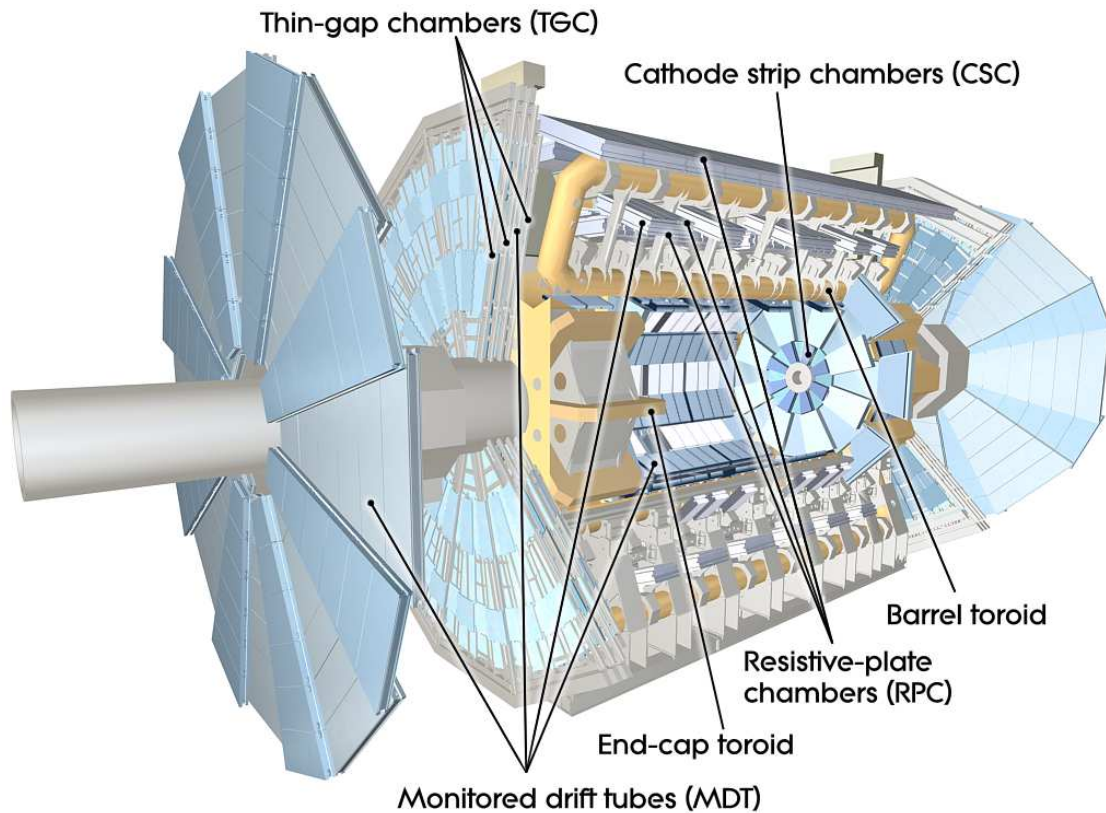
Figure 3.21: Cut-away of the ATLAS muon system [22].

Table 3.1: Summary of the main parameters of the muon spectrometer.

Monitored Drift Tubes	**MDT**
- Coverage	$\lvert\eta\rvert < 2.7$ (innermost layer: $\lvert\eta\rvert < 2.0$)
- Number of chambers	1150
- Number of channels	354000
- Function	Precision tracking
Cathode Strip Chambers	**CSC**
- Coverage	$2.0 < \lvert\eta\rvert < 2.7$
- Number of chambers	32
- Number of channels	31000
- Function	Precision tracking
Resistive Plate Chambers	**RPC**
- Coverage	$\lvert\eta\rvert < 1.05$
- Number of chambers	606
- Number of channels	373000
- Function	Triggering, second (ϕ) coordinate
Thin Gap Chambers	**TGC**
- Coverage	$1.05 < \lvert\eta\rvert < 2.7$ (2.4 for triggering)
- Number of chambers	3588
- Number of channels	318000
- Function	Triggering, second (ϕ) coordinate

3.6.1 Toroid Magnets

The MS magnet system comprises of two end-cap toroids inserted at each end of the barrel toroid. Each toroid consists of eight coils assembled radially and symmetrically around the beam axis. The end-cap coil system is rotated by 22.5° with respect to the barrel toroid to provide radial overlap and to optimize the magnetic bending power at the interface. The end-cap coils are assembled as a single cold mass and are housed in one large cryostat. This allows the internal forces of the toroids

to be taken by the cold supporting structure. The barrel toroid coils are housed in eight individual cryostats with linking elements that provide mechanical stability.

The performance of the magnetic bending power is characterized by the field integral $\int \mathrm{B}dl$ where B is the field component normal to the muon direction and the integral is over the (infinite-momentum) muon trajectory between the innermost and outermost chamber planes. The barrel toroids provide a bending power of 1.5 to 5.5 Tm in the region $0 < |\eta| < 1.4$. In the end-cap toroids, the bending power is 1 to 7.5 Tm in the region $1.6 < |\eta| < 2.7$. The bending power is lower in the barrel/end-cap transition region $(1.4 < |\eta| < 1.6)$ where the two magnets overlap (Figure 3.22).
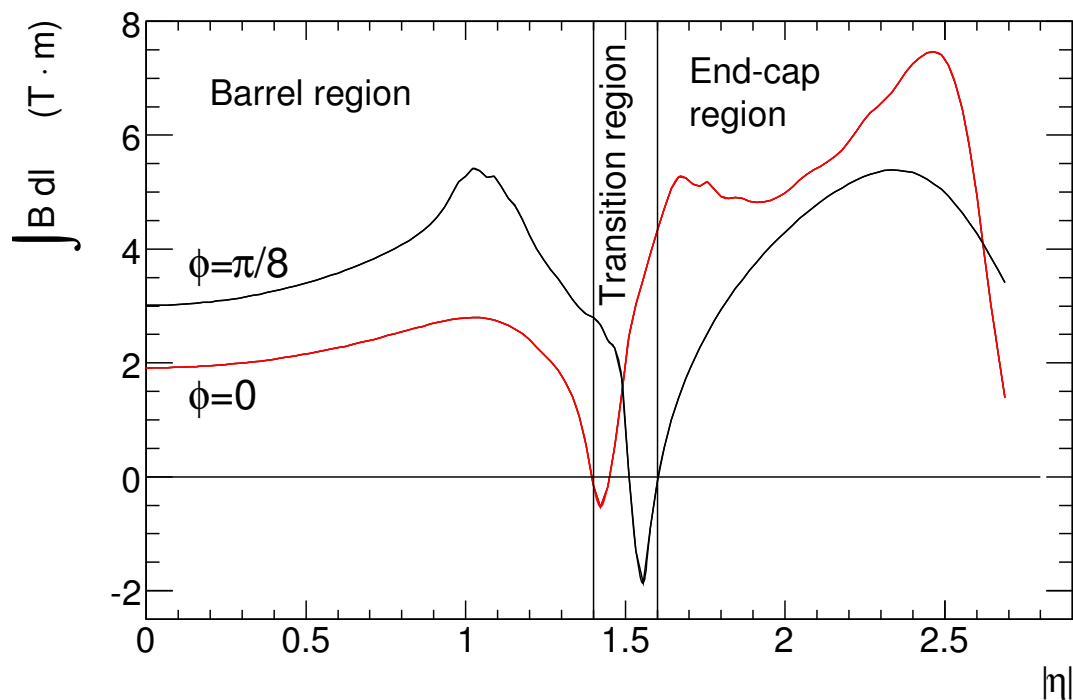
Figure 3.22: Predicted field integral at different ϕ as a function of $|\eta|$ from the inner to outer layer of the MDT in one toroid octant [22].

3.6.2   Monitored Drift Tube Chambers

The monitored drift tube chambers (MDTs) provide precise coordinate information and momentum measurements in the bending direction of the air-core toroid magnets. They cover a pseudorapidity

range $|\eta| < 2.7$ except in the innermost end-cap layer, where the coverage is only up to $|\eta| = 2$ and chambers are replaced by CSCs (discussed below) at $2 < |\eta| < 2.7$. There are 1150 MDT chambers that cover an area of 5500 m^2. The chambers consist of three to eight layers of drift tubes operating with Ar/CO$_2$ drift gas (97%/7%) at an absolute pressure of 3 bar and diameter 29.970 mm. This operating pressue achieves an average spatial resolution of 80 μm per tube (35 μm per chamber). Muon tracks typically cross three MDT stations. Figure 3.23 depicts a low p_T (4 GeV) and high p_T (20 GeV) muon traversing the inner, middle, and outer layers of the MDTs.
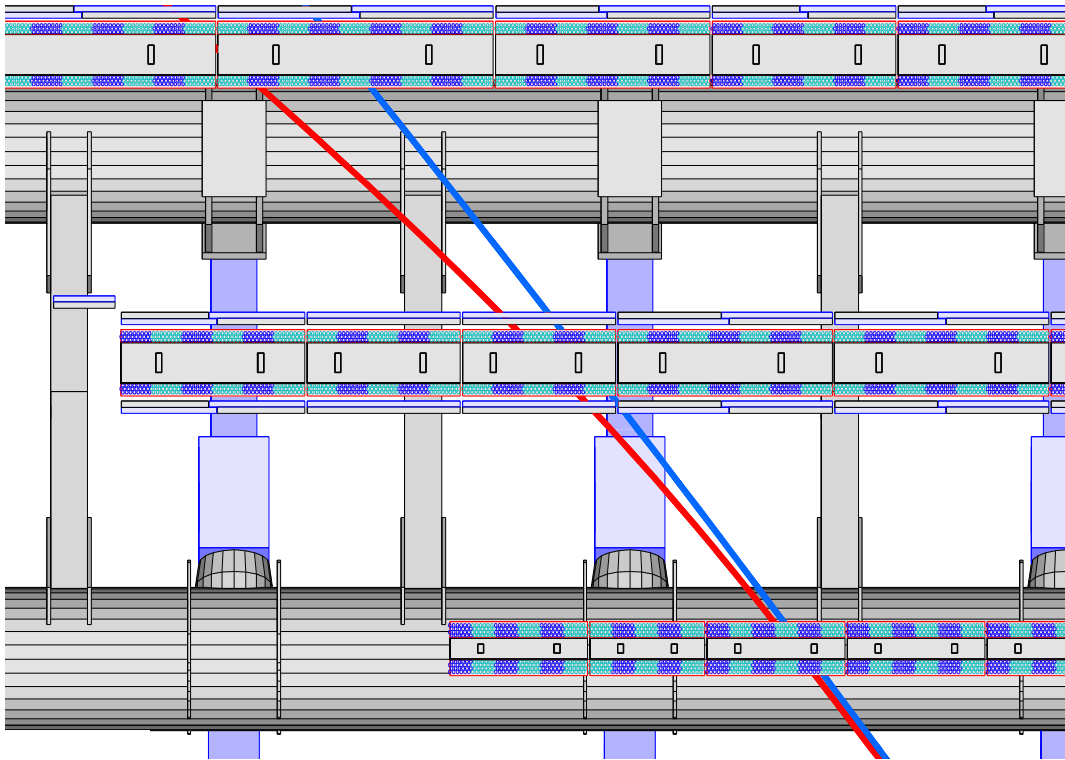
Figure 3.23: Trajectories of a low p_T (4 GeV) and high p_T (20 GeV) muon in the bending $(R - z)$ plane of the barrel. The tracks are crossing the inner, middle, and outer layers of the MDTs [22].

Muons traversing the drift tube chambers ionize the gas mixture, and the resulting electrons collect at a central tungsten-rhenium wire. The wire has a 50 μm diameter and is at a potential of 3080 V. The cylindrical structure of the drift tubes results in a radial electric field. Therefore, the measurement accuracy depends only weakly on the angle of incidence of the muon with respect

to the chamber plane, and the track coordinate is determined from the radius of the circle around the anode wire to which the muon is tangential (Figure 3.24). However, segments far from the tangential point may produce several hits per track, possibly resulting in an inflation of data volume. To prevent this from occuring, the front-end electronics are implemented with an adjustable dead-time.
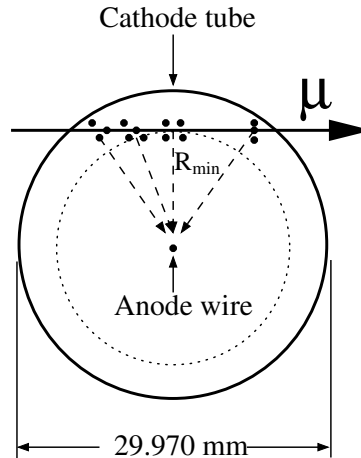
Figure 3.24: Cross-section of a MDT [22].

The MDT chambers are rectangular in the barrel and trapezoidal in the end-caps. This geometry optimizes solid angle coverage while avoiding spatial conflicts with the magnetic coils and support structures. The tubes in the barrel and end-cap regions run along the ϕ direction. The chambers are named based on their location in the barrel (B) or end-cap (E) as well as their chamber layer: inner (I), middle (M), outer (O). The chambers are also given a large (L) or small (S) sector designator over a total of 16 sectors. These designators define chamber stations. For example, the 72 chambers in the BOS station are located in a small sector in the outer layer of the barrel (see Figure 3.25). Sectors 12 and 14 in the barrel have special chambers designed to minimize acceptance losses due to the support structures (feet). These special chambers replace the sector designator with a feet designator (e.g. BOS becomes BOF). There are also special chambers called BEE (Barrel End-cap Extra) chambers that are used to measure tracks passing from the barrel to end-cap region. Figure 3.25 also shows areas where the EI chambers do not overlap with the EO chambers. Thus, intermediate ring chambers (EES and EEL, where "E" is extra) are introduced with an offest of 3-3.6 m to allow for momentum measurements in this region.
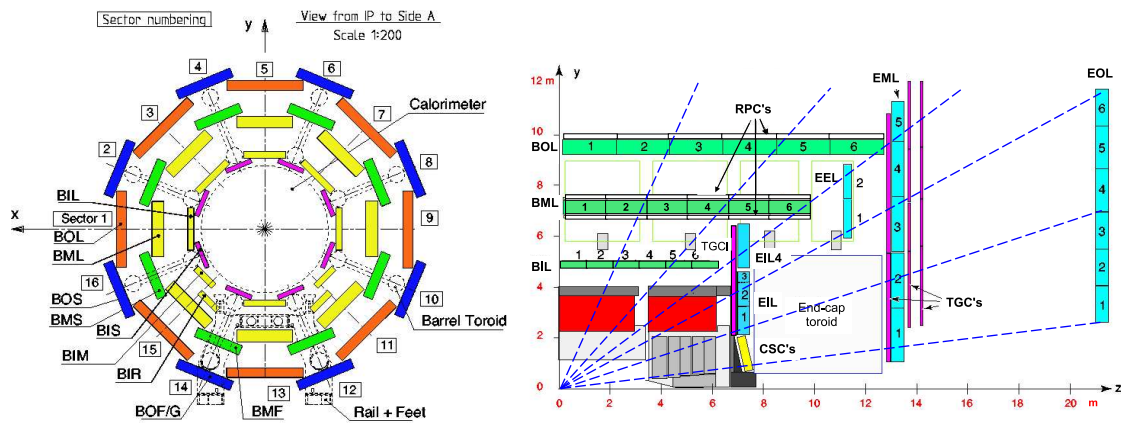
Figure 3.25: (Left) Cross-section of the barrel muon system perpendicular to the beam axis (non-bending plane). (Right) Cross-section of the muon system in the plane containing the beam axis (bending plane) [22].

All MDT chambers consist of two groups of tube layers called multi-layers. The number of tube layers in each group vary. In the innermost part of the MS, each group in the multi-layer consists of four tube layers, whereas in the middle and outer portions, there are only three tube layers per group. This is illustrated in Figure 3.26.
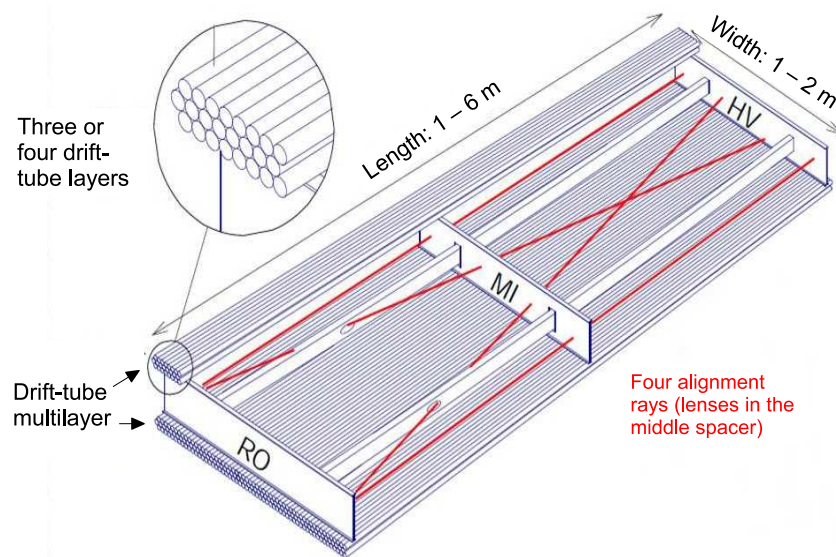
Figure 3.26: Illustration of the mechanical structure of a MDT chamber [22].

3.6.3   Cathode-strip Chambers

The Cathod Strip Chambers (CSCs) in the muon system are used to detect tracks at large pseu-dorapidities ($|\eta| > 2$). The CSCs can tolerate counting rates up to ~ 1000 Hz/cm^2, whereas in the MDTs the rate cannot exceed ~ 150 Hz/cm^2. The CSCs are segmented into large and small chambers in ϕ, as in the case of the MDTs. The CSCs consist of two disks with eight small and eight large chambers each, as shown in Figure 3.27. Each chamber contains four CSC planes, resulting in four independent measurements of η and ϕ. The CSCs are located 7 m from the interaction point and are titled towards the interaction point to reduce the effect of inclined tracks and the Lorentz angle on the spatial resolution. They are mounted with the MDTs and TGCs (see below) to form the "small wheel" of the detector. The CSCs cover a radial space between 881 mm and 2081 mm, corresponding to a coverage region $2.0 < |\eta| < 2.7$. Figure 3.28 presents an $\eta - \phi$ map of coverage areas in the MS.
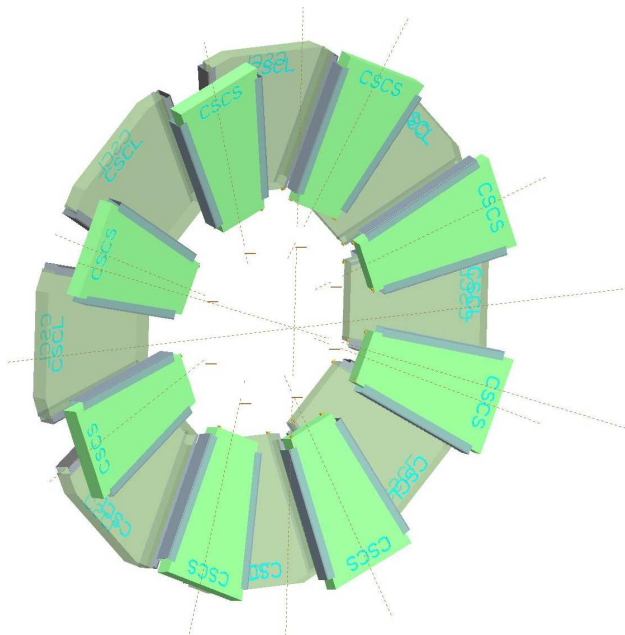
Figure 3.27: Depiction of a CSC with eight small and eight large chambers [22].

The CSCs are multiwire proportional chambers that measure ion pairs produced in Ar/CO$_2$ gas chambers. A track typically produces 90 ion pairs while traversing the CSCs. The anodes have a diameter of 30 μm and are made of gold-plated tungsten with 3% rhenium. The cathodes are
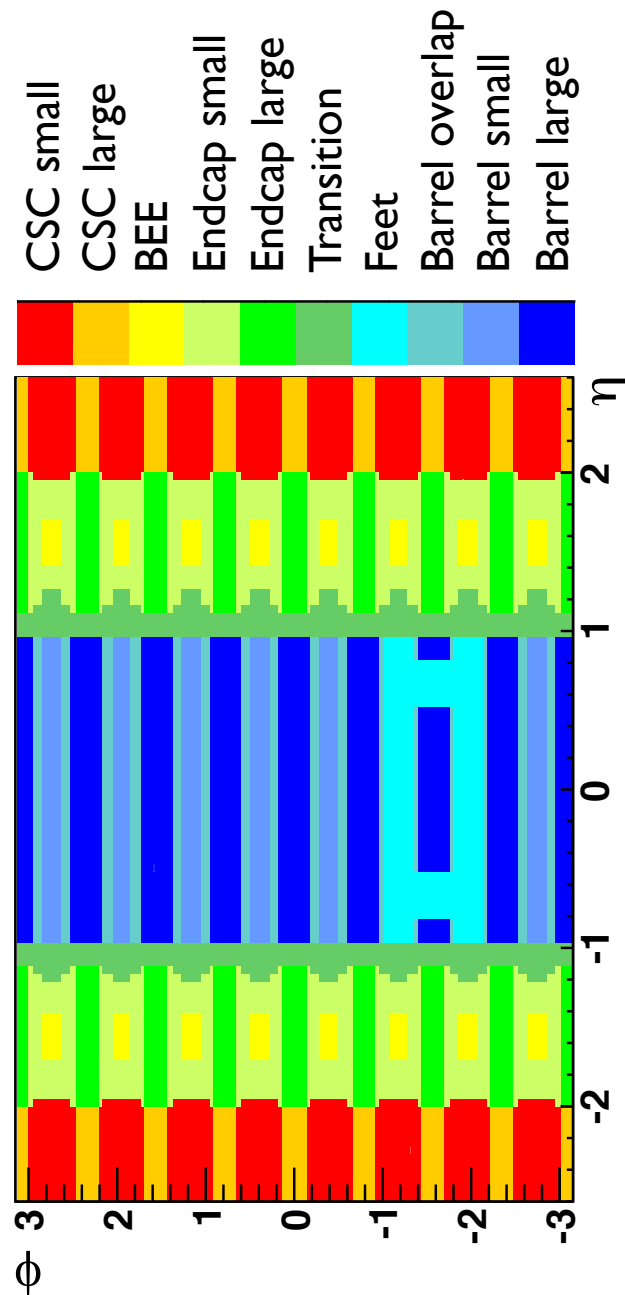
Figure 3.28: $\eta - \phi$ map of the different detector regions [23].

made of copper and are segmented into strips perpendicular to the radially directed wires and into strips parallel to the wires. The perpendicular strips provide precision coordinates in the bending (η) direction by measuring the charges induced on adjacent strips from the avalanche. The parallel

cathode strips provide transverse coordinates of the track. The position of the muon is obtained by an interpolation between the charges induced on neighboring cathode strips, where the signal is directly connected to the front-end boards. This procedure results in a spatial resolution of 60 μm in the bending direction per CSC plane. In the non-bending (ϕ) direction, the cathode segmentation is not as fine, resulting in a resolution of 5 mm. Figure 3.29 shows an illustration of the structure of a CSC cell and the segmentation in the CSC cathodes.

The CSCs are well-suited for handling high particle densities for several reasons. First, they provide good two-track resolution by allowing unambiguous η/ϕ assignments of the tracks. Next, the electron drift times are small (< 40 ns), resulting in a good time resolution of 7 ns per plane. Lastly, the small gas volume in the chambers and absence of nuclides with a high neutron cross-section (e.g. hydrogen) [212] make the CSCs insensitive to neutrons, which could interfere with the muon measurements.

3.6.4 Alignment System

In order to measure the muon momentum at the desired accuracy of 10% for $p_\mathrm{T} = 1$ TeV, the precision chambers (MDTs and CSCs) must be aligned such that the measurement error due to the alignment contribution is less than the intrinsic measurement error of the chamber. It is not possible to obtain the required resolution by stabilizing the geometry and position of the MS components. Rather, optical alignment systems are used to correct for movements in the detector elements offline.

The alignment schemes are based on optical straightness monitors (RAS-NIK and MPA-ALMY systems). The optical elements are mounted on the precision chambers. The schemes are different in the barrel and end-cap regions due to geometrical constraints. To reduce cost, only the three-layered (triplet) chambers are equipped with optical systems in the barrel.

The alignment system in the MS is shown in Figure 3.30. The system relates the position of each chamber to its neighbors. In the barrel, MDT chambers are related to each other using chamber-to-chamber alignment sensors (praxial and axial systems). The inner, middle, and outer layers use a projective system, which simulates the trajectories of infinitie momentum tracks originating from the interaction point. In conjuction with a track-based alignment system, the optical sensors in the barrel can detect relative chamber movements to within 30 μm.
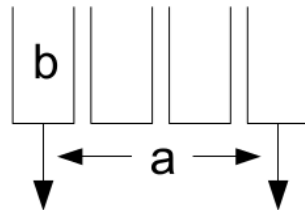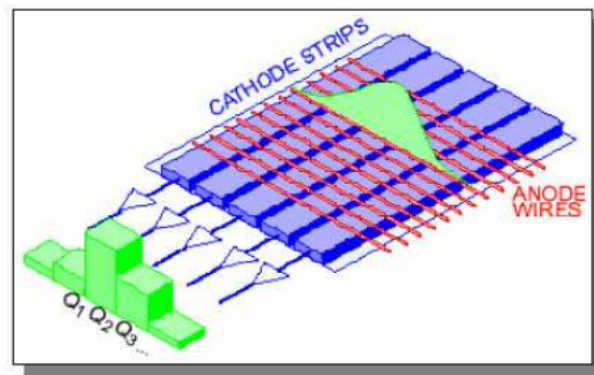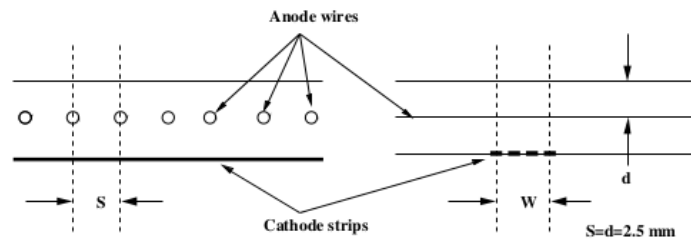
Figure 3.29: (Top) The structure of a CSC cell look down the anode wires and also in the perpendicular (bending) direction. The anode-cathode spacing is $d = 2.5$ mm. (Bottom) Segmentation of the CSC cathodes and charge distribution of the avalanche on the wires. The strip width is $b = 1.519$ mm and 1.602 mm for the small and large chambers, respectively. The distance between the centers of two strips (pitch) is $a = 5.308$ mm and 5.567 mm [22].

In the end-caps, light traveling from the inner to middle layers are obstructed by the toroid cryostats. Thus, alignment bars are used as an intermediate reference. They are installed in each EI, EM, and EO layer and are connected by polar optical lines. The chambers are optically connected

to the alignment bars by proximity sensors. This arrangement allows relative chamber positions in the end-caps to be located to within 40 μm.
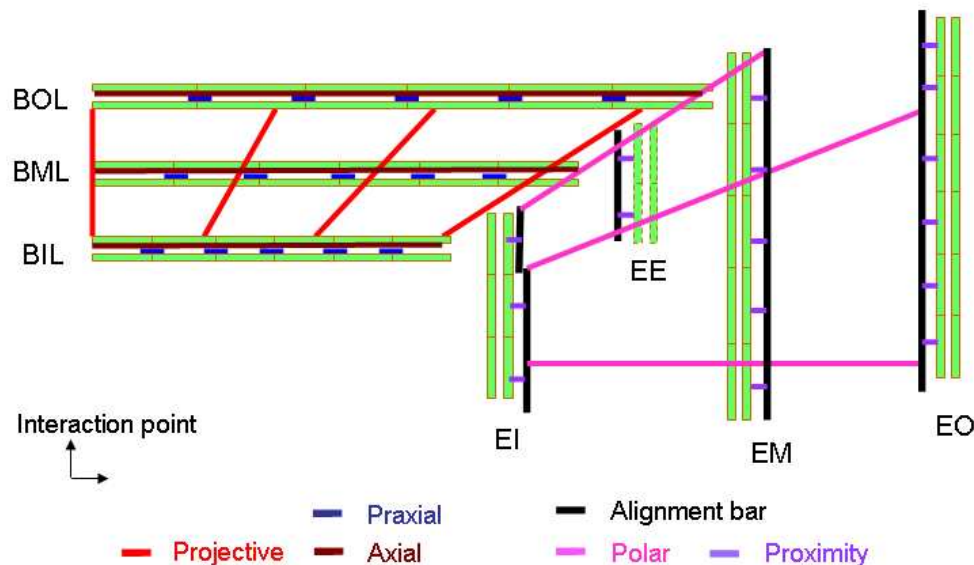
Figure 3.30: Schematic of the alignment system in the MS. See text for details [22].

3.7   Trigger and Data Acquisition Systems

The ATLAS detector is equipped with a system that decides whether to record an event. This system is called a *trigger*. The trigger system is based on precisely defined criteria that enable ample information storage for data analysis while maintaining the amount of data stored within capacity. This is particularly useful in analyses concerned with low-rate physics processes. As an example, the event rate at the LHC is 10^9 Hz for the design luminosity of $L = 10^{34}\text{cm}^{-2}\text{s}^{-1}$. The Higgs boson is produced at a rate of $\sim 10^{-2}$ Hz [213]. Thus, the ideal trigger would select 1 in 10^{11} events while discarding the others from the dataset. This example illustrates the importance of using a trigger for event selection.

In ATLAS, the Trigger and Data Acquisition (TDAQ) systems have three distinct levels: Level-1 (L1), Level-2 (L2), and the event filter (EF). Each successive level refines decisions made by the previous level and, when necessary, applies additional selection criteria. The data acquisition

system receives and buffers the event data from the detector-specific readout electronics at the L1 acceptance rate.

The L1 trigger searches for physics signatures (trigger chains) from muons, electron/photons, jets, and τ-leptons. It can also select events with large missing energy. Decisions are made at L1 using a limited amount of detector information from the calorimeters and MS. The decision is reached within $< 2.5~\mu$s after the bunch-crossing and reduces the event rate to 75 kHz. In each event, the L1 trigger will define detector regions in $\eta - \phi$ space where the interesting feature was identified. These regions are referred to as *Regions-of-Interest* (RoIs; see Figure 3.31). The RoI data include information on the coordinates, energy, and type of signature and constitute $\sim 1 - 2\%$ of the full event data.

The overall L1 decision is made by the Central Trigger Processor (CTP). The CTP receives information from the calorimeter and muon trigger processors, which consist of multiplicities[1] of physics objects (e.g. muon, electrons, jets, etc.) and of flags indicating which energy thresholds were passed. The trigger conditions for each object are formed from look-up tables – for example, a condition that the muon multiplicity be ≥ 1 for a particular p_T threshold. If the conditions are satisified, the CTP sets the trigger condition to *true*. The maximum number of trigger conditions at any one time is 256. The trigger conditions are combined to form trigger items. Several trigger conditions may contribute to a single trigger item. For example, a trigger item may consist of two conditions that there be at least one muon and two jets that pass particular thresholds in the event. Each trigger item is given an eight-bit trigger word that is turned on when the trigger conditions are satisfied. The CTP also contains pre-scaling factors to reduce frequent physics processes from consuming too much bandwidth. Once the event is accepted by the L1 trigger, the CTP transfers the trigger decision information to the DAQ/HLT system via point-to-point Readout Links (ROLs). Readout system (ROS) units contain Readout Buffers (ROBs) of event fragments, which are stored and provided to the DAQ/HLT upon request.

The readout data from the CTP contains information on the luminosity block, which is the shortest time unit in which the integrated luminosity can be determined. Storing the luminosity block allows for the rejection of data in the case of detector failures. The CTP increments the luminosity block by temporarily pausing trigger generation, registering the block, and releasing the

---

[1]The multiplicity is the total number of particles produced in a collision.

trigger. The luminosity block numbers stored in the readout data are used to construct *good run lists* (GRLs).

At L2, the full detector information in the RoI is used to either accept or reject the event according to an hypothesis algorithm that determines whether the identified feature meets specific criteria (e.g. p_T threshold). This reduces the trigger rate to 3.5 kHz with an average event processing time of 40 ms. Once the L2 accepts the event, all the event data is sent to an event-building node (called SFI). The SFI collects the event data from the ROSs and assembles the event into a single event data structure. These events are then transmitted by the DAQ system to the EF.

At the EF, offline ATLAS event reconstruction and analysis procedures are implemented to further select events, reducing the event rate to 200 Hz. The average EF processing time for an event is ~ 4 seconds. Events that pass the EF decision are classified by a predetermined set of ATLAS physics streams (e.g. muons) and are sent to the output nodes (SFOs) of the DAQ/HLT system. Events received by the SFOs are categorized by their physics streams and stored in a local file system. The files are then moved to permanent storage at the CERN computer center. A block diagram of the ATLAS TDAQ is shown in Figure 3.32.
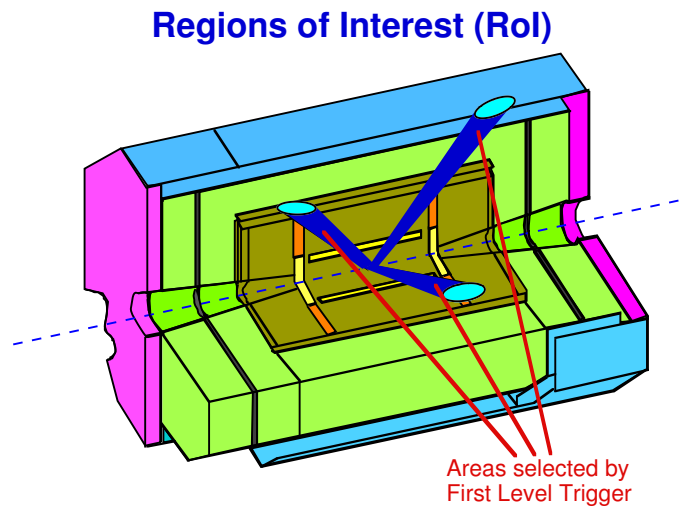
Figure 3.31: Illustration of ATLAS Regions-of-Interest (RoIs).
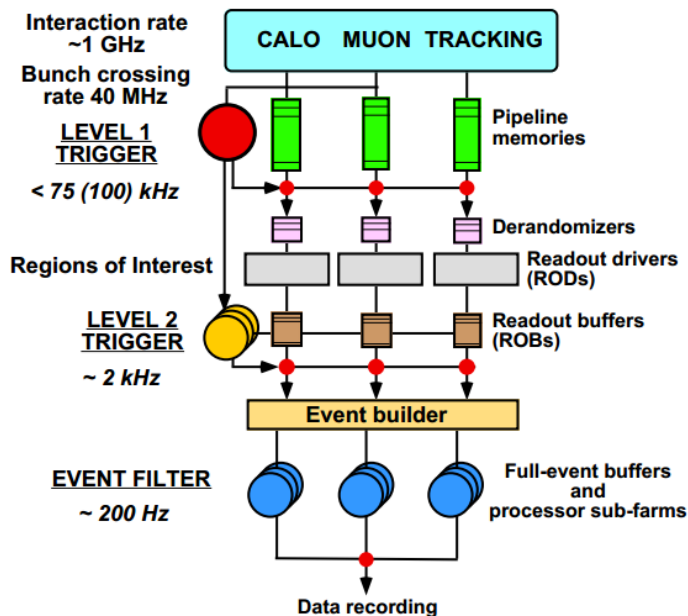
Figure 3.32: Block diagram of the ATLAS trigger and data acquisition systems [24].

3.7.1 Muon Triggers

The muon trigger system consists of Resistive Plate Chambers and Thin-Gap Chambers that have the ability to discriminate events based on muon p_T requirements, identify bunch-crossings, provide fast and coarse tracking information to be sent to the HLT, determine coordinate information in the non-bending (ϕ) plane to complement MDT measurements, and provide robustness against random triggering from background particles. These sub-detectors provide triggering up to $|\eta| = 2.4$ and over the full ϕ range. Figure 3.33 shows a schematic of the muon trigger system in the barrel ($|\eta| < 1.05$) and end-cap ($1.05 < |\eta| < 2.4$) regions. Because muons at large η have a large p_z component and the magnetic bending power at large η is only twice the value at $\eta = 0$, the technologies in the barrel and end-cap are different in order to keep the resolution the same in each region.

3.7.1.1 Resistive Plate Chambers

The trigger system in the barrel uses Resistive Plate Chambers (RPCs). The RPCs consist of three concentric cylindrical layers around the beam axis (trigger stations). Figure 3.34 provides a bird's
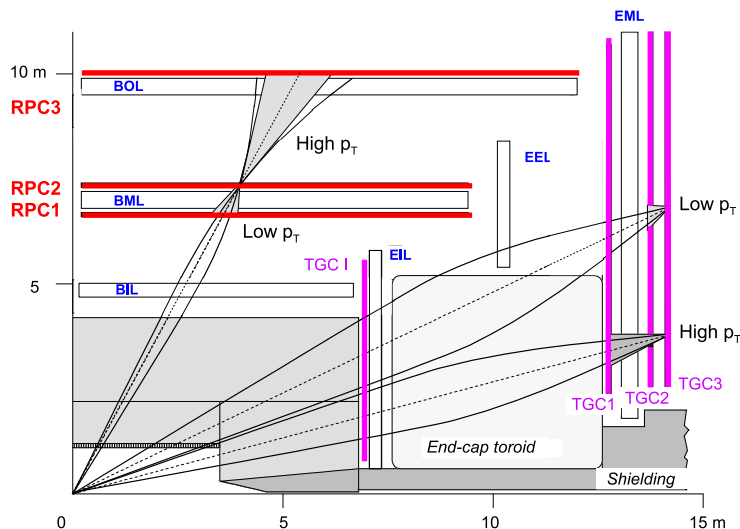
Figure 3.33: Schematic of the muon trigger systems in the barrel (RPC) and end-cap (TGC) regions [22].

eye cross-section of the RPCs. The two inner layers (RPC1 and RPC2) are located on both sides of the MDT BM at a radial distance of ~ 7.5 m from the interaction point. RPC1 and RPC2 trigger on muons with $4 \leq p_T \leq 9$ GeV. The outer layer (RPC3) is mounted on the inside of the large sector and outside of the small sector MDT BO stations at ~ 10 m from the interaction point. The RPC3 triggers on muon tracks in the range $9 \leq p_T \leq 35$ GeV. Each trigger station consists of two independent detector layers that measure η and ϕ, resulting in a total of six $\eta - \phi$ measurements for a track crossing all three stations. This redundancy enhances fake rejection and improves the trigger efficiency. The η-strips are parallel to the MDT wires whereas the ϕ-strips are perpendicular and provide a second coordinate measurement.

The RPCs are gaseous parallel electrode-plate detectors, using a gas mixture of $C_2H_2/Iso - C_4H_{10}/SF_6$ (94.7/5/0.3%). They consist of two resistive plates made of phenolic-melaminic plastic laminate and are separated by 2 mm with an insulating spacer. An electric field of 4.9 kV/mm allows avalanches to form as the tracks ionize the gas. Standard RPCs are assembled together with a MDT, however special RPCs are located in regions where the MDTs cannot be installed. This minimizes the trigger acceptance loss.

The trigger algorithm requires that a signal from a RPC be compared with the other RPCs along
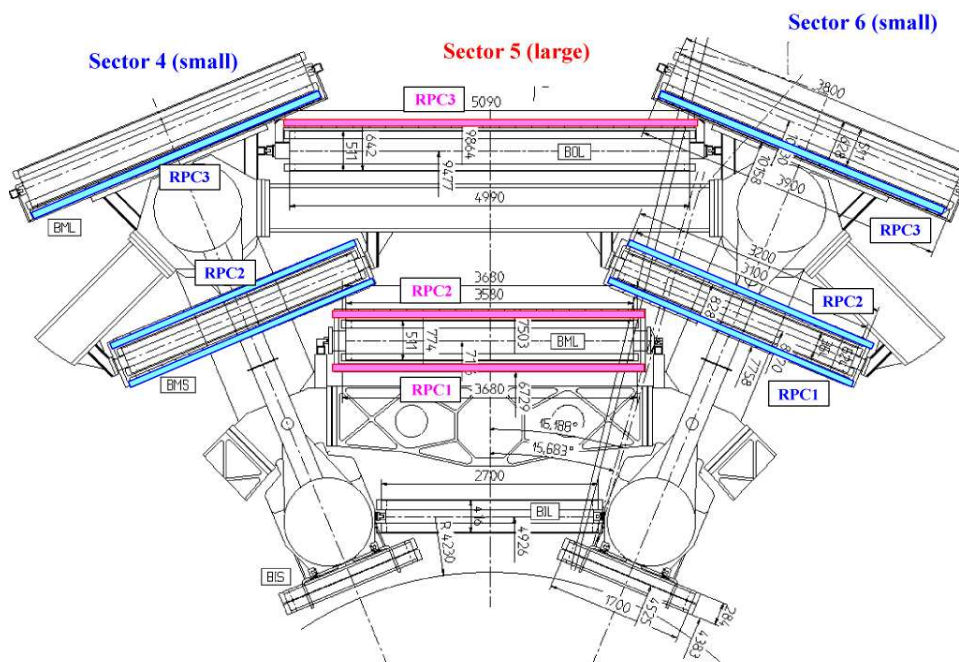
Figure 3.34: Bird's eye cross-section of the RPCs (colored). The MDTs are also shown. [22].

the trajectory of the particle. For low-p_T triggers, if a track is generated in RPC2, the algorithm searches for a corresponding hit in RPC1 along a road with a center defined by the straight line trajectory between the hit in RPC2 and the interaction point. The width of the road is a function of the p_T requirement on the track: smaller widths are used for higher p_T cuts. The algorithm is performed in η and ϕ projections to reduce the fake rate. Of the four layers in RPC1 and RPC2, a 3-out-of-4 coincidence is required. The high-p_T algorithm operates in a similar manner, except that in addition to a 3-out-of-4 coincidence in RPC1 and RPC2, a 1-out-of-2 coincidence is required in RPC3. Both the low-p_T and high-p_T trigger algorithms can operate using three p_T thresholds simultaneously, resulting in six thresholds reported to the central trigger logic. A schematic of the barrel muon trigger readout chain is shown in Figure 3.35.

3.7.1.2   Thin Gap Chambers

The muon trigger system in the end-caps uses Thin Gap Chambers (TGCs). Figure 3.36 presents a schematic of the TGCs as well as the MDT small (S) and large (L) sectors for reference. TGCs are
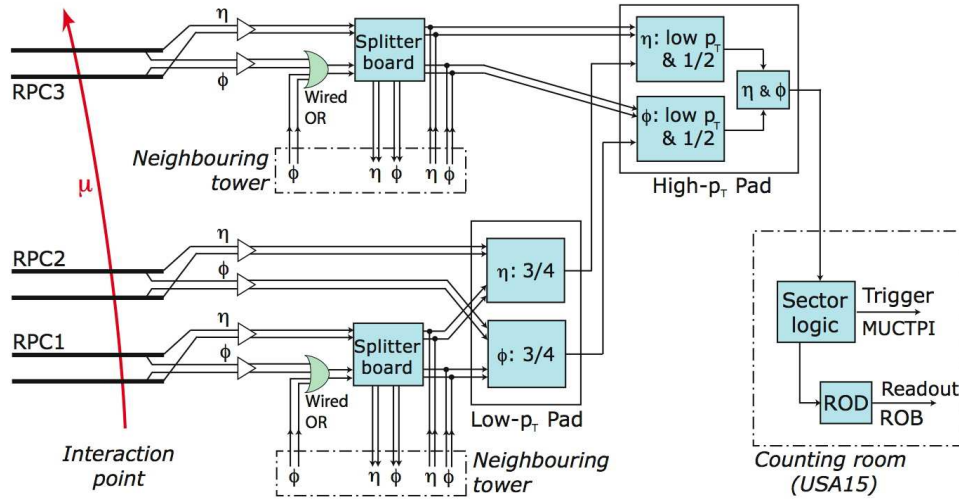
Figure 3.35: Schematic of the trigger signal and readout chain of the L1 barrel muon trigger [22].

located in the inner layer (I) at $|z| \sim 7$ m and middle layers (EM-wheels M1-M3 corresponding to TGC1-3) at $|z| \sim 14$ m. The middle layers consist of seven TGC layers. The inner layer has only two TGC layers and is segmented into two non-overlapping end-cap (EI) and forward (FI) regions.

The TGCs are proportional chambers filled with a CO_2/n-pentane (55/45%) gas mixture. They operate in units of triplets or doublets. A triplet has three chambers whereas a doublet has two (Figure 3.37). The triplet and doublet modules consist of anode wires arranged in the ϕ direction that provide R information for the track and of copper readout strips orthogonal to these wires that provide ϕ information. Both the wires and strips are used for the muon trigger. The trigger detectors are mounted in two concentric rings: an end-cap ring covering $1.05 < |\eta| < 1.92$ and a forward ring covering $1.92 < |\eta| < 2.4$. TGCs in the big wheel (EM) are segmented into 12 sectors of 30° in ϕ. Each sector in the forward ring consists of four modules of 7.5°, whereas each sector in the end-cap ring is comprised of two modules of 15°. This segmentation results in 1704 chambers in the big wheel. In the inner layer, the TGC wheel contains only 90 chambers on each side.

The trigger algorithm operates in a similar manner as for the RPCs, except that R and ϕ coincidence signals are generated independently. A 3-out-of-4 coincidence is required for the doublet modules at M2 and M3 for both the R and ϕ directions. For the triplet modules at M3, a 2-out-of-3 coincidence is required in the R direction and a 1-out-of-2 coincidence in the ϕ direction.
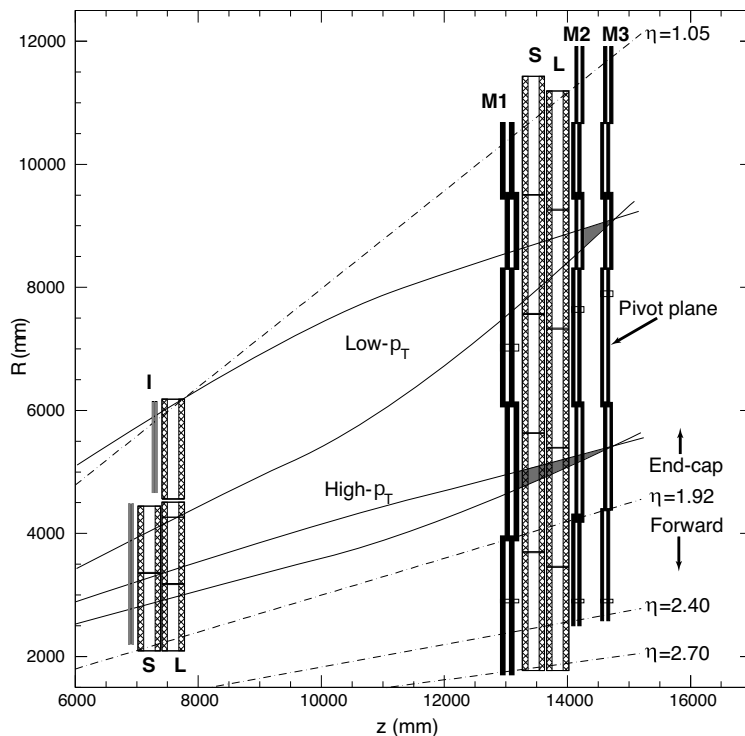
Figure 3.36: Longitudinal cut of the muon end-cap TGCs. MDTs in the small (S) and large (L) sectors are also shown for reference. The EM wheels are marked M1-3, corresponding to TGC1-3 [22].

The final trigger decision is made by merging the $R - \phi$ coincidences with information from the EI/FI chambers. A detailed schematic of the end-cap trigger signal and readout chain is shown in Figure 3.38. High-p_{T} muon candidates are identified with trigger signals from both the doublets and triplets. For low-p_{T} candidates, the triplet station may be omitted to retain high efficiency.

3.8 Minimum Bias Trigger Scintillators

The Minimum Bias Trigger Scintillators (MBTS) [214] are used to select minimum bias collision events with low out-of-time beam background. The detector consists of 32 polystyrene scintillator counters organized into two disks, one on each side of the ATLAS detector (sides A and C). The scintillators are installed on the inner surface of the end-cap calorimeter cryostats at $z \pm 3560$ mm and the disks are perpendicular to the beam axis. Each disk is comprised of an inner ring that
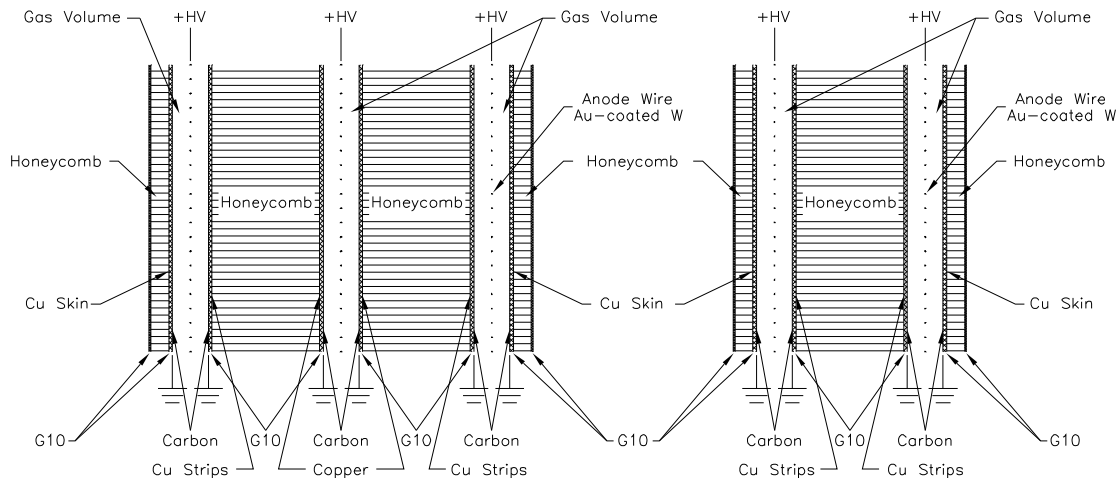
Figure 3.37: Cross-section of a TGC triplet (left) and doublet (right) module [22].

covers $2.82 < |\eta| < 3.84$ and an outer ring that covers $2.09 < |\eta| < 2.82$. Each ring is segmented into eight sectors symmetric in ϕ, resulting in a total of 16 sectors.

Light emitted from the scintillators is collected by wavelength-shifting optical fibers and guided to a photomultiplier tube (PMT). The signal is read out by the calorimeter – specifically Tile Calorimeter or TileCal – electronics. The TileCal shapes and amplifies the MBTS signals and feeds them into a leading-edge discriminator. If the MBTS hit is above the discriminator threshold, the signals are sent to the CTP (discussed above).

At the CTP, 32 MBTS signals are used to calculate the event multiplicity. The multiplicity is calculated for each side independently. L1 items are built using the multiplicity and are designated L1_MBTS_N_N, where N signifies the number of hits on each side of the MBTS.

Additionally, the MBTS is used for offline timing selections. Timing measurements for the A (t_A) and C (t_C) sides can be made with respect to the LHC clock. The difference $\Delta t_{\mathrm{MBTS}} = t_A - t_C$ may be used to reject out-of-time background.

3.9 LUCID

ATLAS is equipped with a Cerenkov detector called LUCID (LUminosity measurements using Cerenkov Integrating Detector) [215] to provide online monitoring of the instantaneous luminosity
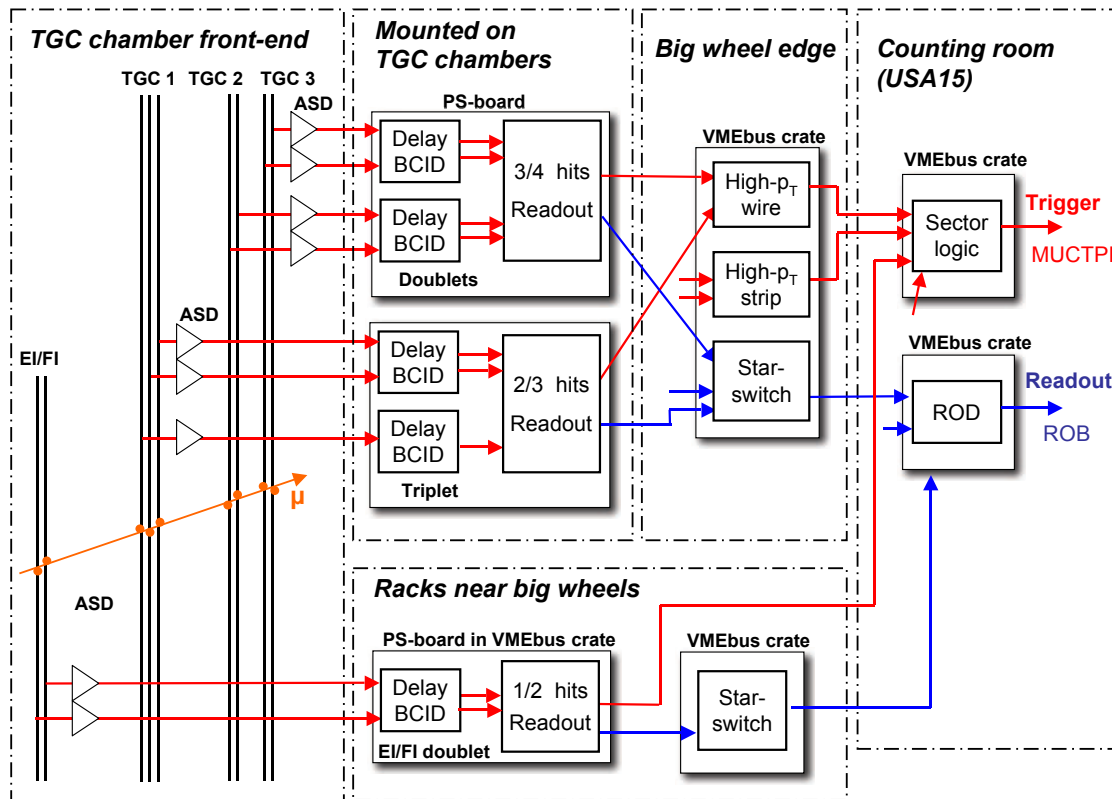
Figure 3.38: Schema of the trigger signal and readout chain for the L1 end-cap muon trigger [22].

and beam conditions. Its main purpose is to detect inelastic pp scattering in the forward direction but may also be used for studies involving diffractive events [216]. Determination of the luminosity is based on the principle that the number of interactions per bunch crossing is proportional to the number of particles measured in the detector.

LUCID detectors are located on both end-caps at a distance ± 17 m from the interaction point and are radially positioned approximately 10 m from the beam pipe at $|\eta| \approx 5.8$. Each detector consists of twenty aluminum tubes surrounding and pointing toward the interaction point. The tubes are filled with C_4F_{10} gas at a constant pressure of 1.2-1.4 bar, providing a Cerenkov threshold of 2.8 GeV for pions and 10 MeV for electrons. The Cerenkov light emitted by a particle is measured by photomultiplier tubes (PMTs) and the signal amplitude from these PMTs are used to distinguish the number of particles per tube. The fast timing response (~ 5 ns) allows for unambiguous

measurements of individual bunch crossings.

A hit is registererd if the PMT pulse height in the analog signal is above a preset threshold. A charge-to-digital converter allows offline analysis of the signal amplitudes. Digital outputs are sent to a readout card and are used to calculate the luminosity for each bunch crossing.

Chapter 4

Muon Identification and Tracking

The purpose of the muon spectrometer (MS) is to measure the momentum of muons passing through the fiducial volume with excellent precision and resolution. The first step in this process is using the MS detectors discussed in Chapter 3 to recognize hits created by a muon along its trajectory (i.e. pattern recognition). These patterns provide an initial estimate of a muon's position, direction, and momentum, which are used as initial parameters during the next step of muon reconstruction: track fitting. Track fitting provides the best estimation of the muon's parameters. Once a trajectory has been determined, the track purity can be improved by associating the muon with corresponding hits in the inner detector (ID).

However, there are several challenges to muon reconstruction. Measurements are typically made in the inner, middle, and outer layers of the MS. Therefore, reconstructing tracks involves extrapolations over large distances, increasing measurement errors. The inhomogeneity in the toroid magnetic field also contributes to extrapolation uncertainties. The detector material needs to be well described to understand how it affects the muon's energy and trajectory. The background rate is high, particularly in the forward (large η) region. Also, the lack of an accurate ϕ measurement in the precision chambers requires a matching ϕ measurement in the trigger chambers (RPCs, TGCs).

These difficulties are overcome by using several sophisticated, independently operating, identification algorithms. The algorithms employ strategies that differ based on how they combine data from different subdetectors. During the 2011 heavy-ion run, the algorithms were grouped into

two [1] families: Staco [217] [2] (Chain 1) and Muid [218] [3] (Chain 2). A CaloMuon family also exists, however it will only be discussed briefly and the reader is directed to Ref. [219]. For each strategy, the reconstruction chains employ different algorithms, as summarized in Table 4.1.

Table 4.1: Summary of the muon reconstruction families in ATLAS.

Strategy	Muid	Staco	CaloMuon
StandAlone	Moore	Muonboy	
Combined	Muid/Mugirl	Staco	
Tagging	Mugirl/MutagIMO	Mutag	CaloMuonTag

The choice of which reconstruction chain to use depends mainly on the goals of the analysis. Both chains have excellent performance, however Staco is typically more robust against background whereas Muid has a slightly higher efficiency [41]. This work uses muons reconstructed with Muid, and therefore the reconstruction algorithms in this family will be discussed. For more information on the Staco chain, the reader is directed to Appendix A and the references therein.

The aim of this chapter is to provide the reader with an understanding of muon reconstruction in ATLAS. The following sections will give a general overview of each identification strategy, followed by a more exhaustive discussion of the Muid algorithms. This will enhance the understanding and appreciation of the analysis methods that will be presented in subsequent chapters.

4.1 Muon Identification Strategies

Muons can be identified using three strategies: *standalone* (SA) reconstruction from MS information alone; *combined* (CB) reconstruction from a combination of information from the ID and MS; and a strategy called *tagging*, which extrapolates ID tracks to segments in the MS stations (*segment tagging*) or energy deposits in the calorimeters (*calorimeter tagging*). These strategies are

---

[1]It should be mentioned that a third reconstruction chain has been developed that merges the MuiD and Staco chains. This third chain is simply called the Muon chain and has been used in 2012 data.

[2]STAtical COmbination

[3]Muon Identification

summarized schematically in Figure 4.1. *Muon types* are defined by which identification strategy is used. Both Muid and Staco use each identification strategy. However, as mentioned previously, these reconstruction chains differ on the specific algorithms used to define each muon type.
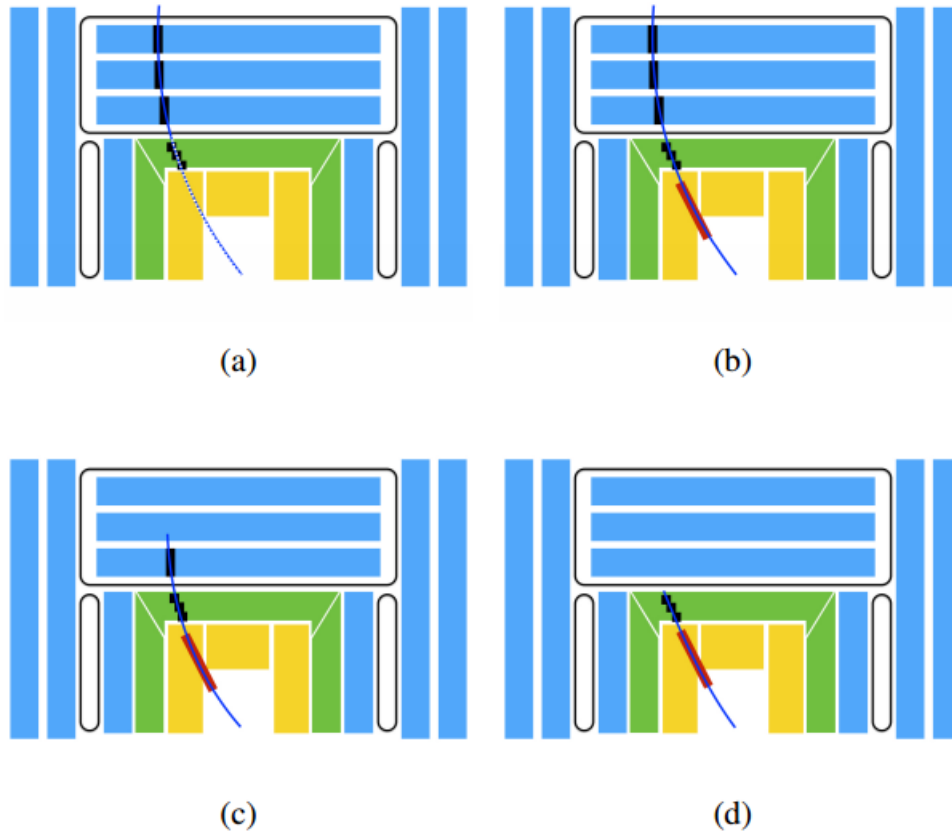
Figure 4.1: Different muon identification strategies used in ATLAS: (a) Standlone (b) Combined (c) Segment-tagged (d) Calorimeter-tagged [25]. The ID is in yellow, the calorimeters in green, and the MS stations in blue.

4.1.1 Standalone

Standalone muon reconstruction begins by searching for hit patterns in the MS. Clusters of hits in each chamber are fitted to produce *segments*. A segment is a straight-line track within a single MDT or CSC station. The segments from each of the three MS stations are used to perform a global fit for the entire track. The global fit extrapolates back to the interaction point (IP), taking

into account energy loss and multiple scattering in the calorimeters and inhomogeneities in the magnetic field (discussed in Sec. 4.2 and 4.3).

The SA strategy has the advantage that it can reconstruct muons at larger η ($|\eta| < 2.7$) than the ID system ($|\eta| < 2.5$). However, the MS has coverage deficiencies at $\eta \approx 0$ and $1.05 < \eta < 1.3$, as can be seen in Figure 4.2. Moreover, the efficiency is poor for very low-p_{T} muons since they do not penetrate the outermost MS stations.
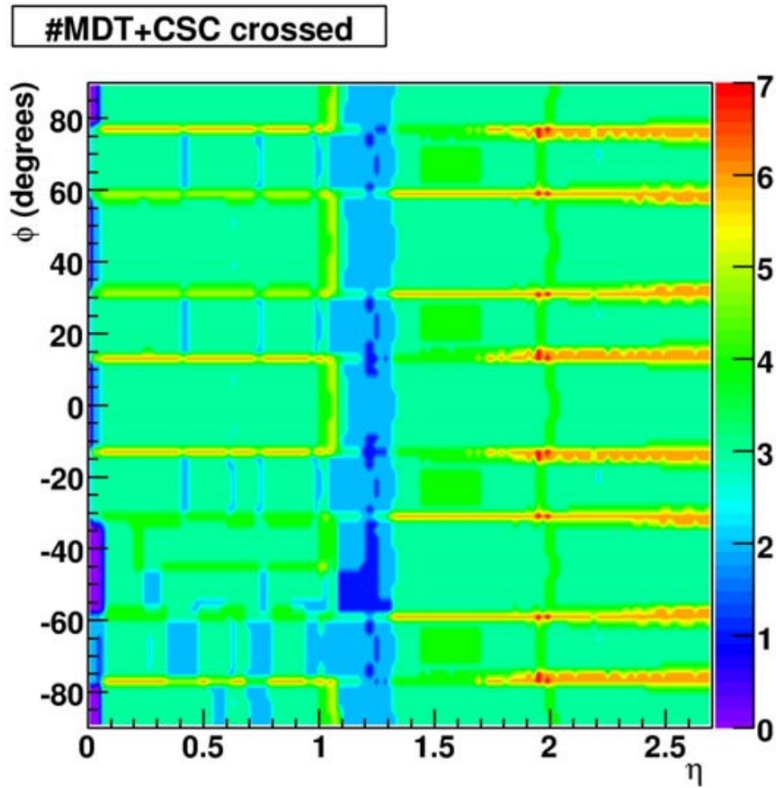
Figure 4.2: $\eta - \phi$ map of the number of MDT/CSC detector stations traversed by muons passing the MS.

4.1.2 Combined

The combined reconstruction strategy starts from standalone tracks and matches them with reconstructed tracks in the ID. CB muons are the highest quality type of muon. The quality of the combination is given by a match χ^2 (discussed in Sec. 4.6).

4.1.3 Segment-Tagged

The segment-tagging algorithms propagate ID tracks with sufficient momentum to the first MS station and search for nearby segments. If segments are sufficiently close to the predicted track position, the ID track is tagged as a muon.

Muons may also be identified using calorimeter measurements. The calorimeter-tagging algorithm identifies ID tracks by searching for energy deposition patterns in the calorimeter consistent with minimum ionizing particles [219]. Muon identification in the calorimeters can be used to locate low-p_T muons with marginal activity in the MS layers.

Tagging ID tracks with MS or calorimeter measurements has the advantage that it is less sensitive to Coulomb scattering and energy loss. Therefore, this strategy can recover muons with low p_T in MS regions with limited coverage (e.g. the gap region at $\eta \approx 0$). ST muons are only used in cases where CB muons cannot be reconstructed.

4.2 Track Extrapolation

Track reconstruction in both the ID and MS relies heavily on extrapolation techniques [30] for local pattern recognition, track fitting, and track matching. *Extrapolation* is the transport of track parameters and covariances to a destination detector surface, as illustrated in Figure 4.3. During the extrapolation, it is important to take into account interactions with the detector material. Extrapolations are used in ID reconstruction to extend tracks from the silicon layers to the TRT and in MS reconstruction to extend muon trajectories to the interaction point or to match muon segments with ID tracks.

Particles follow a helix in the presence of a homogenous magnetic field. For these types of trajectories, the extrapolation can be solved analytically. However, in ATLAS, tracks are extrapolated through the magnetic fields of the toroid and solenoid magnets, which have highly inhomogenous fields (see Figure 3.16 and 3.22). Therefore, to evaluate the equations of motion of a particle, numerical methods must be used. The numerical propagation of the track parameters through the detector is conducted by:

- Evaluating the equation of motion, defined by the Lorentz force, without multiple scattering and energy loss effects:
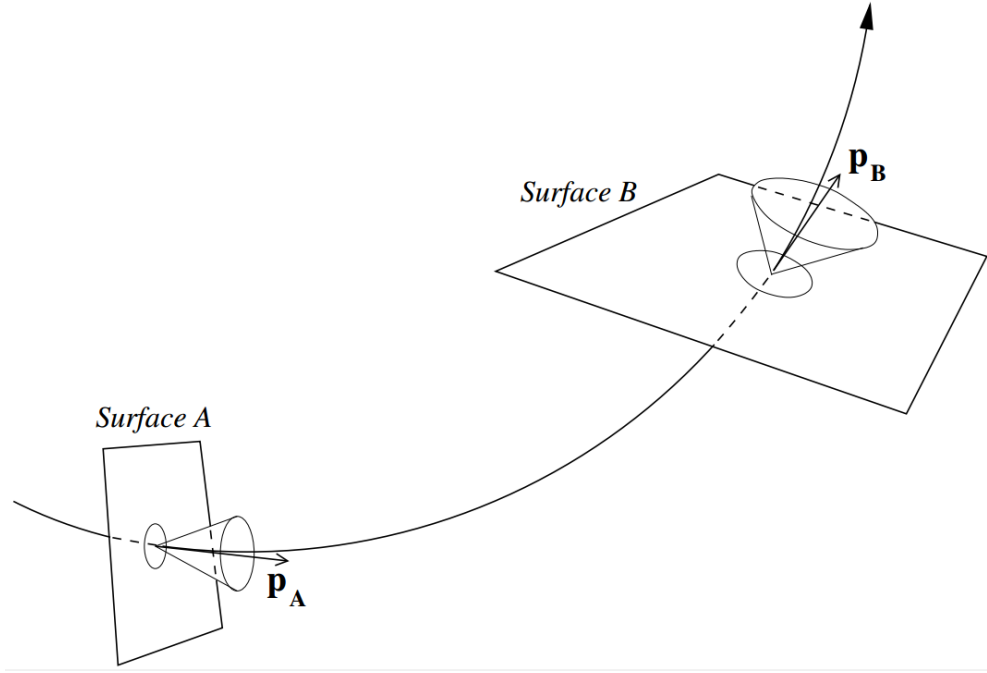
Figure 4.3: Transporting the track parameters and covariances from one surface to another [26].

$$\frac{d^2\vec{r}}{ds^2} = \frac{q}{p}\left[\frac{d\vec{r}}{ds} \times \vec{B}(\vec{r})\right] \tag{4.1}$$

where $\vec{r}$ is the position of the particle along path s and $\vec{B}$ is the magnetic field.

- Applying an energy loss at each integration step. Equation 4.2 is then extended with an energy loss function:

$$\frac{d^2\vec{r}}{ds^2} = \frac{q}{p}\left[\frac{d\vec{r}}{ds} \times \vec{B}(\vec{r})\right] + \frac{d(q/p)}{ds} \tag{4.2}$$

where $\frac{d(q/p)}{ds} = -\frac{qE}{p^3}\left(\frac{dE}{ds}\right)$ and $\frac{dE}{ds}$ is the total mean energy loss per unit distance.

These equations are solved using the Runge-Kutta-Nystrøm [220, 221] integration formulism with adaptive step estimation. The last step of the numerical iteration is reached when the distance to the destination surface is below a certain value. The final propagation to the destination surface is performed using a Taylor expansion. Figure 4.4 illustrates the extrapolation process.
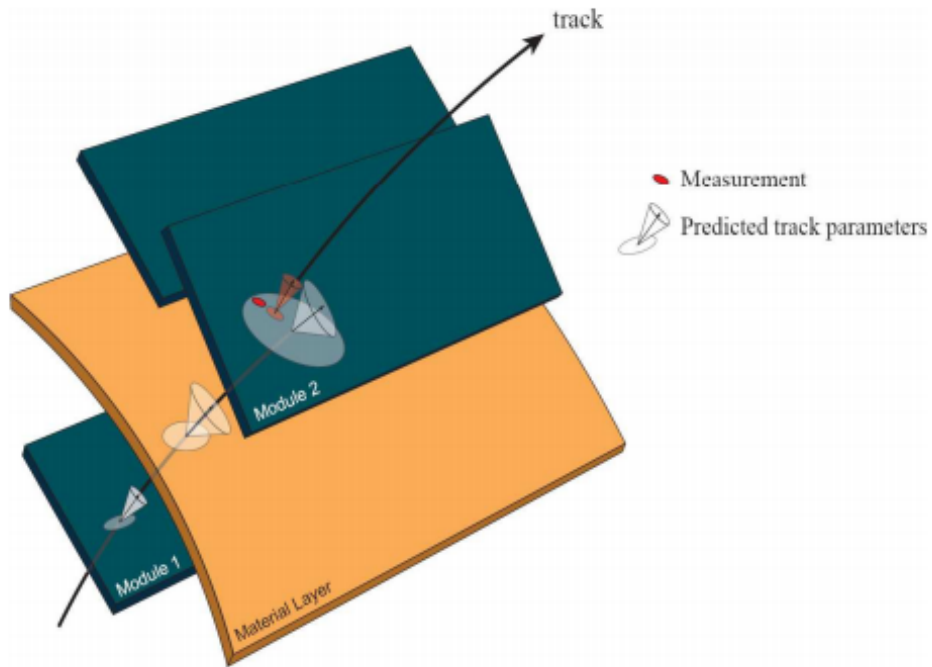
Figure 4.4: Illustration of the extrapolation process. Track parameters from Module 1 are propagated through the material layer to the destination surface in Module 2, where the track parameters are updated. The material layer is associated with the uncertainties on the track parameters. The weighted mean between prediction and measurement updates the track parameters and builds a starting point for the next step [27].

4.3 Material Effects

Muons traverse the ID and calorimeters before reaching the MS, corresponding to > 100 radiation lengths (X_0), as shown in Figure 4.5. Over 80% of the material is in the calorimeters. As they pass through the detector, muons are subject to both energy loss (ionization, bremsstrahlung, pair production, and photonuclear interactions) and directional scattering (Coulomb or multiple scattering). It is important to understand the effects of these processes in order to accurately determine the muon trajectory.
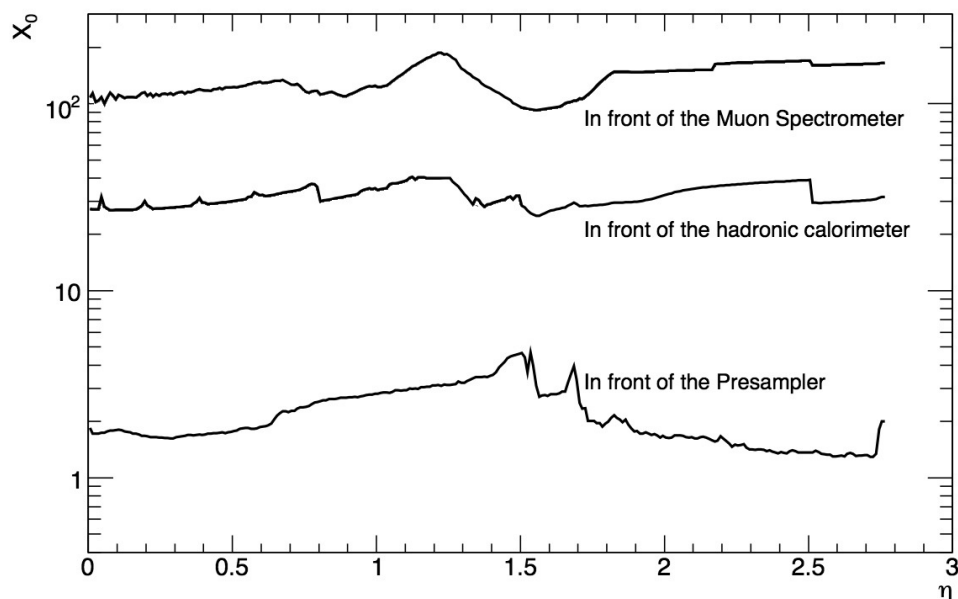
Figure 4.5: Material distribution in front of the ATLAS EM calorimeter (pre-sampler), hadronic calorimeter, and MS as a function of η expressed in radiation lengths X_0 [28].

4.3.1   Ionization and Radiative Losses

Energy loss effects include ionization, bremsstrahlung (radiation of photons), pair production (radiation of virtual photons which convert to e^+e^- pairs), and photonuclear interactions (radiation of virtual photons which directly interact with a nucleus). These mechanisms contribute to both changes in the track trajectory and parameter uncertainties. To take these effects into account, tracking algorithms require that the energy loss be calculated and added back to the track. This requires the use of parametrizations.

At energies up to a few hundred GeV, ionization is the dominant energy loss process for muons, as shown in Figure 4.6 for different materials. Thus, these muons can be treated as minimum ionizing particles whose energy loss dE/dx in Equation 4.2 can be estimated. The expected mean energy loss per unit length x due to ionization is described by the Bethe-Bloch formula [222]:

$$\frac{dE}{dx} = \alpha^2 2\pi N_a \lambda_e^2 \frac{Z m_e}{A\beta^2} \left[\ln \frac{2m_e\beta^2\gamma^2 E_m'}{I^2(Z)} - 2\beta^2 + \frac{E_m'^2}{4E^2} - \delta \right] \tag{4.3}$$

where $\alpha \approx 1/137$ is the fine structure constant, N_a is Avagadro's number, Z and A are the number of protons and mass number of the medium, m and m_e are the rest masses of the muon and electron, $\beta = p/E$, λ_e is the Compton wavelength of an electron, $I(Z)$ is the mean ionization potential of the medium, δ is the density correction [29], and

$$E'_m = 2m_e \frac{p^2}{m_e^2 + m^2 + 2m_e\sqrt{p^2 + m^2}} \tag{4.4}$$

is the maximum energy transferred to the electrons of the medium.

Equation 4.3 only describes the expected mean energy loss due to ionization. However, in reality, ionization loss is a stochastic process with fluctuations around the most probable value (MPV), which can be much different than Equation 4.3. Thus, the Landau [223, 224] MPV (Δ_p^L) is more appropriate to use in estimating the energy loss of muons. Δ_p^L is expressed as:

$$\Delta_p^L = \xi \left[\ln \frac{2mc^2\gamma^2}{I} + \ln \frac{\xi}{I} - \beta^2 - \delta(\beta\gamma) + 0.200 \right] \tag{4.5}$$

where $\xi = 2\pi N_A r_e^2 m_e c^2 (Z/A)(x/\beta^2)$ MeV for a detector of thickness x.

In ATLAS reconstruction, the most probable value and width parameter for the Landau distribution can be parametrized as a function of the material thickness x and muon momentum p_μ with the following function [225]:

$$E_{loss}^{mpv/\sigma}(p_\mu, x) = a_0 x + a_1 x \ln(x/X_0) \tag{4.6}$$

where

$$a_i = b_{i,0} + b_{i,1} \ln B p_\mu + b_{i,2} p_\mu \tag{4.7}$$

with the first term corresponding to ionization, the logarithmic term to the relativistic rise, and the linear term to radiative effects [226]. Figure 4.7 shows E_{loss}^{mpv} as a function of η for a single muon with 10 GeV and 1 TeV traversing the ATLAS detector. The energy loss is propagated to the entrance and exit of the hadronic calorimeters, illustrating that a muon typically loses ~ 3 GeV before reaching the MS stations.

Because Equation 4.6 is most valid in the peak region of the Landau distribution for energy loss, measurements from the calorimeters are also used to describe energy loss in the tails, where the energy deposition is significantly larger than the most probable value [28]. This "hybrid method" is
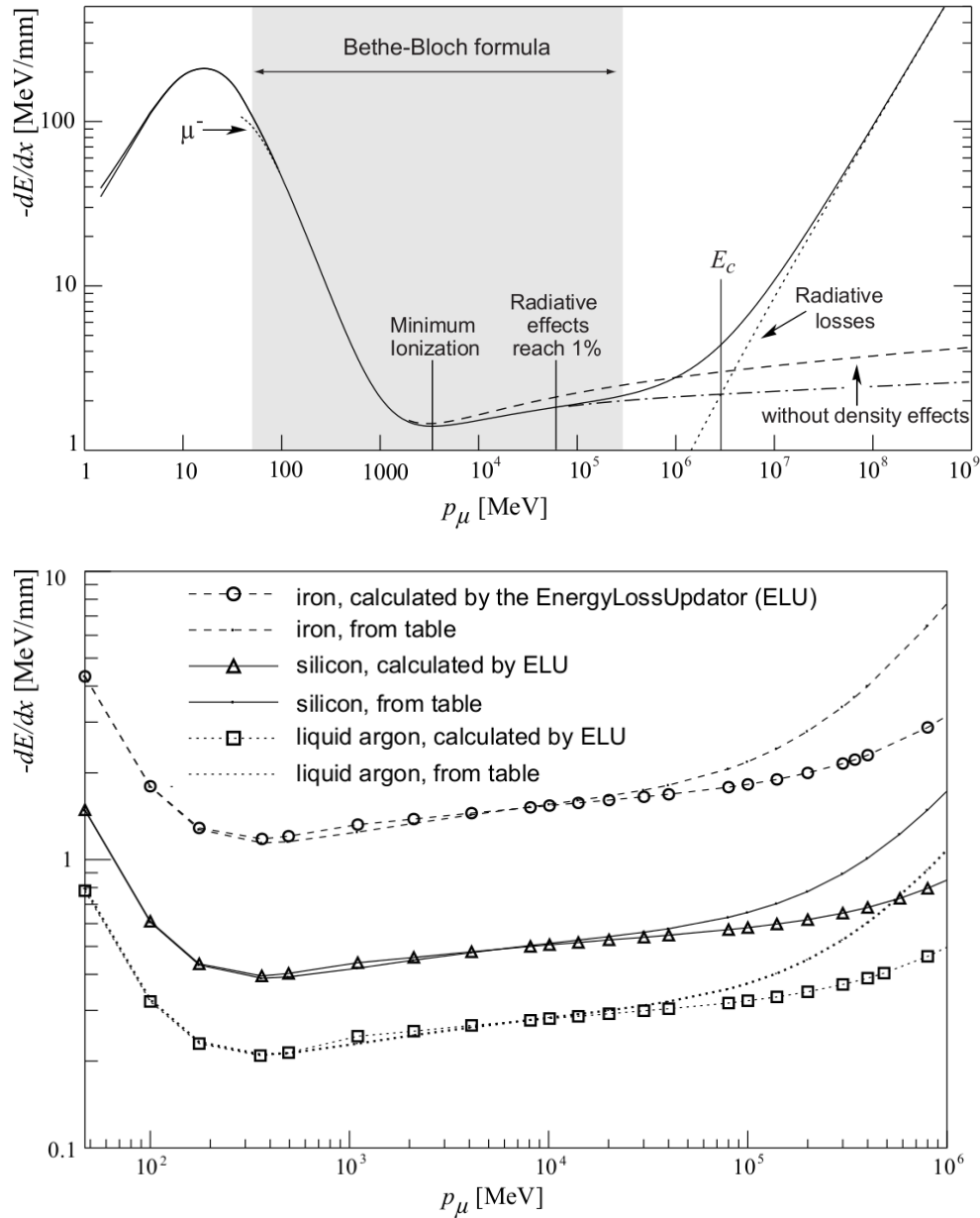
Figure 4.6: (Top) Stopping power ($\langle -dE/dx \rangle$) for muons in copper as a function of momentum $p = M\beta c\gamma$. The solid curve indicates overall stopping power [2]. (Bottom) Mean energy loss for muons in silicon, LAr, and iron from Refs. [29] and [30].
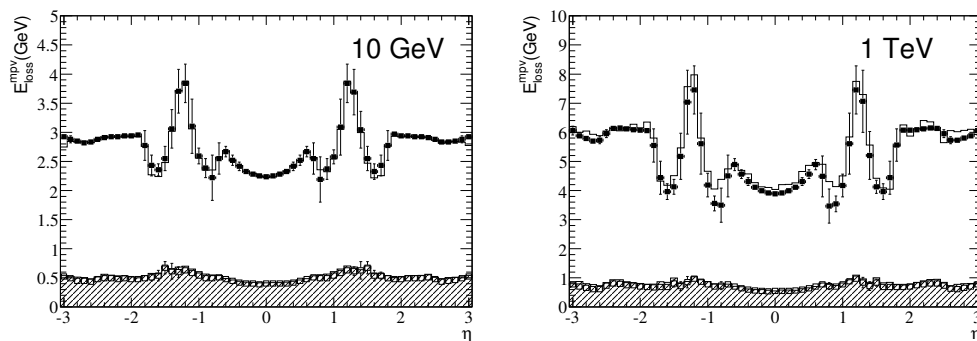
Figure 4.7: Most probable energy loss E_{loss}^{mpv} obtained from the parametrization in Equation 4.6 as a function of η for a muon with (left) 10 GeV and (right) 1 TeV [28]. The shaded histogram is the energy loss propagated to the entrance of the hadronic calorimeters, whereas the non-shaded histogram is propagated to the exit of the hadronic calorimeters.

used in the muon reconstruction algorithms to provide reliable track transport through the detector material.

4.3.2 Multiple (Coulomb) Scattering

A particle traversing material will undergo small deflections in its trajectory caused by multiple (Coulomb) scattering. According to the central limit theorem, it can be assumed that the sum of these small angular variations is Gaussian and symmetric about zero. Large scattering angles cause deviations from a Gaussian and add non-Gaussian tails, however the Gaussian assumption of the probability density function is valid to 98% and is limited to the core of the distribution [30].

Multiple scattering effects for muons are treated using the Highland formula [227], which is an empirical adoption of the Molière solution [228] of the transport equation starting from the classical Rutherford cross-section of a single scattering process. The Highland formula adds an empirical logarithmic correction term to the original Molière expression for the root mean square σ_{ms}^{proj} of the projected scattering angle θ^{proj}, giving larger weight to the screening of the nucleus Coulomb potential in materials with lower Z. This results in the expression of the RMS of the scattering angle:

$$\sigma_{ms}^{proj} = \frac{13.6 \text{ MeV}}{\beta c p_\mu} Z \sqrt{t/X_0}[1 + 0.038 \ln(t/X_0)] \tag{4.8}$$

where t is the pathlength, X_0 the radiation length, and Z and p_μ are the charge and momentum of the incident muon, respectively. Equation 4.8 assumes the magnitude of the momentum does not change. This is valid for muons but not for electrons (see Ref. [30]). Figure 4.8 illustrates an example of a multiple scattering process.
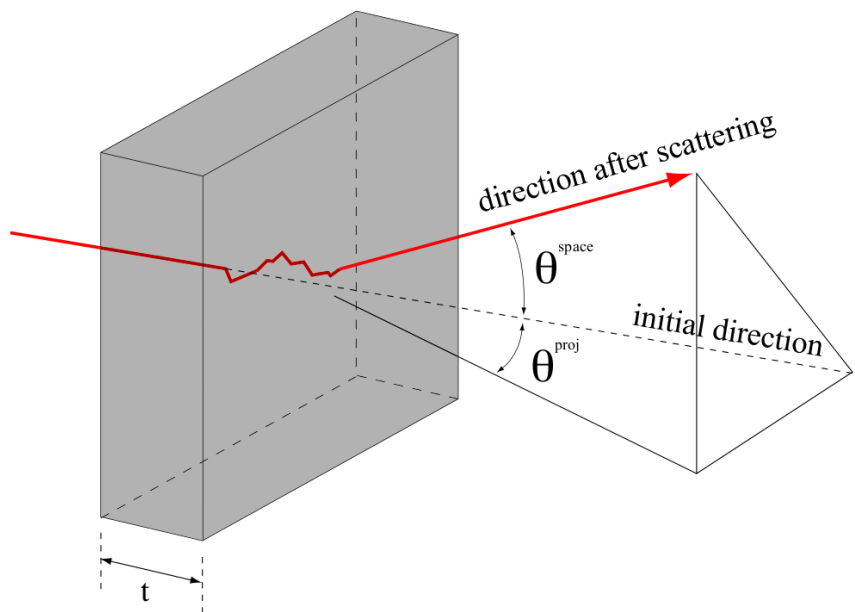
Figure 4.8: Example of a multiple scattering process [30].

4.4   ID Track Reconstruction

ATLAS reconstruction of ID tracks [32] combines the concepts of pattern recognition and track fitting. The reconstruction begins with a global pattern search, followed by local pattern recognition and track fitting. Pattern recognition involves using the reduced output from the global search to select hits along the trajectory of the track. This pattern provides an initial estimate of the track's position, direction, and momentum at each point. The estimate of the track parameters [229] is refined by using the hits from the pattern recognition to perform a track fit. ID track reconstruction

can be performed using an *inside-out* and *outside-in* approach.

The inside-out reconstruction begins with three-dimensional representations (space points) of measurements in the pixel and SCT layers. These serve as seeds for track candidates. The hits in the pixel layer are used to perform a fast primary vertex reconstruction, which further constrains the seeds and allows for three or more hits to be associated with them. The trajectory is then followed through a window of successive silicon hits in the SCT and a global χ^2 [230] fit is performed. The fit yields scattering angle information.

Since the seed search results in a high multiplicity of track candidates, many fake tracks and overlapping segments exist (Figure 4.9). In order to remove ambiguities, track candidates are ranked by their likelihood of describing real trajectories. This is performed by refitting the track candidates using more accurate information of the detector material and assigning a score based on the fit quality. The scoring uses the χ^2 probability, number of measurements, and number of holes[4]. Precision measurements in the pixels are given a larger weight than non-precision measurements in the SCT strips. Track scores exceeding a predefined threshold or χ^2 are rejected.

Track candidates in the silicon layers are then used as seeds to define narrow roads in the TRT (Figure 4.10). A fit combining TRT, SCT, and pixel layer measurements is performed with scoring criteria as described above. Interactions with the detector material are taken into account during the fit. If the TRT extension improves the quality of the fit, the TRT measurements are associated to the track. Otherwise, the original fit is used.

The inside-out approach has limitations, however. For example, photon conversions or bremmstrahlung electrons may not have enough hits in the silicon layers to form seeds. In these cases, an outside-in strategy is employed where seeds from the TRT are back-tracked to silicon hits. In this approach, a global pattern search is conducted to find TRT segments. Tracks with $p_\mathrm{T} > 500$ MeV are treated as straight lines. A Hough transform [231] (discussed below) along with a Kalman-fitter-smoothing procedure [27] is used to find these straight-line patterns. The TRT segments are extrapolated to the silicon layers and a global fit is performed. Ambiguities are resolved as in the inside-out approach, and the track is refit.

Reconstructed tracks are typically expressed as a vector of parameters and their covariance matrices are determined with respect to a reference surface (see Figure 4.11). The reference surface

---

[4]A hole is a sensor passed by a track without a measurement
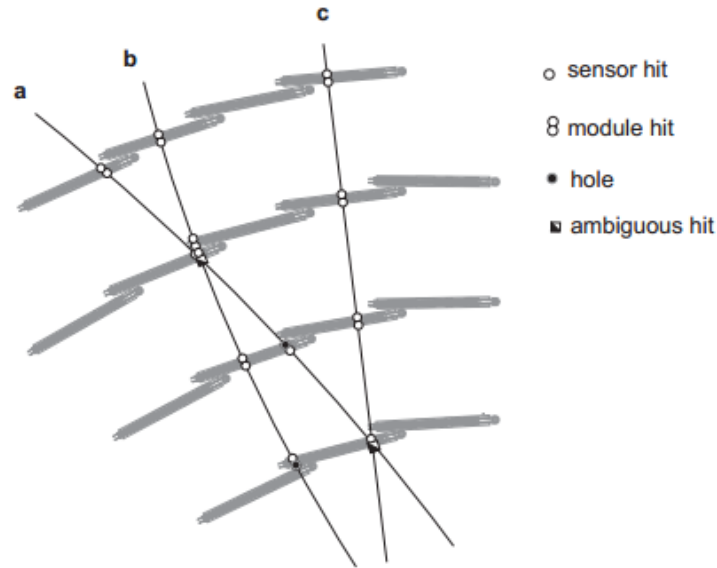
Figure 4.9: Illustration of the track ambiguity-solving process in the SCT. Tracks a, b, and c share several hits [31].

can be a detector element or material layers. The track parameters are expressed at the *perigee* (point of closest approach to the interaction point), as shown in Figure 4.12, and consist of:

- transverse impact paramter d_0

- longitudinal impact parameter z_0

- azimuthal angle ϕ of the track at the IP

- polar angle θ of the track at the IP

- signed ratio of the charge to momentum q/p

4.5 Standalone Muon Tracking

The strategy for reconstructing muons in the MS is comprised of four main steps [232]:
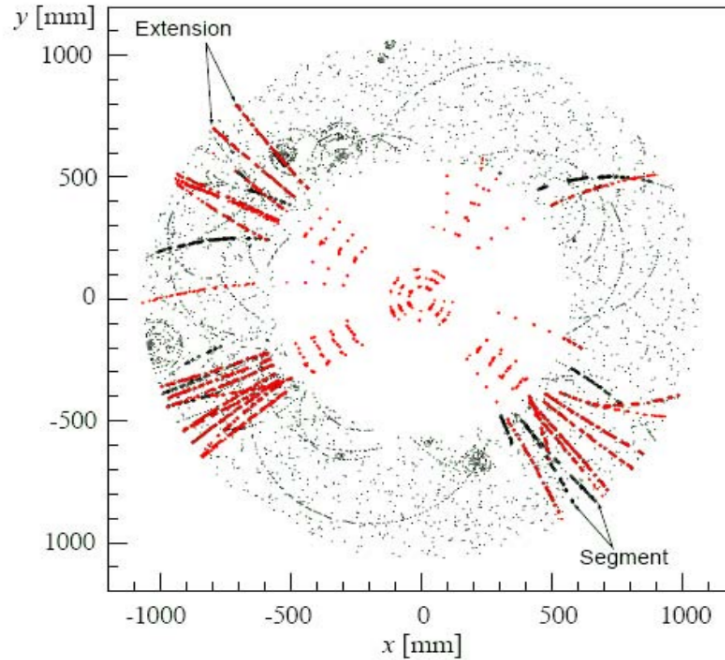
Figure 4.10: Tracks seeds in the silicon layers extending to the TRT (red). Also shown are TRT segments (black) [32].

- The identification of roads and patterns in the muon system starting from hits in the trigger chambers (RPCs/TGCs)

- Reconstruction of local segments within the muon stations of each road

- A combination of segments from different muon stations to form muon candidates using three-dimensional tracking in the magnetic field

- A global track fit of the muon candidate trajectories using the full system and individual hit information

The reconstruction algorithm used by the Muid chain is called `Moore` (Muon Object Oriented REconstruction) [233]. Each step of the algorithm will be described below.
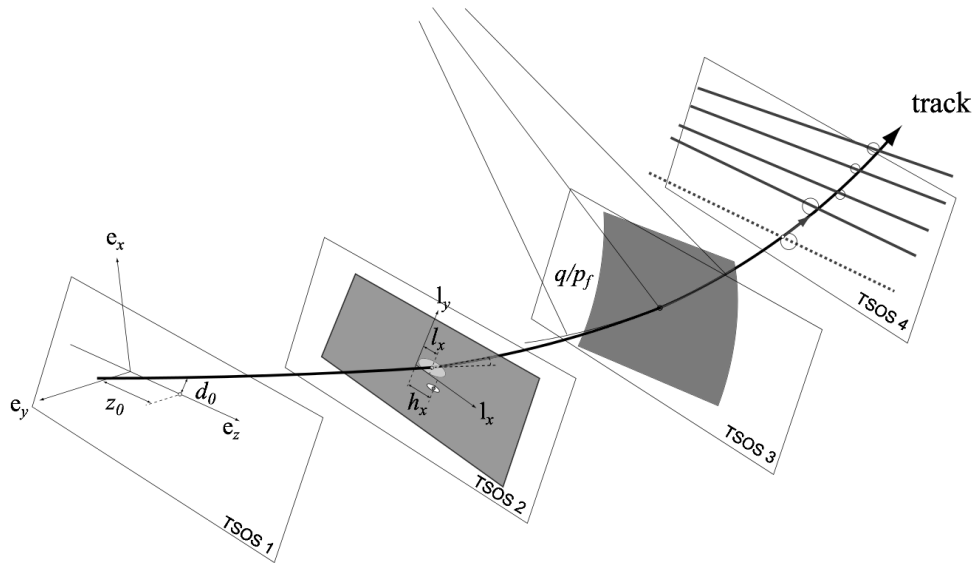
Figure 4.11: Illustration of a track-state-on-surface (TSOS). The state of the track is represented at each surface [33].
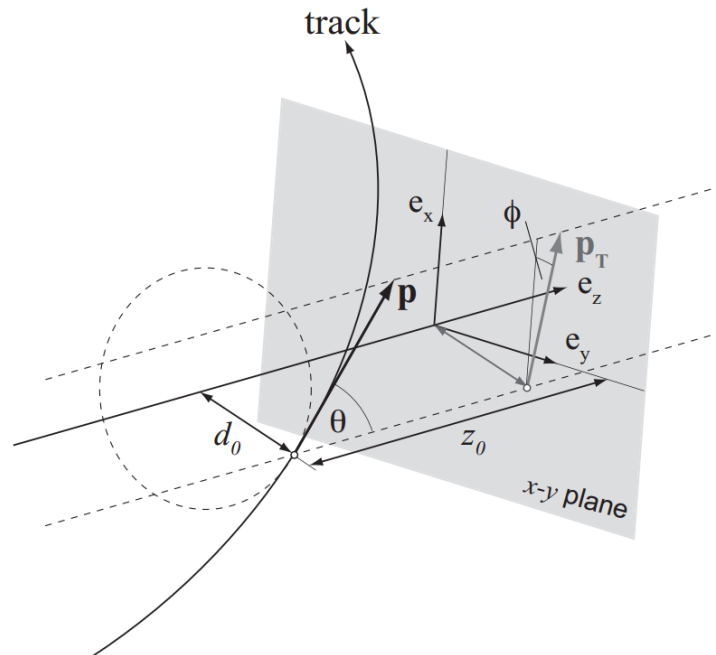
Figure 4.12: The perigee representation in the track parametrization [30].

4.5.1   Pattern Recognition

Pattern recognition in `Moore` begins by searching for hits within roads extending from regions of activity in the trigger chambers. The process is conducted in two steps: two-dimensional searches in the bending $(R - z)$ and non-bending $(x - y)$ planes followed by three-dimensional reconstruction. Roads in the bending plane consist of η patterns in the MDT+CSC/RPC/TGC. Roads in the non-bending plane consist of ϕ patterns from the CSC/RPC/TGC. The η and ϕ patterns are then combined using Hough transforms [231], resulting in a three-dimensional road of hits.

A Hough transform is a technique to identify multidimensional shapes and patterns. As an example, consider the case for finding lines in two-dimensional space. The line may be written as:

$$x \cos \phi + y \sin \phi = r \tag{4.9}$$

which specifies a line perpendicular to the line drawn from the origin to point (r, ϕ) in polar coordinates, as depicted in Figure 4.13.
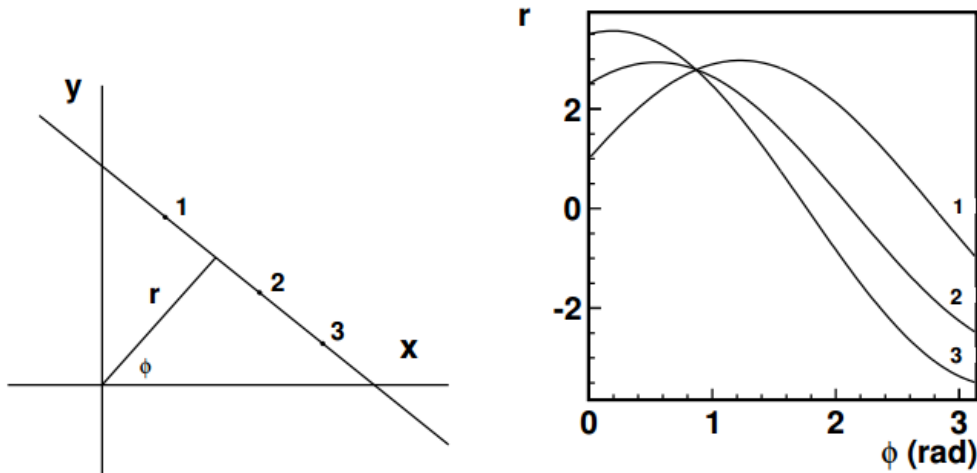
Figure 4.13: (Left) Normal form of a two-dimensional line. (Right) Representation of points 1, 2, and 3 in Hough space. The intersection represents the original two-dimensional line [34].

However, an infinite number of lines may be drawn through a point (x, y), resulting in an infinite number of corresponding perpendicular lines with polar coordinates (r, ϕ). Therefore, every point (x, y) in Equation 4.9 describes a curve in (r, ϕ) space, which is called Hough space. Figure 4.13

shows points 1, 2, and 3 in Hough space where the intersection of the curves represents the original two-dimensional line.

In practice, the intersecting points are found by binning the Hough space into a Hough histogram and locating the maxima (Figure 4.14). Any trajectory can be found using the appropriate transformation. In general, a Hough transform is a function f_H that transforms points in $\mathbb{R}^n$ to Hough space H:

$$f_H : \mathbb{R}^n \to H \tag{4.10}$$

For pattern recognition in the MS, a straight-line $R - \phi$ transformation is used for finding patterns in the non-bending $(x - y)$ plane. A curved $R - \theta$ transformation is used to find patterns in the bending $(R - z)$ plane of the barrel and inner part of the end-caps, and a straight-line $R - \theta$ transformation is used to find hit patterns in the bending $(R - z)$ plane of the outer end-caps. Figure 4.15 shows the regions in the bending plane where these transformations are performed. The combined patterns provide an initial estimate of the position and direction of the muon candidate track. Refs. [34] and [35] provide more details on this procedure.
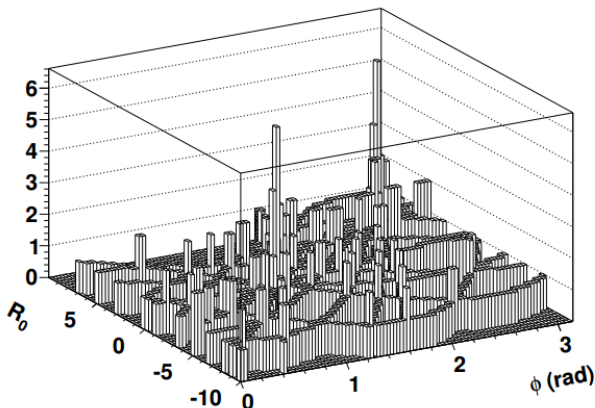
Figure 4.14: Representation of a Hough histogram. Maxima correspond to intersection points in Hough space [34].
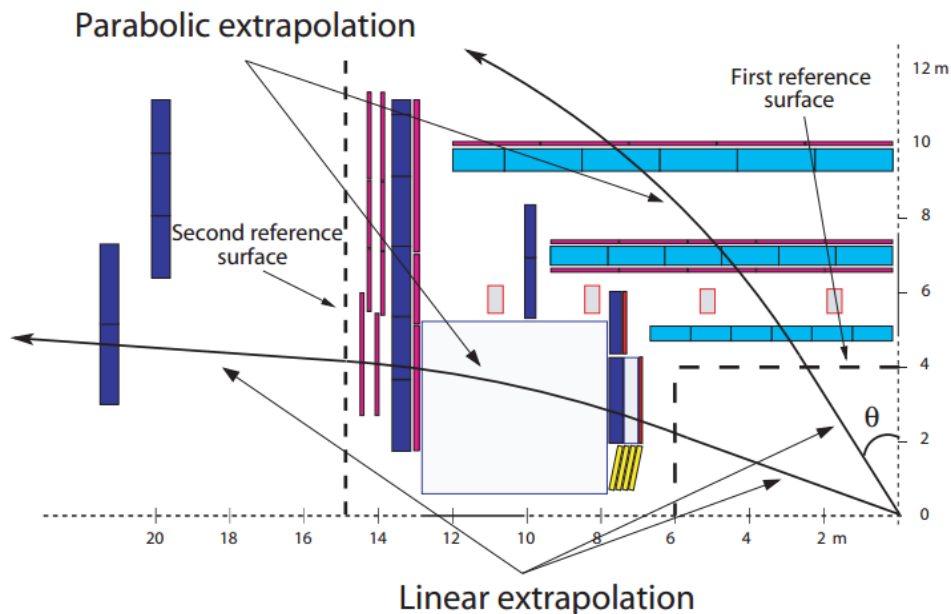
Figure 4.15: Regions in the bending $(R - z)$ plane where different Hough transformations are performed [34].

4.5.2   Segment Finding

A muon segment is defined as a locally reconstructed three-dimensional track segment within a muon station. The `Moore` algorithm searches for segments in both the CSCs and MDTs. Segments in the CSCs are locally reconstructed using clusters formed by fitting the charge depositions on the η and ϕ strips within a chamber. The η and ϕ clusters are fitted independently, resulting in η and ϕ segments. The segments from each of the four CSC layers are then combined to form three-dimensional segments and to provide information on the position and direction of the muon candidate.

Segments in the MDT chambers are located within roads given by the Hough transformations. The search is conducted in the $y - z$ (precision) plane, and the algorithm uses MDT hits together with hits in the trigger chambers as inputs to the segment finding. The MDT hits form pairs in each chamber multilayer. For each pair, tangent lines to the drift circles are used as seeds for segment finding, as shown in Figure 4.16. Hits in the chamber are associated to the seed lines to form segment candidates (Figure 4.17). At least three hits-on-track are required for a segment

(Figure 4.18), where a hit-on-track is defined as a sufficiently small difference (1.5 mm) between the measured and predicted drift radius. The algorithm also checks for the following scenarios: δ-electrons[5] passing closer to the wire than the muon, resulting in a drift radius too small; out-of-time hits that result in unphysical drift times that are too large; and empty tubes crossed but without a hit (i.e. holes). A cut on the sum of the number of empty crossed-tubes N_{empty}, the number of δ-electrons N_δ, and the number of out-of-time hits N_{out} is used to reject fake segments.
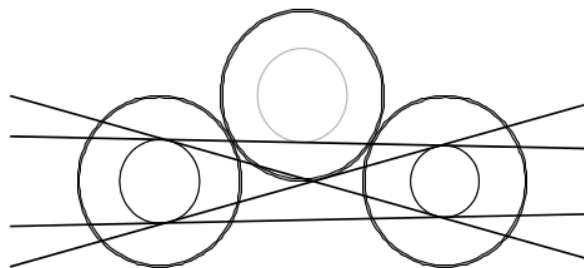
Figure 4.16: Drift circle seeds with possible tangets (lines) [35].
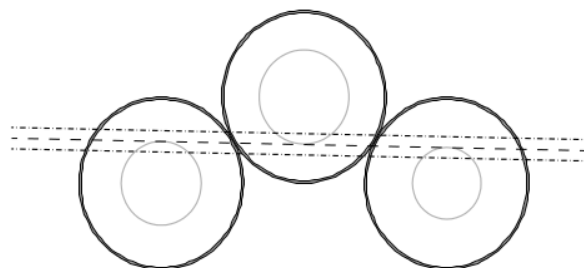
Figure 4.17: Road formed from hits associated to seed lines [35].

Segment candidates which pass these criteria are fit to a straight line. The fit minimizes:

$$\chi^2 = \sum_{i=1}^{n} \frac{(\Delta_i - r_i)^2}{\sigma_i^2} \tag{4.11}$$

where Δ_i is the distance between the track and the anode wire, r_i is the drift radius, and σ_i is the error [35]. Hits are dropped if the χ^2 is larger than ten and the fit is reperformed. If the number of

---

[5]δ-electrons are energetic electrons resulting from ionization by the passing muon
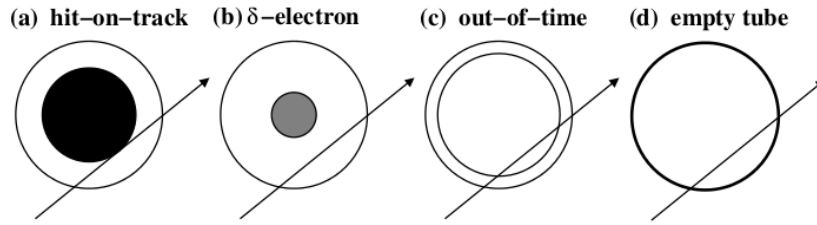
Figure 4.18: Schematic of four different classifications for MDT hits: a) hit-on-track b) δ-electron c) out-of-time d) tube crossed by the seed line but no hit [35].

hits-on-track drops below three, the segment is rejected. Otherwise, the fit is performed until the $\chi^2 < 10$.

The algorithm then improves the quality of the segment by matching with TGC/RPC hits in the viscinity of the MDT chamber. An example of a segment reconstructed in the BML chamber with seven MDT hits associated with five RPC η-hits is shown in Figure 4.19. Ambiguities are resolved by sorting the segments based on the following priority list: (1) most hits-on-track (2) smallest $N_\delta + N_{out} + N_{empty}$ (3) most trigger hits (4) smallest χ^2. Segments that share hits with higher-ranked segments are removed. In the final step of the segment search, the ϕ coordinate is recalculated. The segment is refitted in three dimensions if it can be associated with at least two trigger hits. If only one hit in the trigger chambers is available, ϕ and position information in the non-bending plane are calculated by extrapolating the segment back to the interaction point.

4.5.3 Track Finding

The final step in SA muon reconstruction is track finding. The track-finding algorithm proceeds according to the following steps:

- Selection of seed segments

- Track building

- Track fitting

- Hit recover and final fit
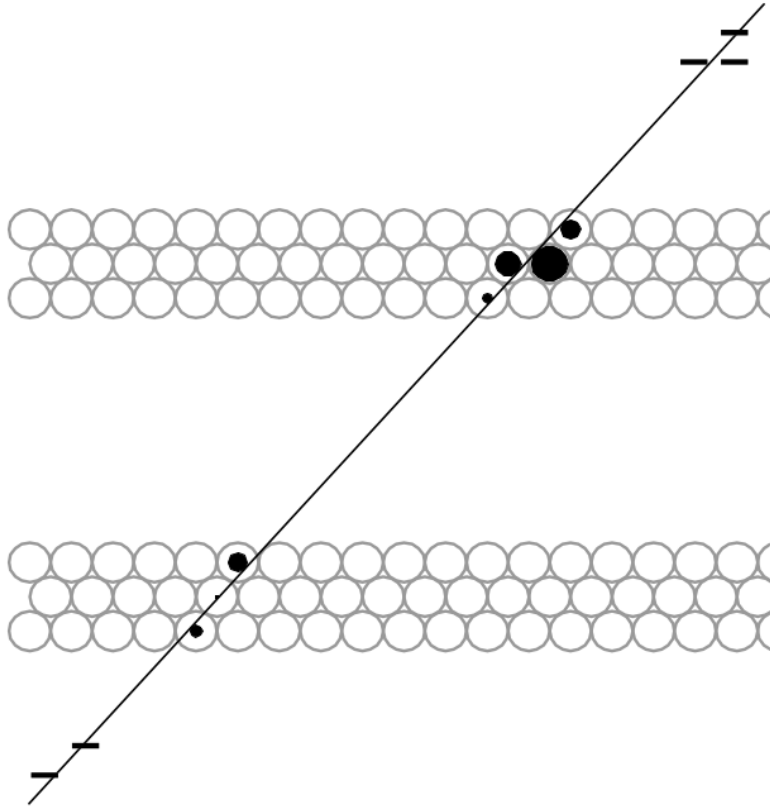
Figure 4.19: A muon segment reconstructed in the BML. The segment has seven MDT hits (filled circles) and five RPC hits (rectangles) [35].

- Hole searching

- Ambiguity solving

A *muon track candidate* is a set of MS segments compatible with a curved trajectory. Segments in a road are categorized by station layer and are sorted by quality. Segments that pass the criteria discussed above and that are not already part of a track are used as seeds. The seed segments are combined with segments in another station layer. This begins with a loose matching procedure that compares the positions and angles of the segments from each station in the bending $(R - z)$ plane. Poor combinations are rejected. If the match succeeds, a fit is performed and used to compare the momenta of the segments at each station, further rejecting poor segment combinations. Segments that are successfully fit are considered muon candidates. The candidates are then matched with

segments in all other stations to form full tracks. The track segments are fit using the same global χ^2 method as is used in ID track reconstruction [230].

In the final stage of muon track finding, unassociated hits in layers crossed by the track are added to the track. Holes (tubes passed by a track but without a measurement) are located along the track trajectory. Ambiguities are resolved by removing duplicate tracks, overlapping tracks, or tracks that share hits with higher quality tracks. A refit is then performed, and if the refit fails, the track is rejected. Accepted tracks are extrapolated to the beam line and the muon parameters are evaluated at the perigee, as depicted in Figure 4.20. The extrapolation corrects for energy loss and multiple scattering in the detector material (Sec. 4.3). Muon track parameters are available at three points: the entrance to the MS, the entrance to the calorimeter, and the perigee.

4.6 Combined Muon Reconstruction

The previous sections have described tracking in the ATLAS ID and MS. This section will discuss how these measurements are combined using the `Muid Combined` algorithm. As previously mentioned, standalone muons are extrapolated to the perigee. This process involves having a good description of material effects on the muon trajectory and introduces a source of uncertainty. Uncertainties are reduced and the track parameters are improved by matching measurements in the MS with those in the ID.

The method by which the combined track parameters are obtained differs in the `Staco` (Appendix A) and `Muid` algorithms. In brief, `Staco` uses a statistical combination of the corresponding covariance matrices of the ID and MS tracks to calculate combined track parameters. `Muid` performs a global refit of the muon track using hits in the ID and MS.

The `Muid` algorithm begins by matching the `Moore` tracks with ID tracks using a match χ^2. The match χ^2 is defined as the difference between the MS and ID track vectors, weighted by their combined covariance matrix:

$$\chi^2_{match} = (\mathbf{T}_{MS} - \mathbf{T}_{ID})^{\mathrm{T}}(\mathbf{C}_{ID} + \mathbf{C}_{MS})^{-1}(\mathbf{T}_{MS} - \mathbf{T}_{ID}) \tag{4.12}$$

where $\mathbf{T}_{ID(MS)}$ denotes the vector of five track parameters expressed at the perigee and $\mathbf{C}_{ID(MS)}$ are the covariance matrices from the ID and SA track fits.
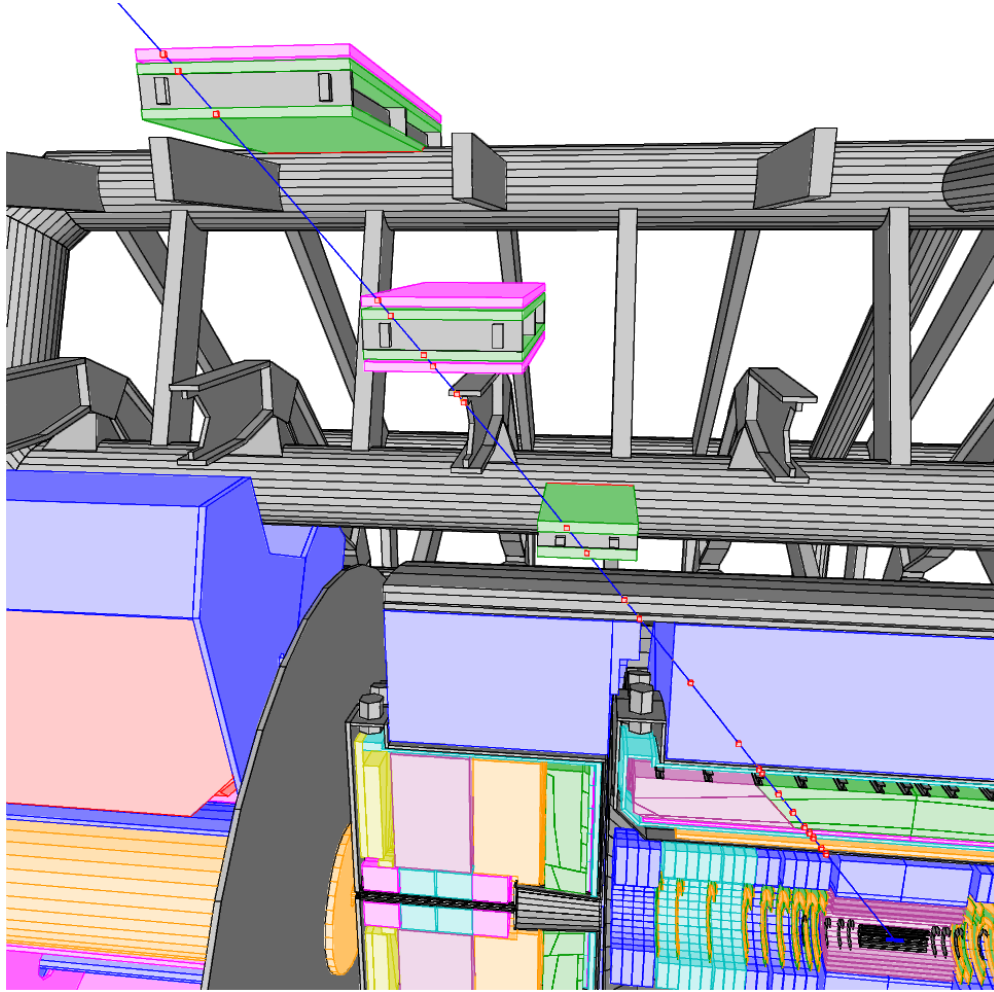
Figure 4.20: Event display of a muon extrapolated to the interaction point. The track is shown crossing three MDT stations.

For matches with a χ^2 probability above 0.001, a combined fit is performed. The fit uses ID tracks as seeds and iteratively adds measurements from the MS. During the combined fit, interactions with the calorimeter are taken into account by five additional track parameters: η and ϕ measurements at two scattering centers and an energy loss parameter. The energy loss is estimated from the observed calorimeter energy deposition or from Equation 4.6. The combined fit is performed until the χ^2 is below a given value. If this criterion cannot be satisfied, the fit is attempted within a road around the SA track. All matches that give a satisfactory combined fit are classified as combined muons. Figure 4.21 provides an event display of two combined muons

from a $H \to ZZ^* \to ee\mu\mu$ simulated event.
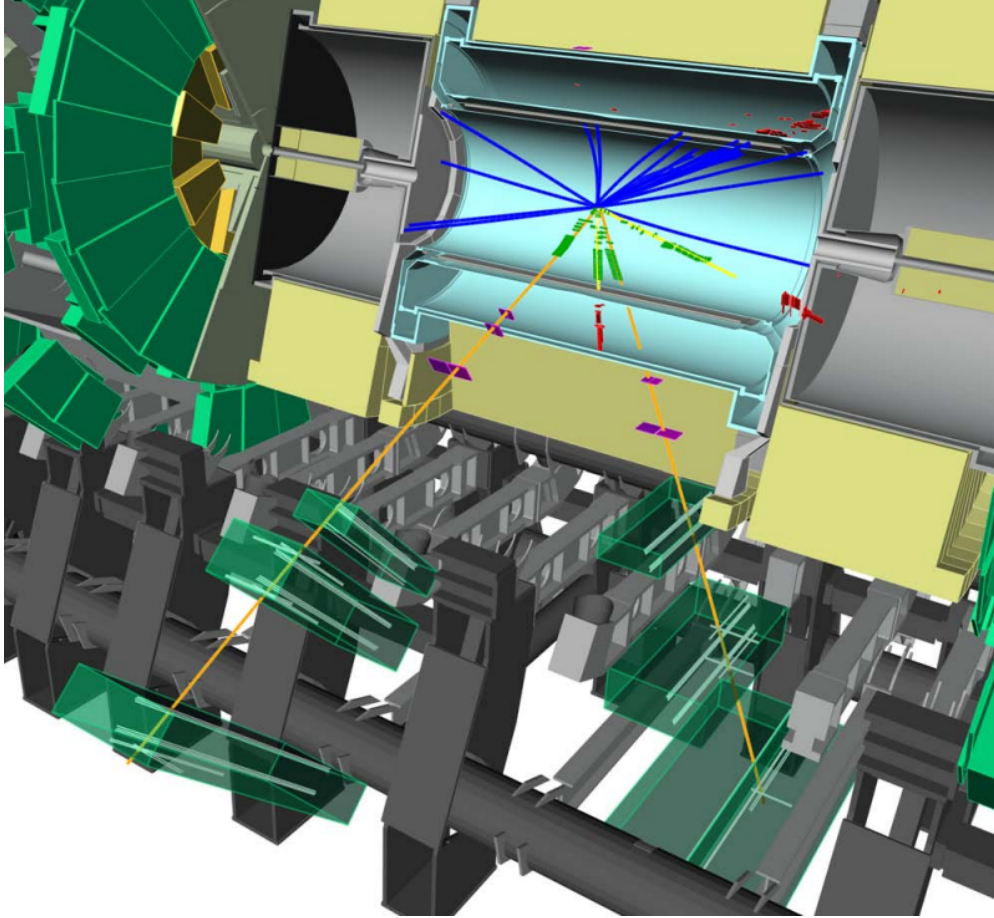
Figure 4.21: Event display of $H \to ZZ^* \to ee\mu\mu$ after full reconstruction. The two combined muons are shown as the orange tracks traversing the MDT and ID layers. The energy lost in the tile calorimeter is also shown in purple [28].

4.7 Segment-Tagging

Segment-tagging uses ID tracks as seeds to search for muon segments in the MS stations (see Figure 4.22). Extrapolation to the MS results in a prediction of where the ID track would be located under the hypothesis that it is a muon. Since a muon typically loses ~ 3 GeV in the calorimeters, tracks with momentum less than this are not extrapolated.

Tagged muons complement combined muons in regions where the MS has poor coverage. This is particularly useful in the barrel-to-end-cap transition region ($|\eta| \approx 1.05$) and the gap region ($\eta \approx 0$). Tagging also recovers low-p_T muons that do not traverse all three layers of the MS stations. In comparison to the other muon reconstruction strategies, segment-tagging does not require fully reconstructed tracks in the MS.

The segment-tagging algorithms in the Muid family are called `MuGirl` [234] and `MuTagIMO` [33]. `MuGirl` extrapolates the ID track to the entrance of the MS. Hits are collected within a narrow road around the extrapolated trajectory and are used to create segments in the inner, middle, and outer layers of the MS. The algorithm uses an artificial neural network (ANN) to define a muon discriminant [235]. If the ANN determines the track is a muon, a full track refit is performed. If the refit is successful, a `MuGirl` muon becomes a `Muid Combined` muon. Otherwise, a segment-tagged muon is made.

`MuTagIMO` extrapolates ID tracks to surfaces corresponding to positions in the inner, middle, and outer layers of the MS. The algorithm searches for nearby `Moore` segments by performing a loose matching between η and ϕ of the track and segment parameters, as shown in Figure 4.23. Ambiguities (e.g. multiple segments in the same muon station associated with the same ID track) are resolved by segment cleaning, track cleaning, and final cuts on the track and segment. The best MS segment will have the smallest distance to the extrapolated track. Multiple ID tracks sharing MS segments are resolved by using the likelihood that the track is a muon. Non-muon background is reduced by requiring at least one associated MDT segment and a cut on the number of MDT holes. In addition, since non-muon background generally has lower momenta, a cut on the p_T is also applied to improve the quality of the match.
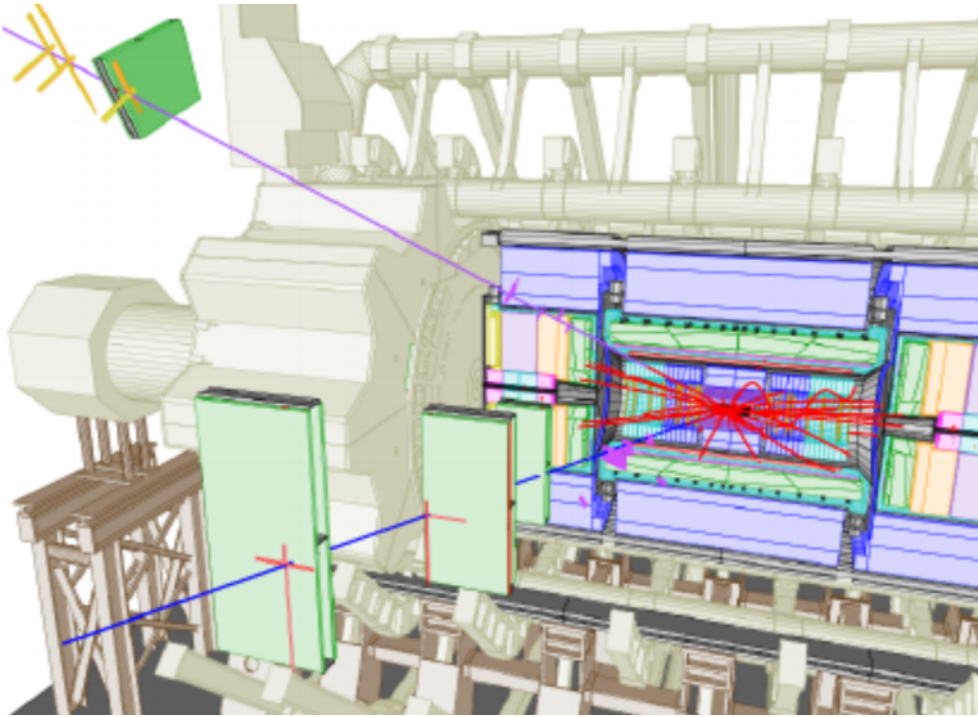
Figure 4.22: Example of a segment-tagged muon. The ID seed is shown in red and the extrapolation to the MS in purple. MS segments are in orange. Also shown is a standalone muon (blue).
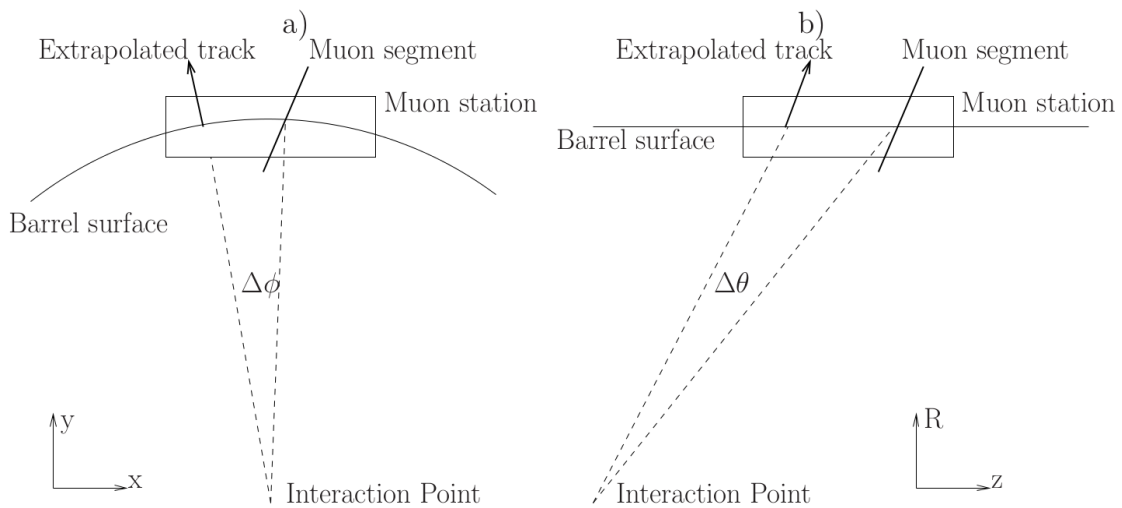
Figure 4.23: Schematic of η and ϕ matching of ID tracks to MS segments in the barrel non-bending (left) and bending (right) planes [33].

Chapter 5

Data Analysis

This chapter details the analysis chain for measuring $W \rightarrow \mu\nu_\mu$ events in heavy-ion collisions. The first section discusses the different datasets used and the global event selection requirements. The next section provides a discussion on the muon selection requirements and includes a description of each cut applied in the analysis. This is followed by an explanation of the background estimation procedure for different background sources. The next sections introduce the muon efficiencies and correction factors. The chapter concludes with a discussion on the systematic uncertainties.

5.1 Datasets

5.1.1 Data Samples

The data used in the measurements presented in this work were collected during the 2011 heavy-ion run period from November to December 2011 at a center-of-mass energy $\sqrt{s_{\mathrm{NN}}}$=2.76 TeV. During the run, luminosity blocks with stable operating conditions in the ID, calorimeters, and MS were used to construct a "Good Run List" (GRL). Table 5.1 presents the run numbers from the GRL and the corresponding luminosities. The run numbers range from 193211 to 194382. The cumulative integrated luminosity and peak luminosity per day during the run period are presented in Figure 5.1.

During data collection, the triggers were segmented into four streams in order to enrich the data samples with pertinent physics information and facilitate end-user analysis. These streams include:
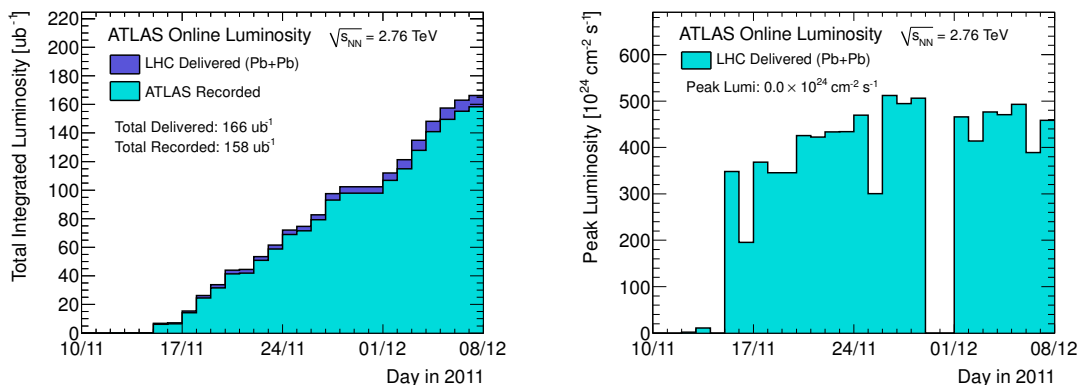
Figure 5.1: (Left) Cumulative integrated luminosity (before GRL selection) as a function of day in the November/December 2011 Pb+Pb run period. (Right) Peak instantaneous luminosity during the same time period.

- A *Hard Probes* (HP) stream containing events associated with high-p_T jets, photons, electrons, and muons. This stream contains 54M events after GRL selection and is the primary stream used in this work.

- A *Minimum Bias* (MB) stream that collected events over a range of multiplicities and physics processes. This stream was prescaled in order to allow sufficient bandwidth for the other streams. The average prescale factor during the run period was 15.6, resulting in 68.7M MB events. For this thesis, the MB stream is used for performance studies, efficiency calculations, and the centrality determination.

- An *Ultra Peripheral* stream that recorded information from peripheral Pb+Pb collisions. This stream consists of 7.3M events and is not used in this work.

- An *Overlay* stream containing MB events for embedding data into simulated samples. Embedding real data into simulation allows for better modeling of the actual heavy-ion environment. This stream contains 3M events and will be referred to hereafter as "data overlay."

Each stream used various triggers. In the MB stream, two complementary triggers were used: `EF_L1TE50_NoAlg` and `EF_mbZdc_a_c_L1VTE50_trk`. TE represents the total transverse energy E_T of the event as measured in the calorimeters. `L1TE50` implies that the $E_T > 50$ GeV, whereas `L1VTE50`

Table 5.1: Summary of run number and integrated luminosity for runs from the GRL.

Index	Run	$L_{int}(\mu\mathrm{b}^{-1})$	Index	Run	$L_{int}(\mu\mathrm{b}^{-1})$
1	193211	0.014	23	193687	0.043
2	193270	0.126	24	193718	5.299
3	193291	1.286	25	193795	5.303
4	193295	0.083	26	193823	0.757
5	193321	3.949	27	193825	5.985
6	193403	2.766	28	193826	5.152
7	193412	3.607	29	193834	6.578
8	193447	3.809	30	193890	1.751
9	193463	4.117	31	194017	5.438
10	193481	4.886	32	194060	3.139
11	193491	2.505	33	194061	5.150
12	193492	0.062	34	194121	4.908
13	193493	0.969	35	194160	2.522
14	193494	0.582	36	194163	6.453
15	193546	5.428	37	194179	3.600
16	193558	4.202	38	194192	5.338
17	193599	0.385	39	194193	6.168
18	193604	5.504	40	194370	1.774
19	193641	3.160	41	194374	0.923
20	193655	4.200	42	194382	2.077
21	193662	5.244			
22	193679	5.308			

("V" stands for "veto") means that the event $E_\mathrm{T} < 50$ GeV. This trigger combination was used to sample events over the entire multiplicity spectrum. `mbZdc_a_c` is a coincidence trigger requirement in which at least one neutron is required in both the A and C sides of the ZDC. This reduces

photonuclear [1] [236] background events, which are typically asymmetric and occur in events with impact parameter $b > 2R$, where R is the nuclear radius. The suffix `NoAlg` implies that no further event processing is performed from L1 to the HLT, and the `trk` suffix signifies that the online tracking is used to search for tracks within the triggered event.

During the run, high-p_T muon triggers in the HP stream were used to construct samples with a high concentration of $W \rightarrow \mu\nu_\mu$ events. Since the muon has $\langle p_T \rangle \approx \frac{1}{2}m_W = 40.183$ GeV, events were required to contain at least one muon with $p_T > 10$ GeV. This selection used the following set of muon triggers: `EF_mu10_MSonly_EFFS_L1ZDC`, `EF_mu10_MSonly_EFFS_L1TE10`, and `EF_mu10_MSonly_EFFS_L1TE20`. `L1ZDC` and `L1TE50` have the same meaning and serve the same purpose as for the MB triggers. The integer number after "`mu`" indicates the lower muon p_T threshold (in this case, 10 GeV). `EFFS` stands for "event filter full scan" and signifies that rather than starting reconstruction from Regions of Interest (RoI) determined at previous trigger levels ("seeded mode"), the EF uses the entire MS to perform full event reconstruction ("full-scan mode"). The full-scan method allows the EF to locate additional muons missed at the previous levels and is less affected by the coverage deficiencies in the muon barrel region (e.g. gap region, feet structures). `MSonly` implies that the trigger decision is based only on MS reconstruction rather than on a combination with ID information [237, 238].

5.1.2 Simulated Samples

Simulated event samples are used for efficiency studies, background estimations, and model comparisons. The samples were generated using the Monte Carlo (MC) method (see Refs. [235],[239]), which is a numerical technique for providing the probability density functions (pdfs) of functions of random variables. The MC method is performed in two stages: event generation and detector simulation. The *event generator* can predict and use the probability (i.e. cross section) of an event to simulate the sequence of hard scattering processes to final-state particle production. In this work, two event generators are used: `POWHEG` [240] and `PYTHIA` [241]. In brief, `PYTHIA` is a general-purpose, standalone event generator capable of running with LO and NLO parton distribution functions (PDFs). Moreover, `PYTHIA` can be interfaced with any external program that generates

---

[1]These are events in which photons are exchanged between the nuclei, typically resulting in the production of a vector meson. The number of photons scale with Z^2.

a Les Houches Event file [242]. The `POWHEG` algorithm implements a matrix element reweighting procedure in the cross-section calculation and is used to interface NLO calculations with parton shower generators (e.g. `PYTHIA`) [243, 244].

Final-state particles produced from the event generation step are interfaced with detector simulation. The detector response in ATLAS is simulated using the GEANT4 simulation toolkit [245]. This software emulates the digitization, reconstruction, and geometric configuration (e.g. alignment) that exists during actual data-taking conditions. The detector response in all the simulated samples used in this work are modeled using GEANT4. Table 5.2 summarizes the simulated datasets.

Table 5.2: Summary of signal and background MC samples used in this work. $W \to \mu\nu_\mu$, $W \to \tau\nu_\tau$, and Jxμ are embedded into MB events (i.e. data-overlaid). $Z \to \mu\mu$ are embedded into HIJING (see text). $\hat{p}_T$ represents the average p_T of the outgoing partons involved in the hard scattering process before initial-state or final-station radiative corrections.

Process	Generator	PDF Set	$\sigma_X \times$ B.R. (nb)	N_{ev}
$W \to \mu\nu_\mu$	`POWHEG+PYTHIA8`	CT10		
	pp		3.354	130K($\times$2)
	pn		3.320	205K($\times$2)
	np		3.320	205K($\times$2)
	nn		3.345	315K($\times$2)
Jxμ	`PYTHIA6`	MRST LO*		
	J1μ ($17 < \hat{p}_T < 35$ GeV)		1.877×10^5	1M
	J2μ ($35 < \hat{p}_T < 70$ GeV)		8.279×10^3	1M
	J3μ ($70 < \hat{p}_T < 140$ GeV)		2.943×10^2	1M
$Z \to \mu\mu$	`PYTHIA6+HIJING`	MRST LO*	0.2629	1.1M
$W \to \tau\nu_\tau$	`PYTHIA6`	MRST LO*	2.817	1M

A description of the signal and background samples is provided below:

- $W \to \mu\nu_\mu$ events are generated at NLO using `POWHEG` with parton showering provided by `PYTHIA8`. CT10 [246] is used as the PDF set. Simulated events are embedded into MB data

from the data-overlay stream. To take into account isospin effects on physical observables – particularly η – the sample includes all nucleon combinations and is weighted according to the relative number of nn, $pn(np)$, and pp interactions in a Pb+Pb collision:

$$\frac{1}{A^2} \cdot (Z^2 + 2Z(A - Z) + (A - Z)^2) \tag{5.1}$$

where A is the mass number and Z the atomic number. In Pb, $A = 208$ and $Z = 82$. This corresponds to a collision rate of 15.5% for pp, 47.8% for $pn+np$, and 36.7% for nn. The di-jet and $Z \to \mu^+\mu^-$ background processes described below are insensitive to the isospin of the nucleus, and thus this weighting procedure is not performed on these samples. The charged current interaction mediating the process $\tau \to \mu\nu\bar{\nu}$ follows the $V - A$ structure [247], and thus this sample is sensitive to isospin effects. However, rather than performing the reweighting, a charge inclusive sample is used in the background estimation. This may result in a slight overestimation of the background in particular pseudorapidity intervals, however this is the smallest background source and the effects from not reweighting are expected to be negligible.

- $Jx\mu$ events are defined as a di-jet event in coincidence with a muon. The muons are primarily from b and c decays within the jet and constitute a major portion of the total background. The integer number x in Jx indicates the range of $\hat{p_T}$ used in the generation, where $\hat{p_T}$ represents the average p_T of the outgoing partons in the hard scattering process. These ranges are presented in Table 5.2. Generating each range separately maximizes the statistics in each region of phase space. The $Jx\mu$ samples are generated with `PYTHIA6` and are embedded into MB events from the data-overlay stream. The generation uses the MRST LO* [248] PDF set, which is a modified version of the LO PDF set in that it uses a NLO definition of the coupling α_S.

- $Z \to \mu^+\mu^-$ events are also a significant background source. These events are simulated using the MRST LO* PDF set with `PYTHIA6`. $Z \to \mu^+\mu^-$ events are embedded into `HIJING` (Heavy Ion Jet INteration Generator) [249] since the overlay stream was unavailable at the time of production. HIJING emulates a heavy-ion environment by modeling initial-state interactions, multi-jet production with associated semihard and soft background enhancement, impact

parameter dependence of inelastic processes, nuclear shadowing, and jet energy loss in a nuclear medium.

- $W \to \tau\nu_\tau$ events are the smallest, yet non-negligible, background source. The background stems from the tau decay mode: $W \to \tau\nu_\tau \to \mu\nu_\mu\nu_\tau\nu_\tau$. These events are generated using the MRST LO* PDF set with `PYTHIA6` and are embedded into MB events from the overlay stream.

5.2 Event Selection

Collision events within the GRL are required to satisfy specific selection criteria. These include:

- A hit on both the A and C sides of the MBTS (see Section 3.8) with a timing coincidence that satisfies $|\Delta t_{MBTS}| < 3$ ns. This reduces background from out-of-time pile-up events.

- At least 3 reconstructed tracks with $p_T > 500$ MeV associated with the primary vertex. The tracks are required to fulfill heavy-ion track selection requirements [250]:

  - $|\eta_{trk}| < 2.5$
  - A minimum number of hits in the pixel and SCT layers ($N_{pixel} \geq 2$, $N_{SCT} \geq 8$, 1 hit in the innermost pixel layer (B-layer))
  - A B-Layer measurement if expected from the interpolated track trajectory (i.e. $N_{B-LayerHitsExpected} = 0$ or $N_{B-LayerHits} = 1$)
  - No holes in the pixel layer and no more than 1 SCT hole if hits are expected from the interpolated track trajectory
  - Transverse and longitudinal impact parameter requirements: $|d_0|, |z_0 \sin\theta| < 1$ mm (see Figure 4.12)

- A trigger selection that depends on the sample (Section 5.1.1):

  - At least one muon with $p_T > 10$ GeV (Hard Probes)
  - An event with $E_T > 50$ GeV or $E_T < 50$ GeV with a coincidence in the ZDCs (Minimum Bias)

The event selection samples $(98 \pm 2)\%$ [251] of the total inelastic cross section. After correcting for the prescale (Section 5.1.1), 1.03×10^9 minimum bias Pb+Pb events (hereafter denoted as N_{events}) are sampled, corresponding to an integrated luminosity of approximately 0.14 nb^{-1}.

5.3 Centrality Determination in ATLAS

The centrality definition and its relation to the Glauber model was discussed in Section 2.8.2. In that section, the general method by which measurable quantities are mapped to Glauber parameters was discussed. This section will describe how the centrality is determined in ATLAS specifically.

In ATLAS, the centrality is determined from the total transverse energy measured in the FCal ΣE_T^{FCal}. Since the detector is located at very forward pseudorapidity ($3.2 < |\eta| < 4.9$), there is less risk of centrality-dependent processes biasing the measurement. Furthermore, ΣE_T^{FCal} is strongly correlated with the total energy deposited in the calorimeters at $|\eta| < 3.2$ (See Figure 5.2) and thus serves as an excellent indicator of global event activity.
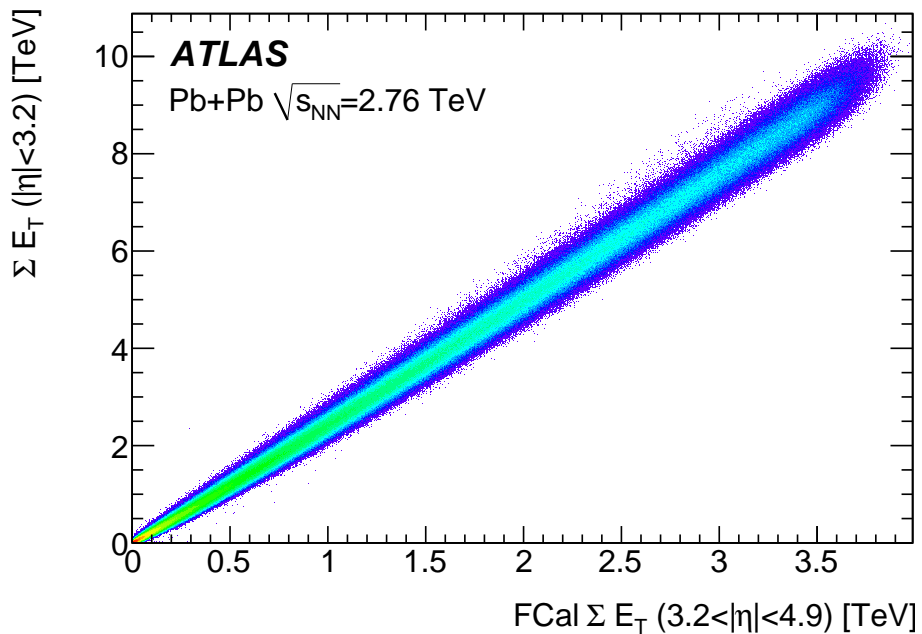
Figure 5.2: Correlation between the total energy in the electromagnetic calorimeter ($|\eta| < 2.8$) and the ΣE_T^{FCal} ($3.2 < |\eta| < 4.9$) [36].

The $\Sigma E_{\mathrm{T}}^{\mathrm{FCal}}$ distribution is shown in Figure 5.3. The distribution is fit with the two-component model given by Equation 2.89. Centrality classes are determined by categorizing Pb+Pb events into percentiles from large to small $\Sigma E_{\mathrm{T}}^{\mathrm{FCal}}$ (see Equation 2.88). Smaller percentiles correspond to central events (i.e. small b) and larger percentiles correspond to peripheral events (i.e. large b).
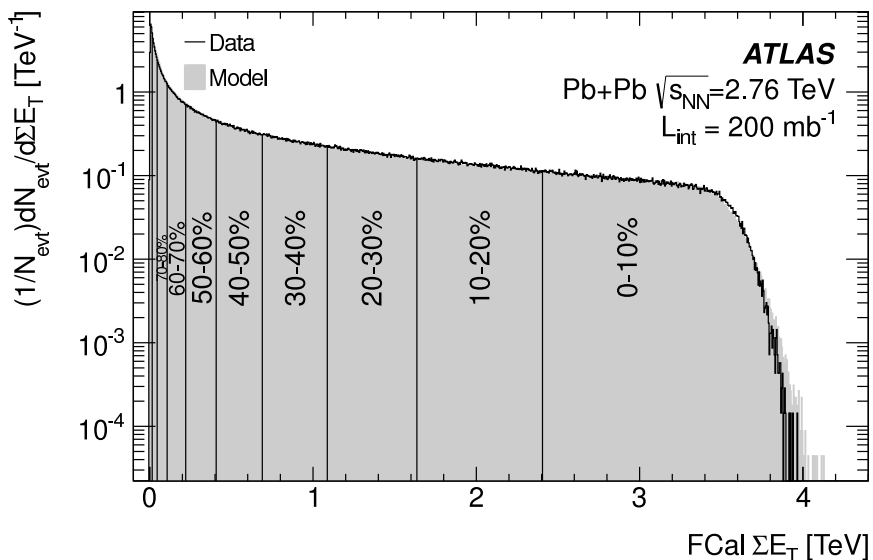
Figure 5.3: Measured $\Sigma E_{\mathrm{T}}^{\mathrm{FCal}}$ distribution divided into 10% centrality bins. The distribution is fit with the two-component model given by Equation 2.89.

The $\Sigma E_{\mathrm{T}}^{\mathrm{FCal}}$ distribution is divided into 6 centrality classes in this work. A summary of each centrality class is presented in Table 5.3. The $\langle N_{\mathrm{part}} \rangle$ and $\langle N_{\mathrm{coll}} \rangle$ are determined by averaging over the events in each centrality class of the Glauber MC. The uncertainties arise primarily from the Glauber model parameters and include uncertainties in $\sigma_{\mathrm{inel}}^{\mathrm{NN}}$, the nuclear density profile (Equation 2.86), and the uncertainty in the sampled fraction of inelastic events. Correlations in the uncertainties between different centrality intervals are appropriately accounted for. The uncertainty in $\langle N_{\mathrm{part}} \rangle$ is less than that of the corresponding $\langle N_{\mathrm{coll}} \rangle$ since a single participant can interact inelastically with several nucleons in a collision. Due to the large uncertainties in $\langle N_{\mathrm{coll}} \rangle$, the 80-100% centrality class is ignored in this work.

Table 5.3: Average number of participating nucleons $\langle N_{\mathrm{part}} \rangle$ and binary collisions $\langle N_{\mathrm{coll}} \rangle$ for the centrality classes used in this analysis. Relative uncertainties δ are also shown.

Centrality [%]	$\langle N_{\mathrm{part}} \rangle$	$\delta \langle N_{\mathrm{part}} \rangle$ [%]	$\langle N_{\mathrm{coll}} \rangle$	$\delta \langle N_{\mathrm{coll}} \rangle$ [%]
0–5	382	0.5	1683	7.7
5–10	330	0.9	1318	7.5
10-15	282	1.3	1035	7.4
15-20	240	1.6	811	7.4
20-40	158	2.6	441	7.3
40–80	46	6.0	78	9.4
0–80	140	4.7	452	8.5

5.4   Selection of $W \to \mu\nu_\mu$ Events

This section explains the muon selection cuts applied to the data sample. The selection chain proceeds by applying what are referred to as *preselection* cuts. The preselection requirements are intended to yield only the highest quality muons for further analysis. Once a sample of preselected muons has been obtained, further cuts are applied to select for muons from $W \to \mu\nu_\mu$ events. These types of muons are referred to as *signal candidates*. The specific criteria of both the preselection and signal candidate selection will be discussed in the following sections.

5.4.1   Muon Preselection

Preselection cuts are required to reduce non-collision (e.g. cosmic, beam halo) [252] muons as well as to reduce "fake" muons from hadronic sources. Beam halo muons arise from protons striking limiting aperatures, producing pions and kaons π/K that decay into muons. The global event cuts introduced in Section 5.2 are effective at reducing non-collision muons. Cosmic muons are generally asynchronous with collision events. Therefore, these types of muons can be rejected by selecting only muons that can be associated to events that satisfy the MBTS coincidence requirement and that have a reconstructed vertex with at least three associated ID tracks. Furthermore, non-collision muons do not originate from the interaction point and thus their trajectories are typically

different from those originating from the collision. For example, the $|z_0|$ and $|d_0|$ for combined muons originating from the collision are a few mm from the IP, whereas cosmic muons are several tens of cm. Therefore, placing requirements on the impact parameters $|z_0|, |d_0|$ with respect to the IP can be effective at further reducing non-collision muons in coincidence with a collision event.

Fake muons arise from misidentification of *sail-through* hadrons that pass through the calorimeters without showering, misidentification of *punch-through* hadrons that emerge from hadronic showers, and π/K decays-in-flight. These processes are difficult to model with Monte Carlo methods and become an increasingly important background source at muon $p_\text{T} < 15$ GeV or in muon channels with a small cross section (e.g. $t\bar{t}$) [253]. False reconstruction of sail-through and punch-through hadrons occurs rarely and is neglected in this work. π/K decays-in-flight are mainly considered in analyses concerned with semileptonic decays of b and c quarks. However, a small percentage of muons from π/K decays in the tails of the p_T distribution could leak into the signal region of this analysis (Figure 5.4). Therefore, a method of reducing this muon source was adopted from Ref. [37]. This method utilizes two discriminants that are used to reduce muons from π/K decays within different regions of the detector.

The decays fall into three categories: *early decays* before the ID ($R = 50.5$ mm from the beam line), *late decays* after the ID ($R = 1082$ mm from the beam line), and *intermediate decays* between ID measurements. Early decays cannot be distinguished from prompt muons originating from the IP, however given the short distances, this type of event has a low probability of occuring. Late decays are reduced using a discriminant called the *momentum balance*. When π/K's decay, they lose a fraction of their energies to neutrinos. The track parameters measured in the ID correspond to the π/K before the decay, whereas the MS measures the muon from the decay. Therefore, for late decays, there will exist a significant difference between the momentum measurement in the ID and in the MS. This can be quantified with the momentum loss parameter:

$$\frac{\Delta p_{loss}}{p_{ID}} = \frac{p_{ID} - (p_{MS} + p_{param})}{p_{ID}} \tag{5.2}$$

where p_{ID} and p_{MS} are the momenta measured in the ID and MS, respectively, and p_{param} is the parametrization of the energy loss discussed in Section 4.3.

The second discriminant reduces the contribution from intermediate π/K decays. This discriminant locates sudden changes in the direction (i.e. "kinks") of the reconstructed muon track
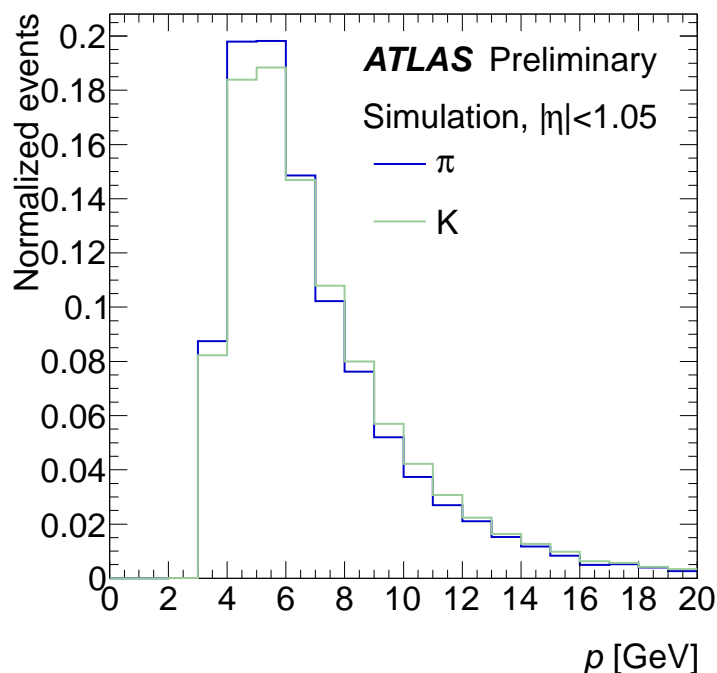
Figure 5.4: Reconstructed muon momentum for π/K decays-in-flight in a simulared di-jet sample [37].

trajectory within the ID. As discussed in Section 4.2, track parameters are evaluated at detector surfaces, which are used to perform a χ^2 track fit. The fit yields scattering angle information at each detector surface (see Figure 4.8). Scattering angles due to multiple scattering are typically an order of magnitude less than the decay angle of a π/K, and generally the decay will take place in between measurements at two detector surfaces. Therefore, a scattering angle outlier in the track fit could indicate the presence of a decay-in-flight. The variable used to locate outliers is called the *scattering angle significance*. The expected change in angle in the bending plane from detector surface i to $i+1$ ($\Delta\phi_i^{ms}$) can be determined from the Highland formula described in Section 4.3. Let the measured change in angle between detector surface i and $i+1$ be written as $\Delta\phi_i$. Then the signed residual from the track fit is defined as:

$$s_i \equiv q\frac{\Delta\phi_i}{\Delta\phi_i^{ms}} \tag{5.3}$$

where q is the charge of the track. The scattering angle signficance S of a track traversing n detector

surfaces is measured at every surface. So at surface k:

$$S(k) \equiv \frac{1}{\sqrt{n}} \left(\sum_{i=1}^{k} s_i - \sum_{k+1}^{n} s_j \right) \tag{5.4}$$

The surface k that gives the largest $|S(k)|$ is used as the scattering angle significance of the track. If there is no decay, the measured angular deviations will be similar to the expected value due to multiple scattering and $|S(k)|$ will be small. However, if there is a π/K decay-in-flight, the large change in angle between measurements will result in a large $|S(k)|$.

In addition to those cuts already discussed, further selection requirements are imposed to yield a high-quality muon sample. Reconstructed offline muons are required to match online trigger objects within a cone radius $\Delta R = \sqrt{\Delta \eta^2 + \Delta \phi^2} = 0.2$. This reduces the probability of introducing muons into the sample that did not trigger the event readout("random benefit"). All muons are required to be matched to an ID track (i.e. all muons are combined muons). Cuts on the ID components of the muon track are imposed (e.g. pixel hits/holes, SCT hits/holes) to improve the track quality. In addition, the p_T of the ID component of the muon track is required to be greater than 3 GeV (the minimum energy to reach the MS) to reduce associated ID tracks unlikely to be muons. A selection on the χ^2/n.d.o.f. is imposed to ensure a good track fit. Finally, the $|\eta|$ of the muon is required to be within the coverage of the trigger chambers and excludes the MS gap region at $\eta \approx 0$. The preselection cuts are summarized in Table 5.4.

The number of preselected muons per unit luminosity as a function of the run number is presented in Figure 5.5. This shows a stable muon multiplicity over the entire run period. The average number of preselected muons per nb^{-1} is ≈ 1.2. The total number of preselected muons in each run is presented in Table 5.5.

5.4.2 Signal Candidate Selection

The preselection affords a sample of high-quality muons produced from the collision event. However, the sample still contains a large fraction of muons produced from processes other than $W \rightarrow \mu\nu_\mu$ events. These background sources include muons from b and c quarks, Z bosons, and τ leptons and can be reduced by selecting events with signatures inherent to W decays. The methods by which these signatures are located are discussed below.

Table 5.4: Preselection cut-flow for muons. Each muon is given an index equal to the number of cuts passed.

Muon Preselection Cuts	
Quality Index	Applied Cut
1	Offline muon matched to online muon trigger object within $\Delta R < 0.2$
2	Combined muon
3	$N_{pixel} > 0$ (pixel hits) and $N_{SCT} > 6$ (SCT hits)
4	$N_{B-Layer} > 0$ (B-Layer hits if expected)
5	$N_{holes}^{pixel} + N_{holes}^{SCT} < 2$
6	$|d0| < 5.0$mm
7	$|z0| < 5.0$ mm
8	$p_{\mathrm{T}}^{\mu,ID} > 3.0$ GeV (ID component of muon track)
9	$0.1 < |\eta| < 2.4$ (trigger chamber coverage, excluding gap region)
10	$\chi^2/\mathrm{n.d.o.f.} < 10$
11	$\frac{\Delta p_{loss}}{p_{ID}} < 0.5$ (momentum loss corrected for energy loss)
12	$|S(k)| < 4$ (scattering angle significance)

5.4.2.1   Isolation

The production of muons from open heavy-flavor quarkonium states constitutes a significant fraction to the background in the soft kinematic region of signal events. These muons primarily come from semileptonic decays of bottom and charm mesons via the $B \to \mu + X$ and $D \to \mu + X$ modes, where X is any decay product in accordance with charge and momentum conservation. Muons from $Z \to \mu^+\mu^-$, $W \to \tau\nu_\tau \to \mu\nu_\mu\nu_\tau\nu_\tau$, and $W \to \mu\nu_\mu$ events are typically isolated. However, muons produced from b and c quarks are generally in close proximity to collimated jets. Therefore, imposing an energy or spatial requirement around the muon can drastically reduce these types of background events.

Methodology   Two methods for separating isolated from non-isolated muons were studied. The first involves using muon-jet correlations in ΔR space to locate muons in the viscinity of a jet.
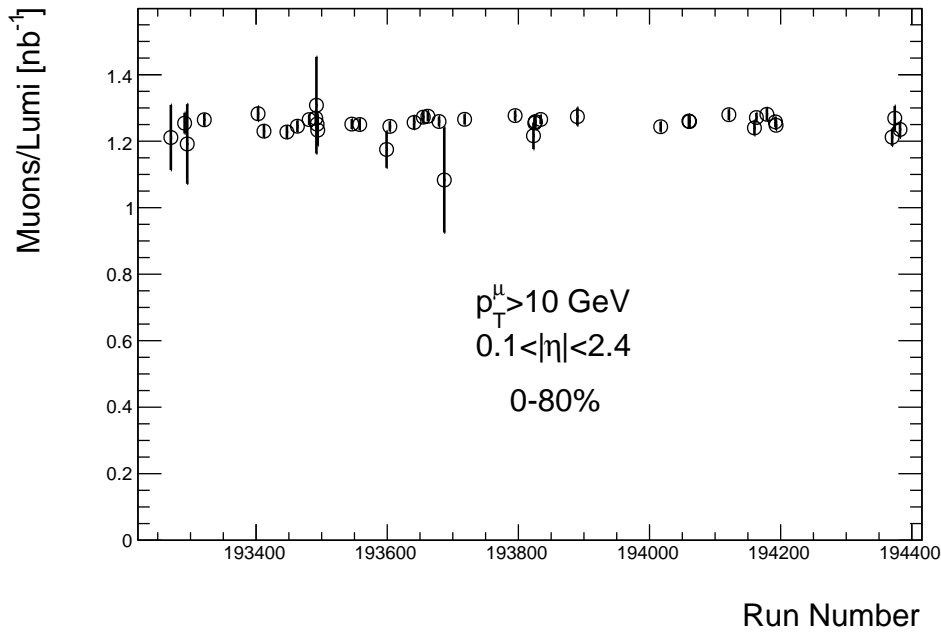
Figure 5.5: Preselected muon per unit luminosity as a functin of the run number.

The muon is considered isolated if a jet cannot be located within some ΔR value around the muon trajectory (Figure 5.6). Figure 5.7 shows the ΔR between muons from $W \rightarrow \mu\nu_\mu$ events and reconstructed jets in MC simulation. The left panel presents the ΔR for different lower jet E_T thresholds with $p_T^\mu > 4$ GeV and the right panel for different lower p_T^μ thresholds with $E_T^{jet} > 30$ GeV. Ideally, all the jets would be located beyond some ΔR threshold so that a cut can be effectively applied to reduce the multi-jet background. However, Figure 5.7 clearly shows an excess of μ+jet correlations at $\Delta R \approx 0$. This excess is attributed to photons from final-state radiation (i.e. muon bremmstrahlung) that shower in the EM calorimeter and emulate a jet. This is further supported by Figure 5.8, which shows the ΔR for bremmstrahlung photons from $W \rightarrow \mu\nu_\mu$ events.

The number of signal events affected by bremmstrahlung radiation is non-negligible, and it is experimentally difficult to disentangle signal muons from heavy-flavor muons in this ΔR region. Therefore, a second isolation method was adopted that uses the total energy around the muon as a discriminant. The total energy around an isolated muon, relative to its p_T, will be small if the muon is isolated – even for those muons that radiate photons. The total energy can be calculated by summing the p_T of all ID tracks within some ΔR around the muon, excluding the muon p_T

Table 5.5: Number of preselected muons per run.

Index	Run	L_{int} [μb^{-1}]	Preselected N_μ	Index	Run	L_{int} [μb^{-1}]	Preselected N_μ
1	193270	0.126	153	22	193687	0.043	47
2	193291	1.286	1613	23	193718	5.299	6707
3	193295	0.083	99	24	193795	5.303	6772
4	193321	3.949	4993	25	193823	0.757	921
5	193403	2.766	3548	26	193825	5.985	7509
6	193412	3.607	4437	27	193826	5.152	6485
7	193447	3.809	4676	28	193834	6.578	8323
8	193463	4.117	5126	29	193890	1.751	2230
9	193481	4.886	6180	30	194017	5.438	6762
10	193491	2.505	3179	31	194060	3.139	3957
11	193492	0.062	81	32	194061	5.150	6484
12	193493	0.969	1213	33	194121	4.908	6280
13	193494	0.582	718	34	194160	2.522	3127
14	193546	5.428	6793	35	194163	6.453	8202
15	193558	4.202	5254	36	194179	3.600	4610
16	193599	0.385	453	37	194192	5.338	6716
17	193604	5.504	6850	38	194193	6.168	7696
18	193641	3.160	3970	39	194370	1.774	2150
19	193655	4.200	5343	40	194374	0.923	1172
20	193662	5.244	6686	41	194382	2.077	2565
21	193679	5.308	6684				

itself:

$$i_\mu(\Delta R, p_{T,min}^{trk}, \langle N_{\text{coll}} \rangle) \equiv \frac{\sum_{i=min}^{N_{\text{trk}}} p_{T,i}^{trk} - p_{T,\text{trk}}^\mu}{p_T^\mu}, \tag{5.5}$$

where the isolation variable i_μ is a function of ΔR, centrality ($\langle N_{\text{coll}} \rangle$), and the minimum track transverse momentum $p_{T,min}^{trk}$ in the summation of ID tracks $\sum_{i=min}^{N_{\text{trk}}} p_{T,i}^{trk}$. In the summation, tracks
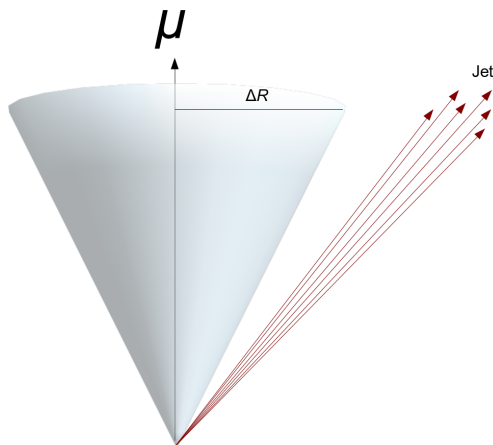
Figure 5.6: Schematic of an isolated muon with a nearby jet.
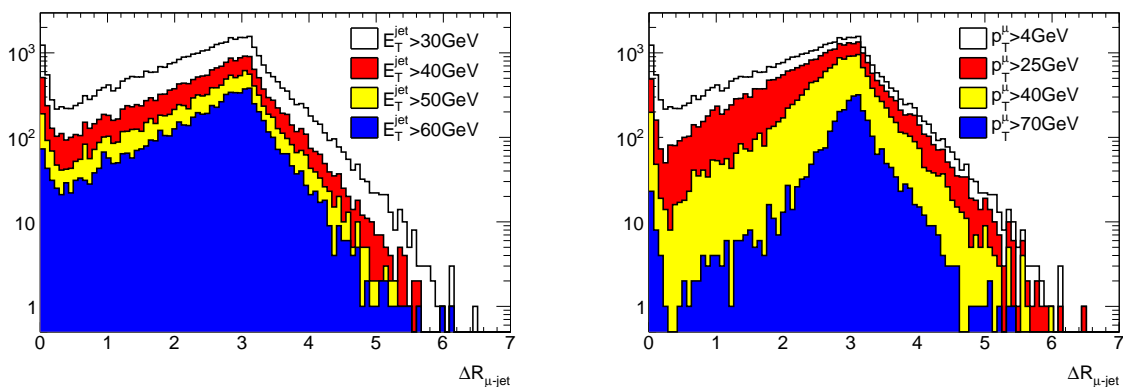
Figure 5.7: ΔR distribution between muons from $W \to \mu \nu_\mu$ events and reconstructed jets from MC simulation. (Left) Different lower jet E_T thresholds with muon $p_T > 4$ GeV(Right) Different muon lower p_T thresholds with jet $E_T > 30$ GeV.

are required to pass the stringent heavy-ion requirements presented in Section 5.2. Equation 5.5 neglects neutral particles. However, the majority of the jet energy is carried by charged particles (mostly charged pions), and therefore this does not limit the ability of i_μ to efficiently discriminate between non-isolated muons from QCD multi-jet events and isolated muons from W bosons, Z bosons, and τ leptons.

The dependence of i_μ on ΔR, $p_{T,min}^{trk}$, and centrality must be carefully evaluated to optimize
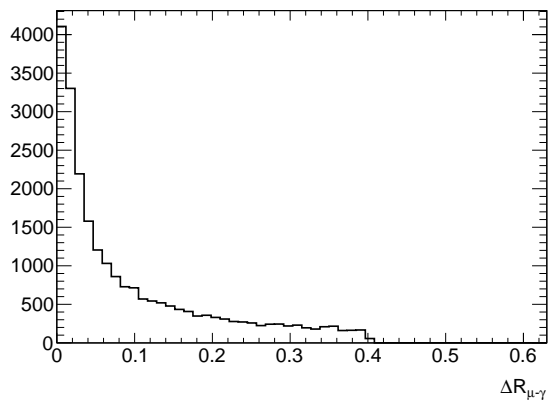
Figure 5.8: ΔR distribution between bremmstrahlung photons and muons from $W \to \mu\nu_\mu$ events in MC simulation.

the discriminating power of the isolation cut. The calculation of i_μ is only concerned with locating muons from b and c quarks, which originate from hard scattering processes. Therefore, other aspects of the collision not identified with the hard process (i.e. the "underlying event" or UE) should not be included in Equation 5.5. Since the UE is dominated by low-momentum QCD processes [254], its effects on the isolation can be reduced by raising $p^{trk}_{T,min}$. However, raising the track p_T threshold too high results in an insufficient number of tracks. Increasing ΔR increases the number of tracks in the summation but also loosens the cut. Therefore, it is imperative to choose a value for both $p^{trk}_{T,min}$ and ΔR that minimizes contributions from the UE while maintaining the discriminatory power of the cut. This is achieved by studying the performance of i_μ with several combinations of $p^{trk}_{T,min}$ and ΔR.

Figure 5.9 presents the QCD multi-jet background rejection ϵ_B as a function of the signal efficiency ϵ_S for various working points in $(i_\mu, p^{trk}_{T,min}, \Delta R)$ space. $\epsilon_{S(B)}$ is defined as:

$$\epsilon_{S(B)} = \frac{N^{\Phi+i_\mu}_{S(B)}}{N^{\Phi}_{S(B)}} \tag{5.6}$$

where Φ is the phase space of the muon samples and $\Phi+i_\mu$ indicates the application of the isolation requirement. The centrality dependence of i_μ arises from the larger charged particle multiplicities in central events, which is where the isolation is most difficult to apply. Therefore, the optimization of i_μ is conducted only in the most central (0-5%) centrality class (see Appendix B for other centrality

classes). The background rejection and signal efficiencies are determined after all signal selection cuts (discussed below) have been applied. This is performed in order to improve the optimization by eliminating the effect that other cuts have on the background and signal muon samples.
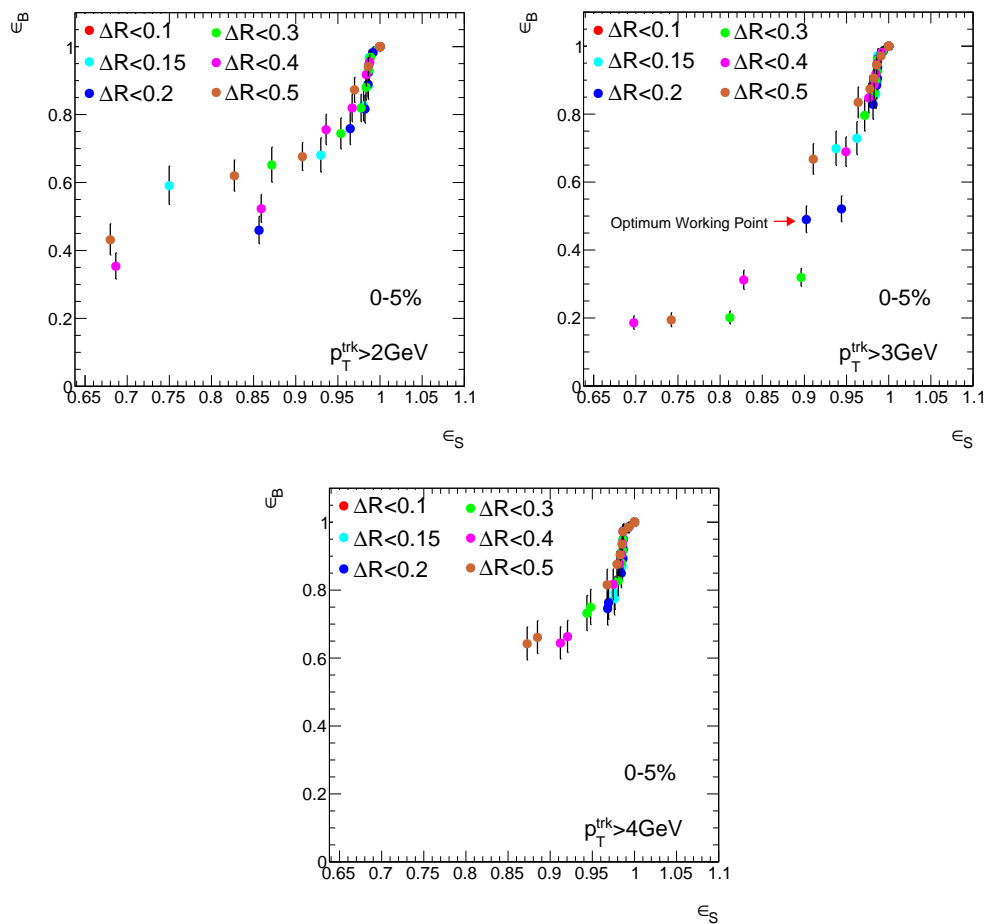
Figure 5.9: Background rejection (ϵ_B) as a function of signal efficiency (ϵ_S) in the 0-5% centrality class using a sample of J$x\mu$ and $W \to \mu\nu_\mu$ events. The working points are evaluated at different $(i_\mu, p^{trk}_{T,min}, \Delta R)$ in order to determine the most optimal analysis cut.

Optimization of i_μ From the library of isolation definitions, the optimum working point is determined from the combination of $p^{trk}_{T,min}$ and ΔR that minimizes ϵ_B and maximizes ϵ_S (i.e. the lower right-hand corner of Figure 5.9). However, the statistical uncertainties of the *actual* number of background and signal events in the data must also be taken into consideration. So to find an

isolation definition that maximizes the signal to background ratio in the data, an "effective signal" N_{eff} is used. N_{eff} is calculated by starting with the number of signal events in the *data* after final selection:

$$N_S = N - N_B \qquad (5.7)$$

The relative error on N_S is given by:

$$\frac{\delta N_S}{N_S} = \frac{\sqrt{N + N_B}}{N_S} \qquad (5.8)$$

where the total number of events in the data N is:

$$N = N_S + N_B = \epsilon_S \cdot \tilde{N}_S + \epsilon_B \cdot \tilde{N}_B \qquad (5.9)$$

where $\tilde{N}_{S(B)}$ is the number of signal (background) events *before* applying the isolation cut i_μ and $\epsilon_{S(B)}$ is the signal efficiency and background rejection as defined in Equation 5.6. Equation 5.8 can then be written as:

$$\frac{\delta N_S}{N_S} = \frac{\sqrt{\epsilon_S \cdot \tilde{N}_S + 2\epsilon_B \cdot \tilde{N}_B}}{\epsilon_S \cdot \tilde{N}_S} \equiv \frac{1}{N_{\text{eff}}} \qquad (5.10)$$

which is the inverse of the effective signal. Therefore, by *maximizing* N_{eff}, the relative uncertainty of the signal is minimized and the sample purity $\left(= \frac{N_S}{N_S + N_B} \right)$ is maximized. Figure 5.10 show distributions of N_{eff} as a function of i_μ. Each point corresponds to an isolation definition in $(i_\mu, p_{T,min}^{trk}, \Delta R)$ space used in Figure 5.9.

Based on the studies of ϵ_S, ϵ_B, and N_{eff}, the optimum upper threshold for the isolation cut in Equation 5.5 is $i_\mu < 0.1$ using $p_{T,min}^{trk} = 3$ GeV and $\Delta R < 0.2$. Figure 5.11 shows the number of muons per event in the data satisfying the isolation criteria. These events are before applying other W boson selection requirements. Events with ≥ 1 isolated muon are most likely from $Z \to \mu^+\mu^-$, $W \to \tau\nu_\tau \to \mu\nu_\mu\nu_\tau\nu_\tau$, or $W \to \mu\nu_\mu$ events.
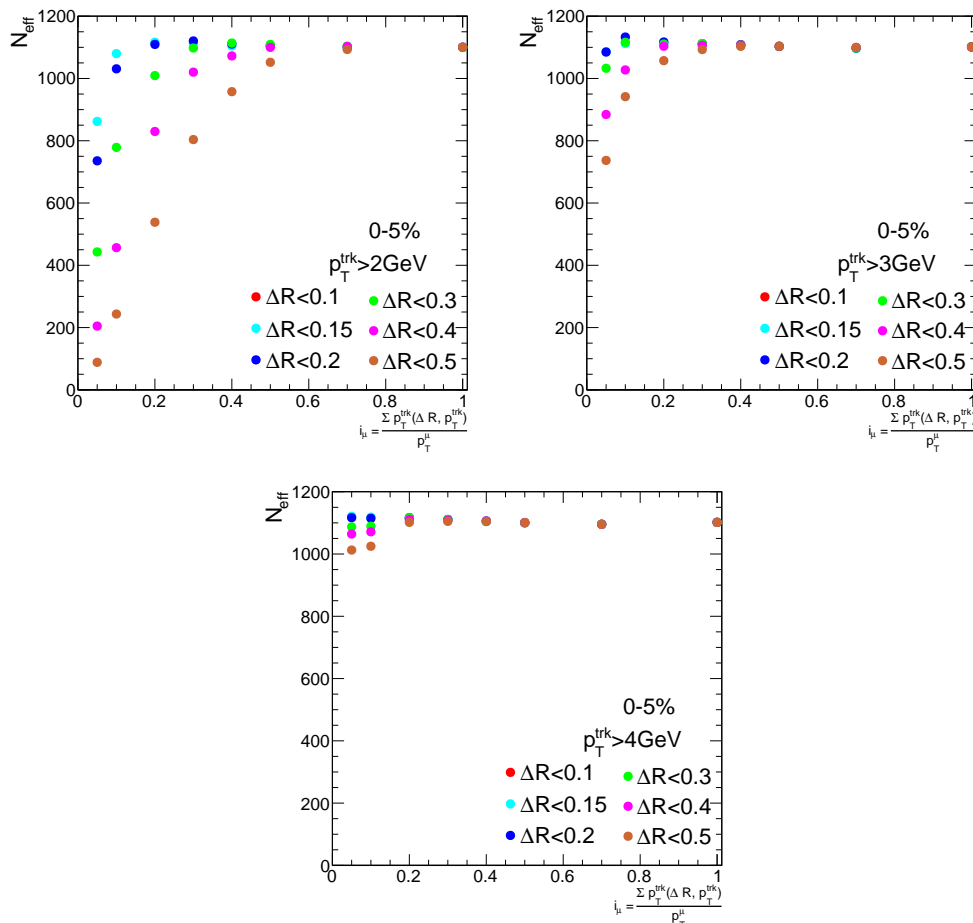
Figure 5.10:   Effective signal N_{eff} from Equation 5.10 as a function of the isolation variable i_μ in the 0-5% centrality class using $p^{trk}_{\text{T},min} = 2,3,4$ GeV and various upper ΔR thresholds. Each point corresponds to a working point in Figure 5.9.

5.4.2.2   Invariant Mass $m_{\mu\mu}$

High-mass Drell-Yan (DY) processes [255] involve an s-channel exchange of a virtual photon or Z boson and can produce $\mu^+\mu^-$ pairs over a range of invariant mass $m_{\mu\mu}$, as shown in Figure 5.12. These muon pairs are isolated and are produced with large p_{T}, making them kinematically indistinguishable from muons produced from $W \rightarrow \mu\nu_\mu$ events. Thus the most efficient way of reducing their contribution to the signal sample is by reconstructing the $m_{\mu\mu}$ distribution using muons of opposite charge and rejecting pairs that fall within the Z mass window. This is performed by
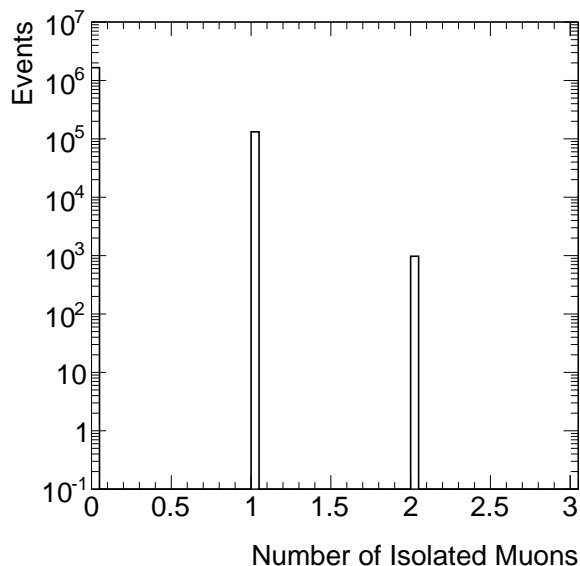
Figure 5.11: Distribution of the number of isolated muons per event in the data. Other than the preselection requirements, no further cuts are applied to the sample.

testing all combinations of preselected (Table 5.4) muons in an event with all reconstructed muons with $p_T > 20$ GeV. If the mass combination results in $m_{\mu\mu} > 66$ GeV, both muons are vetoed.

The distribution of the number of isolated single muons per event in the data after applying the Z boson veto is shown in Figure 5.13. It can be observed by comparing to Figure 5.11 that the number of events with two isolated muons drops by approximately 60% while retaining almost 100% of events with one isolated muon. This lends credence to the effectiveness of $m_{\mu\mu}$ as a powerful discriminant against Z boson events.

5.4.2.3 Muon p_T

As mentioned in earlier sections, due to the large mass of the W and Z bosons, muons from $W \to \mu\nu_\mu$ and $Z \to \mu^+\mu^-$ decays are produced with large p_T. However, muons from $W \to \tau\nu_\tau \to \mu\nu_\mu\nu_\tau\nu_\tau$ and QCD multi-jet processes typically appear in softer regions of the p_T spectrum. This is illustrated in Figure 5.14, which shows the muon p_T spectra for simulated signal and background samples at $p_T > 25$ GeV after applying the isolation and $m_{\mu\mu}$ requirements. The distributions are normalized by their respective cross sections and are scaled to the number of binary collisions in
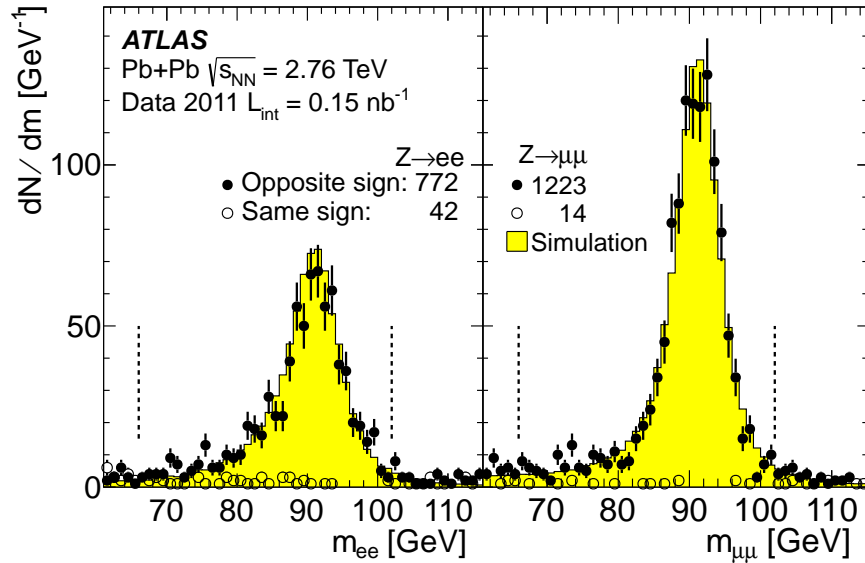
Figure 5.12:   The measured (points) and simulated (solid histogram) invariant mass distribution of $Z \to \mu^+\mu^-$ events (Right) in Pb+Pb collisions. $Z \to e^+e^-$ events are also shown (Left) [38].

the data. The QCD multi-jet distribution is also scaled by an additional factor (discussed later in Section 5.5) to take into account jet quenching.

It can be seen from the figure that at $p_T = 25$ GeV, the QCD multi-jet background is $\sim 50\%$ of the signal, whereas the other background sources are at the level of $\sim 5 - 7\%$. However, as one moves to higher p_T, the QCD multi-jet contribution drops exponentially and the signal increases. Therefore, a p_T cut at 25 GeV is used as part of the selection criteria for signal candidates.

5.4.2.4   Missing Transverse Energy p_T^{miss}

In $W \to \mu\nu_\mu$ events, the neutrino is undetectable. So the mass of the W boson cannot be reconstructed in the same manner as for the Z boson (Figure 5.12). However, momentum conservation is expected in the transverse plane (see Section 3.3.1), and thus the momentum vectors of undetectable particles can be estimated by measuring the missing transverse momentum (E_T^{miss},p_T^{miss}) of the event. This observable is a powerful proxy for the kinematics of undetectable particles, and in addition to its utility in detecting the presence of neutrinos, it has also proven useful in searches for physics beyond the Standard Model (e.g. supersymmetric particles [256], additional heavy-gauge
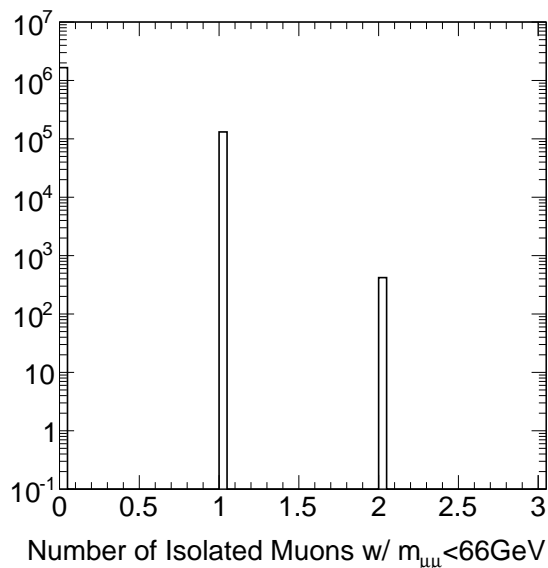
Figure 5.13: Distribution of the number of isolated muons per event in the data after applying the Z boson veto (see text). Other than the preselection requirements, no further cuts are applied to the sample.

bosons [257], and dark matter searches [258]).

The vector momentum imbalance in the transverse plane is calculated slightly differently in pp and Pb+Pb collisions. The reason is that the resolution of E_T^{miss} using the same method as in pp collisions is far worse in central Pb+Pb events and will be discussed in more detail below. This section will begin with a description of the $E_T^{\mathrm{miss}}(p_T^{\mathrm{miss}})$ reconstruction in both systems.

E_T^{miss} **Reconstruction in** pp **Collisions** In pp collisions [39], $\boldsymbol{E}_T^{\mathrm{miss}}$ is calculated from the negative vector sum of the momenta of all detected particles in the event. The $\boldsymbol{E}_T^{\mathrm{miss}}$ reconstruction consists of contributions from energy deposits in the calorimeters and muons reconstructed in the MS. The missing momentum is then calculated as:

$$E_{x(y)}^{\mathrm{miss}} = E_{x(y)}^{\mathrm{miss,calo}} + E_{x(y)}^{\mathrm{miss},\mu} \tag{5.11}$$

The magnitude of E_T^{miss} is calculated as:

Figure 5.14: Muon p_T distribution in simulated signal and background samples for preselected muons with $p_T > 25$ GeV after applying isolation and $m_{\mu\mu}$ requirements. The distributions are normalized by their respective cross sections and are scaled to the number of binary collisions in the data. The QCD multi-jet distribution is rescaled to take into account jet quenching.

$$E_T^{\mathrm{miss}} = \sqrt{(E_x^{\mathrm{miss}})^2 + (E_y^{\mathrm{miss}})^2} \tag{5.12}$$

and the azimuthal coordinate of the vector is given by:

$$\phi^{\mathrm{miss}} = \arctan\left(\frac{E_y^{\mathrm{miss}}}{E_x^{\mathrm{miss}}}\right) \tag{5.13}$$

The $\boldsymbol{E}_T^{\mathrm{miss}}$ calorimeter term is calculated from the negative sum of the cell energies corresponding to each physics object and can be expressed as:

$$E_{x(y)}^{\text{miss,calo}} = E_{x(y)}^{\text{miss,e}} + E_{x(y)}^{\text{miss,}\gamma} + E_{x(y)}^{\text{miss,}\tau} + E_{x(y)}^{\text{miss,jets}}$$
$$+ E_{x(y)}^{\text{miss,softjets}} + \left(E_{x(y)}^{\text{miss,calo,}\mu} \right)$$
$$+ E_{x(y)}^{\text{miss,CellOut}} \tag{5.14}$$

where the summation of cell energies is over $|\eta| < 4.5$. In Equation 5.14,

- $E_{x(y)}^{\text{miss,e}}, E_{x(y)}^{\text{miss,}\gamma}, E_{x(y)}^{\text{miss,}\tau}$ are associated to electrons, photons, and τ-jets from hadronically decaying τ leptons, respectively;

- $E_{x(y)}^{\text{miss,jets}}$ is associated to jets with $p_{\text{T}} > 20$ GeV;

- $E_{x(y)}^{\text{miss,softjets}}$ is associated to jets with $7 < p_{\text{T}} < 20$ GeV;

- $E_{x(y)}^{\text{miss,calo,}\mu}$ is the contribution from muon energy loss in the calorimeters, which is only added for non-isolated muons since the energy deposited in the calorimeters by the muon cannot be resolved from the energy deposited by particles in a jet. In this case, the energy of the muon in the MS before correcting for energy loss in the calorimeters is used.

- $E_{x(y)}^{\text{miss,CellOut}}$ includes energies from cells not associated to the reconstructed objects mentioned above. However, the deposited energy in the cell must still meet a lower threshold to be included in the summation.

The $\boldsymbol{E}_{\text{T}}^{\text{miss}}$ muon term in Equation 5.11 is calculated from the momenta of muon tracks with $|\eta| < 2.7$:

$$E_{x(y)}^{\text{miss,}\mu} = - \sum_{\text{muons}} p_{x(y)}^{\mu} \tag{5.15}$$

The p_{T} of combined muons, which is corrected for energy loss in the calorimeters, is used for isolated muons. In this case, the $E_{x(y)}^{\text{miss,calo,}\mu}$ term is not included in Equation 5.14 to avoid double counting. Otherwise, this term is included and Equation 5.15 uses the muon p_{T} before energy-loss correction.

The distributions for $E_{x(y)}^{\text{miss}}$ in minimum bias pp events in the data are shown in Figure 5.15. In minimum bias events, no genuine $E_{\text{T}}^{\text{miss}}$ is expected. The width of the distributions indicates the effect of imperfections in the reconstruction process on the resolution. The $(E_{\text{x}}^{\text{miss}}, E_{\text{y}}^{\text{miss}})$ resolution

as a function of the total transverse energy of the event ΣE_{T} from data is shown in Figure 5.16. The resolution is shown in $Z \to l^+l^-$, QCD di-jet, and minimum bias events, which are not expected to have any genuine $E_{\mathrm{T}}^{\mathrm{miss}}$. This allows the resolution to be measured from the width of the combined $E_{x(y)}^{\mathrm{miss}}$ distributions (denoted $(E_{\mathrm{x}}^{\mathrm{miss}}, E_{\mathrm{y}}^{\mathrm{miss}})$ in the figure) assuming that the true values of $E_{\mathrm{x}}^{\mathrm{miss}}$ and $E_{\mathrm{y}}^{\mathrm{miss}}$ are zero. The distributions in Figure 5.16 are fit with the function $\sigma = k \cdot \sqrt{\Sigma E_{\mathrm{T}}}$.
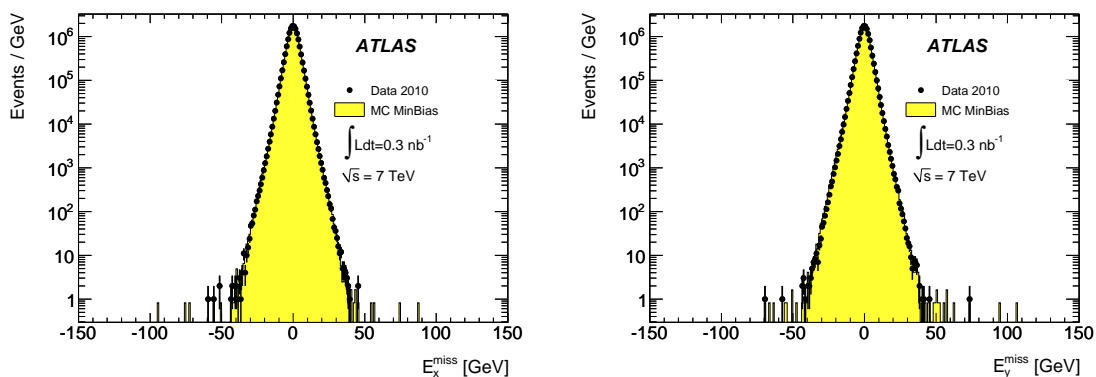
Figure 5.15: Distribution of $E_{\mathrm{x}}^{\mathrm{miss}}$ and $E_{\mathrm{y}}^{\mathrm{miss}}$ in a data sample of minimum bias pp events. The expectation from MC simulation is also included [39].

The same procedure for the $E_{\mathrm{T}}^{\mathrm{miss}}$ calculation was conducted in a sample of Pb+Pb events. A comparison of the resolution in Pb+Pb collisions and in pp collisions is presented in Figure 5.17. It is evident from this figure that the $(E_{\mathrm{x}}^{\mathrm{miss}}, E_{\mathrm{y}}^{\mathrm{miss}})$ resolution in the most central Pb+Pb events is approximately a factor of 6 larger than in pp events. This is attributed to the enhanced multiplicities in heavy-ion collisions, which result in large fluctuations of the terms in Equation 5.14. Therefore, in this work, a new method for deriving the event $E_{\mathrm{T}}^{\mathrm{miss}}$ is applied.

$p_{\mathrm{T}}^{\mathrm{miss}}$ **Reconstruction in Pb+Pb Collisions**   The poor resolution in central Pb+Pb events makes the canonical method for calculating the $E_{\mathrm{T}}^{\mathrm{miss}}$ untenable. Therefore, an alternative method [40, 259] is applied using only information from the ID. In this formulism, the missing momentum $p_{\mathrm{T}}^{\mathrm{miss}}$ (also referred to as $\not{p}_{\mathrm{T}}$ in the Feynman notation) is defined as the negative vector sum of the momenta of all ID tracks:
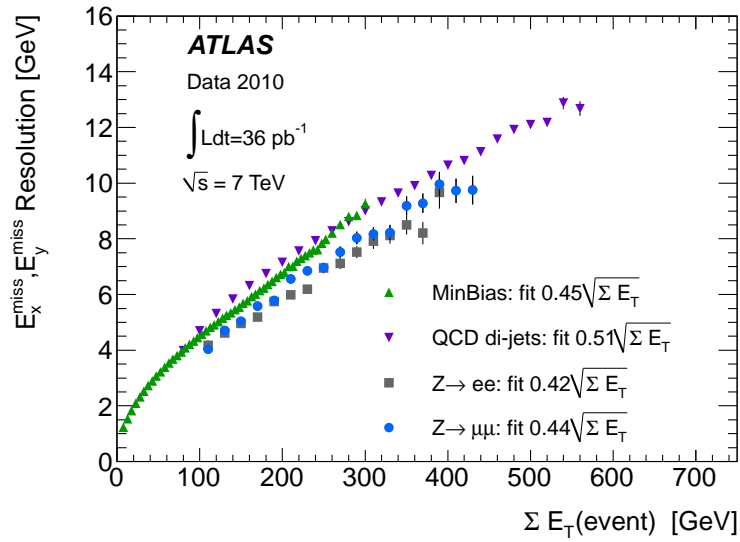
Figure 5.16: E_x^{miss} and E_y^{miss} resolution as a function of ΣE_T in pp collision data. The resolution is fitted with the function $\sigma = k \cdot \sqrt{\Sigma E_T}$ [39].
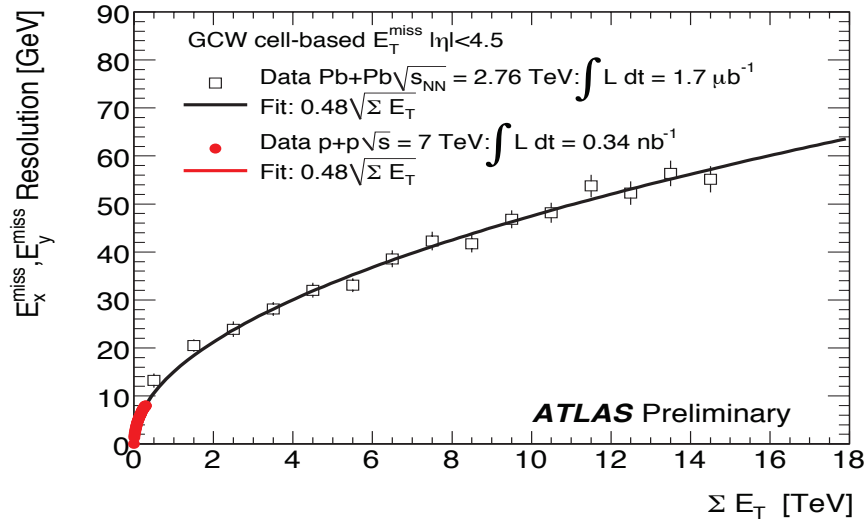
Figure 5.17: E_x^{miss} and E_y^{miss} resolution as a function of ΣE_T in pp and Pb+Pb collision data. The resolution is fitted with the function $\sigma = k \cdot \sqrt{\Sigma E_T}$.

$$p_{x(y)}^{\mathrm{miss}} = - \sum_{\mathrm{tracks}} p_{x(y)}^{\mathrm{track}} \qquad (5.16)$$

where the summation is over high quality heavy-ion tracks (see Section 5.2) within $|\eta| < 2.5$. The calculations of the magnitude of $p_{\mathrm{T}}^{\mathrm{miss}}$ and the azimuthal angle ϕ^{miss} are analogous to Equations 5.12 and 5.13.

Shortcomings of this method are that it neglects neutral particles in the vector summation and is limited to the ID coverage. This contributes to the $p_{\mathrm{x}}^{\mathrm{miss}}, p_{\mathrm{y}}^{\mathrm{miss}}$ resolution and the effects are exacerbated by increasing the number of tracks in the summation of Equation 5.16. These effects are in addition to other factors that contribute to the resolution: fake $p_{\mathrm{T}}^{\mathrm{miss}}$ introduced from dead material in the detector, finite detector resolution, and different sources of noise. To better understand the dependence of the $p_{\mathrm{x}}^{\mathrm{miss}}, p_{\mathrm{y}}^{\mathrm{miss}}$ resolution on the number of tracks in the vector summation, several different lower track p_{T} thresholds were studied. The resulting $p_{\mathrm{x}}^{\mathrm{miss}}$ and $p_{\mathrm{y}}^{\mathrm{miss}}$ distributions in minimum bias Pb+Pb events are shown in Figure 5.18. The width of the distributions are negatively correlated with the lower track p_{T} threshold. However, at very high thresholds, too many tracks are removed from the summation. This results in unbalanced tracks in the event and is visible as peaks at the positive and negative ends of the $p_{\mathrm{x}}^{\mathrm{miss}}, p_{\mathrm{y}}^{\mathrm{miss}}$ distributions.

The resolutions in $p_{\mathrm{x}}^{\mathrm{miss}}, p_{\mathrm{y}}^{\mathrm{miss}}$ are determined from the widths of Figure 5.18 and are shown in Figure 5.19. As in the case for the $E_{\mathrm{x}}^{\mathrm{miss}}, E_{\mathrm{y}}^{\mathrm{miss}}$ resolution, it is assumed that the true $p_{\mathrm{x}}^{\mathrm{miss}}, p_{\mathrm{y}}^{\mathrm{miss}}$ is zero in minimum bias events. It is evident that even for the lowest track p_{T} threshold, the resolution is still better than that obtained using calorimeter cells. At the highest threshold, the resolution is improved by a factor of four. However, as stated above, the highest threshold removes too many tracks in the calculation of $p_{\mathrm{T}}^{\mathrm{miss}}$. Therefore, this work uses a lower track p_{T} threshold of 3 GeV, and hereafter this threshold will be implied unless stated otherwise. The mean $p_{\mathrm{x}}^{\mathrm{miss}}, p_{\mathrm{y}}^{\mathrm{miss}}$ is plotted in Figure 5.20 to show the bias (i.e. deviation from zero) for each threshold. The bias for the 3 GeV threshold is small, however it is subtracted before calculating the final $p_{\mathrm{T}}^{\mathrm{miss}}$ of each event.

Validation and Performance The correlation between $p_{\mathrm{T}}^{\mathrm{miss}}$ and the true neutrino p_{T} in a simulated sample of $W \to \mu\nu_{\mu}$ events is shown in Figure 5.21. The figure demonstrates that the correlation is better in more peripheral events, where smearing effects in the resolution are less
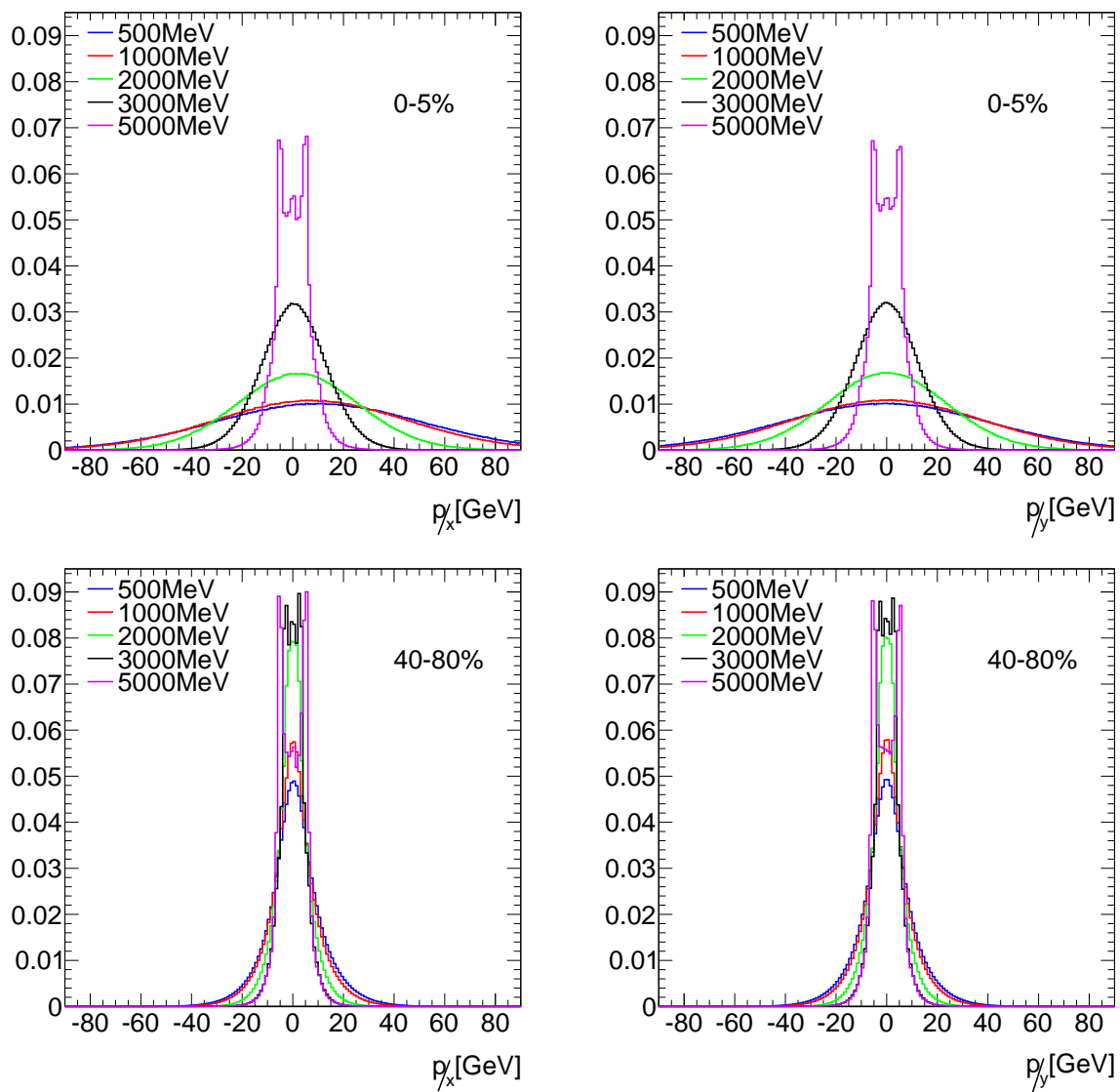
Figure 5.18: Distribution of p_x^{miss} (Left) and p_y^{miss} (Right) in a data sample of minimum bias Pb+Pb events. Distributions are shown for the most central 0-5% (Top) and peripheral 40-80% (Bottom) classes. The set of p_x^{miss}, p_y^{miss} distributions in each panel are calculated using various lower track p_T thresholds in the vector summation of Equation 5.16. All distributions are normalized to unity.

pronounced. The difference between the azimuthal angle of p_T^{miss} and the azimuthal angle of the neutrino as a function of the difference between the magnitude of the p_T^{miss} and neutrino p_T vectors is presented in Figure 5.22. Both central and peripheral events show a strong peak at zero, again
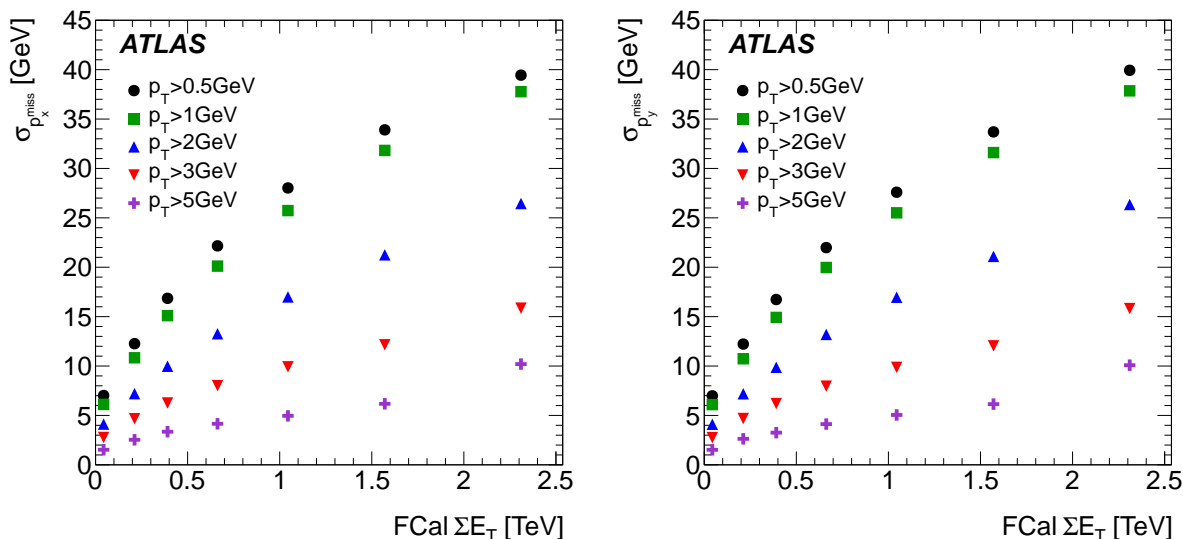
Figure 5.19: p_x^{miss} and p_y^{miss} resolution as a function of $\Sigma E_T^{\mathrm{FCal}}$ in a data sample of minimum bias Pb+Pb events. The distributions in each panel are shown for various lower track p_T thresholds used in the vector summation of Equation 5.16.

with a tighter correlation in peripheral events. Overall, the correlation between the p_T^{miss} and neutrino p_T is strong enough to reliably reconstruct the transverse mass of $W \to \mu\nu_\mu$ events in a heavy-ion environment.

The p_T^{miss} distributions from simulated $W \to \mu\nu_\mu$, QCD di-jet, $Z \to \mu^+\mu^-$, and $W \to \tau\nu_\tau$ events are shown in Figure 5.23. The distribution is plotted after applying the isolation, $m_{\mu\mu}$, and p_T^μ requirements discussed in Sections 5.4.2.1, 5.4.2.2, and 5.4.2.3. The distributions are normalized by their respective cross sections and are scaled to the number of binary collisions in the data, as in Figure 5.14. The figure shows that the number of background events declines rapidly with increasing p_T^{miss}. Therefore, a p_T^{miss} cut at 25 GeV is used as part of the signal selection criteria to increase the sample purity.

5.4.2.5 Transverse Mass m_T

p_T^{miss} and p_T^μ are used to reconstruct the transverse mass of the W boson:
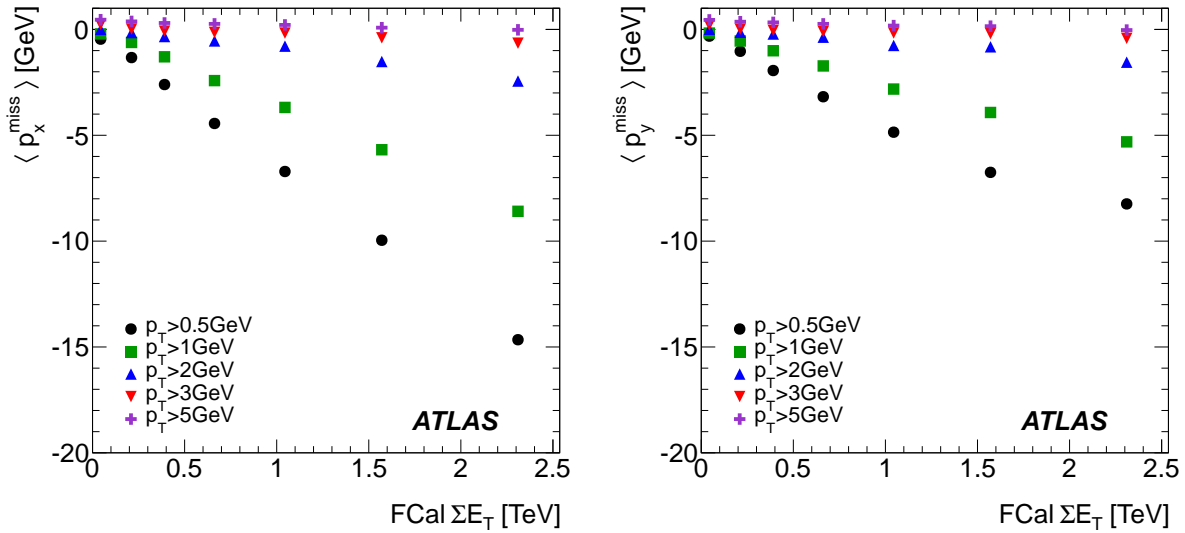
Figure 5.20: Mean p_x^{miss} and p_y^{miss} as a function of $\Sigma E_T^{\mathrm{FCal}}$ in a data sample of minimum bias Pb+Pb events. The distributions in each panel are shown for various lower track p_T thresholds used in the vector summation of Equation 5.16. Deviations from zero indicate a bias.
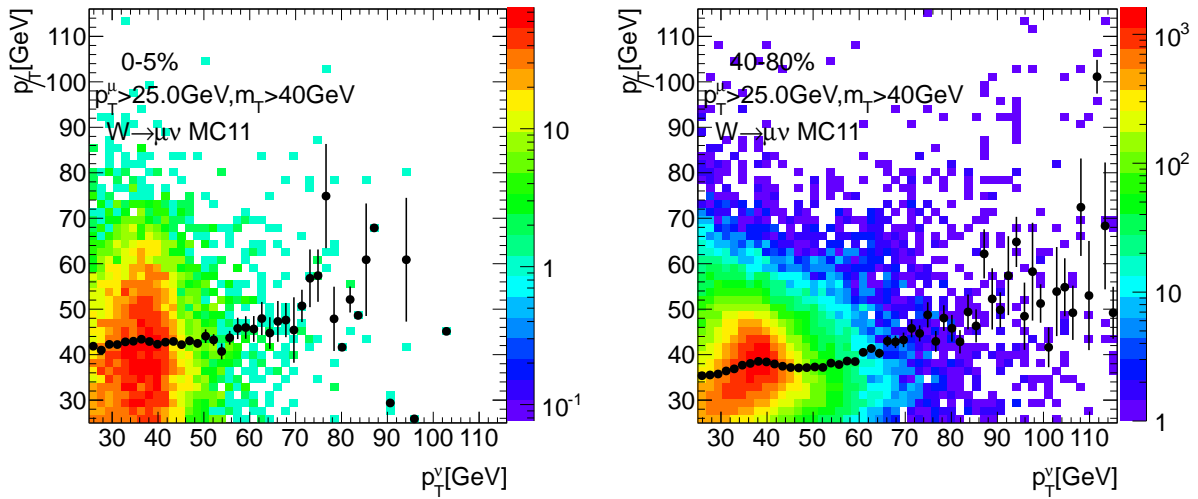
Figure 5.21: Correlation of p_T^{miss} with the true neutrino p_T in a simulated MC sample of $W \rightarrow \mu\nu_\mu$ events for the central 0-5% and peripheral 40-80% classes.
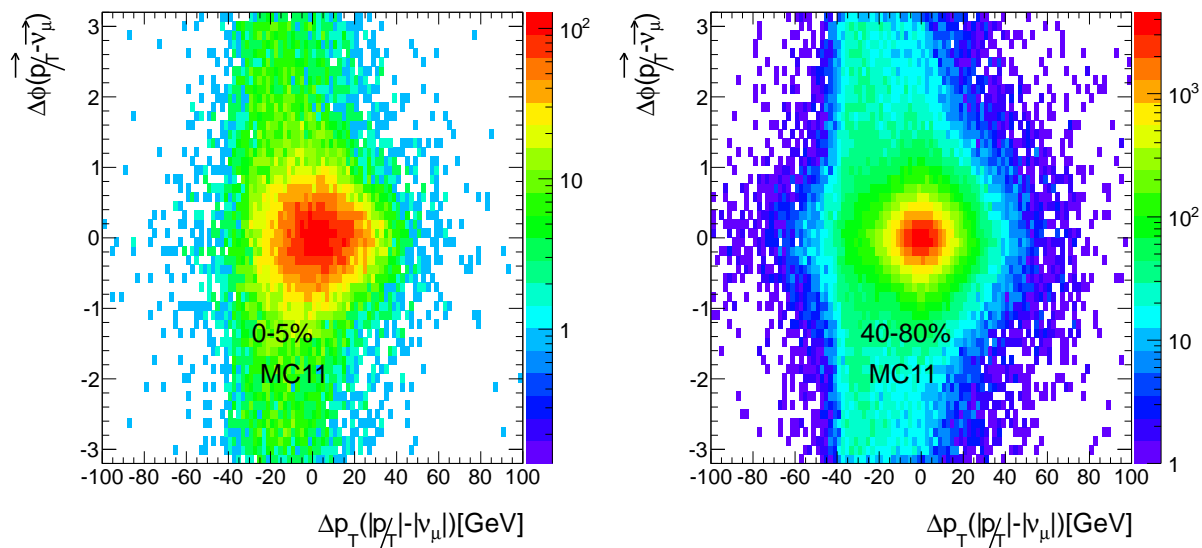
Figure 5.22: Difference in the azimuthal angle of the $p_\mathrm{T}^\mathrm{miss}$ vector and $p_\mathrm{T}^{\nu,truth}$ as a function of the difference in the magnitude of the $p_\mathrm{T}^\mathrm{miss}$ and $p_\mathrm{T}^{\nu,truth}$ vectors for the central 0-5% and peripheral 40-80% classes.

$$m_T^W = \sqrt{2p_\mathrm{T}^\mu p_\mathrm{T}^\mathrm{miss}(1 - \cos \Delta\phi_{\mu,p_\mathrm{T}^\mathrm{miss}})} \qquad (5.17)$$

where $\cos \Delta\phi_{\mu,p_\mathrm{T}^\mathrm{miss}}$ is the azimuthal separation between the p_T^μ and $p_\mathrm{T}^\mathrm{miss}$ vectors. The m_T distributions for simulated signal and background samples are shown in Figure 5.24. The distributions are normalized in the same manner as in Figures 5.14 and 5.23 and are plotted after all final selection cuts have been applied. The figure clearly shows that signal candidates start to dominate at $m_\mathrm{T} \approx 40$ GeV, which is the requirement used for selecting $W \to \mu\nu_\mu$ events in this work.

5.4.2.6   Signal Selection Chain

A summary of the final selection requirements is provided in Table 5.6. Also provided in the same table are the number and percentage of events in the data surviving each selection cut. The absolute percentage is calculated relative to the number of preselected muons, whereas the relative percentage is calculated relative to the preceding cut. Table 5.6 shows that the majority of muons are rejected after applying the p_T selection. After final selection, only 3.7% of preselected muons
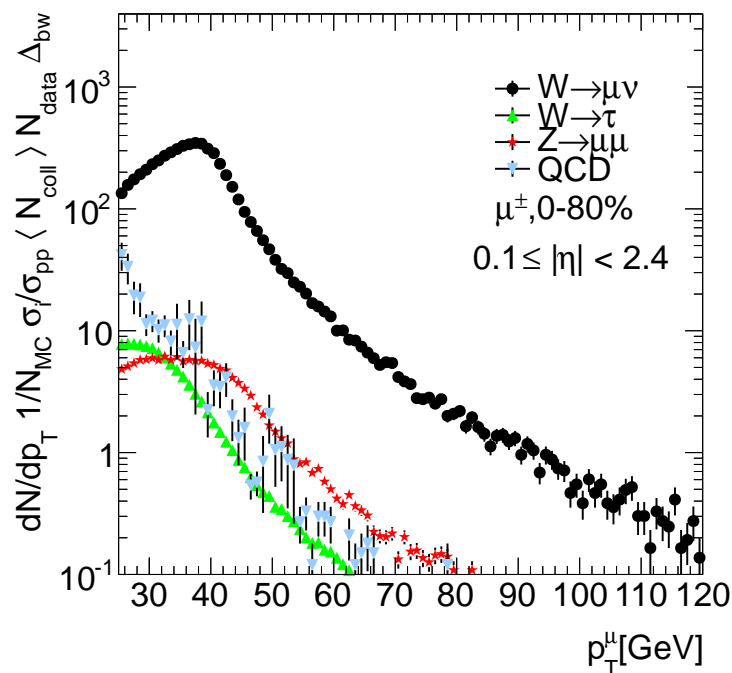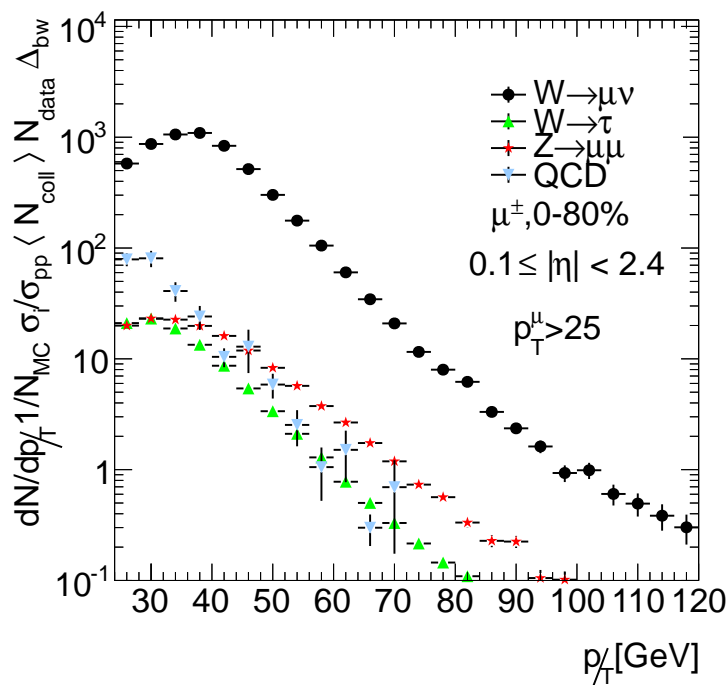
Figure 5.23: Muon p_T^{miss} distribution in simulated signal and background samples for preselected muons with p_T^μ and $p_T^{miss} > 25$ GeV after applying isolation and $m_{\mu\mu}$ requirements. The distributions are normalized by their respective cross sections and are scaled to the number of binary collisions in the data. The QCD multi-jet distribution is rescaled to take into account jet quenching.

are signal candidates.

Tables 5.7-5.10 present the same information as in Table 5.6 but for simulated $W \to \mu\nu_\mu$, QCD di-jet, $Z \to \mu^+\mu^-$, and $W \to \tau\nu_\tau$ events. Table 5.7 shows that $\sim 57\%$ of W candidates survive preselection to final selection. The p_T cut removes the majority of QCD di-jet and $W \to \tau\nu_\tau$ events, with the p_T^{miss} and m_T cuts also contributing. In the $Z \to \mu^+\mu^-$ sample, most of the Z candidates are removed by applying the $m_{\mu\mu}$ requirement. These data show that the analysis selection chain is very efficient at eliminating background events while maintaining a large concentration of signal candidates.

The distribution of W candidates per event in the data after final selection is presented in Figure 5.25. Events with zero candidates include events without a muon. One observed event has two W candidates. After final selection, the sample contains 3348 W^+ and 3185 W^- candidates.

Table 5.6: Number of events in the data surviving each analysis cut.

Pb+Pb Data 2011

Cut	Events	absolute eff. (%)	relative eff.(%)
Preselection	175792	-	-
Isolation	133929	76.2	76.2
$m_{\mu\mu} < 66$ GeV	132219	75.2	98.7
$p_\mathrm{T} > 25$ GeV	10092	5.7	7.6
$p_\mathrm{T}^{\mathrm{miss}} > 25$ GeV	6856	3.9	67.9
$m_\mathrm{T} > 40$ GeV	6533	3.7	95.3

Table 5.7: Number of events in the $W \to \mu\nu_\mu$ MC surviving each analysis cut.

$W \to \mu\nu_\mu$ MC

Cut	Events	absolute eff. (%)	relative eff.(%)
Preselection	355181	-	-
Isolation	346657	97.6	97.6
$m_{\mu\mu} < 66$ GeV	346187	97.5	99.9
$p_\mathrm{T} > 25$ GeV	255648	72.0	73.8
$p_\mathrm{T}^{\mathrm{miss}} > 25$ GeV	201972	56.8	79.0
$m_\mathrm{T} > 40$ GeV	200706	56.5	99.4

Table 5.8: Number of events in the QCD di-jet (Jx+1μ) MC surviving each analysis cut.

QCD Di-jet MC			
Cut	Events	absolute eff. (%)	relative eff.(%)
Preselection	4964700	-	-
Isolation	4089730	82.4	82.4
$m_{\mu\mu} < 66$ GeV	4088680	82.4	100
$p_\mathrm{T} > 25$ GeV	4077	0.08	0.1
$p_\mathrm{T}^\mathrm{miss} > 25$ GeV	1197	0.02	29.4
$m_\mathrm{T} > 40$ GeV	566	0.01	47.3

Table 5.9: Number of events in the $Z \rightarrow \mu\mu$ MC surviving each analysis cut.

$Z \rightarrow \mu\mu$ MC			
Cut	Events	absolute eff. (%)	relative eff.(%)
Preselection	557980	-	-
Isolation	543044	97.3	97.3
$m_{\mu\mu} < 66$ GeV	119509	21.4	22.0
$p_\mathrm{T} > 25$ GeV	60913	10.9	51.0
$p_\mathrm{T}^\mathrm{miss} > 25$ GeV	39423	7.1	64.7
$m_\mathrm{T} > 40$ GeV	37570	6.7	95.3
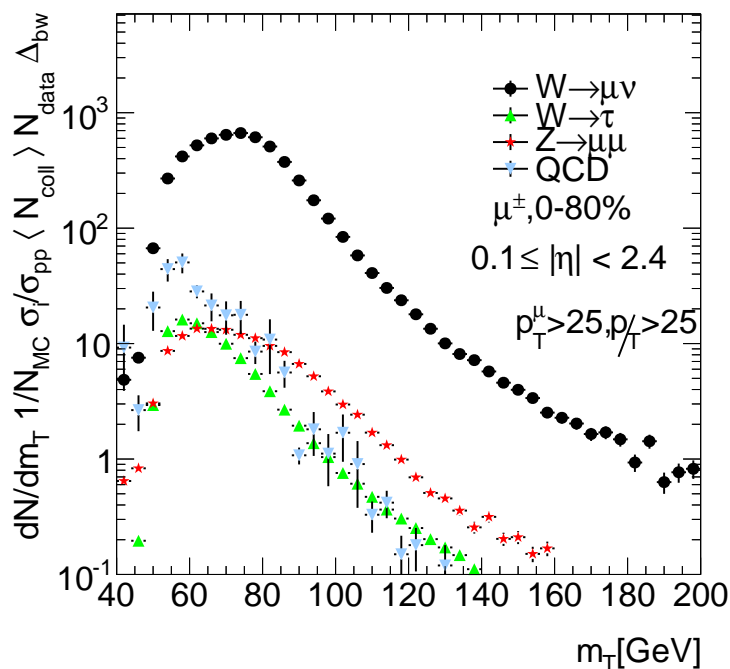
Figure 5.24: Muon m_T distribution in simulated signal and background samples for preselected muons with $p_T^\mu > 25$ GeV, $p_T^{miss} > 25$ GeV and $m_T > 40$ GeV after applying isolation and $m_{\mu\mu}$ requirements. The distributions are normalized by their respective cross sections and are scaled to the number of binary collisions in the data. The QCD multi-jet distribution is rescaled to take into account jet quenching.

5.5 Background Determination

After applying the final selection criteria, a non-negligble number of background events from QCD di-jet, $Z \to \mu^+\mu^-$, and $W \to \tau\nu_\tau$ processes remain in the data sample. Other background sources that are considered include $Z \to \tau\tau$ events where at least one τ decays into a muon and $t\bar{t}$ events where at least one t quark decays semileptonically. However, based on the cross sections of each channel [260, 261], their contributions are expected to be negligible ($< 0.2\%$) and thus are not considered in the total background estimation. This section describes how the major residual background sources are estimated and subtracted from the number of signal candidates.

Table 5.10: Number of events in the $W \to \tau\nu_\tau \to \mu\nu_\mu\nu_\tau\nu_\tau$ MC surviving each analysis cut.

	$W \to \tau\nu_\tau \to \mu\nu_\mu\nu_\tau\nu_\tau$ MC		
Cut	Events	absolute eff. (%)	relative eff.(%)
Preselection	641882	-	-
Isolation	626477	97.6	97.6
$m_{\mu\mu} < 66$ GeV	625628	97.5	99.8
$p_\mathrm{T} > 25$ GeV	290787	45.3	46.5
$p_\mathrm{T}^{\mathrm{miss}} > 25$ GeV	222106	34.6	76.4
$m_\mathrm{T} > 40$ GeV	222009	34.6	100
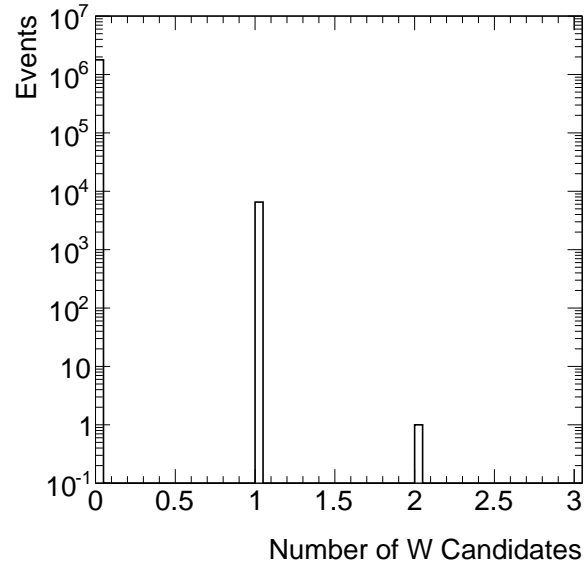
Figure 5.25: Distribution of the number of W candidates per event in the data after applying final selection requirements.

5.5.1 QCD Multi-Jet

As mentioned previously, muons from semileptonic decays of bottom and charm mesons ($B \to \mu + X$, $D \to \mu + X$) constitute a significant portion of background events. These types of muons are reduced mainly from the isolation and kinematic requirements discussed in the previous sections. However, muons produced in the high p_T tail of the QCD multi-jet distribution, in association with a significant amount of fake p_T^{miss} (e.g. jets produced outside the ID acceptance), can result in a small percentage of background contamination in the signal region. These types of muons are plotted in Figure 5.26, which shows the p_T^μ distributions for preselected muons from each simulated di-jet sample. The distributions are normalized to the respective di-jet cross sections, taking into account the probability of a $\mu+$jet event in each p_T region, and are scaled to the mean number of binary collisions in the data.
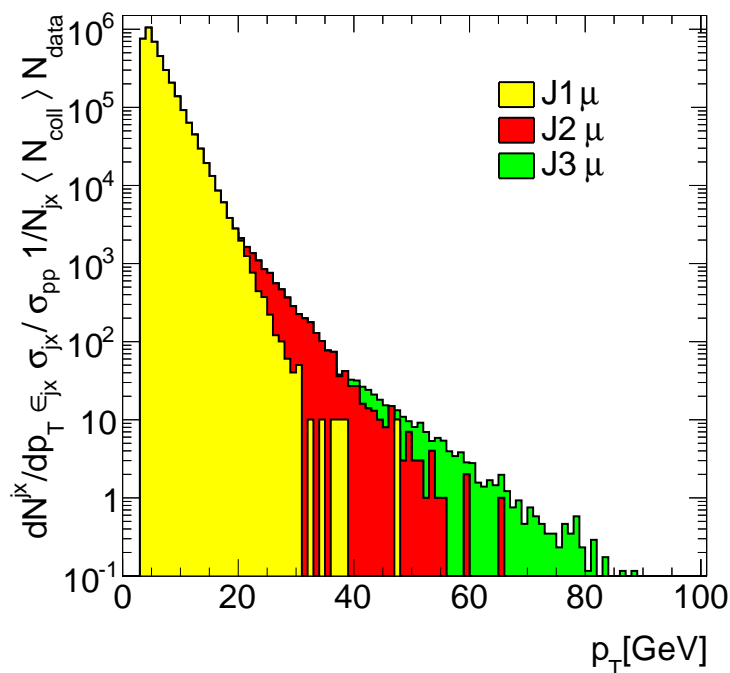
Figure 5.26: p_T^μ distributions for preselected muons from MC samples of QCD di-jet events. The QCD di-jet samples are normalized to their respective cross sections and are scaled to the mean number of binary collisions in the data. The probability of a muon-jet event in each energy region is taken into account.

Figure 5.27 shows the muon p_T distribution obtained from the combination of the QCD di-jet samples in Figure 5.26 (shaded histogram). To account for jet energy loss in the medium, a scale factor is determined by comparing the QCD di-jet distribution from MC to the muon p_T distribution from the data in the same phase space. The jet-quenching scale factor is calculated by scaling the MC distribution to the data in a control region dominated by QCD multi-jet events ($10 < p_\mathrm{T} < 20$ GeV). This procedure assumes that the scale factor is constant as a function of p_T. In Section 5.8, a systematic uncertainty is assigned to this assumption. The average scale factor is 0.4 over all $|\eta|$ and centrality classes and is independent of muon charge. The rescaled QCD di-jet distribution is included in Figure 5.27 (solid histogram).

As a cross-check, the shapes of QCD multi-jet distributions from data and MC simulation in the high p_T region are compared. The comparison is performed by inverting the isolation requirement from Section 5.4.2.1. The anti-isolation requirement is applied to both the QCD multi-jet and data samples, as shown in Figure 5.28. In this figure, the data are shown before and after applying the anti-isolation requirement, as well as after subtracting the estimated signal leakage from $W \to \mu\nu_\mu$ events (triangle points). The resulting distribution is compared to the QCD multi-jet distribution after anti-isolation has been applied (solid histogram). The distribution from MC simulation is normalized to the expected number of events in the data. The slight excess at $p_\mathrm{T} \approx 40$ GeV is mainly due to unsubtracted $Z \to \mu^+\mu^-$ and $W \to \tau\nu_\tau$ events. The overall shapes of the data and QCD multi-jet MC sample are in agreement, further validating the background estimation procedure.

5.5.1.1 QCD Background Fraction

After applying the scaling procedure described above, the estimated fraction of signal candidates from QCD multi-jet events is determined by applying the final selection requirements to both the data and background sample, as shown in Figure 5.29 for μ^+ and μ^- events. No charge dependence is observed, and so the background fraction f_{QCD} is only calculated as a function of $|\eta|$ and centrality, as shown in Figure 5.30. The left panel of Figure 5.30 also shows the integrated background fraction, which is approximately 3.7% of the number of signal candidates. The background fraction as a function of centrality decreases linearly from peripheral to mid-central events due to jet quenching. However, in more central collisions, the centrality dependence of the signal selection
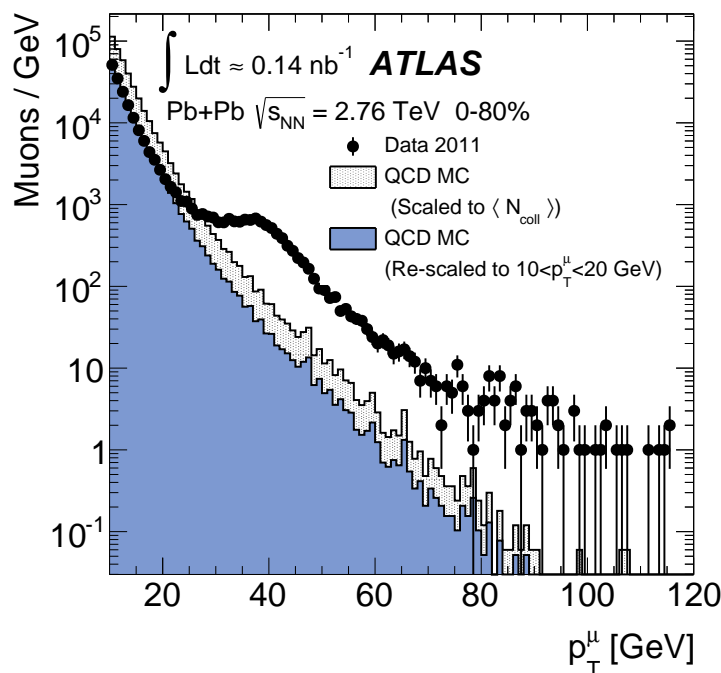
Figure 5.27: Muon p_T distribution in the data after preselection (points). p_T distributions from QCD multi-jet processes from MC simulation is shown in the same figure. The shaded histogram is scaled to the mean number of binary collisions in the data but does not take into account jet quenching. The solid histogram takes into account jet quenching by the use of a scale factor, which is determined in a background control region defined by $10 < p_T < 20$ GeV. Using this procedure, the QCD multi-jet background fraction can be determined from the number of muons surviving final selection requirements [40].

starts to play a role. The larger background fraction at mid-rapidity than at forward rapidity can be explained by the different kinematics between muons from QCD multi-jet processes and $W \to \mu\nu_\mu$ decays (i.e. the η distributions for $W \to \mu\nu_\mu$ events have longer tails).

5.5.2 Electroweak

Background contributions from $Z \to \mu^+\mu^-$ and $W \to \tau\nu_\tau \to \mu\nu_\mu\nu_\tau\nu_\tau$ events are collectively referred to as *electroweak background*. This background source is less than the background from QCD multi-jet processes but is still large enough that it cannot be neglected.
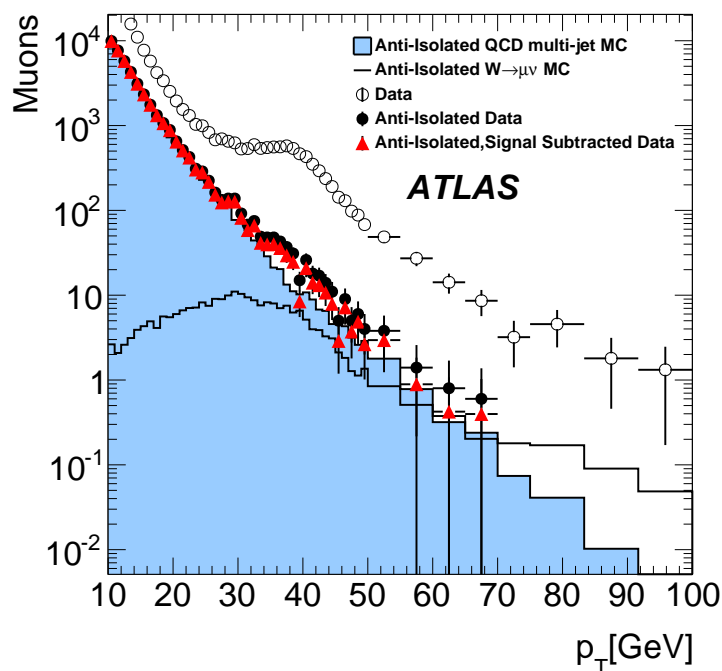
Figure 5.28:   Muon p_T distributions in the data before applying the anti-isolation requirements (open circles), after applying the anti-isolation requirement (points), and after signal subtraction (triangles). The distribution from the data is compared to an anti-isolated QCD multi-jet sample (solid histogram). The QCD multi-jet sample is normalized to the expected number of events in the data.

5.5.2.1 $Z \to \mu^+\mu^-$

A large percentage of $Z \to \mu^+\mu^-$ events are removed by applying the $m_{\mu\mu}$ requirement discussed in Section 5.4.2.2. However, if one muon from the decay is produced outside the detector acceptance, a dimuon pair cannot be formed and furthermore, the event will have large spurious p_T^{miss}. These types of events are unavoidable and increase the electroweak background in the signal region.

To demonstrate this mechanism, a toy model of $Z \to \mu^+\mu^-$ events at generator level is used to track the muon produced outside the acceptance, which will be called the "lost muon." The other muon from the Z decay is matched to a reconstructed muon. Figure 5.31 shows a distribution of the azimuthal separation between the lost muon and p_T^{miss} vectors. The lost muon and p_T^{miss} are taken from the same event. This distribution shows the lost muon is in the same direction as that
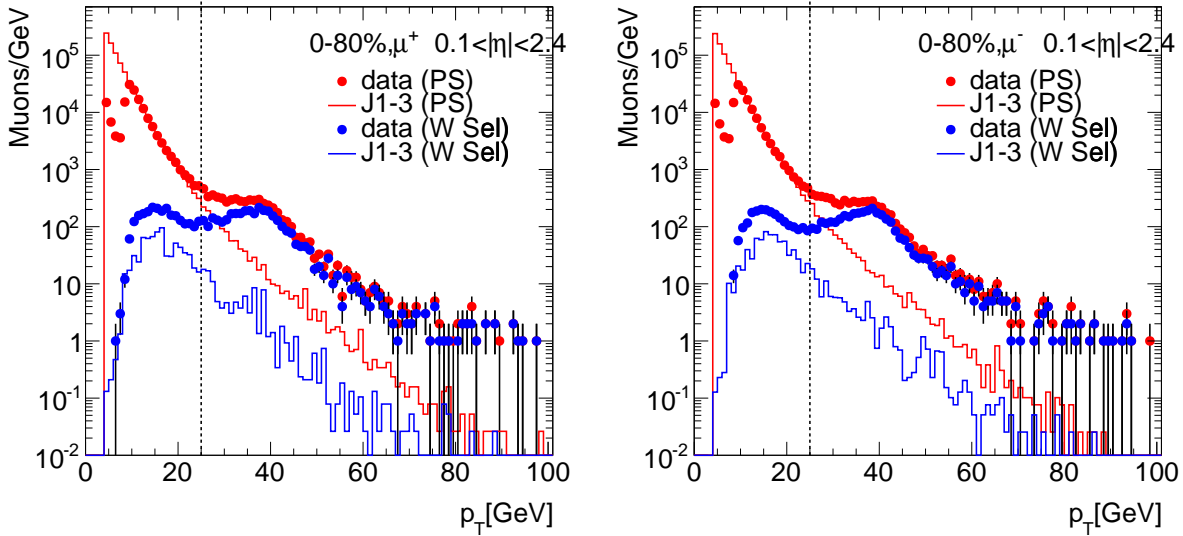
Figure 5.29:   Reconstructed p_T spectra for μ^+ and μ^- from data (points) and QCD multi-jet MC simulation (histograms) before (red; PS=preselection) and after (blue; WSel=W selection) applying final selection criteria. The spectra are integrated over all centrality classes ($0 - 80\%$) and pseudorapidity ($0.1 < |\eta| < 2.4$) windows. The background fraction is determined from the MC/Data ratio after final selection has been applied.

of the p_T^{miss} vector, implying that in these events the p_T^{miss} is fake and attributed to the lost muon. This is further supported by Figure 5.32, which presents the η distribution of the lost muon. As expected, this muon is produced either outside the MS acceptance ($\eta > 2.5$) or in regions of poor MS coverage: the gap region at $\eta \approx 0$ and the barrel/end-cap transition region at $\eta \approx 1.05$.

$Z \rightarrow \mu^+\mu^-$ **Background Fraction**   The fraction of signal candidates from $Z \rightarrow \mu^+\mu^-$ events is determined using the measured cross section in Pb+Pb collisions at $\sqrt{s_{\mathrm{NN}}}$=2.76 TeV [38]. However, since two muons are produced per Z boson, one must be careful to use the correct fraction. The fraction of *single muons* surviving final selection per $Z \rightarrow \mu^+\mu^-$ event is estimated from MC simulation. This fraction is then applied to the corresponding number of measured $Z \rightarrow \mu^+\mu^-$ events, resulting in the number of background muons in each centrality class and $|\eta|$ window. If N_{μ_Z} represents the number of single muons from $Z \rightarrow \mu^+\mu^-$ events surviving final selection, the background can be expressed as:
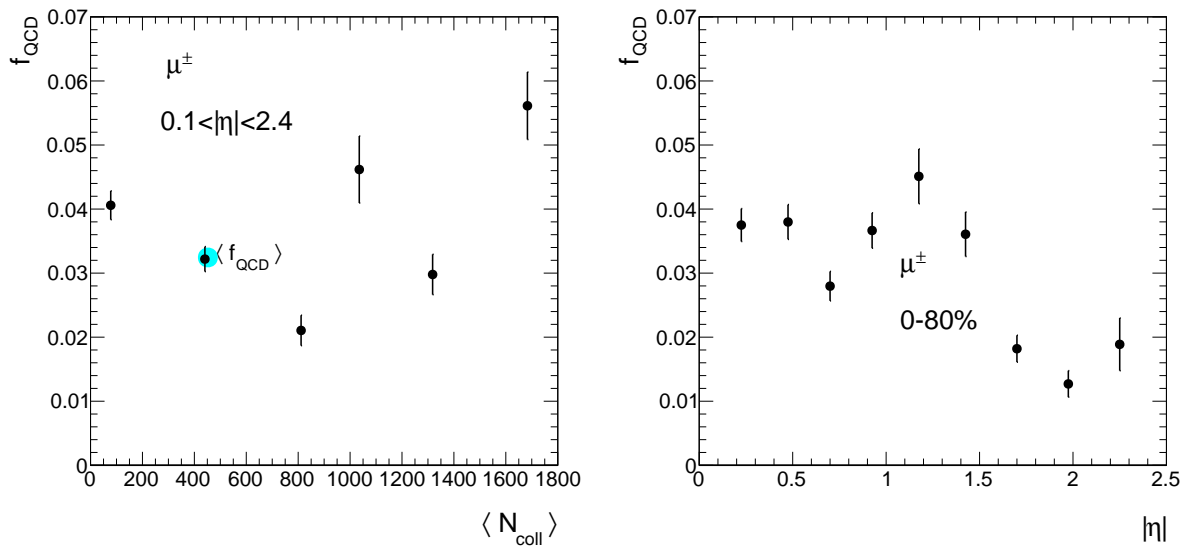
Figure 5.30: Charge inclusive ($\mu^\pm$) QCD multi-jet background fraction as a function of centrality class (Left) and $|\eta|$ (Right). Error bars are statistical only.

$$N_{\mu_Z} = \frac{N_{\mu_Z}^{\text{selected}}}{N_Z^{\text{generated}}} \cdot N_Z^{\text{data}} \tag{5.18}$$

where *selected* represents those muons surviving final selection and *generated* signifies the total number of $Z \to \mu^+\mu^-$ events from MC simulation. The fraction of signal candidates in the data from $Z \to \mu^+\mu^-$ events f_Z is plotted in Figure 5.33 as a function of centrality and $|\eta|$. The integrated background percentage is approximately 2.4% of the number of signal candidates. Very little charge and centrality dependence is observed in f_Z, whereas there may be a slight η dependence, which again can be attributed to the different kinematics between $W \to \mu\nu_\mu$ and $Z \to \mu^+\mu^-$ events.

5.5.2.2 $W \to \tau\nu_\tau \to \mu\nu_\mu\nu_\tau\nu_\tau$

$W \to \tau\nu_\tau \to \mu\nu_\mu\nu_\tau\nu_\tau$ events are associated with large $p_{\text{T}}^{\text{miss}}$, and therefore the $p_{\text{T}}^{\text{miss}}$ and m_{T} requirements are not as effective at reducing this background source. Additionally, the muons are isolated. However, since the muon is produced from the τ lepton rather than directly from the W boson, the p_{T} distribution will be softer than for prompt muons from $W \to \mu\nu_\mu$ events (see Figure 5.14).
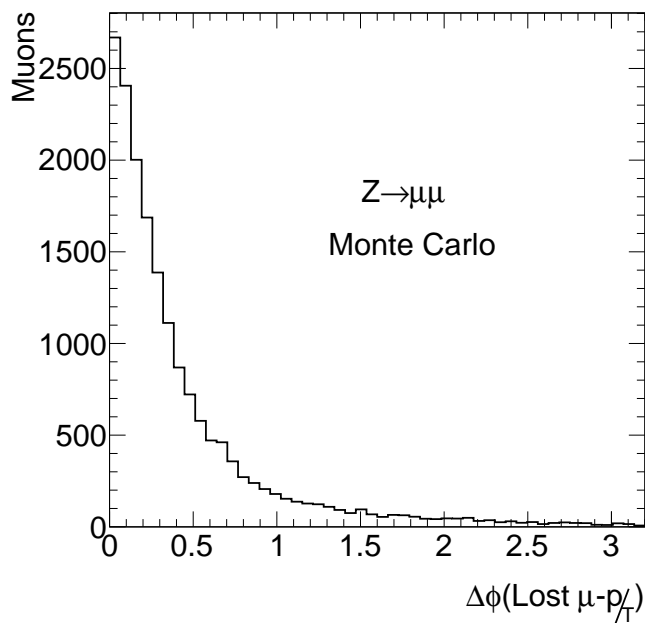
Figure 5.31: $\Delta\phi$ of the "lost muon" from a $Z \to \mu^+\mu^-$ decay and the $p_{\mathrm{T}}^{\mathrm{miss}}$ vector in a MC toy-model.

$W \to \tau\nu_\tau \to \mu\nu_\mu\nu_\tau\nu_\tau$ **Background Fraction** To determine the fraction of signal candidates from $W \to \tau\nu_\tau \to \mu\nu_\mu\nu_\tau\nu_\tau$ events, the branching ratios for the $W \to \tau\nu_\tau$ (11.25%), $W \to \tau\nu_\tau \to \mu\nu_\mu\nu_\tau\nu_\tau$ (17.4%), and $W \to \mu\nu_\mu$ (10.57%) channels [2] are used to calculate the number of $W \to \tau\nu_\tau \to \mu\nu_\mu\nu_\tau\nu_\tau$ events per $W \to \mu\nu_\mu$ event:

$$\left(\frac{\sigma_{W\to\tau\nu_\tau\to\mu\nu_\mu\nu_\tau\nu_\tau}}{\sigma_{W\to\mu\nu_\mu}}\right) = \left(\frac{\sigma_{W\to\tau\nu_\tau\to\mu\nu_\mu\nu_\tau\nu_\tau}}{\sigma_{W\to\tau\nu_\tau}}\right) \cdot \left(\frac{\sigma_{W\to\tau\nu_\tau}}{\sigma_W}\right) \cdot \left(\frac{\sigma_W}{\sigma_{W\to\mu\nu_\mu}}\right) \tag{5.19}$$

The MC simulation is then used to estimate the fraction of $W \to \mu\nu_\mu$ events and fraction of $W \to \tau\nu_\tau \to \mu\nu_\mu\nu_\tau\nu_\tau$ events passing final selection requirements: $f_{W\to\mu\nu_\mu}$ and $f_{\tau\to\mu\nu\nu}$, respectively. Equation 5.19 is used with $f_{W\to\mu\nu_\mu}$ and $f_{\tau\to\mu\nu\nu}$ to calculate the background fraction in the data:

$$f_\tau \equiv \frac{N_{W\to\tau\nu_\tau\to\mu\nu_\mu\nu_\tau\nu_\tau}^{\mathrm{selected}}}{N_{W\to\mu\nu_\mu}^{\mathrm{selected}}} = \left(\frac{\sigma_{W\to\tau\nu_\tau\to\mu\nu_\mu\nu_\tau\nu_\tau}}{\sigma_{W\to\tau\nu_\tau}}\right) \cdot f_{W\to\mu\nu_\mu} \cdot f_{\tau\to\mu\nu\nu} \tag{5.20}$$

where *selected* represents the number of events passing final selection requirements. Figure 5.34 shows the background fraction in the data from τ leptons as function of $|\eta|$ for each centrality class.
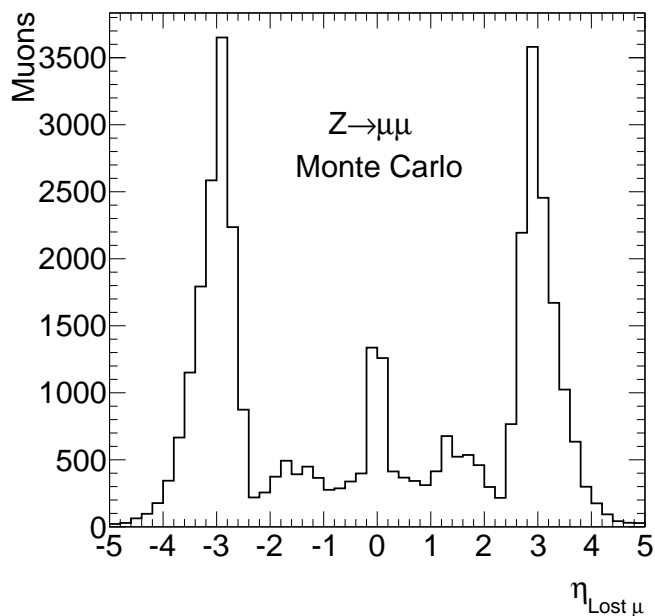
Figure 5.32: η distribution of the "lost muon" from a $Z \to \mu^+\mu^-$ decay in a MC toy-model.
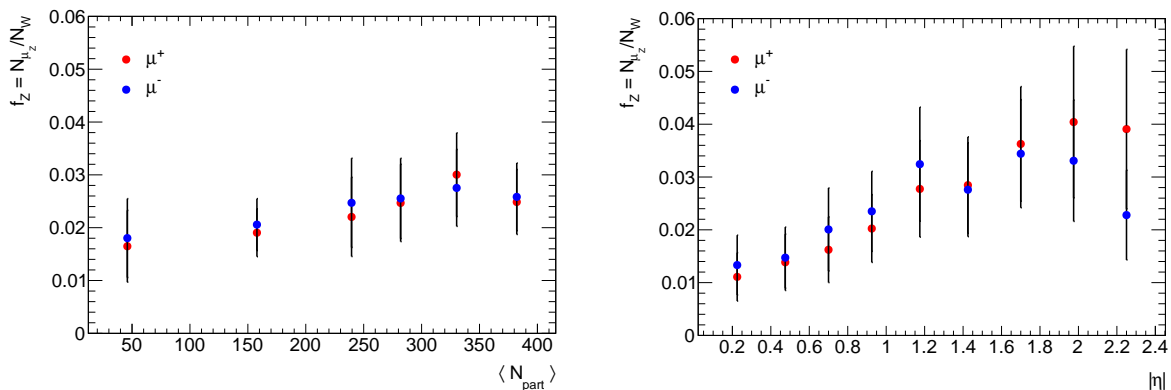
Figure 5.33: Single muon background fraction from $Z \to \mu^+\mu^-$ events as a function of centrality class (Left) and $|\eta|$ (Right). Error bars are statistical only and include errors from the measured Z measurement.

The integrated background percentage is approximately 1.5% of the number of $W \to \mu\nu_\mu$ events.
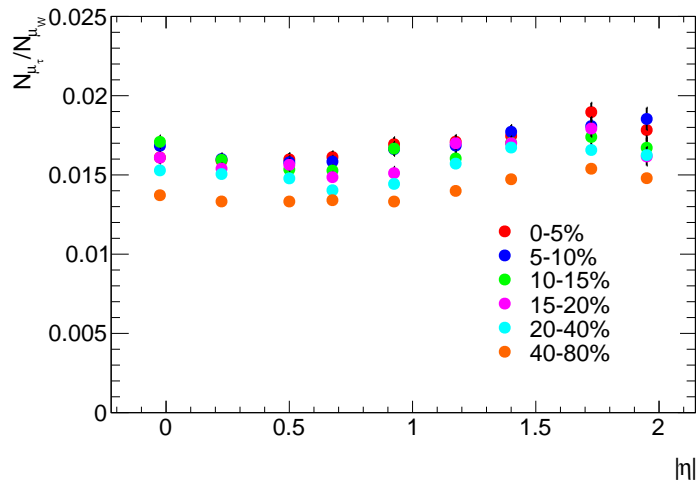
Figure 5.34: Background fraction from $W \to \tau\nu_\tau \to \mu\nu_\mu\nu_\tau\nu_\tau$ events as a function of $|\eta|$ in each centrality class. Error bars are statistical only.

5.6 Muon Trigger and Reconstruction Efficiencies

To better understand muon losses at high p_T due to inefficiencies in the triggers and reconstruction, events from both the data and MC simulation are used. The single muon reconstruction efficiencies are studied using MC simulation of $Z \to \mu^+\mu^-$ events. The dimuon pairs from Z boson decays offer a low background sample for estimating muon performance in a heavy-ion environment. The reconstruction efficiency is defined as the fraction of generated muons that can be matched to reconstructed objects. This implies that a muon produced from the collision but not reconstructed counts as an inefficiency. However, the reconstruction efficiency is distinguished from losses due to detector coverage by considering only muons generated in the fiducial volume [2] of the detector. Figure 5.35 presents the combined muon reconstruction efficiencies from simulated $Z \to \mu^+\mu^-$ events as a function of generated muon p_T and η. This figure shows efficiencies from both the Muid and Staco reconstruction chains as well as from a merged sample of the two. The merged chain slightly increases the efficiency by approximately 1-2%. As stated previously in Chapter 4,

---

[2] The *fiducial volume* denotes a clearly defined region of phase space where the ATLAS detector operates with high efficiency. This is defined as $p_T^l > 25$ GeV, $p_T^{\text{miss}} > 25$ GeV, $m_T > 40$ GeV, and $0.1 < |\eta| < 2.4$ for muons in this work.

this work uses the Muid chain, which has an integrated efficiency of approximately 97%. The reconstruction efficiencies show no p_T dependence, and as expected, are lower in the MS gap region at $\eta \approx 0$ and barrel/end-cap transition regions at $|\eta| \approx 1.05$. The centrality dependence as a function of generated p_T and $|\eta|$ for the most central 0-5% and peripheral 60-80% classes are shown in Figure 5.36. The efficiencies are approximately 1-3% higher in peripheral events due to the higher occupancy of the ID in central Pb+Pb collisions.
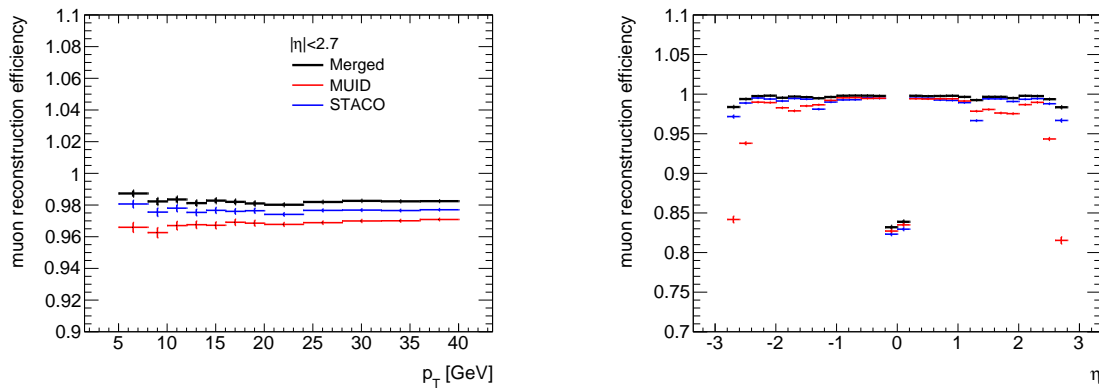
Figure 5.35: Combined muon reconstruction efficiencies as a function of generated p_T (Left) and η (Right) from simulated $Z \rightarrow \mu^+\mu^-$ events in Pb+Pb. Errors are statistical only.
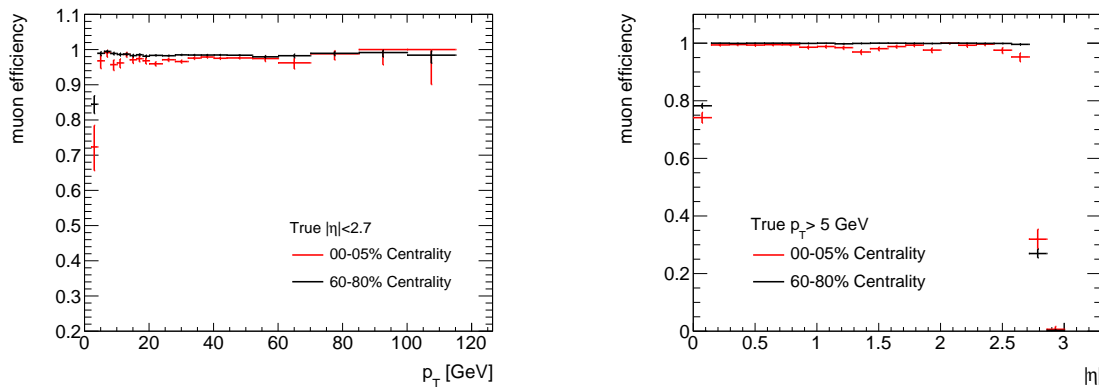
Figure 5.36: Combined muon reconstruction efficiencies as a function of generated p_T (Left) and $|\eta|$ (Right) from simulated $Z \rightarrow \mu^+\mu^-$ events in central (0-5%) and peripheral (60-80%) classes. Errors are statistical only.

The muon triggers used in this work were discussed in Section 5.1.1. Their efficiencies are determined using a minimum bias sample from the data. The trigger efficiency $\epsilon^{\mu}_{\text{trig}}$ is defined with respect to reconstructed muons as:

$$\epsilon^{\mu}_{\text{trig}} = \frac{N_{\mu}(\Phi, \text{trig}, \text{matched})}{N_{\mu}(\Phi)} \tag{5.21}$$

where the numerator represents the number of reconstructed muons in phase space Φ that triggered readout of the event and can be matched to an online trigger object (see Section 5.4.1), and the denominator represents the total number of reconstructed muons in the same phase space.

Since multiple single muon triggers are used, the efficiencies are evaluated from the union of triggered minimum bias events (i.e. the muon must have fired at least one of the triggers). The trigger efficiency as a function of muon p_{T} integrated over $0.1 < |\eta| < 2.4$ and centrality 0-80% is shown in Figure 5.37. The efficiencies are obtained by fitting the distributions to the functional form:

$$\epsilon^{\mu}_{\text{trig}}(p_{\text{T}}) = \epsilon_0 \left[1 + \text{erf} \left(\frac{p_{\text{T}} - p_{\text{T}}^{\text{thresh}}}{s} \right) \right] \tag{5.22}$$

where there are three free parameters: ϵ_0 is a scale fractor that determines the plateau efficiency, $p_{\text{T}}^{\text{thresh}}$ is the "effective" trigger threshold, and s accounts for the slope in the turn-on region. The efficiencies in each $|\eta|$ window and centrality class are evaluated from the plateau efficiency. These values are reported in Table 5.11. Lower efficiencies are expected in the RPCs due to limited coverage in the barrel region and in the outer edges of the TGCs where the magnetic field bends muons away from the acceptance. However, the full scan triggers recover some of these muons. The binning in Table 5.11 is slightly different than the binning used for $W \rightarrow \mu\nu_{\mu}$ events due to limited statistics in the minimum bias sample. However, this bin granularity is sufficient to capture the variation of the efficiencies in different η regions and centrality classes.

5.7 Yield Correction Procedure

The number of raw $W \rightarrow \mu\nu_{\mu}$ events in the data is obtained by subtracting the estimated background from the number of signal candidates. The raw signal counts are corrected for inefficiencies attributed to the triggers, reconstruction, and final selection requirements. The efficiency correc-
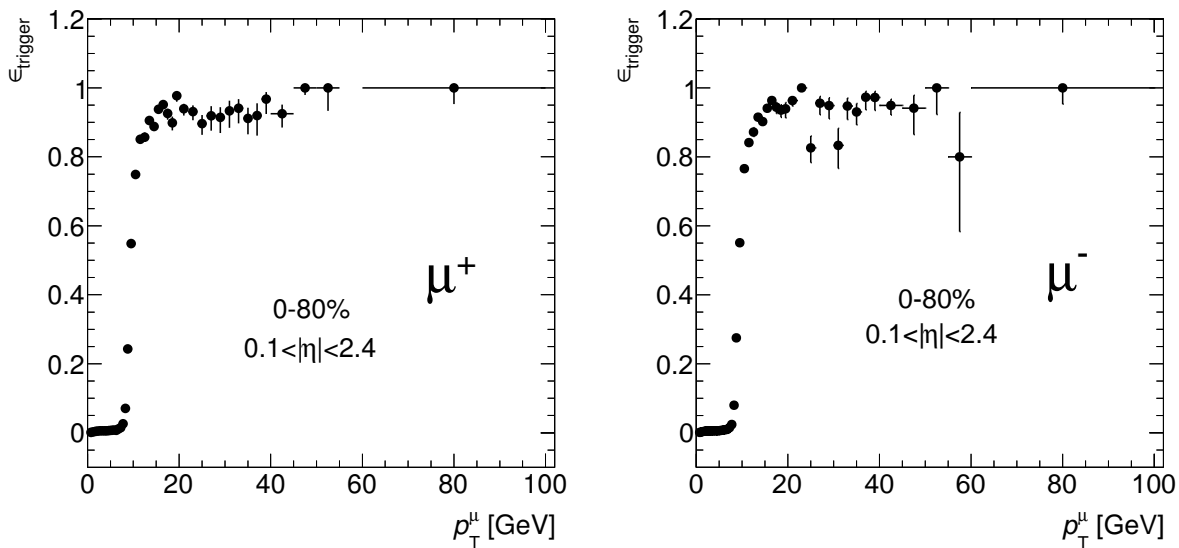
Figure 5.37: Single muon trigger efficiency from minimum bias events as a function of p_T for μ^+ (Left) and μ^- (Right) for $0.1 < |\eta| < 2.4$ and centrality 0-80%. The plateau efficiency is from Equation 5.22 is used to correct the W yields. This is performed in each η and centrality class (Table 5.11).

tion factor can be factorized into two components: one that corrects for signal losses in the fiducial region (C_W) and another that corrects for losses outside measurement regions of the detector (A_W).

5.7.1 C_W

The C_W is used to calculate *fiducial yields* and is defined as:

$$C_{W\pm} = \frac{N_{W\pm}^{\mathrm{rec}}}{N_{W\pm}^{\mathrm{gen,fid}}}, \tag{5.23}$$

where N_W^{rec} represents the number of $W \rightarrow \mu\nu_\mu$ events reconstructed in the fiducial region (i.e. satisfying final selection criteria) and $N_W^{\mathrm{gen,fid}}$ signifies the number of $W \rightarrow \mu\nu_\mu$ events in the same phase space at generator level. Equation 5.23 corrects for signal losses due to the selection requirements, reconstruction, and triggers. However, it does not account for signal events lost due to limited detector coverage. The trigger efficiencies are determined from the data (Table 5.11) and the selection and reconstruction efficiencies are taken from MC simulation. $N_W^{\mathrm{gen,fid}}$ is evaluated

Centrality	$|\eta|$	$\epsilon_{\text{trig}}^{\mu}[\%]$
	(0.0-1.2)	92.7±1.1
(0-10)%	(1.2-2.0)	91.0±0.8
	(2.0-2.5)	89.3±2.8
	(0.0-1.2)	96.4±1.1
(10-20)%	(1.2-2.0)	95.7±0.6
	(2.0-2.5)	98.0±3.4
	(0.0-1.2)	99.6±0.6
(20-40)%	(1.2-2.0)	97.5±0.5
	(2.0-2.5)	95.9±2.6
	(0.0-1.2)	98.7±1.0
(40-80)%	(1.2-2.0)	96.9±0.9
	(2.0-2.5)	99.3±3.2

Table 5.11: Single muon trigger efficiencies $\epsilon_{\text{trig}}^{\mu}$ for muons with $p_{\text{T}} > 25$ GeV as a function of $|\eta|$ and centrality.

directly from the W boson (Born level). This accounts for effects due to bin migration and QED radiation. Migration effects are at most $\sim 0.3\%$ of reconstructed signal events in any given $|\eta|$ bin. This is illustrated in Figure 5.38. which shows the fraction of reconstructed $W \rightarrow \mu\nu_{\mu}$ events generated in the same bin.

The C_W distributions as a function of $|\eta|$ for the most central (0-5%) and peripheral (40-80%) centrality classes are shown in Figure 5.39 for both $W^+ \rightarrow \mu^+\nu_{\mu}$ and $W^- \rightarrow \mu^-\bar{\nu}_{\mu}$ events. Very little charge dependence is observed and the integrated $C_{W^\pm}$ is $(67.4 \pm 0.2)\%$, ranging from 32% in the most central events at forward $|\eta|$ to 85% in the most peripheral events at $0.5 < |\eta| < 1$. The reason for this variation is two-fold: the detector geometry affects the reconstruction and trigger efficiencies, and therefore C_W will be lower in some regions; and the isolation and $p_{\text{T}}^{\text{miss}}$ resolution are centrality dependent.
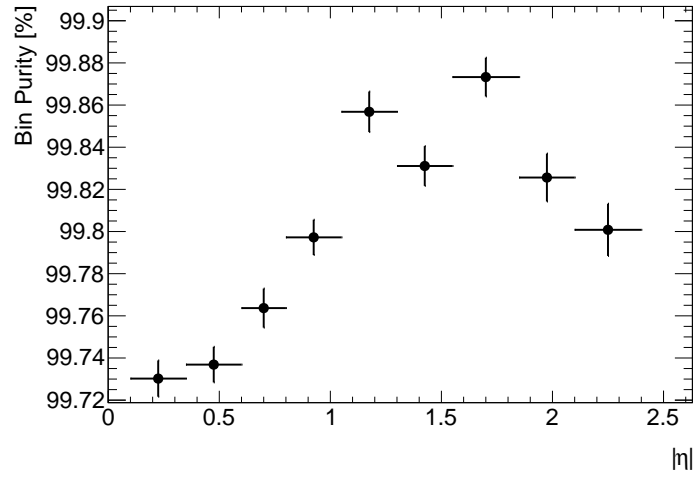
Figure 5.38: Bin purity, defined as the percentage of reconstructed $W \to \mu\nu_\mu$ events generated in the same $|\eta|$ bin.
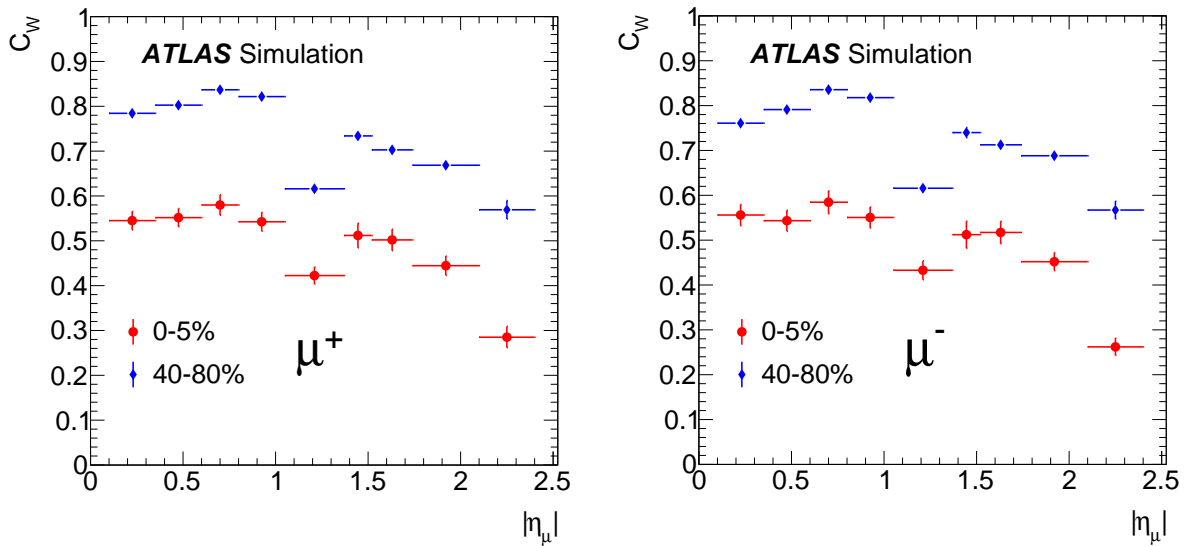
Figure 5.39: C_W distribution as a function of $|\eta|$ for the most central (0-5%) and peripheral (40-80%) centrality classes for $W^+ \to \mu^+\nu_\mu$ (Left) and $W^- \to \mu^-\bar{\nu}_\mu$ (Right) events.

5.7.2 A_W

The A_W is defined as:

$$A_{W^\pm} = \frac{N_{W^\pm}^{\text{gen,fid}}}{N_{W^\pm}^{\text{gen,all}}} \tag{5.24}$$

where $N_W^{\text{gen,fid}}$ is the denominator of Equation 5.23 and signifies events generated in the fiducial region and $N_W^{\text{gen,all}}$ represents all generated $W \to \mu\nu_\mu$ events. The A_W in Equation 5.24 can be used to extrapolate the yields over the entire phase space, which is required when reporting the total integrated cross section. However in this work, only the fiducial W production yields are determined and the A_W is only used to express the yields from the muon and electron channels in a common phase space. A discussion of the channel combination and extrapolated yields will be deferred to Chapter 6.

Figure 5.40 presents the η distributions for $N_W^{\text{gen,fid}}$ and $N_W^{\text{gen,all}}$ in Equation 5.24. The integrated A_{W^+} and A_{W^-} values are 54.4% and 53.6%, respectively. The latter is slightly lower since a larger fraction of $W^- \to \mu^-\bar{\nu}_\mu$ events are produced at large η, outside the detector acceptance.
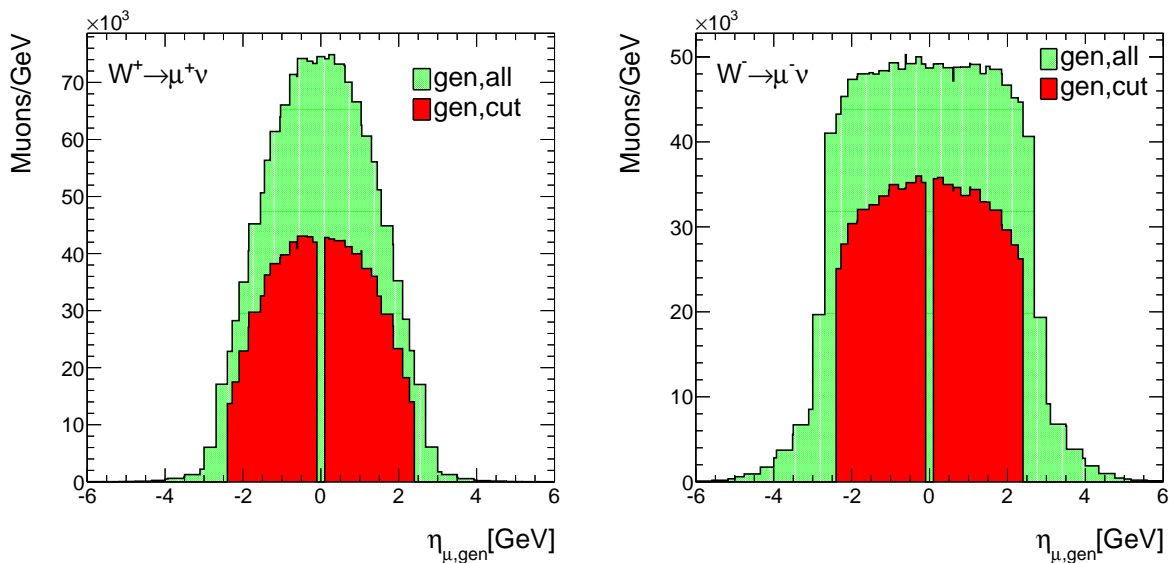
Figure 5.40: Pseudorapidity distributions of $W \to \mu\nu_\mu$ events at generator level for μ^+ (Left) and μ^- (Right) in the fiducial region (gen,cut) and over all phase space (gen,all).

5.8 Systematic Uncertainties

This final section discusses the different sources of systematic uncertainty. Uncertainties correlated between different $|\eta|$ bins and between different centrality classes are distinguished from bin-uncorrelated uncertainties. The bin-correlated uncertainties consist of uncertainties in the $p_\mathrm{T}^\mathrm{miss}$ resolution, background estimation, isolation, reconstruction efficiency, muon p_T resolution, yield extrapolations, and $\langle N_\mathrm{coll} \rangle$. All other uncertainties are uncorrelated between bins. The bin-correlated uncertainties are also distinguished from uncertainties correlated between the muon and electron channels, and this will be discussed in Chapter 6.

5.8.1 $p_\mathrm{T}^\mathrm{miss}$ Resolution

As illustrated in Figure 5.19, the resolution in $p_\mathrm{x}^\mathrm{miss}, p_\mathrm{y}^\mathrm{miss}$ varies with the event multiplicity and lower track p_T threshold used to calculate $p_\mathrm{T}^\mathrm{miss}$ (Equation 5.16). The lower track p_T threshold of 3 GeV was chosen based on two factors: improvement in the $p_\mathrm{T}^\mathrm{miss}$ resolution and low spurious $p_\mathrm{T}^\mathrm{miss}$. The uncertainty in the resolution stems from the uncertainty in the vector summation, which determines the direction and magnitude of the $p_\mathrm{T}^\mathrm{miss}$ vector. Simply smearing the magnitude and azimuthal angle of the vector event-by-event results in a large correlation with the statistical uncertainties of the W candidates. Therefore, the uncertainty in the resolution is evaluated by varying the lower track p_T threshold by ± 1 GeV. Lowering the threshold increases the soft particle contribution in the summation and slightly worsens the resolution. Raising the threshold slightly improves the resolution but also removes tracks, introducing additional sources of spurious $p_\mathrm{T}^\mathrm{miss}$. To observe the effect on the data, Figure 5.41 shows the $p_\mathrm{T}^\mathrm{miss}$ for signal candidates in the 0-5% and 40-80% centrality classes using a lower track p_T threshold of 3 ± 1 GeV. The soft contribution pushes the $p_\mathrm{T}^\mathrm{miss}$ to the tails and has a larger impact on central than peripheral events. Raising the threshold focuses the distribution at ~ 40 GeV. This may be the result of a better resolution in the $p_\mathrm{T}^\mathrm{miss}$ or a consequence of the muon p_T vector biasing the $p_\mathrm{T}^\mathrm{miss}$ reconstruction since less tracks are used in the vector summation.

The uncertainty is determined by recalculating the W yields after varying the threshold. In this procedure, the correction factors and background are also recalculated. The resulting variation in the yields is in the range of 2-4%.
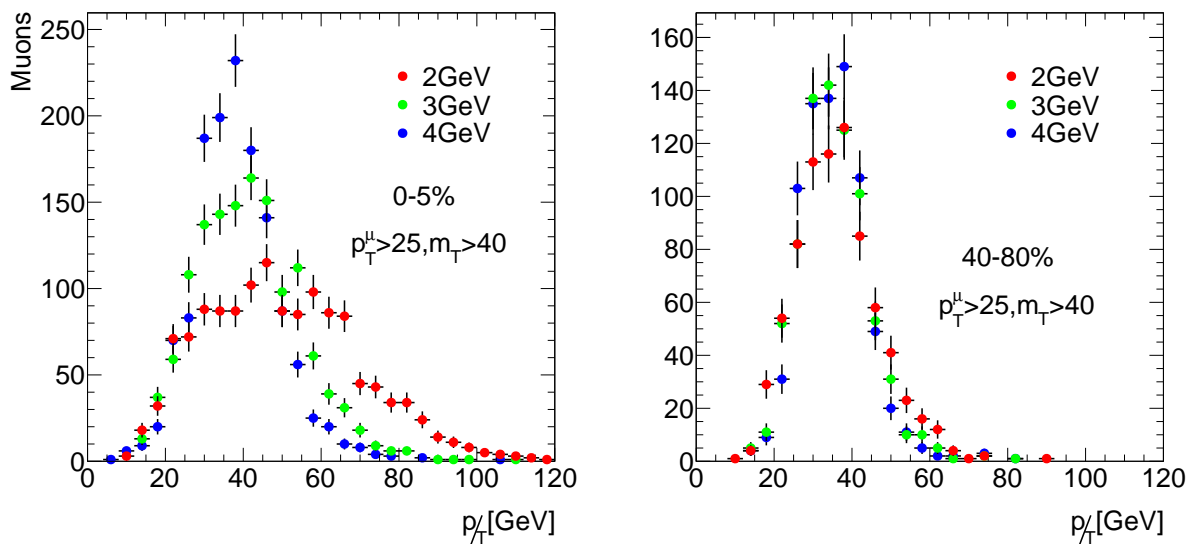
Figure 5.41: p_T^{miss} distribution for $W \to \mu\nu_\mu$ signal candidates in the data using lower track p_T thresholds of $2\,\text{GeV}, 3\,\text{GeV}$, and $4\,\text{GeV}$ to calculate the vector summation. The distributions are shown for the 0-5% (Left) and 40-80% (Right) centrality classes.

5.8.2   Background Estimation

5.8.2.1   QCD Multi-Jet

Uncertainties in the background estimation of QCD multi-jet events is attributed to the extrapolation at high p_T (see Figure 5.27). There are two contributing factors to the uncertainty in the extrapolation procedure: the modeling accuracy of the MC simulation relative to the data in the high p_T region and the effect of jet energy loss in the medium. To assess the uncertainty attributed to these contributions, the QCD multi-jet distributions are reweighted by a nuclear modification factor R_{AA} that measures the extent of jet quenching by using a baseline measurement from pp collisions. This is used in lieu of reweighting the QCD multi-jet distribution to a control region. The R_{AA} is defined as:

$$R_{AA}(p_T) = \frac{\text{d}^2 N_{ch}^{AA}/\text{d}p_T\text{d}\eta}{\langle T_{AA}\rangle \text{d}^2 \sigma_{ch}^{pp}/\text{d}p_T\text{d}\eta} \tag{5.25}$$

where $N_{\mathrm{ch}}^{\mathrm{AA}}$ is the charged particle yield per event in Pb+Pb collisions and $\sigma_{\mathrm{ch}}^{\mathrm{pp}}$ is the charged particle cross section in *pp* collisions. The $\langle T_{\mathrm{AA}} \rangle \equiv \langle N_{\mathrm{coll}} \rangle / \sigma_{\mathrm{inel}}^{NN}$ is the nuclear overlap function and is used to express the Pb+Pb yields as a per-nucleon cross section in each centrality class. The distributions of the R_{AA} as a function of p_{T} in several centrality classes are shown in Figure 5.42. Reweighting by the R_{AA} assumes the modification for heavy-flavor muons is similar to that for inclusive charged particles, which is a reasonable assumption[262, 263].
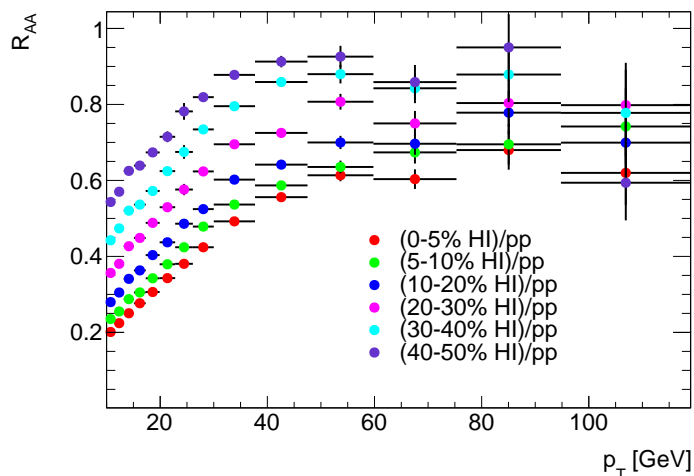
Figure 5.42: Charged particle R_{AA} in Pb+Pb data as a function of p_{T} in different centrality classes.

After reweighting the QCD multi-jet distributions by the R_{AA}, the background fractions and W boson yields are recalculated. Figure 5.43 shows the reweighted QCD di-jet p_{T} distributions in the 0-5% and 40-80% centrality classes along with the measured distributions from the data. These figures are shown at preselection level and after W selection (analogous to Figure 5.29). Figure 5.44 shows the nominal background fraction using the original reweighting procedure and the background fraction after reweighting with the R_{AA}. The background fraction changes by a maximum of 50%, corresponding to a variation in the W yields of 0.2-2%.

5.8.2.2 Electroweak

The uncertainty in the $Z \rightarrow \mu^+ \mu^-$ background estimation arises from the uncertainty in the Z boson cross section. This uncertainty is determined by substituting the measured $Z \rightarrow \mu^+ \mu^-$ yields with the yields estimated from MC simulation and varies the W yields by $< 0.1\%$.
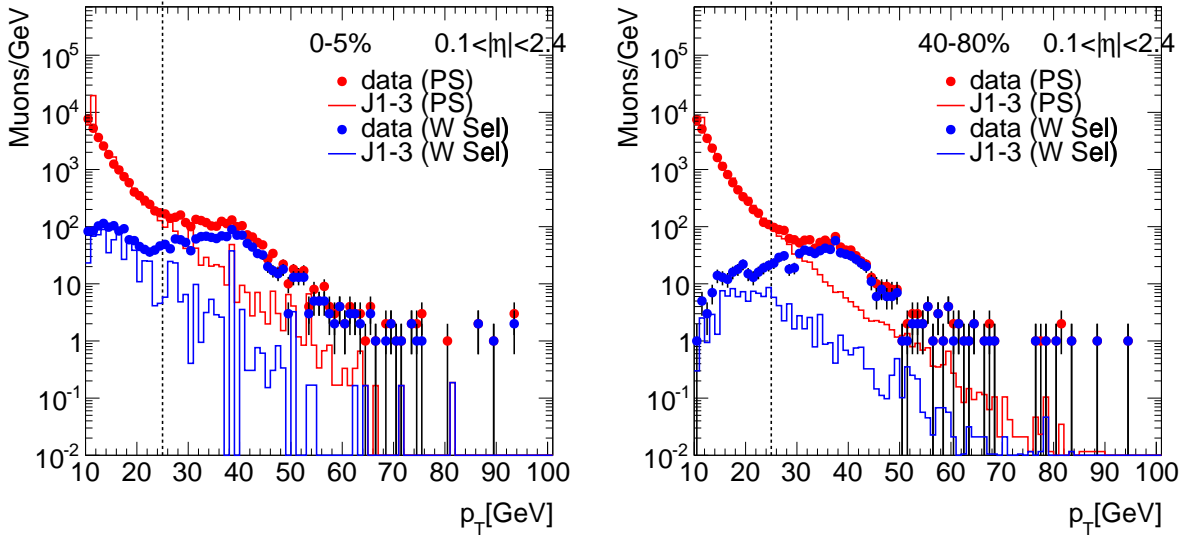
Figure 5.43: Muon p_T spectra in the 0-5% (Left) and 40-80% (Right) centrality classes from data (points) and QCD multi-jet MC simulation (histograms) before (red; PS=preselection) and after (blue; WSel=W selection) applying final selection criteria. The QCD multi-jet distributions are reweighted using the R_{AA} from the corresponding centrality class (see Figure 5.42). The background fraction is determined from the MC/Data ratio after final selection has been applied.

The major contribution to the uncertainty in the $W \to \tau\nu_\tau$ background is also the uncertainty in the fraction of the cross section sampled in the signal region. This uncertainty is evaluated by assuming the selection efficiencies for the p_T^{miss} and m_T requirements in the signal region are identical in the $W \to \tau\nu_\tau \to \mu\nu_\mu\nu_\tau\nu_\tau$ and $W \to \mu\nu_\mu$ channels. Recalculating the number of background events results in a variation in the signal yields no larger than 0.1%.

Since the number of events in the $Z \to \tau\tau$ and $t\bar{t}$ channels are considered negligible ($< 0.2\%$), their small contribution is also added as a systematic uncertainty.

5.8.3 Isolation

The muon isolation is optimized with respect to the background rejection power ϵ_B, signal efficiency ϵ_S, and effective signal N_{eff} (see Figures 5.9 and 5.10). Using these criteria, the optimal working point is determined to be $i_\mu \equiv \frac{\sum_{i=min}^{N_{trk}} p_{T,i}^{trk} - p_{T,trk}^\mu}{p_T^\mu} < 0.1$ using a lower track p_T threshold of 3 GeV and
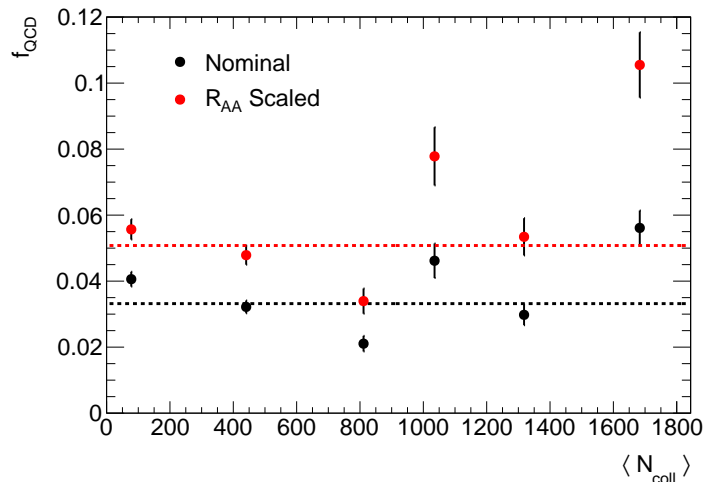
Figure 5.44: QCD multi-jet background fraction using the original reweighting procedure (nominal; black points) and using the R_{AA} (red points). The dotted lines are zeroth order fits.

$\Delta R < 0.2$. However, other isolation definitions have similar performance. This uncertainty in the optimization translates to an uncertainty in the number of signal candidates. The systematic error is estimated by varying the isolation working point. The upper threshold on ΔR is expanded from 0.2 to 0.3 and i_μ is loosened from 0.1 to 0.2, as shown schematically in Figure 5.45 in (ϵ_B, ϵ_S) space. The variation in the working point causes a variation in the W yields of 1-2% in any centrality class or $|\eta|$ interval.

5.8.4 Correction Factors C_W

The systematic uncertainty in the C_W is attributed to errors in the muon reconstruction efficiency, trigger efficiency, and momentum resolution. The momentum resolution [41] is parametrized in the ID by the quadratic sum :

$$\frac{\sigma_{\mathrm{ID}}(p_{\mathrm{T}})}{p_{\mathrm{T}}} = a_{\mathrm{ID}}(\eta) \oplus b_{\mathrm{ID}}(\eta) \cdot p_{\mathrm{T}} \quad \text{for } 0 < |\eta| < 2;$$
$$\frac{\sigma_{\mathrm{ID}}(p_{\mathrm{T}})}{p_{\mathrm{T}}} = a_{\mathrm{ID}}(\eta) \oplus \frac{b_{\mathrm{ID}}(\eta) \cdot p_{\mathrm{T}}}{\tan^2 \theta} \quad \text{for } 2 < |\eta| < 2.5 \quad (5.26)$$

and in the MS by:
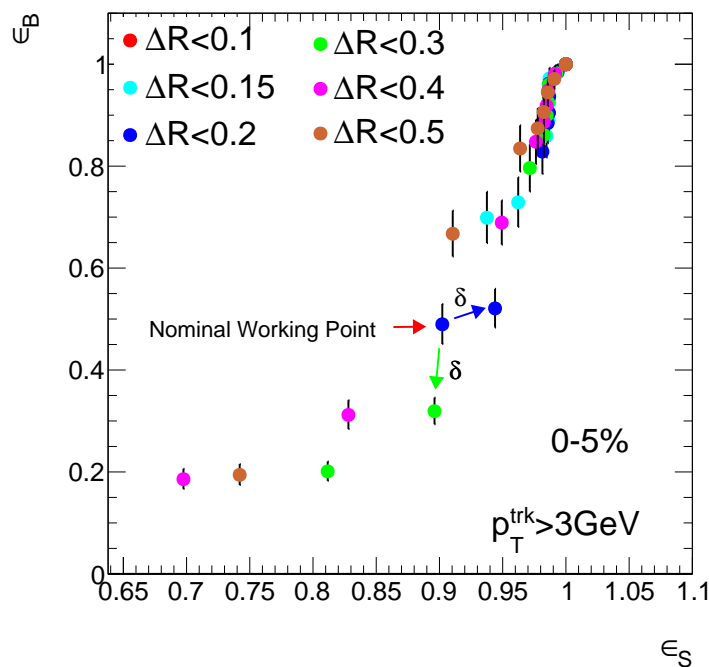
Figure 5.45: Schematic of the variation in the isolation working point in (ϵ_B, ϵ_S) space. The two variations (designated δ) correspond to expanding the ΔR from 0.2 to 0.3 and loosening i_μ from 0.1 to 0.2.

$$\frac{\sigma_{SA}(p_{\mathrm{T}})}{p_{\mathrm{T}}} = a_{\mathrm{MS}}(\eta, \phi) \oplus b_{\mathrm{MS}}(\eta, \phi) \cdot p_{\mathrm{T}} \oplus \frac{c(\eta, \phi)}{p_{\mathrm{T}}} \tag{5.27}$$

where $a_{\mathrm{ID(MS)}}$ account for multiple scattering in the detector material, the second terms describe the intrinsic resolution caused by imperfect knowledge of the magnetic field in the ID and MS, and the third term in Equation 5.27 parametrizes fluctuations in the muon energy loss in the calorimeters. The resolutions are derived from the dimuon invariant mass resolution in $Z \to \mu^+ \mu^-$ decays, $\sigma_{m_{\mu\mu}}$. The measured $\sigma_{m_{\mu\mu}}$ is translated into the momentum resolutions in Equations 5.26 and 5.27 by smearing the generated muon momenta by amounts necessary to reproduce the measured invariant mass distribution. This procedure involves varying b_{ID} and a_{MS}. The momentum resolutions for the barrel and end-cap regions from pp collisions are shown in Figure 5.46 for the ID and MS components. The errors are derived from the parameters in the resolution functions, and the resolutions from MC simulation are shown before and after smearing.
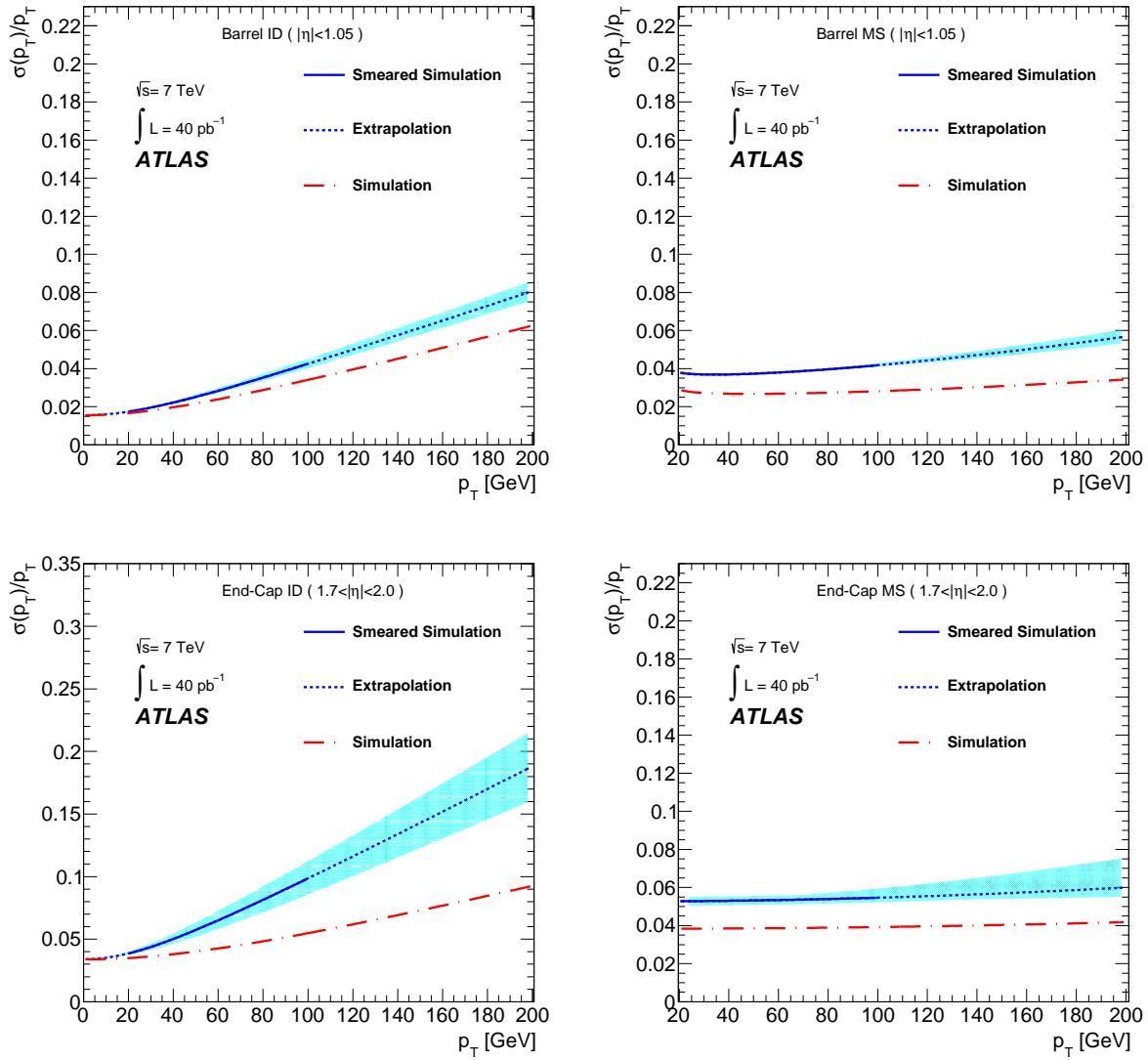
Figure 5.46: Muon momentum resolution in the ID and MS as a function of p_T for the barrel (Top) and end-cap (Bottom) regions. The dot-dashed line is from simulation and assumes perfect detector alignment. The solid/dotted line shows the simulation after smearing to reproduce the measured invariant mass distribution in the data. The solid section shows the measured resolutions, and the dotted section is an extrapolation. Uncertainties in the measured are derived from the parameters in the resolution functions (Equations 5.26 and 5.27) [41].

The momentum resolution is worse in the data than in MC simulation. The differences are partly attributed to residual misalignments of the ID and MS and are considered a source of systematic uncertainty in this analysis. The magnitude of the error is determined by smearing the generator-level muon p_T in $W \to \mu\nu_\mu$ events within the systematic uncertainties of the parameters [264] in Equations 5.26 and 5.27. The correction factors are recalculated, resulting in a variation in the W yields of $< 1\%$.

The uncertainty in the muon reconstruction efficiency at high p_T is determined from a sample of $Z \to \mu^+\mu^-$ decays. To estimate this uncertainty, the ratio of the number of muon pairs reconstructed in both the ID and MS and muon pairs reconstructed in the MS, without any restriction on the ID component, is calculated in both the data and MC simulation. This procedure yields the discrepancy in the combined muon reconstruction efficiency between the data and MC simulation. The events in the MC simulation are reweighted such that the pair ratio agrees with the data. The correction factors are then reevaluated, resuling in a systematic uncertainty of 1.0% in the signal yields.

The uncertainty in the trigger efficiency is obtained by comparing efficiencies calculated using a minimum bias sample of muons and efficiencies determined using a tag-and-probe method with $Z \to \mu^+\mu^-$ decays. The tag-and-probe method requires two oppositely charged muons: a "tag" and a "probe. The tag is a high-quality combined muon that triggered the event. The probe is any type of muon with $p_T > 10$ GeV. The trigger efficiency is calculated based on the fraction of probes that also triggered the readout of the event. Comparisons of the trigger efficiencies using each method are provided below as a function of muon η and p_T. Recalculating the correction factors with the tag-and-probe efficiencies results in a W yield variation of approximately 0.4%.

5.8.5 N_{coll} and N_{part}

The uncertainties in $\langle N_{part} \rangle$ and $\langle N_{coll} \rangle$ are determined by varying parameters in the Glauber MC. The variations consist of:

- Varying the nuclear radius $R \pm 0.06$ fm and skin thickness $a = 0.546 \pm 0.01$ fm by their respective standard deviations.

- A 2% variation in the sampling fraction of the total Pb+Pb inelastic cross section.
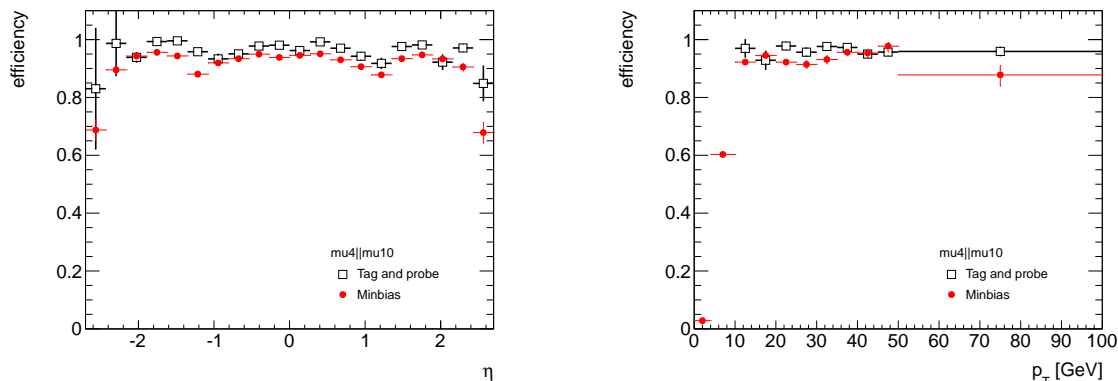
Figure 5.47: Comparison of muon trigger efficiencies obtained from a minimum bias (points) sample and from a tag-and-probe (open squares) method as a function of η (Left) and p_T (Right).

- A variation in $\sigma_{\text{inel}}^{\text{NN}} = 64$ mb by ± 5 mb.

For each variation, new N_{coll} and N_{part} values are obtained and the global fits are reperformed. The uncertainties are shown in Table 5.3 and are correlated across all centrality bins.

5.8.6 Yield Extrapolation A_W

As stated above, the A_W is used to extrapolate the muon and electron yields into a common phase space. For muons, the extrapolation is performed in the regions $0 < |\eta| < 0.1$ and $2.4 < |\eta| < 2.5$. Uncertainties in this procedure are attributed to the PDF used in the MC simulation of $W \rightarrow \mu\nu_\mu$ events. The systematic uncertainties in the PDF are obtained by combining the following components:

- Uncertainties within the CT10 PDF set, derived from the eigenvector error sets at 90% C.L. limit.

- Uncertainties due to differences between different PDF sets, estimated from the maximum difference between CTEQ 6.6 [265], ABKM095fl [266], HERAPDF 1.0 [267], MSTW2008 [268], CT10W [246], and NNPDF2.1 [269]. The CT10 samples are reweighted event-by-event to the other PDFs [270].

- Uncertainties in the modeling of the hard scattering process of W production, derived from comparisons between `MC@NLO` and `POWHEG` using the CT10 PDF set and parton showering from `PYTHIA`.

- Uncertainties in the description of the parton showering and hadronization, derived from the difference in the acceptances calculated by `POWHEG` with different showering and hadronization algorithms from `HERWIG` and `PYTHIA`.

These contributions result in a systematic uncertainty of $\approx 0.3\%$ in the yields of the extrapolated regions.

5.8.7 Summary of Systematic Uncertainties

Table 5.12 provides a summary of the maximum values of the systematic uncertainties. Figure 5.48 shows the relative contributions of each systematic uncertainty as a function of $|\eta|$ and centrality class for both $W^+ \to \mu^+ \nu_\mu$ and $W^- \to \mu^- \bar{\nu}_\mu$ events. The largest source of error (other than that attributed to $\langle N_{\mathrm{coll}} \rangle$) is from the $p_{\mathrm{T}}^{\mathrm{miss}}$ resolution. These errors are added in quadrature to give a maximum total systematic uncertainty in any bin of $\approx 5\%$.

Table 5.12: Maximum values of the relative systematic uncertainties in the number of $W \to \mu\nu_\mu$ events in each $|\eta_\mu|$ interval and centrality class. Correlated uncertainties represent those that are correlated as a function of centrality or $|\eta_\mu|$. Bin–uncorrelated uncertainties represent statistical uncertainties in the background estimation, trigger efficiencies, and yield correction factors.

Source	Uncertainty [%]
$p_{\mathrm{T}}^{\mathrm{miss}}$ resolution	4.0
QCD multi–jet background	2.0
Electroweak $+ t\bar{t}$ backgrounds	0.2
Muon isolation	2.0
Muon reconstruction	1.0
Muon p_{T} resolution	1.0
Muon trigger efficiency	0.4
Extrapolation correction	0.3
Total bin–correlated	5.2
$\langle N_{\mathrm{coll}} \rangle$ determination	9.4
Total bin–uncorrelated	3.0
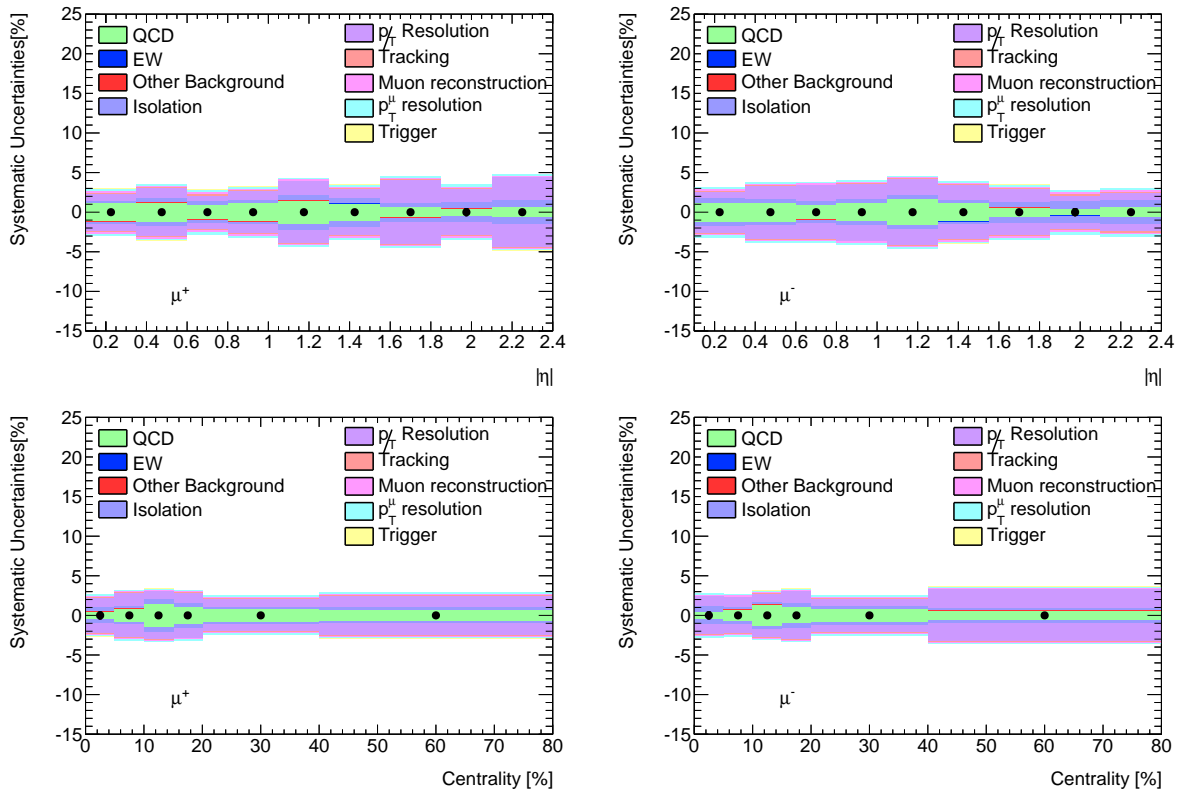
Figure 5.48: Relative systematic uncertainties as a function of $|\eta|$ (Top) and centrality class (Bottom) for μ^+ (Left) and μ^- (Right). These uncertainties are treated in the analysis as fully correlated across $|\eta|$ and centrality class. The figures do not include errors from $\langle N_{\mathrm{coll}} \rangle$.

Chapter 6

Results and Discussion

6.1   Kinematic Distributions

To assess the accuracy of the modeling in the MC simulations and of the background estimation, kinematic distributions from the simulated background and signal samples are compared to the measured distributions of signal candidates in the data. Figures 6.1 and 6.2 show the muon $|\eta|$, p_{T}, event $p_{\mathrm{T}}^{\mathrm{miss}}$, and m_{T} distributions for μ^+ and μ^- signal candidates. In each figure, the background distributions are normalized to the expected number of QCD multi-jet, $Z \to \mu^+\mu^-$, and $W \to \tau\nu_\tau \to \mu\nu_\mu\nu_\tau\nu_\tau$ events calculated using the procedures discussed in Section 5.5. The measured distributions are shown before background subtraction, and the simulated signal $W \to \mu\nu_\mu$ distributions are normalized to the background-subtracted number of events in the data. The errors in the data are statistical only.

The predicted distributions from MC simulation agree with the measured distributions in each region of phase space. This suggests that the estimated background is an accurate representation of the actual background in the data. The numbers of observed signal candidates in the data (i.e. before background subtraction and correction) and background events in each centrality class and $|\eta|$ interval are shown in Tables 6.1 and 6.2, respectively. The background percentage is largest (9-10%) in the most central events and at midrapidity, where high multiplicities are more likely to decrease the signal purity.
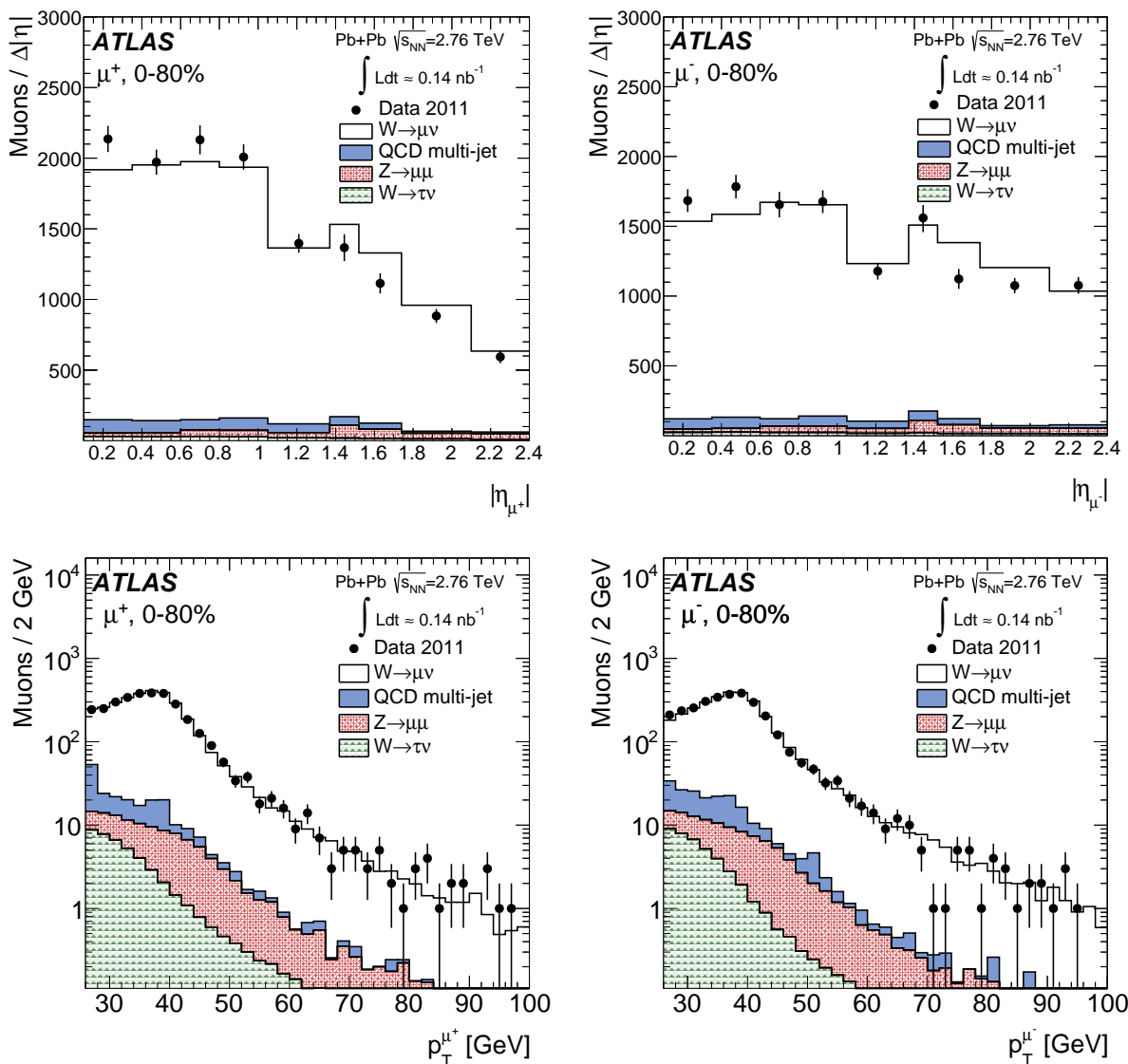
Figure 6.1: Measured absolute pseudorapidity (top) and transverse momentum (bottom) distributions for $W^+ \to \mu^+ \nu_\mu$ (left) and $W^- \to \mu^- \bar{\nu}_\mu$ (right) candidates after applying the complete set of selection requirements in the fiducial region: $p_T^\mu > 25$ GeV, $p_T^{\text{miss}} > 25$ GeV, $m_T > 40$ GeV and $0.1 < |\eta_\mu| < 2.4$. The contributions from electroweak and QCD multi-jet processes are normalised according to their expected number of events and are added sequentially. The $W \to \mu\nu_\mu$ MC events are normalised to the number of background-subtracted signal events in the data. The background and signal predictions are also added sequentially. Errors in the data are statistical only.

Figure 6.2: Measured missing transverse momentum (top) and transverse mass (bottom) distributions for $W^+ \to \mu^+ \nu_\mu$ (left) and $W^- \to \mu^- \bar{\nu}_\mu$ (right) candidates after applying the complete set of selection requirements in the fiducial region: $p_T^\mu > 25$ GeV, $p_T^{miss} > 25$ GeV, $m_T > 40$ GeV and $0.1 < |\eta_\mu| < 2.4$. The contributions from electroweak and QCD multi-jet processes are normalised according to their expected number of events and are added sequentially. The $W \to \mu\nu_\mu$ MC events are normalised to the number of background-subtracted signal events in the data. The background and signal predictions are also added sequentially. Errors in the data are statistical only.

Table 6.1: Summary of observed number of signal events and expected background counts for μ^+ and μ^- for each centrality class ($\langle N_{\mathrm{part}} \rangle$). The kinematic requirements are $0.1 < |\eta_\mu| < 2.4$, $p_{\mathrm{T}}^\mu > 25$ GeV, $p_{\mathrm{T}}^{\mathrm{miss}} > 25$ GeV, and $m_{\mathrm{T}} > 40$ GeV.

| Centrality[%] | $\langle N_{\mathrm{part}} \rangle$ | μ^+ | | μ^- | |
		Observed	Exp. background	Observed	Exp. background
0-5	382	675	65	645	62
5-10	330	493	38	534	38
10-15	282	472	41	453	39
15-20	240	401	24	355	22
20-40	158	945	62	869	58
40-80	46	362	26	329	23

Table 6.2: Summary of observed number of signal events and expected background counts for μ^+ and μ^- in bins of $|\eta_\mu|$. The kinematic requirements are $p_{\mathrm{T}}^\mu > 25$ GeV, $p_{\mathrm{T}}^{\mathrm{miss}} > 25$ GeV, and $m_{\mathrm{T}} > 40$ GeV.

| $|\eta_\mu|$ | μ^+ | | μ^- | |
	Observed	Exp. background	Observed	Exp. background
0.1-0.35	534	38	421	30
0.35-0.6	493	36	446	33
0.6-0.8	426	28	331	22
0.8-1.05	502	39	419	34
1.05-1.3	342	33	287	29
1.3-1.55	350	30	359	31
1.55-1.85	319	24	340	25
1.85-2.1	204	15	259	17
2.1-2.4	178	14	323	20

6.2 Corrected $W \to \mu\nu_\mu$ Yields

The background-subtracted raw signal counts in the fiducial region are corrected for inefficiencies using the C_W introduced in Section 5.7. The corrected number of $W \to \mu\nu_\mu$ events in the data can be expressed as:

$$N_{W^\pm}(|\eta_\mu|, \langle N_{\text{coll}} \rangle) = \frac{N_{W^\pm}^{\text{obs}} - N_{\text{bkg}}}{C_{W^\pm}}, \tag{6.1}$$

where $N_{W^\pm}^{\text{obs}}$ represents the number of signal candidates observed in the data and N_{bkg} is the number of residual background events in a given $|\eta|$ and centrality class after applying signal selection. The corrected yields in each centrality class and in each $|\eta|$ interval are reported in Tables 6.3 and 6.4, respectively. In the tables, statistical uncertainties are from the data, whereas bin-uncorrelated uncertainties are from statistical uncertainties in the efficiency and background calculations. Bin-correlated uncertainties were mentioned in Section 5.8 and include systematic variations that either increase or decrease the yields across all bins. The yields in Tables 6.3 and 6.4 correspond to 5487 ± 96 (stat.) ± 86 (syst.) $W^+ \to \mu^+\nu_\mu$ events and 5262 ± 95 (stat.) ± 83 (syst.) $W^- \to \mu^-\bar{\nu}_\mu$ events. These yields are reported before accomodating the electron channel in the measurement, which requires extrapolating the muon yields to $0 < |\eta^\mu| < 0.1$ and $2.4 < |\eta^\mu| < 2.5$, as will be discussed below.

6.3 Channel Combination

To improve the precision of the measurement, the $W \to e\nu_e$ and $W \to \mu\nu_\mu$ channels are combined. The $W \to e\nu_e$ analysis details are outside the scope of this thesis, and the reader is referred to Refs. [40, 271]. This section will discuss the combination procedure.

Before performing the combination, the respective distributions from each channel are compared to test lepton universality. Both channels share a common kinematic phase space in p_{T}, $p_{\text{T}}^{\text{miss}}$, and m_{T}. However, due to geometric differences in the ATLAS calorimeters and MS, the measurements are performed in different regions of η. Therefore, to cover the maximum phase space for $W \to \ell\nu_\ell$ events, the A_W values calculated from MC simulations are used to extrapolate the $W \to \mu\nu_\mu$ and $W \to e\nu_e$ yields.

In the differential measurements, the muon yields are extrapolated from $2.4 < |\eta| < 2.5$ and

Table 6.3: Summary of corrected W^+ and W^- production yields for each $\langle N_{\text{part}} \rangle$ and centrality class along with the absolute statistical, uncorrelated, and correlated uncertainties. The kinematic requirements are $p_{\text{T}}^{\mu} > 25$ GeV, $p_{\text{T}}^{\text{miss}} > 25$ GeV, and $m_{\text{T}} > 40$ GeV.

Centrality[%]	$\langle N_{\text{part}} \rangle$	μ^+ Corrected yield	δ_{sta}	δ_{unc}	δ_{cor}	μ^- Corrected yield	δ_{sta}	δ_{unc}	δ_{cor}
0-5	382	1214	47	32	33	1188	48	32	35
5-10	330	896	41	22	28	956	42	22	27
10-15	282	796	37	25	26	780	37	22	24
15-20	240	682	34	18	22	595	32	14	20
20-40	158	1448	47	21	36	1324	45	19	34
40-80	46	451	24	7	13	419	23	6	15

the electron yields from $2.47 < |\eta| < 2.5$. Measurements from one channel are used to fill in missing measurements from the other. This decreases the overall systematic uncertainty from the extrapolation. The extrapolation increases the yields in the most forward pseudorapidity bins by 28% in the muon channel and by 7% in the electron channel. The differential yields as a function of $|\eta|$ from $W \to \mu\nu_{\mu}$ and $W \to e\nu_e$ events are shown in Figure 6.3.

For the integrated yields in each centrality class, the $W \to \mu\nu_{\mu}$ events are extrapolated from $0 < |\eta| < 0.1$ and $2.4 < |\eta| < 2.5$ and $W \to e\nu_e$ events from $1.37 < |\eta| < 1.52$ (the "crack region" of the calorimeters). This is necessary since the muon and electron channels must be within the same overall fiducial region when comparing yields within a given centrality class (i.e. acceptance losses vary the yields in each channel). The extrapolation increases the integrated yield for muons by 7.5% and the integrated yield for electrons by 6.6%. These distributions are presented in Figure 6.4 as a function of $\langle N_{\text{part}} \rangle$.

Figures 6.3 and 6.4 validate the assumption of lepton universality. The combination calculates the central value ($\bar{x}$) using a standard weighted-average procedure:

Table 6.4: Summary of corrected W^+ and W^- production yields in each bins of $|\eta_\mu|$ along with the absolute statistical, uncorrelated, and correlated uncertainties. The kinematic requirements are $p_T^\mu > 25$ GeV, $p_T^{\text{miss}} > 25$ GeV, and $m_T > 40$ GeV.

	μ^+				μ^-			
$|\eta_\mu|$	Corrected yield	δ_{sta}	δ_{unc}	δ_{cor}	Corrected yield	δ_{sta}	δ_{unc}	δ_{cor}
0.1-0.35	831	36	27	25	653	32	21	21
0.35-0.6	741	34	23	26	690	33	23	27
0.6-0.8	625	30	18	18	478	26	13	18
0.8-1.05	735	33	22	24	611	30	19	25
1.05-1.3	694	38	20	30	567	34	16	26
1.3-1.55	578	31	16	20	574	30	16	23
1.55-1.85	548	31	12	24	563	31	13	20
1.85-2.1	390	28	9	14	483	30	11	14
2.1-2.4	345	26	8	16	643	37	17	20
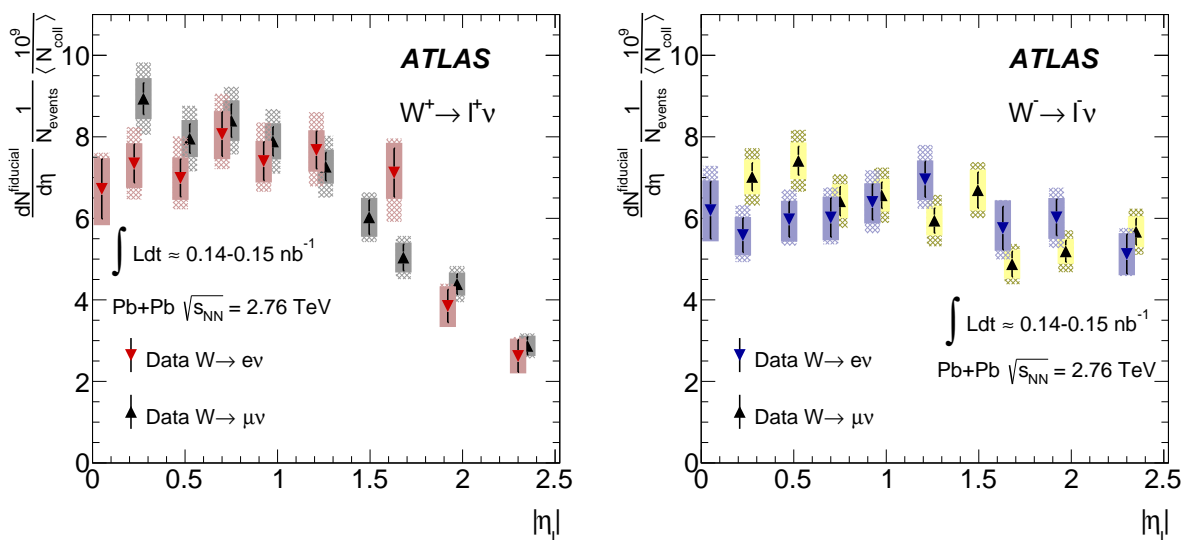
Figure 6.3:   Fiducial differential production yields per binary collision for W^+ (Left) and W^- (Right) events from the electron and muon channels. Due to acceptance in the MS and calorimeters, the first bin in the muon channel and the seventh bin in the electron channel are not covered. Muon points are shifted horizontally for visibility. The kinematic requirements are $p_T^\ell > 25$ GeV, $p_T^{\mathrm{miss}} > 25$ GeV, and $m_T > 40$ GeV. Statistical errors are shown as black bars, whereas bin-uncorrelated systematic and statistical uncertainties are added in quadrature and are shown as the filled error box. Bin-correlated uncertainties are shown as the hatched boxes. These include uncertainties from $\langle N_{\mathrm{coll}} \rangle$.
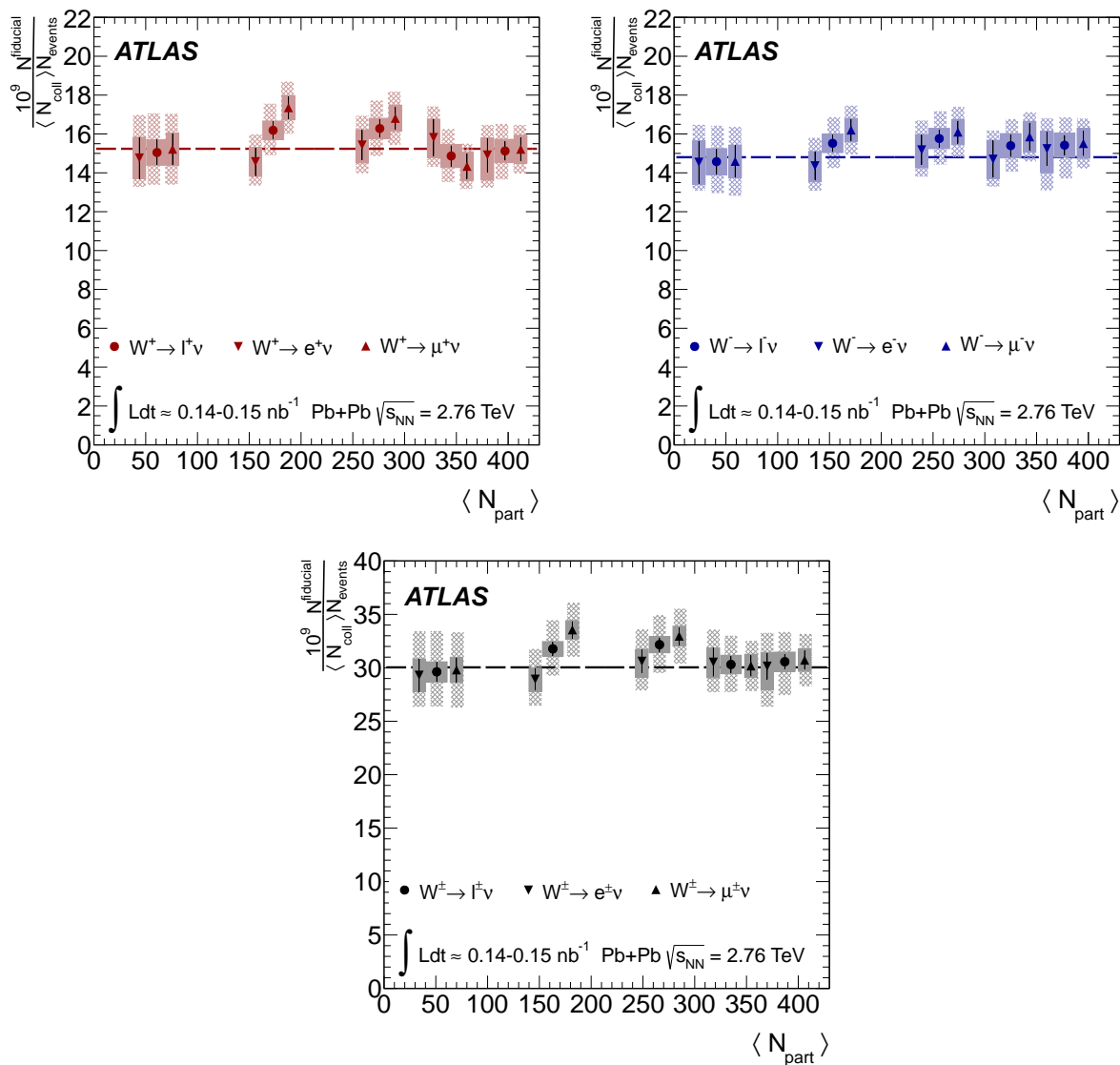
Figure 6.4: Fiducial W^+ (Top Left), W^- (Top Right), and $W^{\pm}$ (Bottom) production yields per binary collision as a function of $\langle N_{\mathrm{part}} \rangle$. Each panel includes measurements from the $W \to \mu\nu_{\mu}$ (upward triangles) and $W \to e\nu_e$ (downward triangles) channels as well as the combined measurement (circles). Muon and electron channels are offset for clarity. The kinematic requirements are $0 < |\eta_l| < 2.5$, $p_{\mathrm{T}}^l > 25$ GeV, $p_{\mathrm{T}}^{\mathrm{miss}} > 25$ GeV, and $m_{\mathrm{T}} > 40$ GeV. Statistical errors are shown as black bars. These are added in quadrature to the bin-uncorrelated systematic uncertainties and are shown as the filled error bands. Bin-correlated uncertainties are shown as the hatched bands.

$$\bar{x} = \frac{\sum_{\ell=\mu,e} w_\ell x_\ell}{\sum_{\ell=\mu,e} w_\ell} \tag{6.2}$$

where

$$w_\ell = \frac{1}{\left(\delta x_\ell^{\mathrm{unc}}\right)^2}$$

Here $\delta x_\ell^{\mathrm{unc}}$ denotes the uncertainies considered uncorrelated across all bins and between the electron and muon measurements. The total uncorrelated uncertainty is given by the sum:

$$\delta \bar{x}^{\mathrm{unc}} = \left(\sum_{\ell=\mu,e} w_\ell\right)^{-1/2}$$

The total correlated uncertainty in the combined measurement is calculated by the average of the uncertainties considered fully correlated bin-to-bin and across both data sets:

$$\delta \bar{x}^{\mathrm{cor}} = \frac{1}{2} \sum_{\ell=\mu,e} \delta x_\ell^{\mathrm{cor}}$$

These uncertainies include the uncertainty in the $p_\mathrm{T}^{\mathrm{miss}}$ measurement, electroweak background subtraction, $\langle N_{\mathrm{coll}} \rangle$, and extrapolation.

The central values of the combined integrated yields in each centrality class are included in Figure 6.4. The physical implications of the combined lepton distributions will be discussed in the following sections.

6.4 Binary Scaling and Pseudorapidity Dependence

Figure 6.5 shows the combined measurement of the number of $W \to \ell\nu_\ell$ events per binary nucleon-nucleon collision in the data as a function of $\langle N_{\mathrm{part}} \rangle$ for W^+, W^-, and $W^\pm$. The yields are independent of centrality. This implies that W bosons can be used in W+jet events to benchmark jet energy loss in the medium by providing information about the modification of jet fragmentation functions in a QGP, as described in Sec. 2.10. An identical centrality dependence has been observed in measurements of other electroweak probes: Z bosons and photons (see Figure 6.6) [38, 42].

The measured W yields in Figure 6.5 are compared to NLO cross-section calculations from POWHEG with the CT10 PDF sets. To describe the W cross section in Pb+Pb collisions, the theory

predictions use a weighted combination of cross sections from the different binary nucleon-nucleon systems: pp, nn, and $pn(np)$. Thus, the predictions have $\langle N_{\mathrm{part}} \rangle = 2$ but are extended over the entire $\langle N_{\mathrm{part}} \rangle$ range for clarity. The NLO calculations describe the data well across all charge classes.
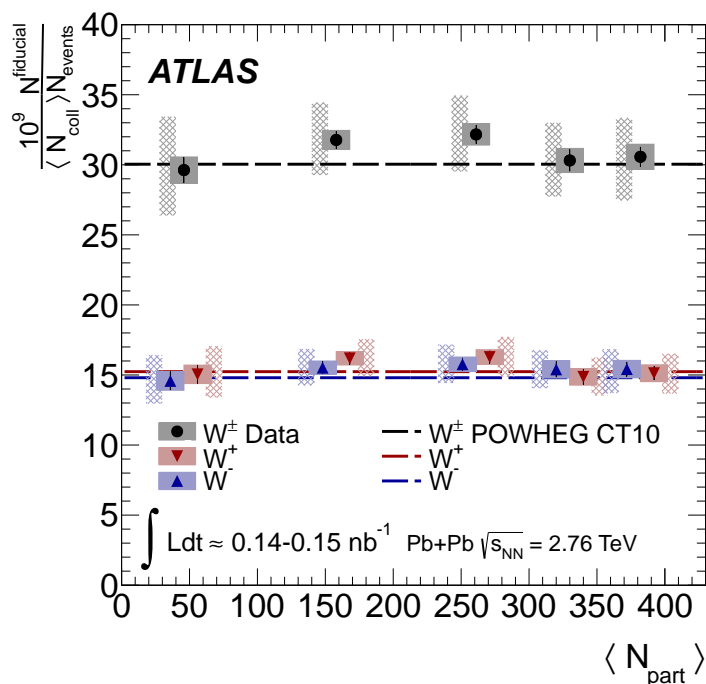
Figure 6.5: Fiducial $W \to \ell\nu_\ell$ production yields per binary collision as a function of $\langle N_{\mathrm{part}} \rangle$ for $W^+ \to \mu^+\nu_\mu$ (downward triangles), $W^- \to \mu^-\bar{\nu}_\mu$ (upward triangles), and $W^\pm \to \mu^\pm\nu_\mu$. The kinematic requirements are $0 < |\eta_l| < 2.5$, $p_T^l > 25$ GeV, $p_T^{\mathrm{miss}} > 25$ GeV, and $m_T > 40$ GeV. Statistical errors are shown as solid bars. These are added in quadrature to the bin-uncorrelated systematic uncertainties and are shown as the filled error bands. Bin-correlated uncertainties are shown as the hatched bands and are offset for clarity. These include uncertainties from $\langle N_{\mathrm{coll}} \rangle$. Also shown are NLO predictions from POWHEG using the CT10 PDF set [40].

The fiducial differential W^+ and W^- yields for the combined muon and electron measurements are shown Figure 6.7. The data are compared to theory predictions from CT10 with and without EPS09 nuclear corrections (see Sec. 2.9.2). The nuclear corrections account for shadowing, anti-shadowing, the EMC effect, and Fermi motion. The uncertainties in the theory predictions are
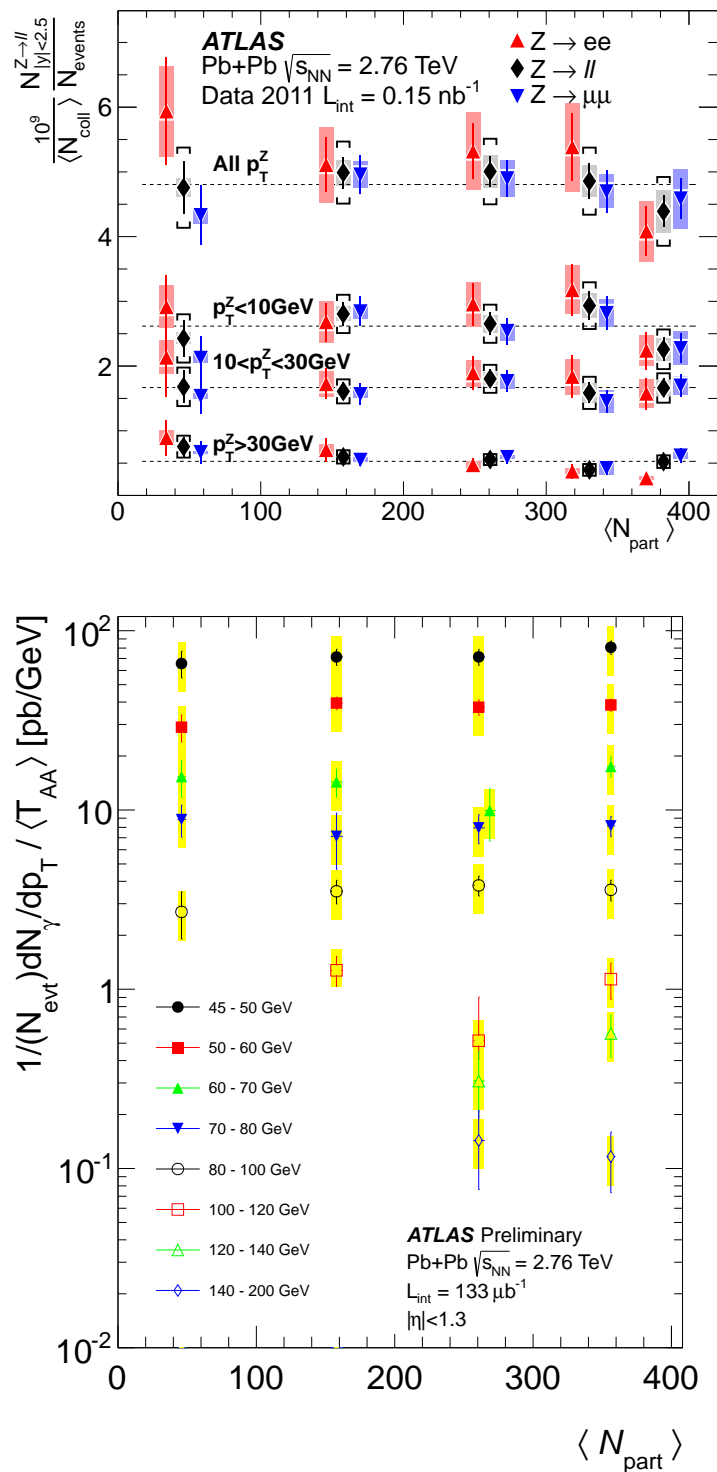
Figure 6.6: Z boson (Top) and photon (Bottom) yields per binary nucleon-nucleon collision as a function of $\langle N_{\mathrm{part}}\rangle$. The Z yields are shown for the $Z \to \mu^+\mu^-$ and $Z \to e^+e^-$ channels as well as for the combined channels for different p_{T}^Z intervals [38]. The photon yields are also shown for different p_{T} intervals [42].

obtained from the PDF uncertainties [12, 246] and uncertainties in the the renormalization and factorization scales in the cross section calculations. Within the uncertainties of the measurement and theory, both predictions describe the data well. Therefore, until the systematic and statistical uncertainties can be reduced, no nuclear effects can be observed in the measured distributions.
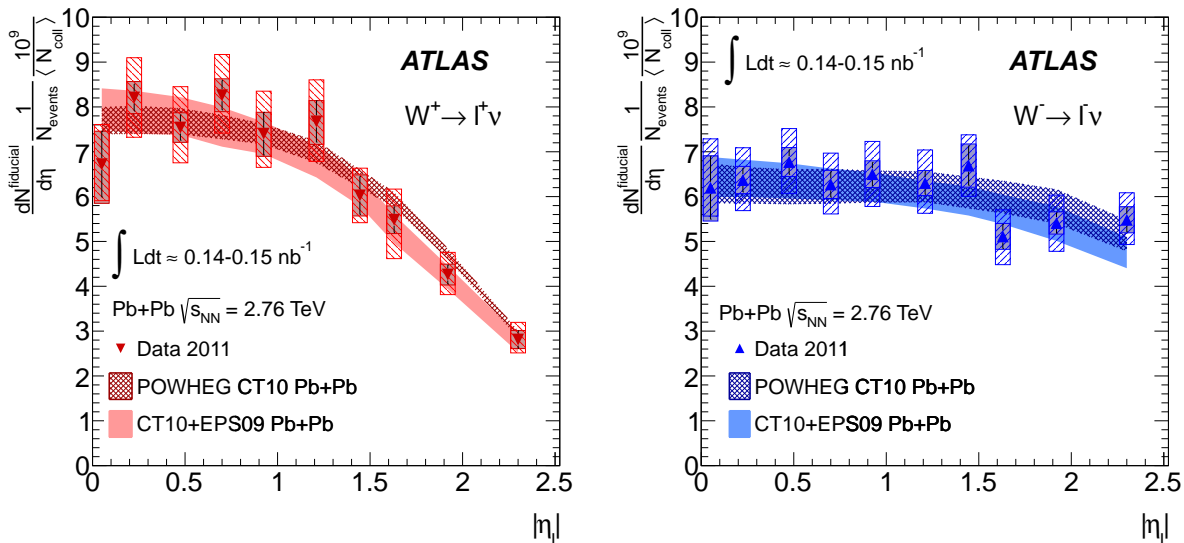
Figure 6.7: Fiducial differential production yields per binary collision in Pb+Pb for $W^+ \to \ell^+ \nu_\ell$ (Left) and $W^- \to \ell^- \bar{\nu}_\ell$ (Right) events. The kinematic requirements are $p_T^l > 25$ GeV, $p_T^{\text{miss}} > 25$ GeV, and $m_T > 40$ GeV. Theory predictions from CT10 (filled) and CT10+EPS09 nuclear corrections (hatched) are also shown [40].

However, the shapes are very different in the $W^+ \to \ell^+ \nu_\ell$ and $W^- \to \ell^- \bar{\nu}_\ell$ distributions. The former drops sharply as a function of $|\eta|$ while the latter has a slope close to zero. This behavior is drastically different from that observed in *pp* collisions at 7 TeV within $|\eta| < 2.5$, as shown in Figure 6.8. However, the measurements in Pb+Pb tend to resemble *pp* measurements at $|\eta| > 2.5$, as shown Figure 6.9. It is difficult to attribute this behavior to $\sqrt{s}$, isospin effects, or some tandem effect. This will be discussed further in the next section in the context of the charge asymmetry.
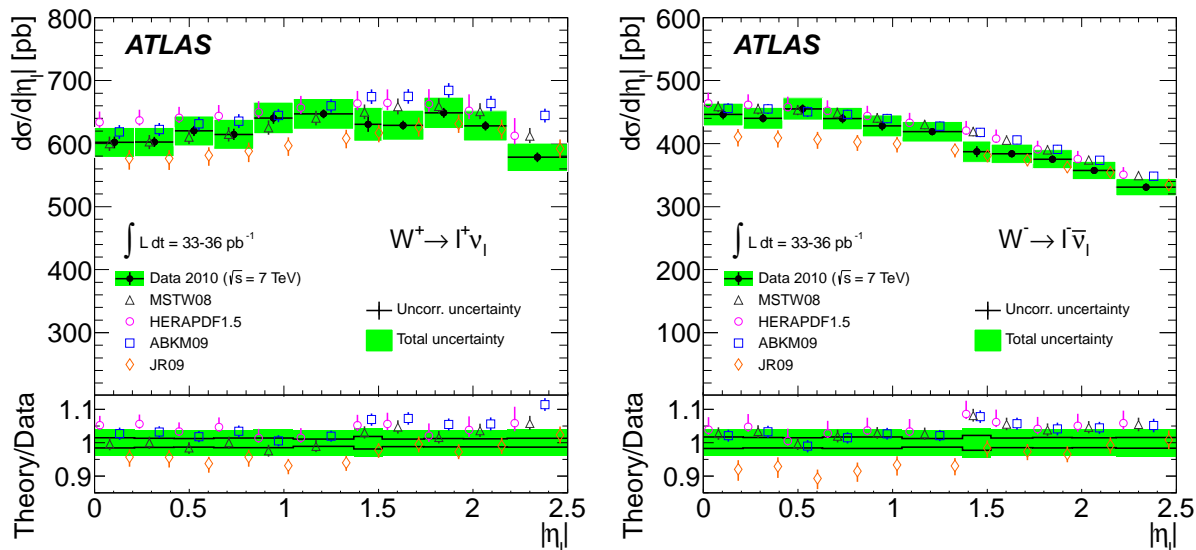
Figure 6.8: Differential $\mathrm{d}\sigma/\mathrm{d}|\eta_{l^+}|$ (Left) and $\mathrm{d}\sigma/\mathrm{d}|\eta_{l^-}|$ (Right) cross section measurements fro $W \to \ell\nu_\ell$ events. NNLO theory predictions are also provided. The kinematic requirements are $p_{\mathrm{T},l} > 20$ GeV, $p_{\mathrm{T},\nu} > 25$ GeV, and $m_{\mathrm{T}} > 40$ GeV [43].
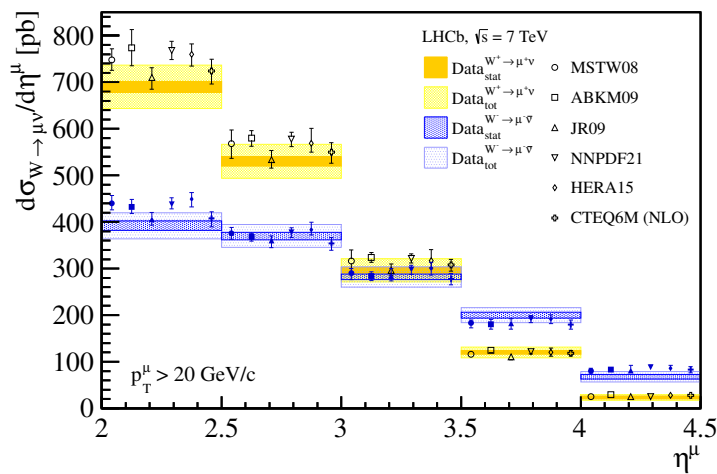
Figure 6.9: Differential $W \to \mu\nu_\mu$ cross section as a function of pseudorapidity at forward $2 < |\eta| < 4.5$ from LHCb [44]. Distributions for mu^+ and μ^- are shown, along with theory predictions at NLO and NNLO. The kinematic requirements are events with exactly one muon with $p_{\mathrm{T},\mu} > 20$ GeV and no other muon with $p_{\mathrm{T},\mu} > 2$ GeV.

6.5   Charge Ratio and Asymmetry

6.5.1   Isospin Effects and $\sqrt{s}$ Dependence

W boson production is sensitive to the color quantum numbers and momentum fractions x of the incoming partons. Therefore, measurements of the charge asymmetry between W^+ and W^- events provide information about the initial hard-scattering process. The leptonic charge asymmetry from $W \to \ell\nu_\ell$ events is a convolution of the W asymmetry and parity-violating asymmetry of W decays (see Chapter 2). Since the V-A interaction is well understood, the lepton asymmetry retains sensitivity to the parton distribution functions.

Figure 6.10 presents the lepton charge asymmetry in Pb+Pb collisions. The figure also includes theory predictions from CT10 with and without EPS09 nuclear corrections. Since systematics correlated between charges cancel in the ratio, the asymmetry provides a more precise measurement. However, even with the reduced uncertainties, nuclear effects are still inapparent in the measured distribution. Based on the theory predictions, the asymmetry would have to be known within ± 0.02, which may be attainable with much higher statistics but will still be challenging given the residual systematic uncertainties.

The asymmetry changes sign at $|\eta| \approx 1.3 - 1.5$, where $W^- \to \ell^- \bar{\nu}_\ell$ events surpass $W^+ \to \ell^+ \nu_\ell$ events and continue to do so at forward pseudorapidities. This anisotropy in the lepton decay angle is expected and is governed by the polarization of the W boson and V-A interaction. As can be inferred from Figures 6.8 and 6.9 above, negative asymmetries are still observed at 7 TeV in pp measurements but outside the ATLAS acceptance. This is further illustrated in Figure 6.11, which shows the combined measurement of the lepton charge asymmetry from ATLAS [43], CMS [272], and LHCb [44]. In data collected from pp collisions, the asymmetry changes sign at $|\eta| \approx 3.3 - 3.5$ (Figure 6.12), a shift of approximately 2 units of pseudorapidity relative to the Pb+Pb measurement.

To further investigate the dependence of the charge asymmetry on $\sqrt{s}$, Figure 6.14 shows the lepton asymmetry at 2.76 TeV from CT10 for pp collisions. The asymmetry from nn and $pn(np)$[1] collision systems are also shown. It can be seen from this figure that the asymmetry prediction

---

[1]The yields in the pn and np systems are parity invariant i.e. $N_{W^{+(-)}}^{np}(-\eta) = N_{W^{+(-)}}^{pn}(+\eta)$. Thus $A_\ell^{pn}(|\eta|) = A_\ell^{np}(|\eta|)$.
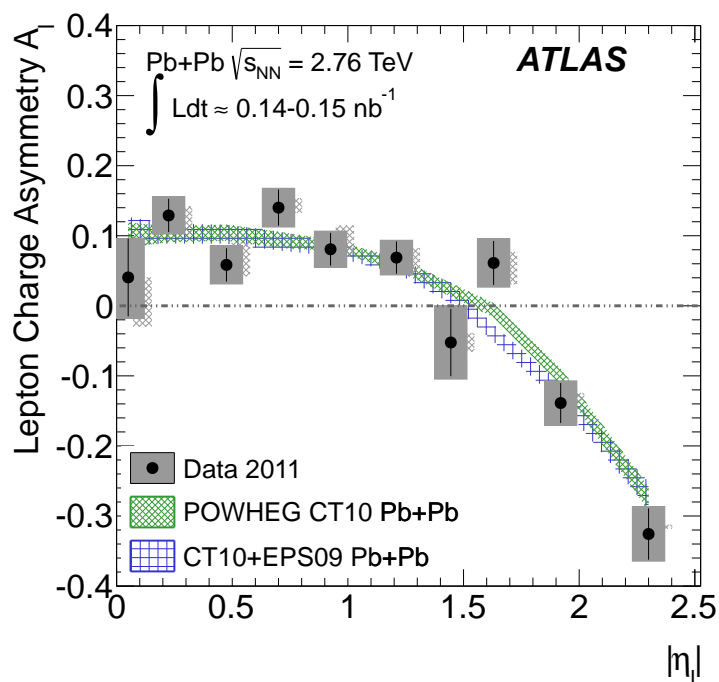
Figure 6.10:   Fiducial lepton charge asymmetry $A_l = (N_{W^+} - N_{W^-})/(N_{W^+} + N_{W^-})$ in Pb+Pb as a function of $|\eta|$. The kinematic requirements are $p_T^{\ell} > 25$ GeV, $p_T^{\mathrm{miss}} > 25$ GeV, and $m_T > 40$ GeV. Statistical uncertainties are shown as black bars, whereas bin–uncorrelated systematic and statistical uncertainties added in quadrature are shown as the filled error box. Scaling uncertainties are shown as the hatched boxes and are offset for clarity. Theory predictions from CT10 (hatched) and CT10+EPS09 nuclear corrections (checkered) are shown also. The PDF uncertainties in both the CT10+EPS09 and CT10 predictions are derived from the PDF error eigensets. The total theoretical uncertainty also includes uncertainties in the renormalisation and factorisation scales in the cross section calculations [40].
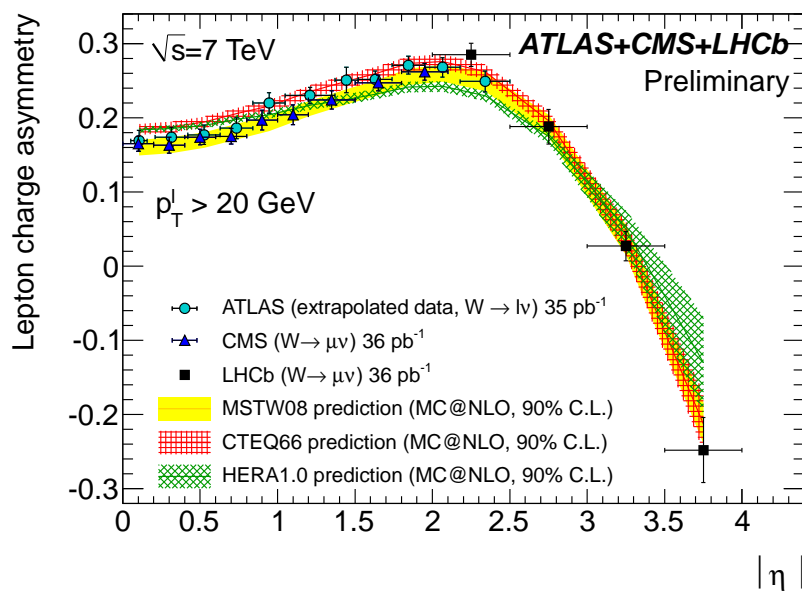
Figure 6.11:   ATLAS+CMS+LHCb combined measurement of the lepton charge asymmetry as a function of $|\eta|$. Notice the measurement extends to $|\eta| = 4$ [45].
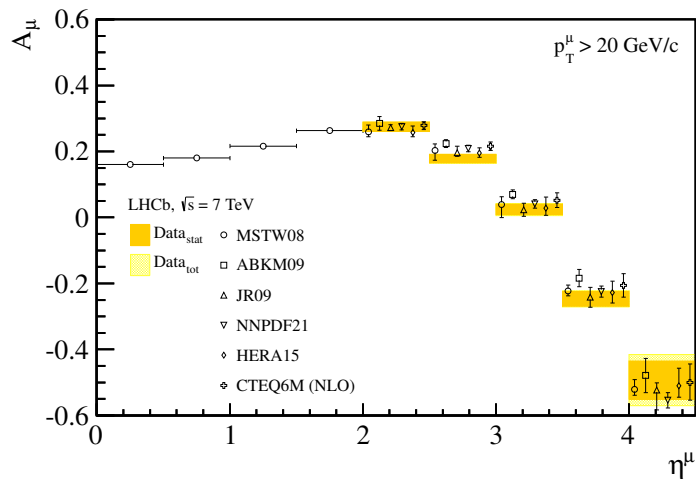
Figure 6.12:   The fiducial muon charge asymmetry from $W \rightarrow \mu\nu_\mu$ events measured by LHCb at forward pseudorapidity [44]. Asymmetry values at $|\eta| < 2$ are from the central values of the MSTW08 PDF set.

from pp at 2.76 TeV changes sign at $|\eta| \approx 2.7$, 0.6-0.8 units of pseudorapidity lower than that from pp at 7 TeV. Therefore, at larger $\sqrt{s}$ in pp collisions, W^+ production exceeds W^- production over a larger $|\eta|$ interval, stretching the tail of the lepton asymmetry distribution. This could be a result of higher order effects from quark-gluon scattering ($qg \to Wq$; Figure 6.13) [46] or of additional sea quark contributions (see Figure 2.13) to the $W^\pm$ cross sections.
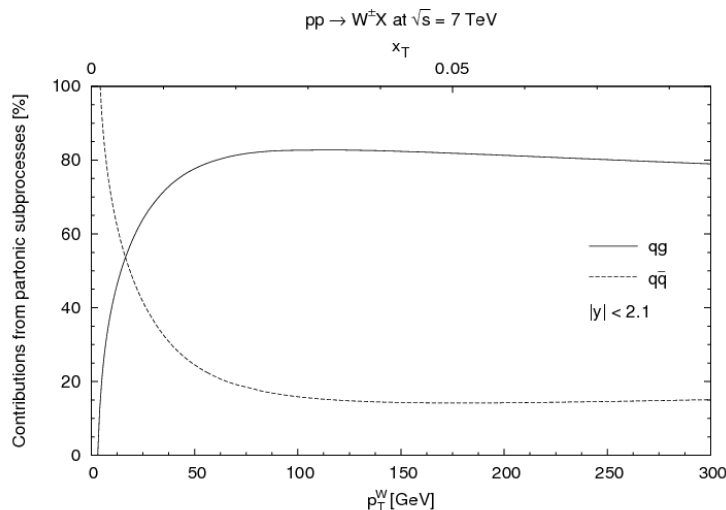
Figure 6.13: Relative contributions at NLO of $q\bar{q}$ and qg subprocesses to W boson production as a function of p_T^W at $\sqrt{s} = 7$ TeV [46].

The isospin contribution can also be observed from Figure 6.14, where the theory prediction for the charge asymmetry in nn collisions is essentially always negative (neglecting uncertainties from the theory). The neutron component increases the relative frequency of $d\bar{u} \to W^- \to \ell^- \bar{\nu}_\ell$ events. Thus, it can be implied that the nn component in Pb+Pb collisions serves to drive the charge asymmetry to more negative values over any pseudorapidity interval.

$pn(np)$ interactions are also interesting since there exists a symmetry in the number of $u\bar{d}$ and $d\bar{u}$ interactions, resulting in an equal production of W^+ and W^- events. The same symmetry exists in $p\bar{p}$ collisions at the Tevatron [47, 273]. However in these collisions, the valence quarks include $\bar{u}$ and $\bar{d}$ quarks from the antiproton. The same mechanism for W production proceeds as in pn collisions but with different valence distributions (i.e. $u_v = u - \bar{u}$ and $d_v = d - \bar{d}$). This results in differences in the W rapidity distributions and thus in the lepton charge asymmetry distributions

between the two collision systems. Figure 6.15 shows the charge asymmetry from $W \to \mu\nu_\mu$ events collected by the D0 detector at 1.96 TeV in $p\bar{p}$ collisions. The measurement is made only up to $|\eta| = 2$ and uses a slightly tighter m_T cut ($m_T > 50$ GeV), but $\sqrt{s}$ is similar to that in this work. The asymmetry appears to change sign in approximately the same region of $|\eta|$ as in the $pn(np)$ collision system at 2.76 TeV. This behavior further demonstrates the isospin effects in the charge asymmetry measurements.
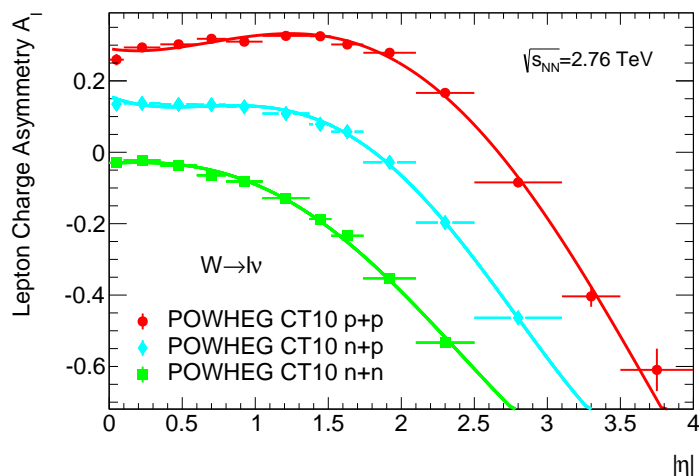
Figure 6.14: Fiducial lepton charge asymmetry as a function of $|\eta|$ from CT10 theory predictions. Asymmetries are shown for each nucleon-nucleon interaction in a Pb+Pb collision. The kinematic requirements are $p_T^\ell > 25$ GeV, $p_T^\nu > 25$ GeV, and $m_T > 40$ GeV. Only statistical uncertainties are shown. Each distribution is fit with a fourth order polynomial for clarity.

6.5.2 Integrated Charge Ratio W^+/W^-

The ratio of the number of $W^+ \to \ell^+\nu_\ell$ and $W^- \to \ell^-\bar{\nu}_\ell$ events integrated over $0 < |\eta| < 2.5$ as a function of $\langle N_{\text{part}} \rangle$ is shown in Figure 6.16. The ratio distribution is flat within the experimental uncertainties, implying an approximately equal production of W^+ and W^- bosons within the fiducial region in each centrality class. This is somewhat counterintuitive since there are more neutrons in Pb nuclei, and thus a higher probability for a $d\bar{u} \to W^-$ event. However, as stated previously, a larger fraction of $W^- \to \ell^-\bar{\nu}_\ell$ than $W^+ \to \ell^+\nu_\ell$ events are produced at forward $|\eta|$. Many of these events are outside the detector acceptance, thus bringing the fiducial W^- yields back
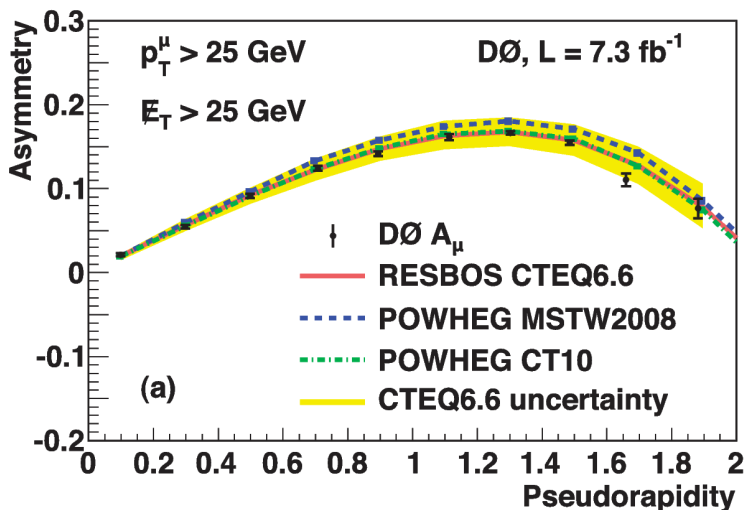
Figure 6.15: Fiducial muon charge asymmetry as a function of $|\eta|$ at $\sqrt{s} = 1.96$ TeV in $p\bar{p}$ collisions [47]. The kinematic requirements are $p_T^\mu > 25$ GeV, $E_T^{\mathrm{miss}} > 25$ GeV, and $m_T > 50$ GeV. The distribution is folded such that $A_\mu(\eta) = -A_\mu(-\eta)$ (CP-folding).

to the level of the W^+ yields.

The integrated charge ratio in Pb+Pb collisions $W^+/W^- = 1.02 \pm 0.02$ (stat.) ± 0.02 (syst.). In pp collisions, within an almost exact phase space, $W^+/W^- = 1.542 \pm 0.007$ (stat.) $\pm$ 0.012 (syst.) [43], as shown in Figure 6.17. The difference is again attributed to the tandem effects of the isospin of the Pb nucleus and $\sqrt{s}$.
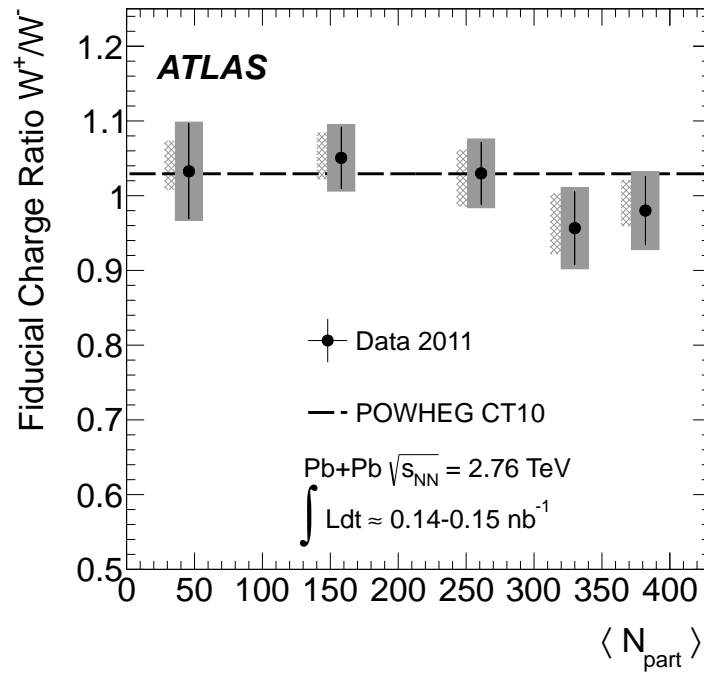
Figure 6.16: Lepton fiducial charge ratio W^+/W^- as a function of $\langle N_{\mathrm{part}} \rangle$. The kinematic requirements are $p_{\mathrm{T}}^{\ell} > 25$ GeV, $p_{\mathrm{T}}^{\mathrm{miss}} > 25$ GeV, $m_{\mathrm{T}} > 40$ GeV, and $|\eta_{\ell}| < 2.5$. Also shown is a QCD NLO prediction from POWHEG using the CT10 PDF set. Statistical uncertainties are shown as black bars. The filled grey boxes represent statistical and bin-uncorrelated systematic uncertainties added in quadrature, whereas the grey-hatched boxes represent bin-correlated uncertainties and are offset for clarity [40].
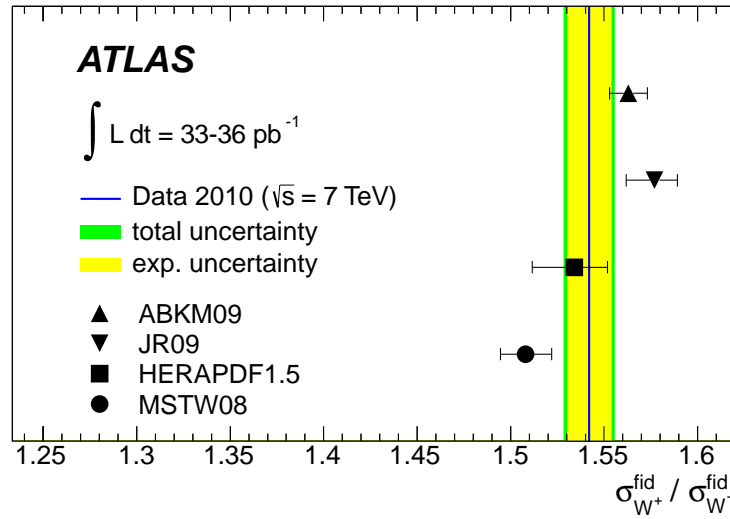
Figure 6.17:   Measured and predicted fiducial cross section ratios $\sigma_{W^+}/\sigma_{W^-}$ in pp collisions at 7 TeV. The total uncertainty includes systematic and statistical uncertainties. Uncertainties in the predictions are given by the PDF uncertainties at 68% C.L.

Chapter 7

Summary and Outlook

This thesis has documented the current ATLAS measurements of W boson production in a dense nuclear environment. The conceptual framework and impetus for electroweak boson measurements in heavy-ion collisions was put forth in Chapter 2, in which it was argued that W bosons are excellent candidates for detecting nuclear modifications to PDFs and benchmarking in-medium parton energy loss. The measurements from Pb+Pb data supporting these predictions were presented in Chapter 6. The presence of nuclear modifications were studied using the lepton absolute pseudo-rapidity and charge asymmetry distributions from $W \rightarrow \ell\nu_\ell$ events. Within the precision of the measurement and current uncertainties in the theory, it was concluded that no nuclear effects in the PDFs could be observed. However, the difficulty in extracting PDF nuclear effects from heavy-ion collisions was somewhat anticipated due to the large PDF uncertainties, and therefore this result does not preclude the existence of such effects. As data from the pp runs at the LHC are included in the free proton PDF fits, the uncertainties in the theory should be reduced. In addition, a higher luminosity is expected in the upcoming Pb+Pb run at 5.5 TeV, and thus should enhance the precision of measurements sensitive to nuclear effects.

W boson measurements sensitive to nuclear effects in $p + \text{Pb}$ collisions have already been reported by CMS [48]. These results were obtained from a data set corresponding to 34.6 nb^{-1} at a collision energy of 5.5 TeV. This accomodates approximately a factor of two higher statistics in W boson measurements and thus allows for construction of the forward-backward asymmetry $(N_{W \rightarrow \ell\nu_\ell}(+\eta)/N_{W \rightarrow \ell\nu_\ell}(-\eta))$ in addition to the charge asymmetry measurement. The CMS measurements for the charge and forward-backward asymmetries are provided below in Figure 7.1. In

this figure, expectations with and without nuclear effects are shown. A χ^2 test statistic is used to differentiate between the two models, resulting in a 12% (29%) probability for the distribution without nuclear effects and 35% (83%) probability for the the distribution with nuclear effects for the charge asymmetry (forward-backward asymmetry). This result is encouraging and further shows the utility of W boson measurements in extracting nuclear modifications.
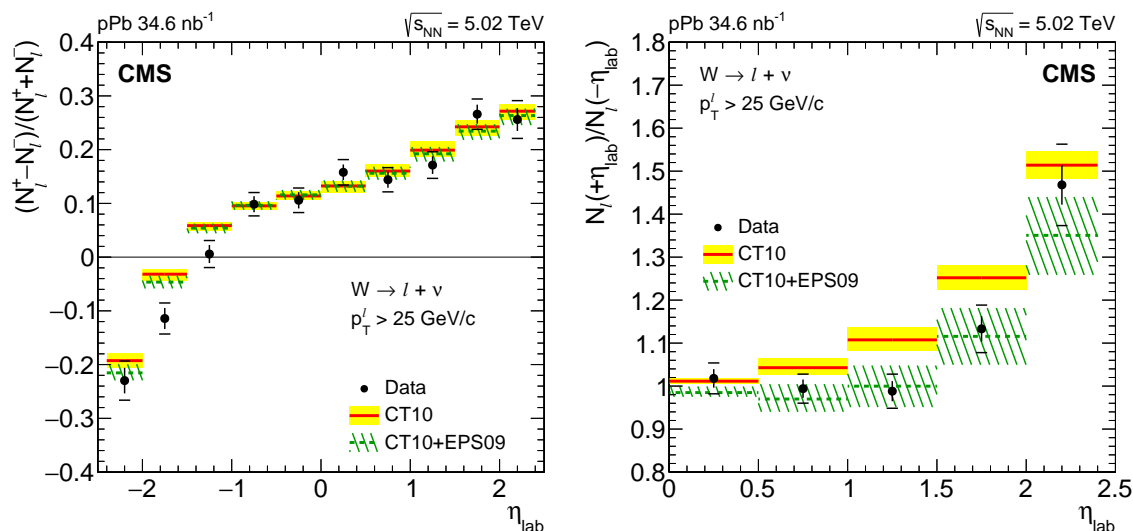
Figure 7.1: The $W \to \ell\nu_\ell$ charge asymmetry (left) and forward-backward asymmetry (right) as a function of lepton pseudorapidity in $p + \mathrm{Pb}$ collisions measured by the CMS collaboration [48]. Predictions from the CT10 PDF set with (green, dashed line) and without (yellow, solid red line) EPS09 nuclear effects.

In this thesis, the lepton charge asymmetry as a function of absolute pseudorapidity in Pb+Pb collisions was compared to the corresponding measurements in pp and $p\bar{p}$ collisions at different center-of-mass energies. This provided a means to investigate isospin effects as well as the energy dependence in the lepton charge asymmetry distribution. It was observed that increasing the collision energy stretches the tail of the distribution such that $W^- \to \ell^-\bar{\nu}_\ell$ production overtakes $W^+ \to \ell^+\nu_\ell$ production at larger values of $|\eta|$. In relation to isospin effects, the neutron contribution in the Pb nucleus was shown to enhance $W^- \to \ell^-\bar{\nu}_\ell$ production, resulting in a sign-change of the charge asymmetry at much smaller values of $|\eta|$ relative to that in pp collisions. The isospin effects in $p\bar{p}$ collisions were shown to be similar to those from the np contribution in Pb+Pb collisions,

which can be attributed to the valence quark distributions and leading-order W boson production mechanism.

This work also presented W production as a function of the mean number of binary nucleon-nucleon collisions. The results show that W yields are independent of impact parameter and scale with the number of binary nucleon-nucleon collisions. This measurement lends credence to Glauber modeling of the collision geometry and furthermore, shows that W bosons can be used to study jet fragmentation functions modified by parton energy loss in a QGP.

Another potential application for W boson production that has not yet been measured is the study of an increased concentration of neutrons toward the surface of spherical, neutron-rich nuclei (i.e. the so-called neutron skin) [49, 274, 275]. In Ref. [49] it is shown that in $p + \mathrm{Pb}$ collisions, the neutron skin effect should be most pronounced in the backward-rapidity (negative y) kinematic region where the large-x nuclear valence quarks contribute to W production. In this rapidity region, the observable $d\sigma(W^+ \to \ell^+\nu_\ell)/d\sigma(W^- \to \ell^-\bar{\nu}_\ell)$ should be sensitive to an "effective" centrality-dependent proton-neutron ratio $\mathrm{Z}_{\mathrm{eff}}^{\mathrm{pPb}}(\mathcal{C}_k)/\mathrm{N}_{\mathrm{eff}}^{\mathrm{pPb}}(\mathcal{C}_k)$, where $\mathcal{C}_k$ represents the centrality class. It is expected that in more peripheral collisions, $\mathrm{Z}_{\mathrm{eff}}^{\mathrm{pPb}}(\mathcal{C}_k)/\mathrm{N}_{\mathrm{eff}}^{\mathrm{pPb}}(\mathcal{C}_k)$ should decrease due to the neutron skin and thus the ratio $d\sigma(W^+ \to \ell^+\nu_\ell)/d\sigma(W^- \to \ell^-\bar{\nu}_\ell)$ should decrease correspondingly. In the forward-rapidity region, this ratio is independent of the effective proton-neutron ratio and only depends on the ratio of the valence quark distributions, thereby driving $d\sigma(W^+ \to \ell^+\nu_\ell)/d\sigma(W^- \to \ell^-\bar{\nu}_\ell)$ to unity. This expected behavior is shown in the left panel of Figure 7.2. In the case of Pb+Pb collisions, the ratio $d\sigma(W^+ \to \ell^+\nu_\ell)/d\sigma(W^- \to \ell^-\bar{\nu}_\ell)$ is again expected to depend on $\mathrm{Z}_{\mathrm{eff}}^{\mathrm{Pb+Pb}}(\mathcal{C}_k)/\mathrm{N}_{\mathrm{eff}}^{\mathrm{Pb+Pb}}(\mathcal{C}_k)$. However, the Pb+Pb system is symmetric and thus the nuclear valence quark contributions to W production occur at both $y << 0$ and $y >> 0$. This should make the neutron skin effect more visible, as shown in the right panel of Figure 7.2.

Figure 7.3 presents a comparison of the centrality-dependent W^+/W^- ratios from the measurements in this thesis with those that incorporate neutron skin effects from Ref. [49]. The data and calculations are in agreement ($\chi^2/N_{data} \approx 0.6$), however the uncertainties in the measurement are still rather large. But this result does open an avenue for further exploration and analysis.

In closing, currently, this work is the most precise measurement of W boson production in high-energy nuclear collisions. The results are in close connection to those in pp, $p\bar{p}$, and $p + \mathrm{Pb}$ systems and will most certaintly be superseded by new measurements in the 2015 heavy-ion run at
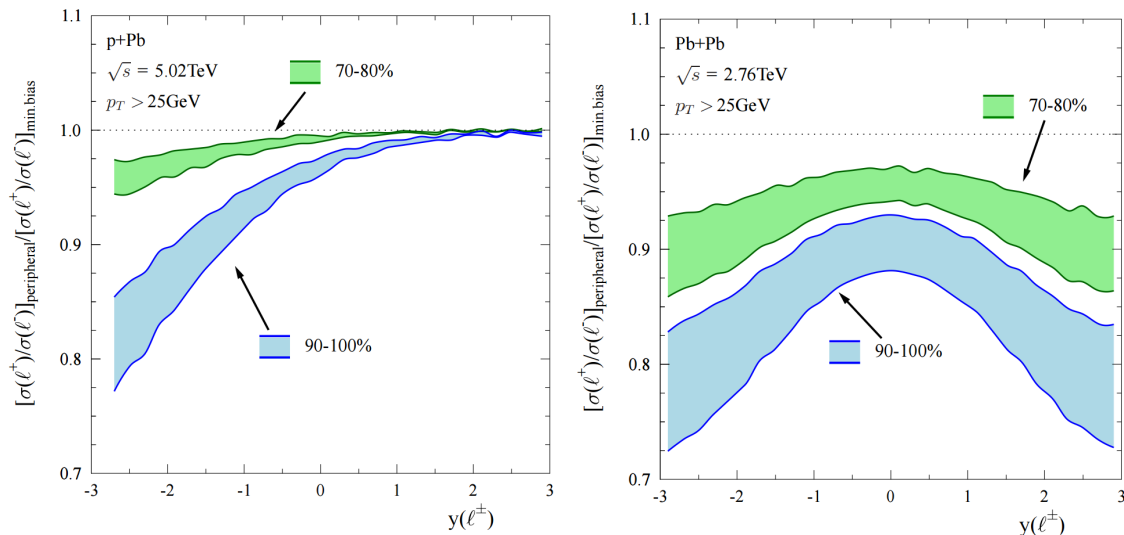
Figure 7.2: Calculated ratio $d\sigma(W^+ \to \ell^+\nu_\ell)/d\sigma(W^- \to \ell^-\bar{\nu}_\ell)$ in $p+\mathrm{Pb}$ (left) and $\mathrm{Pb}+\mathrm{Pb}$ (right) collisions for two peripheral centrality classes [49]. The ratios are normalized by the integrated ratio in minimum bias collisions $(0-100\%)$.
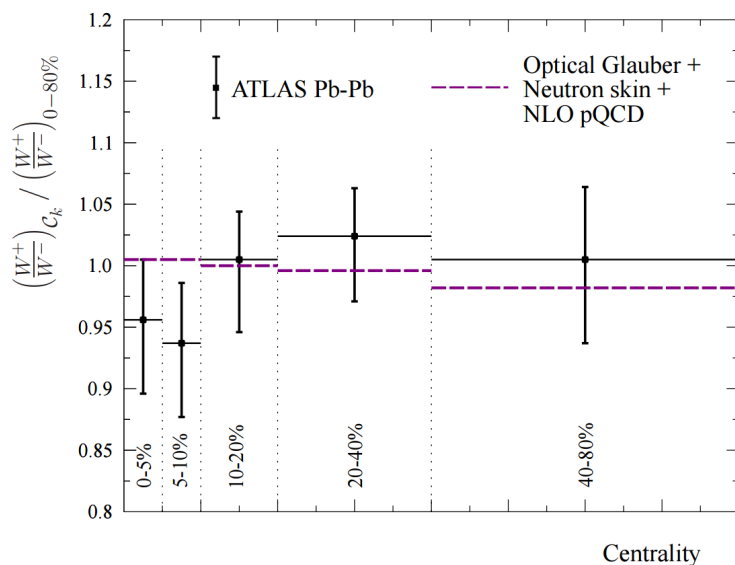
Figure 7.3: Centrality dependence of W^+/W^- as measured by ATLAS [40] and calculated in Ref. [49]. The experimental values are normalized to the integrated ratio in the $0-80\%$ centrality class.

the LHC. It is incredible how more than 30 years after its discovery, the W boson is still being used in new and creative ways to gain physics insights. Hopefully, this thesis has convinced the reader of the utility of W boson measurements in heavy-ion systems and has set a positive precedent for results still to come.

Appendix A

Staco Muon Reconstruction

The following section provides an overview of the other muon reconstruction chain used during the 2011 Pb+Pb run, Staco.

A.1 Standalone Muon Tracking

A.1.1 Pattern Recognition

Muonboy begins searching for hit patterns by identifying Regions of Activity (ROAs) using information from the trigger chambers (TGCs and RPCs), as shown in Figure A.1. The ROAs are simple cones with size $\Delta\eta \times \Delta\phi = 0.4 \times 0.4$ and are centered where there exists at least one RPC/TGC hit in both R and ϕ.

A.1.2 Segment Finding

Muon chambers that intersect the roads from the ROAs are selected for muon reconstruction. The segments are initially reconstructed in the bending $(R - z)$ plane of each muon station. Within a station, trials are performed to match MDT hits in one multilayer with hits in another multilayer using a linear fit (Figure A.2). In some cases hits are only found in one multilayer, and these can also be used for reconstructing track segments. The hits are extrapolated to the other tubes within a station to form segments. This process involves conducting two searches: strict and loose. The strict search requires segments to be associated with at least one second (ϕ) coordinate

Define ROAs
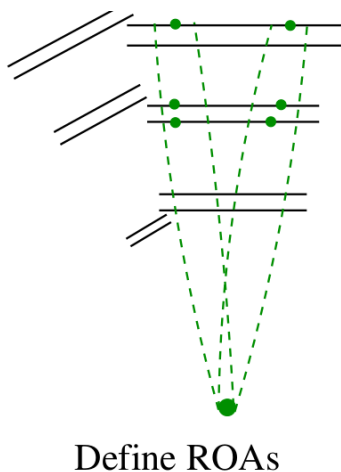
Figure A.1: Regions of Activity (ROAs) used to locate hit patterns in the MS [50].

measurement from the RPCs/TGCs. However, segments in the CSCs are reconstructed in three dimensions directly using CSC clusters. These segments are also considered strict.

A looser search for segments within ROAs is conducted after the strict search. This loose search does not require segments to be matched with a ϕ coordinate measurement, and the χ^2 requirements for segment reconstruction are less stringent. When there are no ϕ measurements from the RPCs/TGCs, five positions along the MDT tube are tested and the position that results in the best χ^2 is retained.

Local Pattern Recognition
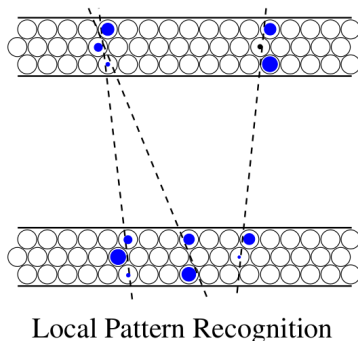
Figure A.2: Local matching and fitting of hits within the multilayers of an MDT chamber [50].

A.1.3 Track Finding

Strict segments in the outer and middle stations of the MS provide an initial rough estimate of the candidate muon momentum. The strict track segments are extrapolated to another muon station (e.g. BOS→BMS), as illustrated in Figure A.3. The extrapolation to the other station involves several trials, using different momentum values for each trial around the initial estimate (momentum scan). If matching exists between the strict segments and loose segments in the other station, a fit is performed, resulting in a more accurate momentum estimate.
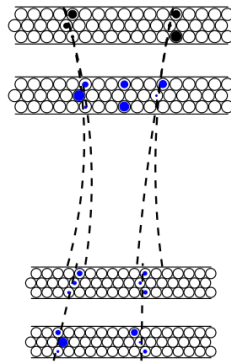
Chamber Interpolation

Figure A.3: Extrapolation of chamber hits to other chamber layer [50].

A second momentum scan is then performed around the improved muon estimate with extrapolations to all other potentially crossed chamber stations (e.g. BOS→BMS→BIS→All). Any matches with loose segments are included in the candidate track. A candidate track is kept if it has at least two segments. Using the new segments, another fit is performed to further improve the accuracy of the muon candidate position, direction, and momentum.

Starting from the previous fit, another fit is performed using the raw information available (i.e. without track segments). This gives a global and more realistic estimate of the likelihood of the candidate track and makes it possible to reject bad hits from δ electrons or γ background, which will appear far away from the reconstructed muon path.

The previous fit result is used to collect dead matter along the track candidate. The chambers and dead matter traversed by a muon are discretized into a finite number of scattering centers. The scattering angles at each scattering center are used as free parameters in a following fit. Energy loss

is also taken into consideration at each point. A final fit is then performed that takes into account the material. This final fit is used to select muons based on the value of the χ^2 (Figure A.4).

Final Track Fit
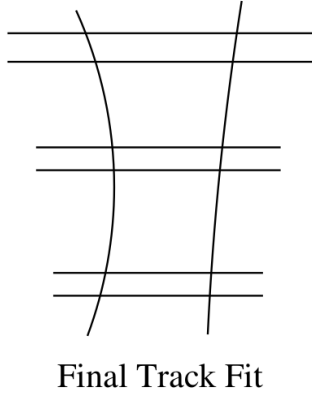
Figure A.4: Final fit across all MS stations used to identify muon candidates [50].

The fit parameters are varied to compute the covariance matrices. The candidate tracks are then back-tracked to the interaction point. Since the uncertainty in the track parameters changes during the propagation, the covariance matrices are propagated accordingly, taking into account energy loss and multiple scattering in the calorimeters.

A.2 Combined Muon Reconstruction

The Staco muon reconstruction method is based on a statistical combination of two measurements of the track in the ID and MS. Let p_{ID}^μ and p_{MS}^μ represent the parameter vectors [276] of two tracks in the ID and MS, respectively. Also, let the covariance matrices in the ID and MS be C_{ID} and C_{MS}. Then the vector of the combined track p^μ is the solution of the equation [229]:

$$C^{-1} \times p^\mu = C_{ID}^{-1} \times p_{ID}^\mu + C_{MS}^{-1} \times p_{MS}^\mu \tag{A.1}$$

where $C^{-1} = (C_{ID}^{-1} + C_{MS}^{-1})$. The corresponding χ^2 of the combination is given by:

$$\chi^2 = (p^\mu - p_{ID}^\mu)^T \times C_{ID}^{-1} \times (p^\mu - p_{ID}^\mu) + (p^\mu - p_{MS}^\mu)^T \times C_{MS}^{-1} \times (p^\mu - p_{MS}^\mu) \tag{A.2}$$

The combination is initially based on a coarse match in η and ϕ. Once this is performed, the combination is further constrained by requiring the χ^2 to be below a maximum value. When multiple combinations are under this value, the algorithm solves the ambiguity by accepting the pair with the lowest χ^2. After the combination, the track is propagated to the beam line.

Appendix B

Isolation Optimization
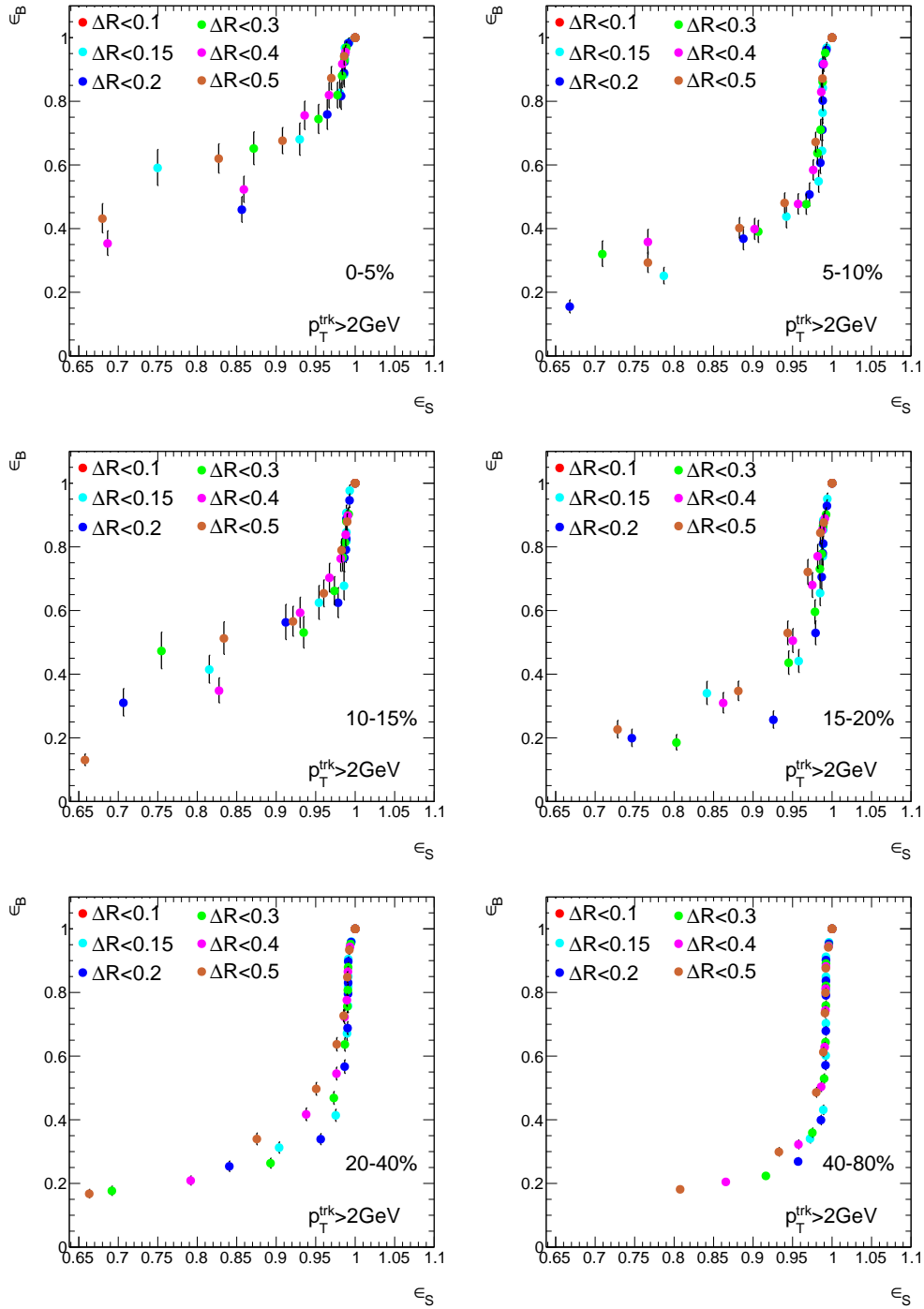
Figure B.1: Background rejection (ϵ_B) as a function of signal efficiency (ϵ_S) for different upper i_μ thresholds using a sample of J$x\mu$ and $W \to \mu\nu_\mu$ events. Distributions are shown for For each i_μ threshold, ϵ_S and ϵ_B are determined for different ΔR. $p_{\mathrm{T},min}^{trk} = 2$ GeV in calculating the isolation variable i_μ. All centrality classes used in this work are shown, however only the 0-5% class is used in the optimization.
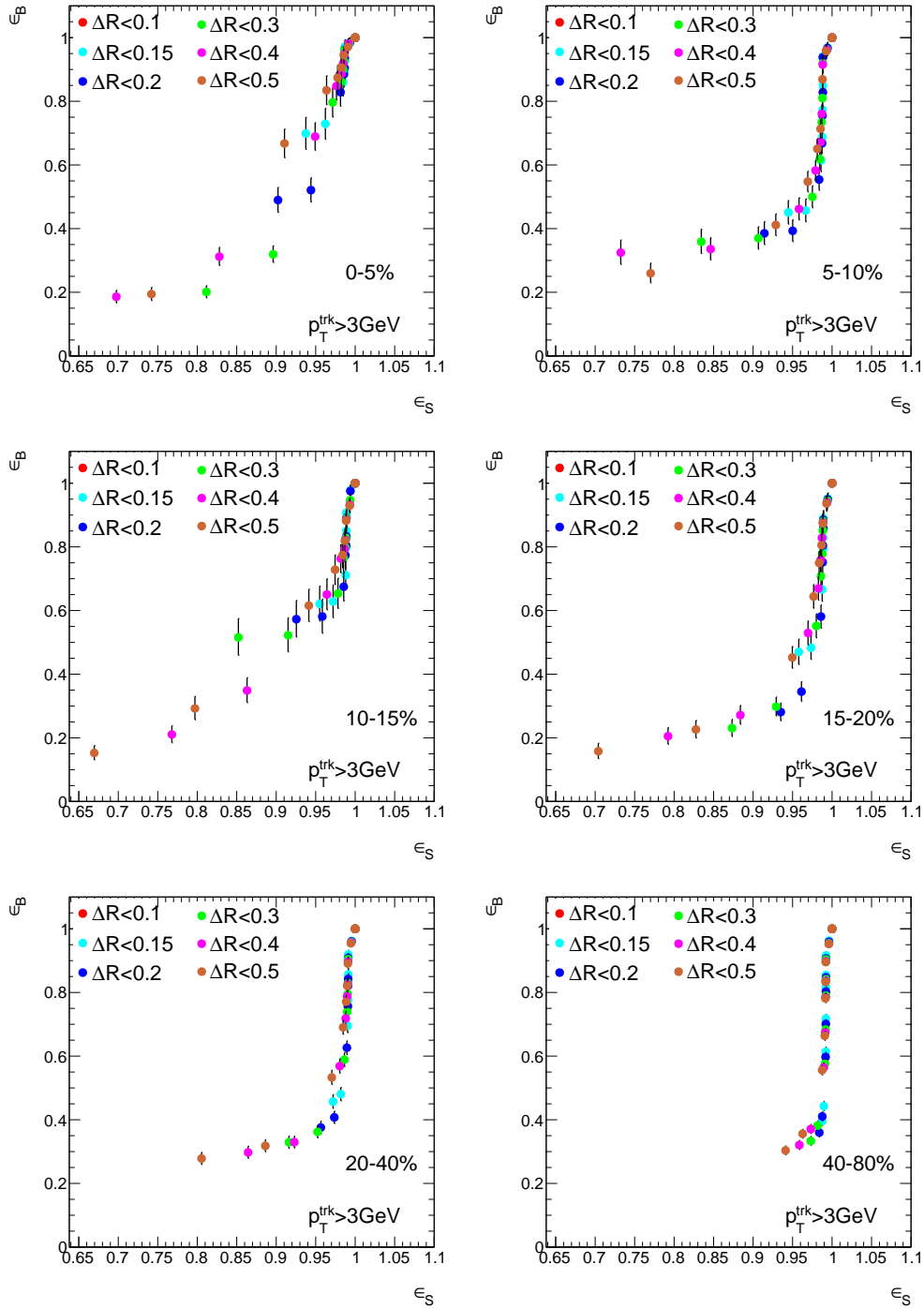
Figure B.2: Background rejection (ϵ_B) as a function of signal efficiency (ϵ_S) for different upper i_μ thresholds using a sample of J$x\mu$ and $W \to \mu\nu_\mu$ events. For each i_μ threshold, ϵ_S and ϵ_B are determined for different ΔR. $p_{\mathrm{T},min}^{trk} = 3$ GeV in calculating the isolation variable i_μ. All centrality classes used in this work are shown, however only the 0-5% class is used in the optimization.
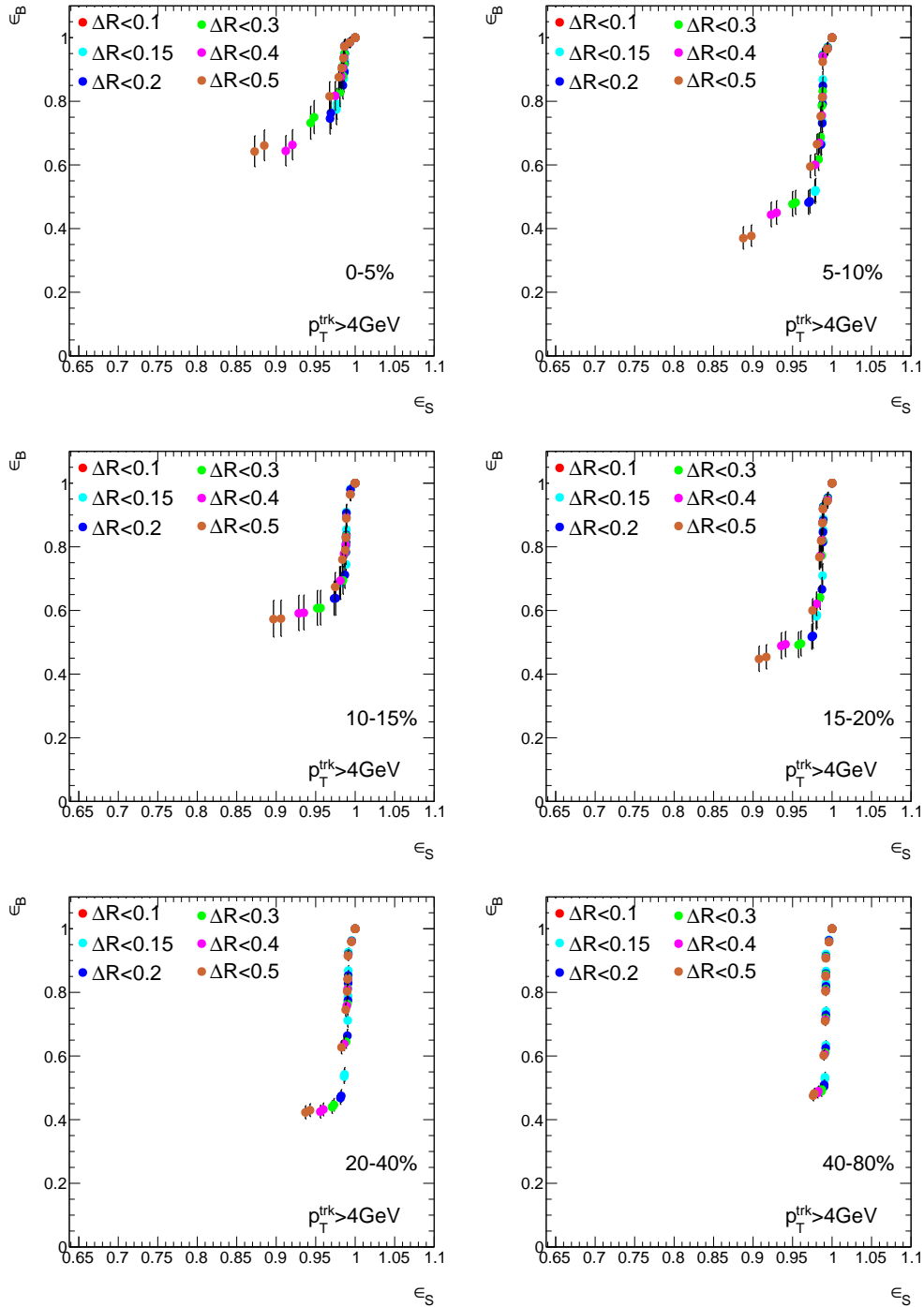
Figure B.3: Background rejection (ϵ_B) as a function of signal efficiency (ϵ_S) for different upper i_μ thresholds using a sample of $Jx\mu$ and $W \to \mu\nu_\mu$ events. For each i_μ threshold, ϵ_S and ϵ_B are determined for different ΔR. $p_{T,min}^{trk} = 4$ GeV in calculating the isolation variable i_μ. All centrality classes used in this work are shown, however only the 0-5% class is used in the optimization.
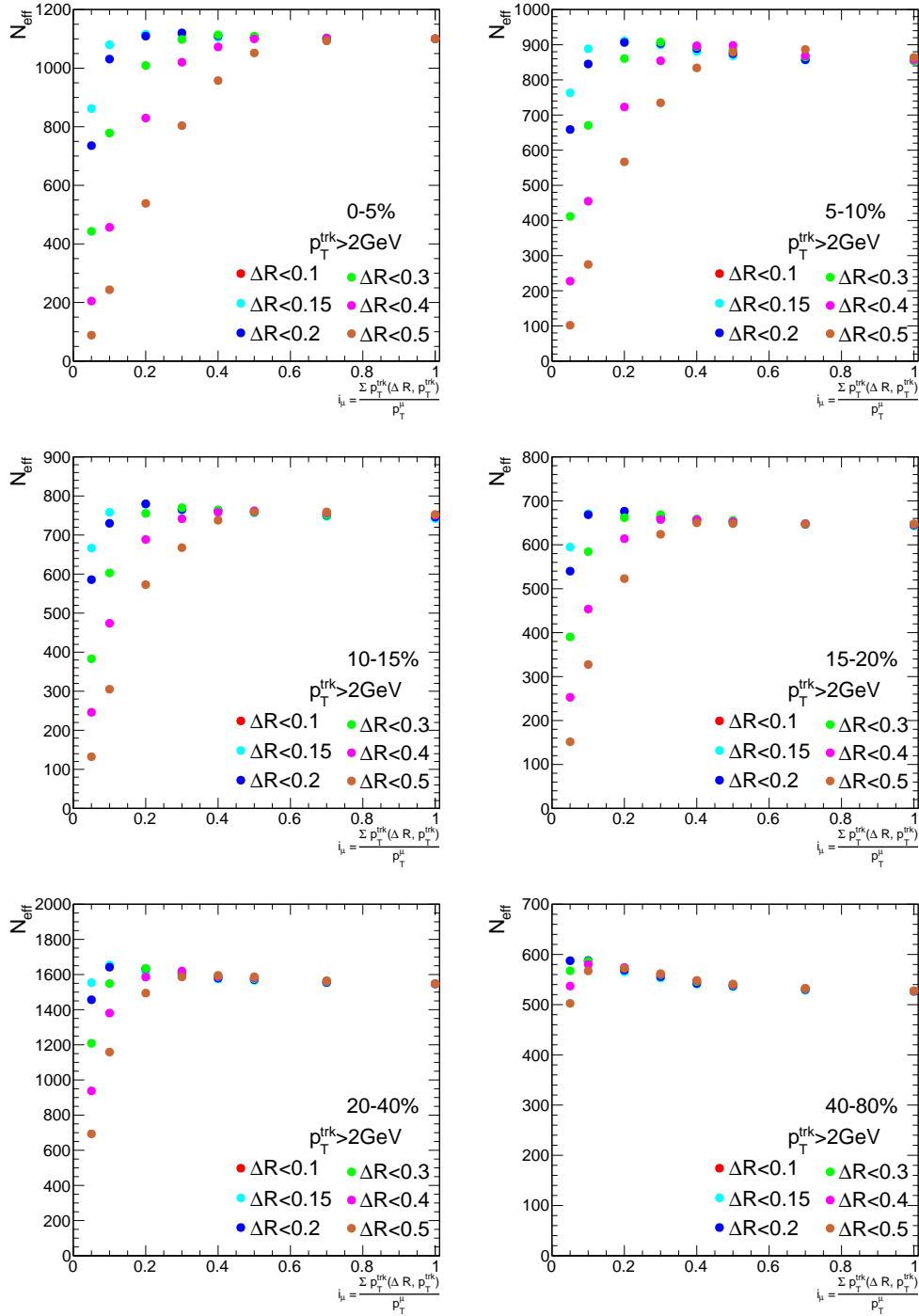
Figure B.4: Effective signal N_{eff} from Equation 5.10 as a function of the isolation variable i_μ using $p_{\text{T},min}^{trk} = 2$ GeV. N_{eff} is calculated for several upper thresholds of ΔR. All centrality classes used in this work are shown, however only the 0-5% class is used in the optimization. Each point corresponds to an isolation definition in Figure 5.9.
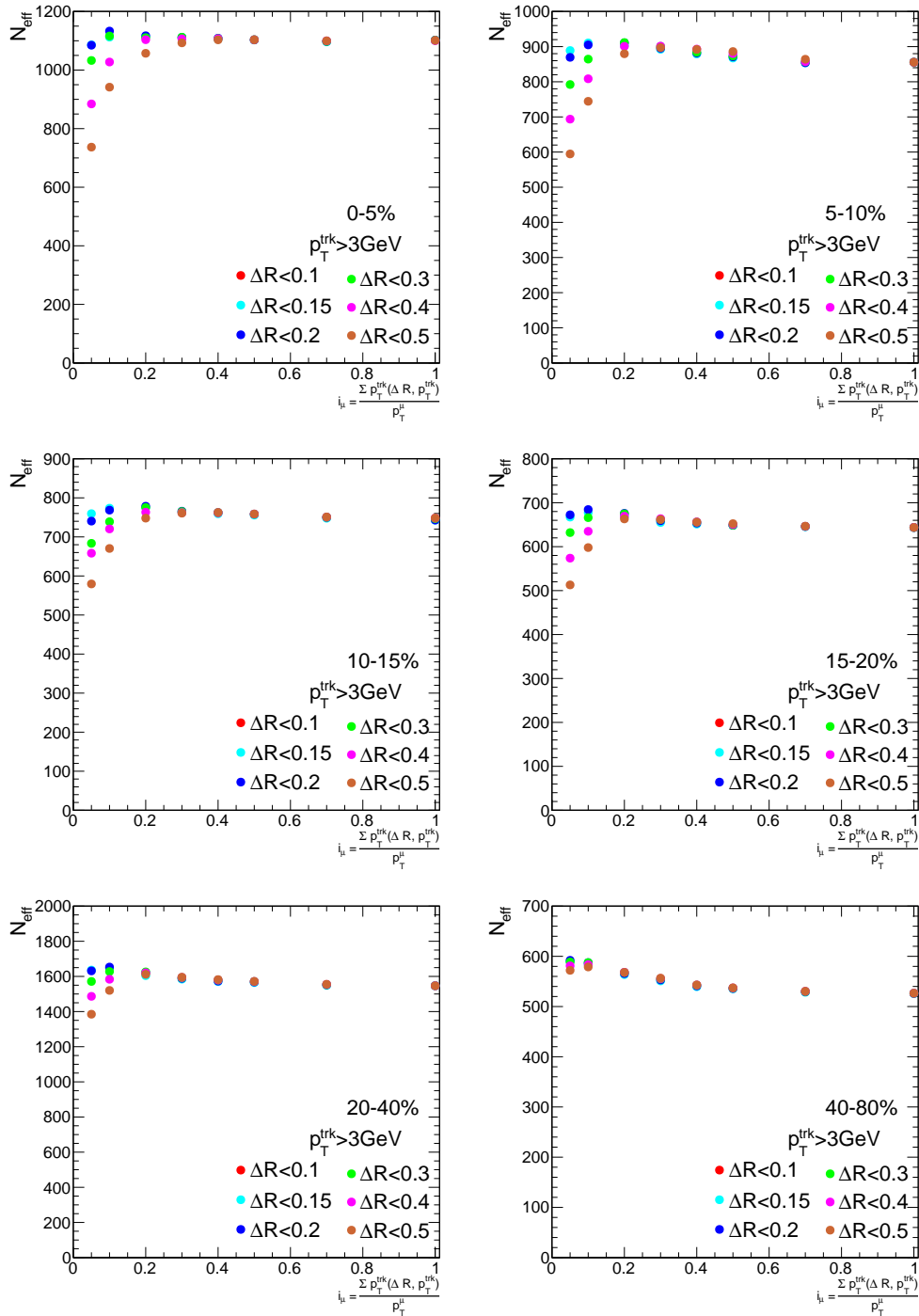
Figure B.5: Effective signal N_{eff} from Equation 5.10 as a function of the isolation variable i_μ using $p_{\text{T},min}^{trk} = 3$ GeV. N_{eff} is calculated for several upper thresholds of ΔR. All centrality classes used in this work are shown, however only the 0-5% class is used in the optimization. Each point corresponds to an isolation definition in Figure B.2.
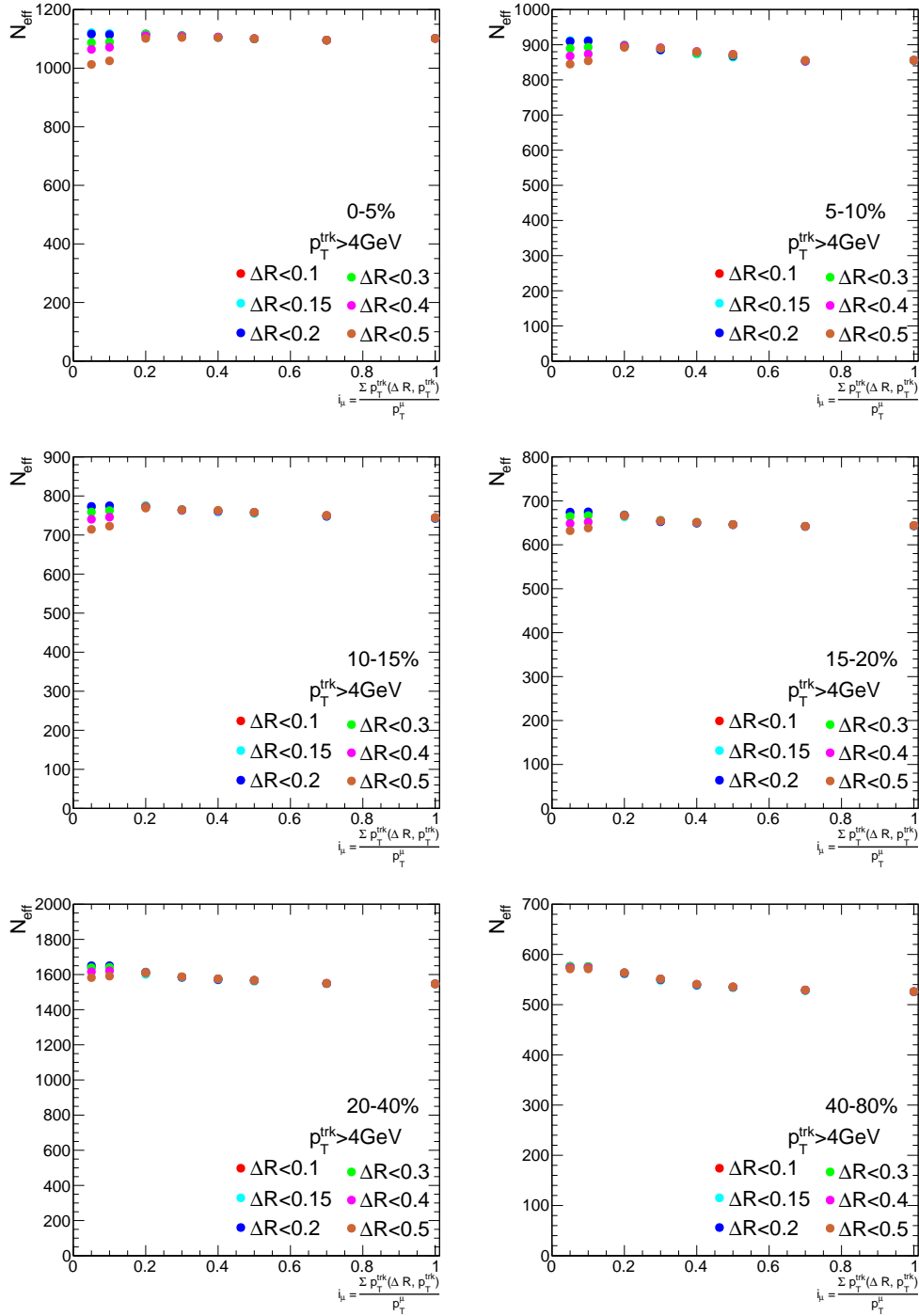
Figure B.6: Effective signal N_{eff} from Equation 5.10 as a function of the isolation variable i_μ using $p_{\text{T},min}^{trk} = 4$ GeV. N_{eff} is calculated for several upper thresholds of ΔR. All centrality classes used in this work are shown, however only the 0-5% class is used in the optimization. Each point corresponds to an isolation definition in Figure B.3.

Appendix C

Binary Scaling and Asymmetry for $W \to \mu\nu_\mu$ Events
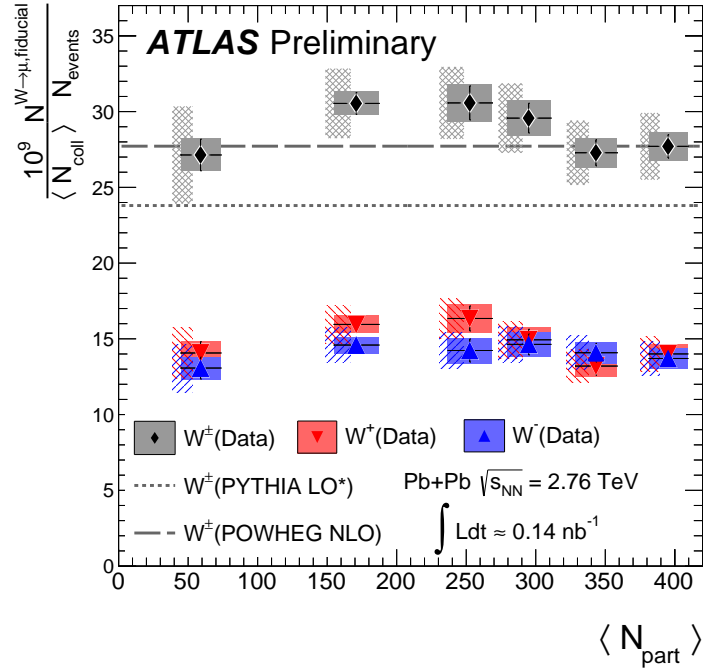
Figure C.1: W production yields per binary collision as a function of $\langle N_{\mathrm{part}} \rangle$ for $W^+ \to \mu^+ \nu_\mu$ (downward triangles), $W^- \to \mu^- \bar{\nu}_\mu$ (upward triangles), and $W^\pm \to \mu^\pm \nu_\mu$. The kinematic requirements are $0.1 < |\eta_\mu| < 2.4$, $p_T^\mu > 25$ GeV, $p_T^{\mathrm{miss}} > 25$ GeV, and $m_T > 40$ GeV. Statistical errors are shown as black bars. These are added in quadrature to the bin-uncorrelated systematic uncertainties and are shown as the filled error bands. Bin-correlated uncertainties are shown as the hatched bands and are offset for clarity. These include uncertainties from $\langle N_{\mathrm{coll}} \rangle$. Also shown are LO* and NLO predictions.
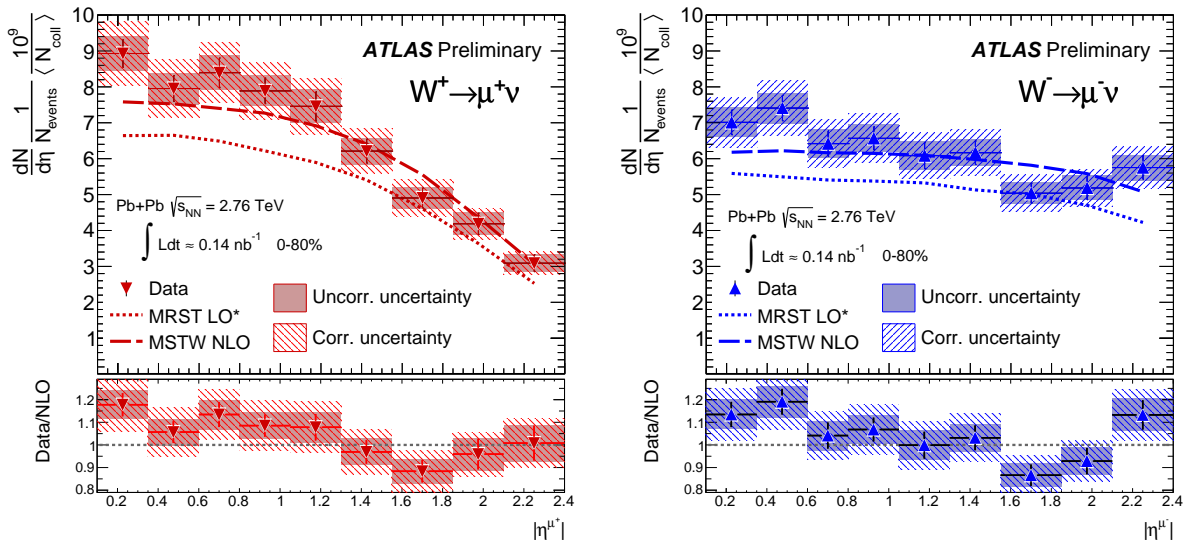
Figure C.2: Differential production yields per binary collision for $W^+ \to \mu^+\nu_\mu$ (Left) and $W^- \to \mu^-\bar{\nu}_\mu$ (Right) events compared to LO* and NLO theoretical predictions. The kinematic requirements are $p_T^\mu > 25$ GeV, $p_T^{miss} > 25$ GeV, and $m_T > 40$ GeV. The bottom panel shows the ratio between the data and NLO prediction.
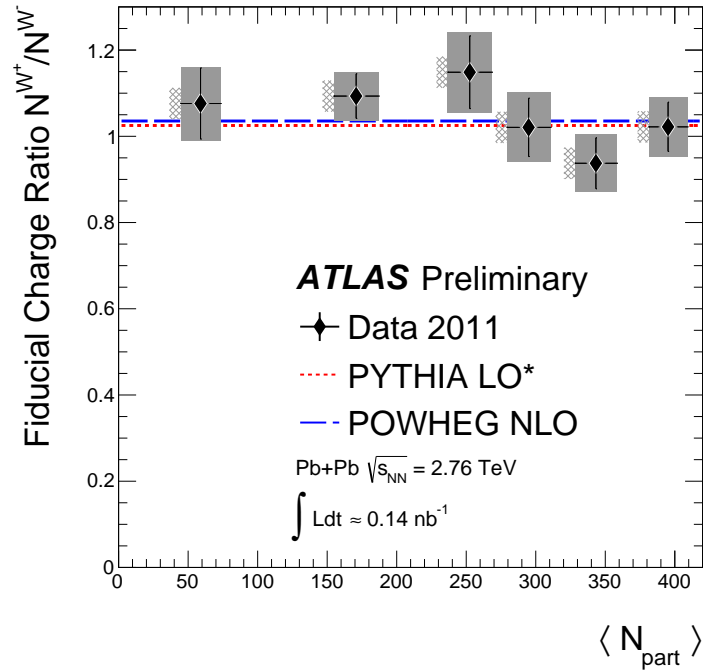
Figure C.3: Fiducial charge ratio N_{W^+}/N_{W^-} as a function of $\langle N_{\mathrm{part}} \rangle$. The kinematic requirements are $p_{\mathrm{T}}^\mu > 25$ GeV, $p_{\mathrm{T}}^{\mathrm{miss}} > 25$ GeV, and $m_{\mathrm{T}} > 40$ GeV. Statistical uncertainties are shown as black bars. Bin-uncorrelated systematic and statistical uncertainties are added in quadrature (filled errors). Scaling uncertainties are shown as the hatched boxes and are offset for clarity. Also shown are theory predictions from MRST LO* (`PYTHIA`) and MSWT2008 (`POWHEG`).
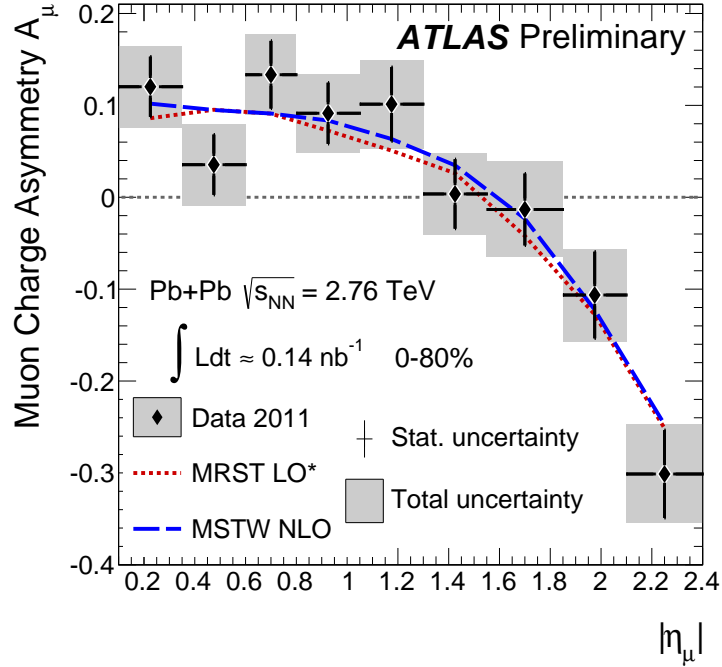
Figure C.4: The muon charge asymmetry $A_\mu = (N_{W^+} - N_{W^-})/(N_{W^+} + N_{W^-})$ as a function of $|\eta|$. The kinematic requirements are $p_T^\ell > 25$ GeV, $p_T^{miss} > 25$ GeV, and $m_T > 40$ GeV. Statistical uncertainties are shown as black bars, whereas bin–uncorrelated systematic and statistical uncertainties added in quadrature are shown as the filled error box. Scaling uncertainties are shown as the hatched boxes and are offset for clarity. The PDF uncertainties in both the CT10+EPS09 and CT10 predictions are derived from the PDF error eigensets. The total theoretical uncertainty also includes uncertainties in the renormalisation and factorisation scales used in the cross-section calculations.

Appendix D

W rapidity charge asymmetry

Considering only the light flavor u and d quarks, the cross section for W production becomes:

$$
\begin{aligned}
\frac{d\sigma_{W+}}{dy} &= \frac{2\pi G_F}{3\sqrt{2}} x_1 x_2 |V_{ud}|^2 \left[u(x_1)\bar{d}(x_2) + \bar{d}(x_1)u(x_2) \right] \\
\frac{d\sigma_{W-}}{dy} &= \frac{2\pi G_F}{3\sqrt{2}} x_1 x_2 |V_{ud}|^2 \left[\bar{d}(x_1)d(x_2) + d(x_1)\bar{u}(x_2) \right]
\end{aligned}
\tag{D.1}
$$

The charge asymmetry in the W rapidity distributions is defined as:

$$
A_W(y) = \frac{d\sigma_{W+}/dy - d\sigma_{W-}/dy}{d\sigma_{W+}/dy + d\sigma_{W-}/dy}
\tag{D.2}
$$

D.0.1   nn collisions

To see how the rapidity asymmetry can be used to constrain $u(x)/d(x)$, consider Equation D.1 for nn collisions:

$$
\begin{aligned}
\frac{d\sigma_{W+}}{dy} &= \frac{2\pi G_F}{3\sqrt{2}} x_1 x_2 |V_{ud}|^2 \left[u_n(x_1)\bar{d}_n(x_2) + \bar{d}_n(x_1)u_n(x_2) \right] \\
\frac{d\sigma_{W-}}{dy} &= \frac{2\pi G_F}{3\sqrt{2}} x_1 x_2 |V_{ud}|^2 \left[\bar{u}_n(x_1)d_n(x_2) + d_n(x_1)\bar{u}_n(x_2) \right]
\end{aligned}
\tag{D.3}
$$

From isospin symmetry, $u^p(x) = d^n(x)$, $d^p(x) = u^n(x)$, $\bar{u}^p(x) = \bar{d}^n(x)$, and $\bar{d}^p(x) = \bar{u}^n(x)$. Equation D.4 then becomes:

$$\frac{d\sigma_{W^+}}{dy} = \frac{2\pi G_F}{3\sqrt{2}} x_1 x_2 |V_{ud}|^2 \left[d_p(x_1)\bar{u}_p(x_2) + \bar{u}_p(x_1)d_p(x_2) \right]$$
$$\frac{d\sigma_{W^-}}{dy} = \frac{2\pi G_F}{3\sqrt{2}} x_1 x_2 |V_{ud}|^2 \left[\bar{d}_p(x_1)u_p(x_2) + u_p(x_1)\bar{d}_p(x_2) \right] \tag{D.4}$$

Assuming that $\bar{u}_p(x) = \bar{d}_p(x)$, the asymmetry can be written as:

$$A(y) = \frac{(d_p(x_1) - u_p(x_1))\bar{u}_p(x_2) + \bar{u}_p(x_1)(d_p(x_2) - u_p(x_2))}{(d_p(x_1) + u_p(x_1))\bar{u}_p(x_2) + \bar{u}_p(x_1)(d_p(x_2) + u_p(x_2))} \tag{D.5}$$

In the limit that $x_1 \sim 1$ and $x_2 << 1$, $\bar{u}_p(x_1)$ is negligible and the asymmetry becomes:

$$A(y) \approx \frac{d_p(x_1) - u_p(x_1)}{d_p(x_1) - u_p(x_1)} \tag{D.6}$$

Since the W rapidity distributions in nn collisions are symmetric (see Figure 2.14), the rapidity charge asymmetry does not change when $x_1 \leftrightarrow x_2$ ($y \leftrightarrow -y$). Therefore, the ratio of the parton distribution functions are directly sensitive to the asymmetry by:

$$\frac{d_p(x)}{u_p(x)} \approx \frac{1 + A(y)}{1 - A(y)} \qquad (nn) \tag{D.7}$$

D.0.2   np collisions

To see how the rapidity asymmetry can be used to constrain $u(x)/d(x)$, consider Equation D.1 for np collisions:

$$\frac{d\sigma_{W^+}}{dy} = \frac{2\pi G_F}{3\sqrt{2}} x_1 x_2 |V_{ud}|^2 \left[u_n(x_1)\bar{d}_p(x_2) + \bar{d}_n(x_1)u_p(x_2) \right]$$
$$\frac{d\sigma_{W^-}}{dy} = \frac{2\pi G_F}{3\sqrt{2}} x_1 x_2 |V_{ud}|^2 \left[\bar{u}_n(x_1)d_p(x_2) + d_n(x_1)\bar{u}_p(x_2) \right] \tag{D.8}$$

From isospin symmetry, $u^p(x) = d^n(x)$, $d^p(x) = u^n(x)$, $\bar{u}^p(x) = \bar{d}^n(x)$, and $\bar{d}^p(x) = \bar{u}^n(x)$. Equation D.4 then becomes:

$$\frac{d\sigma_{W^+}}{dy} = \frac{2\pi G_F}{3\sqrt{2}} x_1 x_2 |V_{ud}|^2 \left[d_p(x_1)\bar{d}_p(x_2) + \bar{u}_p(x_1)u_p(x_2) \right]$$
$$\frac{d\sigma_{W^-}}{dy} = \frac{2\pi G_F}{3\sqrt{2}} x_1 x_2 |V_{ud}|^2 \left[\bar{d}_p(x_1)d_p(x_2) + u_p(x_1)\bar{u}_p(x_2) \right] \tag{D.9}$$

Assuming that $\bar{u}_p(x) = \bar{d}_p(x)$, the asymmetry can be written as:

$$A(y) = \frac{(d_p(x_1) - u_p(x_1))\bar{u}_p(x_2) + \bar{u}_p(x_1)(u_p(x_2) - d_p(x_2))}{(d_p(x_1) + u_p(x_1))\bar{u}_p(x_2) + \bar{u}_p(x_1)(u_p(x_2) + d_p(x_2))} \quad \text{(D.10)}$$

In the limit that $x_1 \sim 1$ and $x_2 << 1$, $\bar{u}_p(x_1)$ is negligible and the asymmetry becomes:

$$A(y) \approx \frac{d_p(x_1) - u_p(x_1)}{d_p(x_1) + u_p(x_1)} \quad \text{(D.11)}$$

The ratio of the parton distribution functions are directly sensitive to the asymmetry by:

$$\frac{d_p(x_1)}{u_p(x_1)} \approx \frac{1 + A(y)}{1 - A(y)} \quad \text{(D.12)}$$

The W rapidity distributions in np collisions are not symmetric (see Figure 2.14). Thus, one cannot simply replace $x_1 \leftrightarrow x_2$ ($y \leftrightarrow -y$). Therefore, in the limit that $x_2 \sim 1$ and $x_1 << 1$, $\bar{u}_p(x_2)$ is negligible and the asymmetry becomes:

$$A(y) \approx \frac{u_p(x_2) - d_p(x_2)}{u_p(x_2) + d_p(x_2)} \quad \text{(D.13)}$$

The ratio of the parton distribution functions are directly sensitive to the asymmetry by:

$$\frac{d_p(x_2)}{u_p(x_2)} \approx \frac{1 - A(y)}{1 + A(y)} \quad \text{(D.14)}$$

Bibliography

[1] P.W. Higgs, Phys.Lett. **12**, 132 (1964). DOI 10.1016/0031-9163(64)91136-9

[2] K. Olive, et al., Chin.Phys. **C38**, 090001 (2014). DOI 10.1088/1674-1137/38/9/090001

[3] J.M. Campbell, J. Huston, W. Stirling, Rept.Prog.Phys. **70**, 89 (2007). DOI 10.1088/0034-4885/70/1/R02. [arXiv:hep-ph/0611148]

[4] K. Jakobs, (2012). [arXiv:1206.7024]

[5] A.D. Martin, R. Roberts, W.J. Stirling, R. Thorne, Eur.Phys.J. **C14**, 133 (2000). DOI 10.1007/s100520050740. [arXiv:hep-ph/9907231]

[6] P. Braun-Munzinger, J. Wambach, Rev.Mod.Phys. **81**, 1031 (2009). DOI 10.1103/RevModPhys.81.1031. [arXiv:0801.4256]

[7] A. Bazavov, et al., Phys.Rev. **D90**(9), 094503 (2014). DOI 10.1103/PhysRevD.90.094503. [arXiv:1407.6387]

[8] A. Bazavov, T. Bhattacharya, M. Cheng, N. Christ, C. DeTar, et al., Phys.Rev. **D80**, 014504 (2009). DOI 10.1103/PhysRevD.80.014504. [arXiv:0903.4379]

[9] G. Martinez, (2013). [arXiv:1304.1452]

[10] A. Angerami, (2012). [arXiv:1208.5043]

[11] M.L. Miller, K. Reygers, S.J. Sanders, P. Steinberg, Ann.Rev.Nucl.Part.Sci. **57**, 205 (2007). DOI 10.1146/annurev.nucl.57.090506.123020. [arXiv:nucl-ex/0701025]

[12]   K. Eskola, H. Paukkunen, C. Salgado, JHEP **0904**, 065 (2009). DOI 10.1088/1126-6708/ 2009/04/065. [arXiv:0902.4154]

[13]   I. Helenius, K.J. Eskola, H. Honkanen, C.A. Salgado, JHEP **1207**, 073 (2012). DOI 10.1007/ JHEP07(2012)073. [arXiv:1205.5359]

[14]   H. Paukkunen, C.A. Salgado, JHEP **1103**, 071 (2011). DOI 10.1007/JHEP03(2011)071. [arXiv:1010.5392]

[15]   X.N. Wang, Z. Huang, I. Sarcevic, Phys.Rev.Lett. **77**, 231 (1996). DOI 10.1103/PhysRevLett. 77.231. [arXiv:hep-ph/9605213]

[16]   CERN. (CERN, Geneva, 2014). CERN Accelerator School in collaboration with The Norwegian University of Science and Technology (NTNU)

[17]   S. Baird, Accelerators for pedestrians; rev. version. Tech. Rep. AB-Note-2007-014. CERN-AB-Note-2007-014. PS-OP-Note-95-17-Rev-2. CERN-PS-OP-Note-95-17-Rev-2, CERN, Geneva (2007)

[18]   B. Holzer, pp. 27–45 (2013). DOI 10.5170/CERN-2013-007.27. [arXiv:1404.0923]

[19]   W. Herr, B. Muratori, *Concept of luminosity* (2006)

[20]   G. Aad, et al., Eur.Phys.J. **C71**, 1630 (2011). DOI 10.1140/epjc/s10052-011-1630-5. [arXiv:1101.2185]

[21]   L. Evans, P. Bryant, JINST **3**, S08001 (2008). DOI 10.1088/1748-0221/3/08/S08001

[22]   G. Aad, et al., JINST **3**, S08003 (2008). DOI 10.1088/1748-0221/3/08/S08003

[23]   Muon reconstruction efficiency in reprocessed 2010 LHC proton-proton collision data recorded with the ATLAS detector. Tech. Rep. ATLAS-CONF-2011-063, CERN, Geneva (2011)

[24]   S. Armstrong, V. Boisvert, S. Brandt, M. Elsing, J. Baines, et al., eConf **C0303241**, TUGT008 (2003). [arXiv:physics/0306101]

[25]   S. Leontsinis, Performance of the muon identification and reconstruction with the ATLAS detector. Tech. Rep. ATL-PHYS-PROC-2014-091, CERN, Geneva (2014)

[26] E. Lund, L. Bugge, I. Gavrilenko, A. Strandlie, J. Instrum. **4**(ATL-SOFT-PUB-2009-002. ATL-COM-SOFT-2008-007), P04016. 14 p (2008). Approved for publication by the ATLAS Publication comitee, submitted to JINST.

[27] E. Lund, L. Bugge, T.G. Cornelissen, M. Elsing, I. Gavrilenko, W. Liebig, D. Lopez Mateos, A. Salzburger, A. Strandlie, S. Todorova, Refitting of combined inner detector and muon spectrometer tracks from Monte Carlo samples by using the Kalman fitter and the STEP algorithm in the ATLAS experiment. Tech. Rep. ATL-SOFT-PUB-2008-005. ATL-COM-SOFT-2008-022, CERN, Geneva (2008). This note has been approved by Markus Elsing (he's also an author).

[28] G. Aad, et al., (2009). [arXiv:0901.0512]

[29] W. Lohmann, R. Kopp, R. Voss, *Energy loss of muons in the energy range 1-10000 GeV* (CERN, Geneva, 1985)

[30] A. Salzburger, The ATLAS Track Extrapolation Package. Tech. Rep. ATL-SOFT-PUB-2007-005. ATL-COM-SOFT-2007-010, CERN, Geneva (2007)

[31] T. Cornelissen, M. Elsing, I. Gavrilenko, W. Liebig, E. Moyse, A. Salzburger, Journal of Physics: Conference Series **119**(3), 032014 (2008). URL `http://stacks.iop.org/1742-6596/119/i=3/a=032014`

[32] T. Cornelissen, M. Elsing, S. Fleischmann, W. Liebig, E. Moyse, A. Salzburger, Concepts, Design and Implementation of the ATLAS New Tracking (NEWT). Tech. Rep. ATL-SOFT-PUB-2007-007. ATL-COM-SOFT-2007-002, CERN, Geneva (2007)

[33] Z. van Kesteren, Identification of muons in ATLAS. Ph.D. thesis, Amsterdam U., Amsterdam (2010). Presented on 12 Mar 2010

[34] J. Snuverink, The ATLAS muon spectrometer: commissioning and tracking. Ph.D. thesis, Twente, Twente U., Enschede, Twente (2009). Presented on 16 Oct 2009

[35] N. Van Eldik, F.L. Linde, P.M. Kluit, S.C.M. Bentvelsen, The ATLAS muon spectrometer: calibration and pattern recognition. Ph.D. thesis, U. Amsterdam, Amsterdam (2007). Presented on 22 Feb 2007

[36] G. Aad, et al., Phys.Rev.Lett. **105**, 252303 (2010). DOI 10.1103/PhysRevLett.105.252303. [arXiv:1011.6182]

[37] Dimuon composition in ATLAS at 7 TeV. Tech. Rep. ATLAS-CONF-2011-003, CERN, Geneva (2011)

[38] G. Aad, et al., Phys.Rev.Lett. **110**(2), 022301 (2013). DOI 10.1103/PhysRevLett.110.022301. [arXiv:1210.6486]

[39] G. Aad, et al., Eur.Phys.J. **C72**, 1844 (2012). DOI 10.1140/epjc/s10052-011-1844-6. [arXiv:1108.5602]

[40] G. Aad, et al., Eur.Phys.J. **C75**(1), 23 (2015). DOI 10.1140/epjc/s10052-014-3231-6. [arXiv:1408.4674]

[41] G. Aad, et al., Eur.Phys.J. **C74**(9), 3034 (2014). DOI 10.1140/epjc/s10052-014-3034-9. [arXiv:1404.4562]

[42] Measurement of high-pT isolated prompt photons in lead-lead collisions at $\sqrt{s_{NN}} = 2.76\,TeV$ with the ATLAS detector at the LHC. Tech. Rep. ATLAS-CONF-2012-051, CERN, Geneva (2012). URL `https://cds.cern.ch/record/1451913`

[43] G. Aad, et al., Phys.Rev. **D85**, 072004 (2012). DOI 10.1103/PhysRevD.85.072004. [arXiv:1109.5141]

[44] R. Aaij, et al., JHEP **1206**, 058 (2012). DOI 10.1007/JHEP06(2012)058. [arXiv:1204.1620]

[45] An extrapolation to a larger fiducial volume of the measurement of the $W \to \ell\nu_\ell$ charge asymmetry in proton-proton collisions at sqrt(s)=7TeV with the ATLAS detector. Tech. Rep. ATLAS-CONF-2011-129, CERN, Geneva (2011). URL `https://cds.cern.ch/record/1383832`

[46] M. Klasen, M. Brandt, Phys.Rev. **D88**, 054002 (2013). DOI 10.1103/PhysRevD.88.054002. [arXiv:1305.5677]

[47] V.M. Abazov, et al., Phys.Rev. **D88**, 091102 (2013). DOI 10.1103/PhysRevD.88.091102. [arXiv:1309.2591]

[48] V. Khachatryan, et al., (2015). [arXiv:1503.05825]

[49] H. Paukkunen, (2015). [arXiv:1503.02448]

[50] W.T.L.P. Lavrijsen, *COmBined muon reconstruction for Atlas* (2002)

[51] G. Arnison, et al., Phys.Lett. **B122**, 103 (1983). DOI 10.1016/0370-2693(83)91177-2

[52] R. Hamberg, W. van Neerven, T. Matsuura, Nucl.Phys. **B359**, 343 (1991). DOI 10.1016/0550-3213(91)90064-5

[53] C. Anastasiou, L.J. Dixon, K. Melnikov, F. Petriello, Phys.Rev. **D69**, 094008 (2004). DOI 10.1103/PhysRevD.69.094008. [arXiv:hep-ph/0312266]

[54] T.P. Cheng, L.F. Li, *Gauge Theory of Elementary Particles* (Oxford Press, 1989)

[55] S. Narison, *QCD as a theory of hadrons from partons to confinement* (Cambridge Press, 2004)

[56] M. Gell-Mann, Phys.Rev. **125**, 1067 (1962). DOI 10.1103/PhysRev.125.1067

[57] Y. Ne'eman, Nucl.Phys. **26**, 222 (1961). DOI 10.1016/0029-5582(61)90134-1

[58] M. Gell-Mann, Y. Neemam, *The Eightfold way: a review with a collection of reprints* (1964)

[59] W. Fowler, R. Shutt, A. Thorndike, W. Whittemore, Phys.Rev. **95**, 1026 (1954). DOI 10.1103/PhysRev.95.1026

[60] A. Pais, Phys.Rev. **86**, 663 (1952). DOI 10.1103/PhysRev.86.663

[61] M. Gell-Mann, Phys.Rev. **92**, 833 (1953). DOI 10.1103/PhysRev.92.833

[62] T. Nakano, K. Nishijima, Prog.Theor.Phys. **10**, 581 (1953). DOI 10.1143/PTP.10.581

[63] V. Barnes, P. Connolly, D. Crennell, B. Culwick, W. Delaney, et al., Phys.Rev.Lett. **12**, 204 (1964). DOI 10.1103/PhysRevLett.12.204

[64] M. Gell-Mann, Phys.Lett. **8**, 214 (1964). DOI 10.1016/S0031-9163(64)92001-3

[65] G. Zweig, *An SU(3) model for strong interaction symmetry and its breaking. Version 1* (1964)

[66] D.J. Griffiths, *INTRODUCTION TO ELEMENTARY PARTICLES* (1987)

[67]   R.P. Feynman, Phys.Rev.Lett. **23**, 1415 (1969). DOI 10.1103/PhysRevLett.23.1415

[68]   F. Close, *An Introduction to Quarks and Partons* (1979)

[69]   F. Aaron, et al., JHEP **1001**, 109 (2010). DOI 10.1007/JHEP01(2010)109. [arXiv:0911.0884]

[70]   A. Benvenuti, et al., Phys.Lett. **B223**, 485 (1989). DOI 10.1016/0370-2693(89)91637-7

[71]   M. Adams, et al., Phys.Rev. **D54**, 3006 (1996). DOI 10.1103/PhysRevD.54.3006

[72]   M. Arneodo, et al., Nucl.Phys. **B483**, 3 (1997). DOI 10.1016/S0550-3213(96)00538-X. [arXiv:hep-ph/9610231]

[73]   L. Whitlow, E. Riordan, S. Dasu, S. Rock, A. Bodek, Phys.Lett. **B282**, 475 (1992). DOI 10.1016/0370-2693(92)90672-Q

[74]   J. Callan, Curtis G., D.J. Gross, Phys.Rev.Lett. **22**, 156 (1969). DOI 10.1103/PhysRevLett. 22.156

[75]   A. Bodek, M. Breidenbach, D. Dubin, J. Elias, J.I. Friedman, et al., Phys.Rev. **D20**, 1471 (1979). DOI 10.1103/PhysRevD.20.1471

[76]   J. Gomez, R. Arnold, P.E. Bosted, C. Chang, A. Katramatou, et al., Phys.Rev. **D49**, 4348 (1994). DOI 10.1103/PhysRevD.49.4348

[77]   W. Melnitchouk, A.W. Thomas, Phys.Lett. **B377**, 11 (1996). DOI 10.1016/0370-2693(96) 00292-4. [arXiv:nucl-th/9602038]

[78]   S. Tkachenko, et al., Phys.Rev. **C89**(4), 045206 (2014). DOI 10.1103/PhysRevC.90.059901, 10.1103/PhysRevC.89.045206. [arXiv:1402.2477]

[79]   P. Bosetti, et al., Nucl.Phys. **B142**, 1 (1978). DOI 10.1016/0550-3213(78)90399-1

[80]   J. Morfin, et al., Phys.Lett. **B104**, 235 (1981). DOI 10.1016/0370-2693(81)90598-0

[81]   C.N. Yang, R.L. Mills, Phys.Rev. **96**, 191 (1954). DOI 10.1103/PhysRev.96.191

[82]   M.E. Peskin, D.V. Schroeder, *An Introduction to quantum field theory* (1995)

[83] S. Narison, Camb.Monogr.Part.Phys.Nucl.Phys.Cosmol. **17**, 1 (2002). [arXiv:hep-ph/0205006]

[84] L. Faddeev, V. Popov, Phys.Lett. **B25**, 29 (1967). DOI 10.1016/0370-2693(67)90067-6

[85] F. Englert, R. Brout, Phys.Rev.Lett. **13**, 321 (1964). DOI 10.1103/PhysRevLett.13.321

[86] R.K. Ellis, W.J. Stirling, B. Webber, Camb.Monogr.Part.Phys.Nucl.Phys.Cosmol. **8**, 1 (1996)

[87] X.G. Wu, S.J. Brodsky, M. Mojaza, Prog.Part.Nucl.Phys. **72**, 44 (2013). DOI 10.1016/j.ppnp.2013.06.001. [arXiv:1302.0599]

[88] H.D. Politzer, Phys.Rev.Lett. **30**, 1346 (1973). DOI 10.1103/PhysRevLett.30.1346

[89] D.J. Gross, F. Wilczek, Phys.Rev.Lett. **30**, 1343 (1973). DOI 10.1103/PhysRevLett.30.1343

[90] Y. Nambu, Sci.Am. **235N5**, 48 (1976). DOI 10.1038/scientificamerican1176-48

[91] K.G. Wilson, Phys.Rev. **D10**, 2445 (1974). DOI 10.1103/PhysRevD.10.2445

[92] J.C. Collins, D.E. Soper, G.F. Sterman, Adv.Ser.Direct.High Energy Phys. **5**, 1 (1988). [arXiv:hep-ph/0409313]

[93] S. Drell, T.M. Yan, Annals Phys. **66**, 578 (1971). DOI 10.1016/0003-4916(71)90071-6

[94] W.A. Bardeen, A. Buras, D. Duke, T. Muta, Phys.Rev. **D18**, 3998 (1978). DOI 10.1103/PhysRevD.18.3998

[95] L. Lipatov, Sov.J.Nucl.Phys. **20**, 94 (1975)

[96] V. Gribov, L. Lipatov, Sov.J.Nucl.Phys. **15**, 438 (1972)

[97] G. Altarelli, G. Parisi, Nucl.Phys. **B126**, 298 (1977). DOI 10.1016/0550-3213(77)90384-4

[98] Y.L. Dokshitzer, Sov.Phys.JETP **46**, 641 (1977)

[99] C. Adloff, et al., Eur.Phys.J. **C13**, 609 (2000). DOI 10.1007/s100520050721. [arXiv:hep-ex/9908059]

[100] S. Chekanov, et al., Eur.Phys.J. **C21**, 443 (2001). DOI 10.1007/s100520100749. [arXiv:hep-ex/0105090]

[101] U.K. Yang, et al., Phys.Rev.Lett. **86**, 2742 (2001). DOI 10.1103/PhysRevLett.86.2742. [arXiv:hep-ex/0009041]

[102] A. Benvenuti, et al., Phys.Lett. **B237**, 592 (1990). DOI 10.1016/0370-2693(90)91231-Y

[103] W. Seligman, C. Arroyo, L. de Barbaro, P. de Barbaro, A. Bazarko, et al., Phys.Rev.Lett. **79**, 1213 (1997). DOI 10.1103/PhysRevLett.79.1213. [arXiv:hep-ex/9701017]

[104] R. Towell, et al., Phys.Rev. **D64**, 052002 (2001). DOI 10.1103/PhysRevD.64.052002. [arXiv:hep-ex/0103030]

[105] G. Moreno, C. Brown, W. Cooper, D. Finley, Y. Hsiung, et al., Phys.Rev. **D43**, 2815 (1991). DOI 10.1103/PhysRevD.43.2815

[106] T. Affolder, et al., Phys.Rev. **D64**, 032001 (2001). DOI 10.1103/PhysRevD.65.039903, 10.1103/PhysRevD.64.032001,10.1103/PhysRevD.64.03200110.1103/PhysRevD.65.039903. [arXiv:hep-ph/0102074]

[107] B. Abbott, et al., Phys.Rev.Lett. **86**, 1707 (2001). DOI 10.1103/PhysRevLett.86.1707. [arXiv:hep-ex/0011036]

[108] E.A. Kuraev, L.N. Lipatov, V.S. Fadin, Sov.Phys.JETP **44**, 443 (1976)

[109] E. Kuraev, L. Lipatov, V.S. Fadin, Sov.Phys.JETP **45**, 199 (1977)

[110] V.S. Fadin, E. Kuraev, L. Lipatov, Phys.Lett. **B60**, 50 (1975). DOI 10.1016/0370-2693(75)90524-9

[111] I. Balitsky, L. Lipatov, Sov.J.Nucl.Phys. **28**, 822 (1978)

[112] J. Pumplin, D. Stump, R. Brock, D. Casey, J. Huston, et al., Phys.Rev. **D65**, 014013 (2001). DOI 10.1103/PhysRevD.65.014013. [arXiv:hep-ph/0101032]

[113] J. Gao, M. Guzzi, J. Huston, H.L. Lai, Z. Li, et al., Phys.Rev. **D89**(3), 033009 (2014). DOI 10.1103/PhysRevD.89.033009. [arXiv:1302.6246]

[114] I. Hinchliffe, A. Kwiatkowski, Ann.Rev.Nucl.Part.Sci. **46**, 609 (1996). DOI 10.1146/annurev. nucl.46.1.609. [arXiv:hep-ph/9604210]

[115] E. Perez, E. Rizvi, Rep.Prog.Phys. **76**, 046201 (2013). DOI 10.1088/0034-4885/76/4/046201. [arXiv:1208.1178]

[116] N. Cabibbo, Phys.Rev.Lett. **10**, 531 (1963). DOI 10.1103/PhysRevLett.10.531

[117] M. Kobayashi, T. Maskawa, Prog.Theor.Phys. **49**, 652 (1973). DOI 10.1143/PTP.49.652

[118] F. Halzen, Y.S. Jeong, C. Kim, Phys.Rev. **D88**, 073013 (2013). DOI 10.1103/PhysRevD.88. 073013. [arXiv:1304.0322]

[119] K. Golec-Biernat, A. Luszczak, Phys.Rev. **D81**, 014009 (2010). DOI 10.1103/PhysRevD.81. 014009. [arXiv:0911.2789]

[120] S. Glashow, Nucl.Phys. **22**, 579 (1961). DOI 10.1016/0029-5582(61)90469-2

[121] S. Weinberg, Phys.Rev.Lett. **19**, 1264 (1967). DOI 10.1103/PhysRevLett.19.1264

[122] A. Salam, Conf.Proc. **C680519**, 367 (1968)

[123] B. Abbott, et al., Phys.Rev. **D63**, 072001 (2001). DOI 10.1103/PhysRevD.63.072001. [arXiv:hep-ex/0009034]

[124] R. Thurman-Keup, A. Kotwal, M. Tecchio, A. Byon-Wagner, Rev.Mod.Phys. **73**, 267 (2001). DOI 10.1103/RevModPhys.73.267

[125] G. Aad, et al., Eur.Phys.J. **C72**, 2001 (2012). DOI 10.1140/epjc/s10052-012-2001-6. [arXiv:1203.2165]

[126] S. Catani, G. Ferrera, M. Grazzini, JHEP **1005**, 006 (2010). DOI 10.1007/JHEP05(2010)006. [arXiv:1002.3115]

[127] R. Hagedorn, Nuovo Cim.Suppl. **3**, 147 (1965)

[128] R. Hagedorn, Nuovo Cim. **A56**, 1027 (1968). DOI 10.1007/BF02751614

[129] J.C. Collins, M. Perry, Phys.Rev.Lett. **34**, 1353 (1975). DOI 10.1103/PhysRevLett.34.1353

[130] N. Cabibbo, G. Parisi, Phys.Lett. **B59**, 67 (1975). DOI 10.1016/0370-2693(75)90158-6

[131] A. Chodos, R. Jaffe, K. Johnson, C.B. Thorn, V. Weisskopf, Phys.Rev. **D9**, 3471 (1974). DOI 10.1103/PhysRevD.9.3471

[132] W. Haxton, L. Heller, Phys.Rev. **D22**, 1198 (1980). DOI 10.1103/PhysRevD.22.1198

[133] P. Hasenfratz, R. Horgan, J. Kuti, J. Richard, Phys.Scripta **23**, 914 (1981). DOI 10.1088/0031-8949/23/5B/003

[134] C. Wong, *Introduction to high-energy heavy ion collisions* (1995)

[135] S. Borsanyi, G. Endrodi, Z. Fodor, A. Jakovac, S.D. Katz, et al., JHEP **1011**, 077 (2010). DOI 10.1007/JHEP11(2010)077. [arXiv:1007.2580]

[136] S. Borsanyi, Z. Fodor, C. Hoelbling, S.D. Katz, S. Krieg, et al., Phys.Lett. **B730**, 99 (2014). DOI 10.1016/j.physletb.2014.01.007. [arXiv:1309.5258]

[137] M. Cheng, N. Christ, S. Datta, J. van der Heide, C. Jung, et al., Phys.Rev. **D77**, 014511 (2008). DOI 10.1103/PhysRevD.77.014511. [arXiv:0710.0354]

[138] R. Hagedorn, Lect.Notes Phys. **221**, 53 (1985)

[139] A. Bazavov, T. Bhattacharya, M. Cheng, C. DeTar, H. Ding, et al., Phys.Rev. **D85**, 054503 (2012). DOI 10.1103/PhysRevD.85.054503. [arXiv:1111.1710]

[140] L.D. McLerran, B. Svetitsky, Phys.Rev. **D24**, 450 (1981). DOI 10.1103/PhysRevD.24.450

[141] A.M. Polyakov, Phys.Lett. **B72**, 477 (1978). DOI 10.1016/0370-2693(78)90737-2

[142] G. 't Hooft, Nucl.Phys. **B138**, 1 (1978). DOI 10.1016/0550-3213(78)90153-0

[143] L. Susskind, Phys.Rev. **D20**, 2610 (1979). DOI 10.1103/PhysRevD.20.2610

[144] J. Bjorken, Phys.Rev. **D27**, 140 (1983). DOI 10.1103/PhysRevD.27.140

[145] B. Muller, J. Schukraft, B. Wyslouch, Ann.Rev.Nucl.Part.Sci. **62**, 361 (2012). DOI 10.1146/annurev-nucl-102711-094910. [arXiv:1202.3233]

[146] K. Krajczar, J.Phys. **G38**, 124041 (2011). DOI 10.1088/0954-3899/38/12/124041

[147] K. Adcox, et al., Phys.Rev.Lett. **87**, 052301 (2001). DOI 10.1103/PhysRevLett.87.052301. [arXiv:nucl-ex/0104015]

[148] T. Csorgo, M. Nagy, M. Csanad, Phys.Lett. **B663**, 306 (2008). DOI 10.1016/j.physletb.2008. 04.038. [arXiv:nucl-th/0605070]

[149] T. Csorgo, M. Nagy, M. Csanad, Braz.J.Phys. **37**, 723 (2007). DOI 10.1590/ S0103-97332007000500012. [arXiv:nucl-th/0702043]

[150] M. Nagy, T. Csorgo, M. Csanad, Phys.Rev. **C77**, 024908 (2008). DOI 10.1103/PhysRevC. 77.024908. [arXiv:0709.3677]

[151] T. Csorgo, M. Nagy, M. Csanad, J.Phys. **G35**, 104128 (2008). DOI 10.1088/0954-3899/35/ 10/104128. [arXiv:0805.1562]

[152] W. Israel, J. Stewart, Annals Phys. **118**, 341 (1979). DOI 10.1016/0003-4916(79)90130-1

[153] J.M. Maldacena, Int.J.Theor.Phys. **38**, 1113 (1999). DOI 10.1023/A:1026654312961. [arXiv:hep-th/9711200]

[154] G. Policastro, D.T. Son, A.O. Starinets, Phys.Rev.Lett. **87**, 081601 (2001). DOI 10.1103/ PhysRevLett.87.081601. [arXiv:hep-th/0104066]

[155] P. Kovtun, D.T. Son, A.O. Starinets, Phys.Rev.Lett. **94**, 111601 (2005). DOI 10.1103/ PhysRevLett.94.111601. [arXiv:hep-th/0405231]

[156] P.B. Arnold, G.D. Moore, L.G. Yaffe, JHEP **0305**, 051 (2003). DOI 10.1088/1126-6708/ 2003/05/051. [arXiv:hep-ph/0302165]

[157] G. Aad, et al., Phys.Rev. **C86**, 014907 (2012). DOI 10.1103/PhysRevC.86.014907. [arXiv:1203.3087]

[158] G. Aad, et al., JHEP **1311**, 183 (2013). DOI 10.1007/JHEP11(2013)183. [arXiv:1305.2942]

[159] G. Aad, et al., Eur.Phys.J. **C74**(11), 3157 (2014). DOI 10.1140/epjc/s10052-014-3157-z. [arXiv:1408.4342]

[160] R. Glauber, *in Lectures on Theoretical Physics*, vol. 1 (Interscience, 1959)

[161] J. Chauvin, D. Lebrun, A. Lounis, M. Buenerd, Phys.Rev. **C28**, 1970 (1983). DOI 10.1103/ PhysRevC.28.1970

[162] T. Wibig, D. Sobczynska, J.Phys. **G24**, 2037 (1998). DOI 10.1088/0954-3899/24/11/006. [arXiv:hep-ph/9809494]

[163] D. Kharzeev, C. Lourenco, M. Nardi, H. Satz, Z.Phys. **C74**, 307 (1997). DOI 10.1007/ s002880050392. [arXiv:hep-ph/9612217]

[164] A. Bialas, M. Bleszynski, W. Czyz, Nucl.Phys. **B111**, 461 (1976). DOI 10.1016/0550-3213(76) 90329-1

[165] H. De Vries, C. De Jager, C. De Vries, Atom.Data Nucl.Data Tabl. **36**, 495 (1987). DOI 10.1016/0092-640X(87)90013-1

[166] G. Antchev, et al., Europhys.Lett. **101**, 21004 (2013). DOI 10.1209/0295-5075/101/21004

[167] G. Aad, et al., Nature Commun. **2**, 463 (2011). DOI 10.1038/ncomms1472. [arXiv:1104.0326]

[168] B. Alver, M. Baker, C. Loizides, P. Steinberg, (2008). [arXiv:0805.4411]

[169] D. Kharzeev, M. Nardi, Phys.Lett. **B507**, 121 (2001). DOI 10.1016/S0370-2693(01)00457-9. [arXiv:nucl-th/0012025]

[170] X.N. Wang, M. Gyulassy, Phys. Rev. Lett. **86**, 3496 (2001). DOI 10.1103/PhysRevLett.86. 3496. URL `http://link.aps.org/doi/10.1103/PhysRevLett.86.3496`

[171] J. Aubert, et al., Phys.Lett. **B123**, 275 (1983). DOI 10.1016/0370-2693(83)90437-9

[172] M. Arneodo, Phys.Rept. **240**, 301 (1994). DOI 10.1016/0370-1573(94)90048-5

[173] I. Schienbein, J. Yu, K. Kovarik, C. Keppel, J. Morfin, et al., Phys.Rev. **D80**, 094004 (2009). DOI 10.1103/PhysRevD.80.094004. [arXiv:0907.2357]

[174] M. Hirai, S. Kumano, T.H. Nagai, Phys.Rev. **C76**, 065207 (2007). DOI 10.1103/PhysRevC. 76.065207. [arXiv:0709.3038]

[175] D. de Florian, R. Sassot, Phys.Rev. **D69**, 074028 (2004). DOI 10.1103/PhysRevD.69.074028. [arXiv:hep-ph/0311227]

[176] I. Helenius, (2014). [arXiv:1408.6660]

[177] S.J. Brodsky, F.E. Close, J. Gunion, Phys.Rev. **D6**, 177 (1972). DOI 10.1103/PhysRevD.6.177

[178] S.J. Brodsky, H.J. Lu, Phys.Rev.Lett. **64**, 1342 (1990). DOI 10.1103/PhysRevLett.64.1342

[179] S.J. Brodsky, AIP Conf.Proc. **792**, 279 (2005). DOI 10.1063/1.2122036

[180] N. Armesto, J.Phys. **G32**, R367 (2006). DOI 10.1088/0954-3899/32/11/R01. [arXiv:hep-ph/0604108]

[181] S. Malace, D. Gaskell, D.W. Higinbotham, I. Cloet, Int.J.Mod.Phys. **E23**, 1430013 (2014). DOI 10.1142/S0218301314300136. [arXiv:1405.1270]

[182] S. Chatrchyan, et al., Phys.Rev. **C84**, 024906 (2011). DOI 10.1103/PhysRevC.84.024906. [arXiv:1102.1957]

[183] S. Chatrchyan, et al., Phys.Lett. **B712**, 176 (2012). DOI 10.1016/j.physletb.2012.04.058. [arXiv:1202.5022]

[184] S. Adler, et al., Phys.Rev.Lett. **91**, 072301 (2003). DOI 10.1103/PhysRevLett.91.072301. [arXiv:nucl-ex/0304022]

[185] J. Adams, et al., Phys.Rev.Lett. **91**, 172302 (2003). DOI 10.1103/PhysRevLett.91.172302. [arXiv:nucl-ex/0305015]

[186] Measurement of momentum imbalance in $Z \to \ell\ell +$ Jet events in Lead-Lead collisions at $\sqrt{s_{NN}}=$ 2.76 TeV with the ATLAS detector. Tech. Rep. ATLAS-CONF-2012-119, CERN, Geneva (2012). URL `https://cds.cern.ch/record/1472941`

[187] S. Chatrchyan, et al., Phys.Lett. **B718**, 773 (2013). DOI 10.1016/j.physletb.2012.11.003. [arXiv:1205.0206]

[188] Measurement of the correlation of jets with high p_T isolated prompt photons in lead-lead collisions at $sqrts_{NN} = 2.76$ TeV with the ATLAS detector at the LHC. Tech. Rep. ATLAS-CONF-2012-121, CERN, Geneva (2012). URL `https://cds.cern.ch/record/1473135`

[189] E.M. McMillan, Phys. Rev. **68**, 143 (1945). DOI 10.1103/PhysRev.68.143. URL `http://link.aps.org/doi/10.1103/PhysRev.68.143`

[190] V.a. Veksler, *Coherent Principle Of Acceleration Of Charged Particles* (1956)

[191] S. Lee, *Accelerator Physics* (World Scientific, 2004)

[192] J. Rossbach, P. Schmser, (DESY-M-93-02), 72 p (1993)

[193] G. Hill, Acta Mathematica **8**(1), 1 (1886). DOI 10.1007/BF02417081. URL `http://dx.doi.org/10.1007/BF02417081`

[194] M.G. Minty, F. Zimmermann, *Beam techniques: Beam control and manipulation* (1999)

[195] Performance of the ATLAS Inner Detector Track and Vertex Reconstruction in the High Pile-Up LHC Environment. Tech. Rep. ATLAS-CONF-2012-042, CERN, Geneva (2012)

[196] C. Moller, K. Danske Vidensk. Selsk., Mat.-fys. Medd. **23** (1945)

[197] S. van der Meer, Calibration of the effective beam height in the ISR. Tech. Rep. CERN-ISR-PO-68-31. ISR-PO-68-31, CERN, Geneva (1968)

[198] S. Chatrchyan, et al., JINST **3**, S08004 (2008). DOI 10.1088/1748-0221/3/08/S08004

[199] K. Aamodt, et al., JINST **3**, S08002 (2008). DOI 10.1088/1748-0221/3/08/S08002

[200] J. Alves, A. Augusto, et al., JINST **3**, S08005 (2008). DOI 10.1088/1748-0221/3/08/S08005

[201] O. Adriani, et al., JINST **3**, S08006 (2008). DOI 10.1088/1748-0221/3/08/S08006

[202] J. Pinfold, et al., Technical Design Report of the MoEDAL Experiment. Tech. rep. (2009)

[203] G. Anelli, et al., JINST **3**, S08007 (2008). DOI 10.1088/1748-0221/3/08/S08007

[204] M. Benedikt, P. Collier, V. Mertens, J. Poole, K. Schindl, LHC Design Report. 3. The LHC injector chain. Tech. rep. (2004)

[205] *ATLAS detector and physics performance: Technical Design Report, 1.* Technical Design Report ATLAS (CERN, Geneva, 1999). Electronic version not available

[206] J. Beringer, et al., Phys. Rev. D **86**, 010001 (2012). DOI 10.1103/PhysRevD.86.010001. URL `http://link.aps.org/doi/10.1103/PhysRevD.86.010001`

[207] N. Wermes, G. Hallewel, *ATLAS pixel detector: Technical Design Report.* Technical Design Report ATLAS (CERN, Geneva, 1998)

[208] A. Ahmad, Z. Albrechtskirchinger, P. Allport, J. Alonso, L. Andricek, et al., Nucl.Instrum.Meth. **A578**, 98 (2007). DOI 10.1016/j.nima.2007.04.157

[209] B. Dolgoshein, Nucl.Instrum.Meth. **A326**, 434 (1993). DOI 10.1016/0168-9002(93)90846-A

[210] P. Jenni, M. Nessi, M. Nordberg, Zero Degree Calorimeters for ATLAS. Tech. Rep. LHCC-I-016. CERN-LHCC-2007-001, CERN, Geneva (2007)

[211] C.W. Fabjan, F. Gianotti, Rev. Mod. Phys. **75**, 1243 (2003). DOI 10.1103/RevModPhys.75.1243. URL `http://link.aps.org/doi/10.1103/RevModPhys.75.1243`

[212] T. Crane, M. Baker, *Neutron Detectors in: Passive Nondestructive Assay of Nuclear Materials* (Los Alamos, 1991)

[213] V. Lindenstruth, I. Kisel, Nuclear Instruments and Methods in Physics Research Section A: Accelerators, Spectrometers, Detectors and Associated Equipment **535**(12), 48 (2004). DOI http://dx.doi.org/10.1016/j.nima.2004.07.267. URL `http://www.sciencedirect.com/science/article/pii/S0168900204015748`. Proceedings of the 10th International Vienna Conference on Instrumentation

[214] Performance of the Minimum Bias Trigger in p-p Collisions at Sqrt(s) = 900 GeV. Tech. Rep. ATLAS-CONF-2010-025, CERN, Geneva (2010)

[215] P. Jenni, M. Nessi, ATLAS Forward Detectors for Luminosity Measurement and Monitoring. Tech. Rep. CERN-LHCC-2004-010. LHCC-I-014, CERN, Geneva (2004). URL `https://cds.cern.ch/record/721908`. Revised version number 1 submitted on 2004-03-22 14:56:11

[216] T.L. Cheng, P. Teixeira-Dias, Sensitivity of ATLAS to FCNC single top quark production. Tech. Rep. ATL-PHYS-PUB-2006-029. ATL-COM-PHYS-2006-056, CERN, Geneva (2006). URL `http://cds.cern.ch/record/976360`. A revised version has been uploaded.

[217] S. Hassani, L. Chevalier, E. Lancon, J. Laporte, R. Nicolaidou, et al., Nucl.Instrum.Meth. **A572**, 77 (2007). DOI 10.1016/j.nima.2006.10.340

[218] T. Lagouri, D. Adams, K. Assamagan, M. Biglietti, G. Carlino, et al., IEEE Trans.Nucl.Sci. **51**, 3030 (2004). DOI 10.1109/TNS.2004.839102

[219] G. Ordonez Sanz, Muon identification in the ATLAS calorimeters. Ph.D. thesis, Nijmegen U., Amsterdam (2009). Presented on 12 Jun 2009

[220] D. Bettis, Celestial mechanics **8**(2), 229 (1973). DOI 10.1007/BF01231421. URL `http://dx.doi.org/10.1007/BF01231421`

[221] J. Dormand, P. Prince, Journal of Computational and Applied Mathematics **6**(1), 19 (1980). DOI http://dx.doi.org/10.1016/0771-050X(80)90013-3. URL `http://www.sciencedirect.com/science/article/pii/0771050X80900133`

[222] H. Bethe, Annalen der Physik **397**(3), 325 (1930). DOI 10.1002/andp.19303970303. URL `http://dx.doi.org/10.1002/andp.19303970303`

[223] L. Landau, J. Exp. Phys. **8**, 201 (1944)

[224] P. Vavilov, Sov. Phys. JETP **5**, 749 (1957)

[225] D. Lopez Mateos, E.W. Hughes, A. Salzburger, A Parameterization of the Energy Loss of Muons in the ATLAS Tracking Geometry. Tech. Rep. ATL-MUON-PUB-2008-002. ATL-COM-MUON-2008-001, CERN, Geneva (2008)

[226] K. Nikolopoulos, D. Fassouliotis, C. Kourkoumelis, A. Poppleton, IEEE Transactions on Nuclear Science **54**, 1792 (2007). DOI 10.1109/TNS.2007.905157

[227] V.L. Highland, Nucl.Instrum.Meth. **129**, 497 (1975). DOI 10.1016/0029-554X(75)90743-0

[228] G. Moliere, Z.Naturforsch. **A2**, 133 (1947)

[229] A. Airapetian, Others, *ATLAS detector and physics performance: Technical Design Report, 1.* Technical Design Report ATLAS (CERN, Geneva, 1999). Electronic version not available

[230] T.G. Cornelissen, M. Elsing, I. Gavrilenko, J.F. Laporte, W. Liebig, M. Limper, K. Nikolopoulos, A. Poppleton, A. Salzburger, Journal of Physics: Conference Series **119**(3), 032013 (2008). URL `http://stacks.iop.org/1742-6596/119/i=3/a=032013`

[231] R.O. Duda, P.E. Hart, Commun. ACM **15**(1), 11 (1972). DOI 10.1145/361237.361242. URL `http://doi.acm.org/10.1145/361237.361242`

[232] E. Moyse, O. Ouraou, D. Quarrie, N. van Eldik, MUON RECONSTRUCTION INTEGRATION TASK FORCE: FINAL REPORT. Tech. Rep. ATL-COM-SOFT-2011-003, CERN, Geneva (2010)

[233] D. Adams, K.A. Assamagan, M. Biglietti, G. Carlino, G. Cataldi, et al., (2003)

[234] S. Tarem, Z. Tarem, N. Panikashvili, O. Belkind, in *Nuclear Science Symposium Conference Record, 2006. IEEE*, vol. 1 (2006), vol. 1, pp. 617–621. DOI 10.1109/NSSMIC.2006.356230

[235] G. Cowan, *Statistical Data Analysis* (Oxford University Press, 1998)

[236] O. Djuvsland, J. Nystrand, Phys.Rev. **C83**, 041901 (2011). DOI 10.1103/PhysRevC.83.041901. [arXiv:1011.4908]

[237] G. Aad, et al., (2014). [arXiv:1408.3179]

[238] M.J. Woudstra, the Atlas Collaboration, Journal of Physics: Conference Series **513**(1), 012040 (2014). URL `http://stacks.iop.org/1742-6596/513/i=1/a=012040`

[239] S. Weinzierl, (2000). [arXiv:hep-ph/0006269]

[240] S. Alioli, P. Nason, C. Oleari, E. Re, JHEP **0807**, 060 (2008). DOI 10.1088/1126-6708/2008/07/060. [arXiv:0805.4802]

[241] T. Sjostrand, S. Mrenna, P.Z. Skands, Comput.Phys.Commun. **178**, 852 (2008). DOI 10.1016/j.cpc.2008.01.036. [arXiv:0710.3820]

[242] J. Alwall, A. Ballestrero, P. Bartalini, S. Belov, E. Boos, et al., Comput.Phys.Commun. **176**, 300 (2007). DOI 10.1016/j.cpc.2006.11.010. [arXiv:hep-ph/0609017]

[243] A. Buckley, J. Butterworth, S. Gieseke, D. Grellscheid, S. Hoche, et al., Phys.Rept. **504**, 145 (2011). DOI 10.1016/j.physrep.2011.03.005. [arXiv:1101.2599]

[244] S. Alioli, P. Nason, C. Oleari, E. Re, JHEP **1006**, 043 (2010). DOI 10.1007/JHEP06(2010) 043. [arXiv:1002.2581]

[245] S. Agostinelli, et al., Nucl.Instrum.Meth. **A506**, 250 (2003). DOI 10.1016/S0168-9002(03) 01368-8

[246] H.L. Lai, M. Guzzi, J. Huston, Z. Li, P.M. Nadolsky, et al., Phys.Rev. **D82**, 074024 (2010). DOI 10.1103/PhysRevD.82.074024. [arXiv:1007.2241]

[247] H. Janssen, et al., Phys.Lett. **B228**, 273 (1989). DOI 10.1016/0370-2693(89)90670-9

[248] A. Sherstnev, R. Thorne, Eur.Phys.J. **C55**, 553 (2008). DOI 10.1140/epjc/ s10052-008-0610-x. [arXiv:0711.2473]

[249] X.N. Wang, M. Gyulassy, Phys.Rev. **D44**, 3501 (1991). DOI 10.1103/PhysRevD.44.3501

[250] G. Aad, et al., Phys.Lett. **B707**, 330 (2012). DOI 10.1016/j.physletb.2011.12.056. [arXiv:1108.6018]

[251] Performance of the ATLAS Minimum Bias and Forward Detector Triggers in 2011 Heavy Ion Run. Tech. Rep. ATLAS-CONF-2012-122, CERN, Geneva (2012)

[252] Non-collision backgrounds as measured by the ATLAS detector during the 2010 proton-proton run. Tech. Rep. ATLAS-CONF-2011-137, CERN, Geneva (2011)

[253] J. Boudreau, J.Phys.Conf.Ser. **452**(1), 012013 (2013). DOI 10.1088/1742-6596/452/1/012013

[254] G. Aad, et al., Eur.Phys.J. **C74**(8), 2965 (2014). DOI 10.1140/epjc/s10052-014-2965-5. [arXiv:1406.0392]

[255] S.D. Drell, T.M. Yan, Phys. Rev. Lett. **25**, 316 (1970). DOI 10.1103/PhysRevLett.25.316. URL `http://link.aps.org/doi/10.1103/PhysRevLett.25.316`

[256] G. Aad, et al., (2015). [arXiv:1502.05686]

[257] G. Aad, et al., Eur.Phys.J. **C72**, 2241 (2012). DOI 10.1140/epjc/s10052-012-2241-5. [arXiv:1209.4446]

[258] G. Aad, et al., (2014). [arXiv:1410.4031]

[259] S. Chatrchyan, et al., Phys.Lett. **B715**, 66 (2012). DOI 10.1016/j.physletb.2012.07.025. [arXiv:1205.6334]

[260] T. Dorigo, (2003). [arXiv:hep-ex/0306008]

[261] Gianluca Petrillo and the Cdf and D0 collaborations, Journal of Physics: Conference Series **452**(1), 012031 (2013). URL `http://stacks.iop.org/1742-6596/452/i=1/a=012031`

[262] S. Chatrchyan, et al., Eur.Phys.J. **C72**, 1945 (2012). DOI 10.1140/epjc/s10052-012-1945-x. [arXiv:1202.2554]

[263] B. Abelev, et al., Phys.Rev.Lett. **109**, 112301 (2012). DOI 10.1103/PhysRevLett.109.112301. [arXiv:1205.6443]

[264] Muon Momentum Resolution in First Pass Reconstruction of pp Collision Data Recorded by ATLAS in 2010. Tech. Rep. ATLAS-CONF-2011-046, CERN, Geneva (2011)

[265] P.M. Nadolsky, H.L. Lai, Q.H. Cao, J. Huston, J. Pumplin, et al., Phys.Rev. **D78**, 013004 (2008). DOI 10.1103/PhysRevD.78.013004. [arXiv:0802.0007]

[266] S. Alekhin, J. Blumlein, S. Klein, S. Moch, Phys.Rev. **D81**, 014032 (2010). DOI 10.1103/PhysRevD.81.014032. [arXiv:0908.2766]

[267] S. Alekhin, J. Blumlein, S.O. Moch, PoS **DIS2010**, 021 (2010). [arXiv:1007.3657]

[268] A. Martin, W. Stirling, R. Thorne, G. Watt, Eur.Phys.J. **C63**, 189 (2009). DOI 10.1140/epjc/s10052-009-1072-5. [arXiv:0901.0002]

[269] R.D. Ball, V. Bertone, F. Cerutti, L. Del Debbio, S. Forte, et al., Nucl.Phys. **B849**, 296 (2011). DOI 10.1016/j.nuclphysb.2011.03.021. [arXiv:1101.1300]

[270] D. Bourilkov, R.C. Group, M.R. Whalley, (2006). [arXiv:hep-ph/0605240]

[271] Measurement of the $W \to \mu\nu$ charge asymmetry and centrality dependence in Pb+Pb collisions at $\sqrt{s_{NN}} = 2.76 \, TeV$ with the ATLAS detector. Tech. Rep. ATLAS-CONF-2013-106, CERN, Geneva (2013)

[272] S. Chatrchyan, et al., JHEP **1110**, 132 (2011). DOI 10.1007/JHEP10(2011)132. [arXiv:1107.4789]

[273] T. Aaltonen, et al., Phys.Rev.Lett. **102**, 181801 (2009). DOI 10.1103/PhysRevLett.102.181801. [arXiv:0901.2169]

[274] C. Tarbert, D. Watts, D. Glazier, P. Aguar, J. Ahrens, et al., Phys.Rev.Lett. **112**(24), 242502 (2014). DOI 10.1103/PhysRevLett.112.242502. [arXiv:1311.0168]

[275] S. Abrahamyan, Z. Ahmed, H. Albataineh, K. Aniol, D. Armstrong, et al., Phys.Rev.Lett. **108**, 112502 (2012). DOI 10.1103/PhysRevLett.108.112502. [arXiv:1201.2568]

[276] P.F. kesson, T. Atkinson, M.J. Costa, M. Elsing, S. Fleischmann, A.N. Gaponenko, W. Liebig, E. Moyse, A. Salzburger, M. Siebel, ATLAS Tracking Event Data Model. Tech. Rep. ATL-SOFT-PUB-2006-004. ATL-COM-SOFT-2006-005. CERN-ATL-COM-SOFT-2006-005, CERN, Geneva (2006)